FOSSIL ENERGY

DOE/BC/15211-14
(OSTI ID: 784112)

INVESTIGATION OF MULTISCALE AND MULTIPHASE FLOW, TRANSPORT AND REACTION IN HEAVY OIL RECOVERY PROCESSES

Annual Report
May 1999-May 2000

By:
Yanis C. Yortsos

Date Published: August 2001

Work Performed Under Contract No. DE-AC26-99BC15211

University of Southern California
Los Angeles, California

National Energy Technology Laboratory
National Petroleum Technology Office
U.S. DEPARTMENT OF ENERGY
Tulsa, Oklahoma

DOE/BC/15211-14
Distribution Category UC-122

Investigation of Multiscale and Multiphase Flow, Transport and Reaction in Heavy Oil Recovery Processes

By
Yanis C. Yortsos

August 2001

Work Performed Under DE-AC26-99BC15211

Prepared for
U.S. Department of Energy
Assistant Secretary for Fossil Energy

Tom Reid, Project Manager
National Petroleum Technology Office
P.O. Box 3628
Tulsa, OK 74101

Prepared by
Petroleum Engineering Program
Department of Chemical Engineering
University of Southern California
Los Angeles, CA 90089-1211

Table of Contents

ABSTRACT v
ACKNOWLEDGEMENTS vii
INTRODUCTION 1
PUBLICATIONS 3

I. INTERNAL DRIVES 5
A Note on the Evaporation of a Stagnant Liquid 7
A 2-D Pore-Network Model of the Drying of Single-Component Liquids in Porous Media 29

II. VAPOR-LIQUID FLOWS 71
Stability of Heat Pipes in Vapor-Dominated Systems 73
The Shape of a Gravity Finger 85

III. DYNAMICS OF IN-SITU COMBUSTION AT VARIOUS SCALES 113
A Pore-Networks Model for In-Situ Combustion 115
Dynamics of Combustion Fronts 125

IV. INSTABILITIES, HETEROGENEITY AND UPSCALING 155
Displacement in Heterogeneous Porous Media with Non-Monotonic Profiles: Stability Analysis 157
Identification of the Permeability field of a Porous Media from the Injection of a Passive Tracer 181

ABSTRACT

This is the first annual report for contract DE-AC26-99BC15211. The report describes progress made in the various thrust areas of the project, which include internal drives for oil recovery, vapor-liquid flows, combustion and reaction processes, instabilities and upscaling and the flow of fluids with yield stress. The report is mainly a compilation of previous topical reports published in the first year of the project, which ended on May 9, 2000. Advances in multiple processes and at various scales are described.

In the area of internal drives, significant progress was made in the modeling of gas-phase growth driven by mass transfer, and in the contexts of drying, evaporation and solution gas-drive processes at the pore-network and continuum scales. In the area of vapor-liquid flows, we describe steady-states and the stability of counter-current vapor-liquid flows, driven by buoyancy. The propagation of a gravity finger in a gas-liquid displacement is also analyzed. In the area of combustion, we report on two studies, one involving pore-network scale modeling, and another involving the propagation of combustion fronts in porous media at the large scale. Finally, in the area of viscous instabilities, upscaling and identification, we report on two studies, one involving the stability of displacements in heterogeneous media, and another on the identification of the permeability heterogeneity from the injection of a passive tracer. On-going work in the area of flow of fluids with yield stress will be reported in future reports.

ACKNOWLEDGEMENTS

This research was possible through the Department of Energy contract DE-AC26-99BC15211, the contribution of which is gratefully acknowledged. Partial support was also provided by Chevron Petroleum Company. The PI would like to express his gratitude to the NPTO Project officers in charge of the contract, Dr. Jerry Casteel and Mr. Thomas Reid for their help and support.

INTRODUCTION

This project is an investigation of various multi-phase and multiscale transport and reaction processes associated with heavy oil recovery. The thrust areas of the project include the following: Internal drives, vapor-liquid flows, combustion and reaction processes, fluid displacements and the effect of instabilities and heterogeneities and the flow of fluids with yield stress. These find respective applications in foamy oils, the evolution of dissolved gas, internal steam drives, the mechanics of concurrent and countercurrent vapor-liquid flows, associated with thermal methods and steam injection, such as SAGD, the in-situ combustion, the upscaling of displacements in heterogeneous media and the flow of foams, Bingham plastics and heavy oils in porous media and the development of wormholes during cold production. Funding of the project is for three years, from May 9, 1999 to May 8, 2002.

In this report, progress made in the various areas outlined above during the first year of the project is described. Work was conducted in all areas, with progress being greater in some areas compared to others, for a variety of circumstances. During the reporting period, a total of up to 8 students plus a post-doctoral associate were supported by the project. A number of publications and 6 topical reports have resulted from this effort. The publications are listed below. The report is essentially, but not exclusively, a compilation of the topical reports.

This report is organized as follows: For each of the four first thrust areas, namely internal drives, vapor-liquid flows, combustion dynamics, and instabilities and heterogeneity, we provide a brief summary of the work performed, followed by two reports each. Work in the thrust area of fluids with yield stress will not be reported here. Although progress was made, the results obtained are preliminary and further work is required before they can become conclusive.

PUBLICATIONS

Lajeunesse, E., Martin J., Rakotomalala, N., Salin, D., and Yortsos, Y.C., "The Threshold of Instability in Miscible Displacements in a Hele-Shaw Cell at High Rates", Phys. Fluids, submitted (2000).

Yiotis, A.G., Stubos, A.K., Bountouvis, A., and Yortsos, Y.C., "A 2-D Pore-Network Model of the Drying of Single-Component Liquids in Porous Media", Adv. Water Res., special issue on Pore-Scale Modeling, accepted (2000).

Yortsos, Y.C., "Immiscible Displacement in Fractured Rocks: Upscaling Issues", Special AGU publication to honor Paul Witherspoon, accepted (2000).

Zhan, L., and Yortsos, Y.C., "Identification of the Permeability Field of a Porous Media from the Injection of a Passive Tracer", Phys. Rev. E, accepted (2000).

Tsimpanogiannis, I.N., Yortsos, Y.C., and Stubos, A.K., "Evaporation of a Stagnant Liquid", Ind. Eng. Chem. Res. **39**, 1505-1513 (2000).

Zhan, L., and Yortsos, Y.C., "Identification of Permeability Heterogeneity from Tracer Displacement: Sensitivity Analysis", proceedings of Conference Tracers and Modelling in Hydrogeology, Tram 2000, Liege, Belgium, pp. 63-73 (May 23-26, 2000).

Shariati, M., and Yortsos, Y.C., "The Effect of Heterogeneity on the Stability of Miscible Displacements in Porous Media", paper presented at the AGU Fall Meeting, San Francisco, CA (December 16, 1999).

Zhan, L., and Yortsos, Y.C., "The Identification of the Permeability Heterogeneity of Porous Media from the Displacement of a Passive Tracer", paper presented at the APS (DFD) Fall Meeting, New Orleans, LA (November 21-23, 1999).

Amili, P. and Yortsos, Y.C., "Stability of Heat Pipes in Vapor-Dominated Systems", paper presented at the ASME Fall Meeting, Nashville, TN (November 14-19, 1999).

Kechagia, P., and Yortsos, Y.C., "A Model Stochastic Equation for Convection-Diffusion Equation in Evolving Porous Media", paper presented at the AIChE Fall Meeting, Dallas, TX (November 1-5, 1999).

I. INTERNAL DRIVES

In many processes associated with heavy oil recovery, internal drives, namely these driven by applied supersaturation in dissolved gases or heat content, are common. These include, but are not limited to the evolution of gas in foamy oils, internal steam drives, the evaporation of volatile components during gas injection or the injection of steam, and other processes. The main result is the growth of a gas phase, which is driven by mass or heat transfer, depending on the kind of the applied supersaturation. We have conducted various studies of this multifaceted problem. In this report, we will present results in two areas, both associated with the evaporation of a liquid in a porous medium. Among others, they find application in the recovery of volatile oil components from a liquid phase in a matrix block in a porous medium. They also find generic applications in drying. The first study describes an analytical mathematical model for the description of the evaporation front in a binary liquid, while the second is the pore-network simulation of drying in a porous medium, driven by the flow of gas. The latter study was a collaborative effort with colleagues from the research institute Demokritos in Athens, Greece. Not described in this report is the on-going effort in the dynamics of gas evolution as a function of the rate of application of the supersaturation for both solution gas and internal steam drives, and the experimental effort under way for understanding the foamy oil process. Both of these are being studied and we hope to report soon on progress along these directions. The issue of the upscaling of the pore-network results to the continuum level will be addressed in the studies in the upscaling thrust area.

A NOTE ON THE EVAPORATION OF A STAGNANT LIQUID

Ioannis N. Tsimpanogiannis, Yanis C. Yortsos and Athanasios K. Stubos

INTRODUCTION

Of interest to certain reservoir engineering applications is the recovery of trapped or immobile oil by its evaporation and subsequent diffusion in a flowing gas. The typical application involves gas injection at high pressures in fractured reservoirs containing light oil (Le Gallo et al. [1]). Oil trapped inside matrix blocks of low permeability evaporates and diffuses in a gas injected at high pressures, which is flowing in the high-permeability fracture network surrounding the porous matrix (see schematic of Figure 1a). A similar problem, although at low pressures, arises in the remediation of contaminated soils, where trapped and immobile organic contaminants vaporize, diffuse and are convected away in a flowing gas (soil vapor extraction, Ho et al. [2]).

The problem involves a variety of processes: diffusion and convection in the gas phase, diffusion, capillary and viscous effects in the liquid phase, heat transfer and vapor-liquid equilibria. In a recent paper (Tsimpanogiannis et al. [3]) we analyzed in detail the motion of the liquid-gas interface in a porous medium, for the geometry described above, but under low pressure conditions and in the context of drying. In that work, emphasis was placed on the effect of capillarity and the pore structure on the scaling of the thickness of the drying front (Shaw [4]), using a thermodynamic description based on the dilute limit approximation. Ignored were effects of dissolution of the injected gas in the liquid and of liquid-phase diffusion, both of which are expected at higher pressures.

In this section, we consider a version of the more general problem, with main objective the understanding of the effect of higher pressures on the velocity of the gas-liquid interface. Experimental evidence (Le Romancer et al. [5]) suggests that high-pressure gas injection results under certain conditions in a decrease of the rate of the interface motion, a result that may be due to gas dissolution and diffusion in the liquid phase. To explore this possibility, we consider in this section a simple 1-D model of this process as illustrated schematically in Figure 1b. A liquid A, originally occupying a semi-infinite medium, is subject to evaporation

and diffusion in a flowing gas B, the composition of which at the top of the medium (at $z = 0$) remains constant. Due to the possible high pressure in the gas, component B may solubilize and counter-diffuse in the liquid phase. For the sake of generality, the liquid is taken to consist initially of a binary mixture of A and B, of mole fraction $x_{A\infty}$. Contrary to our previous work [3], we neglect effects of the pore microstructure, which give rise to 3-D fronts. Such effects can be included in a relatively straight forward analysis, but will not be considered here.

The isothermal, one-dimensional evaporation and diffusion of a solute through a stagnant gas in a tube or a channel, is often referred to as *Stefan diffusion.* The problem analyzed here can also be considered as a variation of the Stefan problem, under somewhat different process and boundary conditions. We note that in the standard references (e.g. Bird et al. [6], Slattery [7], and Taylor and Krishna [8]) unsteady-state evaporation is treated in the dilute-limit approximation, under the assumption that the gas-liquid interface is stationary. Slattery and Mhetar [9] considered evaporation of a liquid in a long vertical tube by relaxing the assumption of a stationary interface, while Mhetar and Slattery [10] modeled the problem of the evaporation of a binary liquid in the same geometry by also including diffusion in the liquid. Our problem is similar to the latter, although differences exist in the specific geometries considered, as well as in the fact that we consider solubilization and diffusion of component B in the liquid, which is expected at higher pressures.

In the following, we present the mathematical formulation of the problem, in which the porous medium is treated as an equivalent continuum. Because the emphasis is on understanding thermodynamic and transport effects, the formulation is relevant to the problem in a tube. It is certainly acknowledged that pore structure will affect diffusion, the formulation of the problem, and the motion and dimensionality of the interface. However, these effects are not in the scope of this investigation. A similarity solution is derived, based on which we analyze the effects of the ratio of diffusivities, pressure, initial composition and temperature on the velocity of the gas-liquid interface. The analysis provides insight on the relevant mass transfer and phase equilibria mechanisms, and can be used to model the more complex interface dynamics in an actual porous medium, where pore-structure effects are important.

MATHEMATICAL FORMULATION

Consider the problem described schematically in Figure 1b. The condensible component A in the gas phase satisfies the mass balance

$$\frac{\partial c_A^v}{\partial t} + \frac{\partial N_{Az}^v}{\partial z} = 0 \tag{1}$$

where N_{Az}^v is the z-component of the molar flux of A in the gas phase, expressed for a binary mixture as

$$N_{Az}^v = -c^v \mathcal{D}_{AB}^v \frac{\partial y_A}{\partial z} + y_A (N_{Az}^v + N_{Bz}^v) \tag{2}$$

Here, c_A^v is the molar concentration, y_A is the molar fraction of A ($c_A^v = c^v y_A$) and $\mathcal{D}_{AB}^v$ is the binary diffusion coefficient in the gas phase. Species B is also conserved, hence

$$\frac{\partial c_B^v}{\partial t} + \frac{\partial N_{Bz}^v}{\partial z} = 0 \tag{3}$$

By adding (1) and (3) and assuming that $c^v = c_A^v + c_B^v$ is constant at a fixed pressure, we get

$$N_{Az}^v + N_{Bz}^v = N_z^v(t) \tag{4}$$

The assumption of spatially constant c^v is quite reasonable for the systems and conditions considered below. Similar balances can be written for the liquid phase

$$\frac{\partial c_A^l}{\partial t} + \frac{\partial N_{Az}^l}{\partial z} = 0 \tag{5}$$

and

$$N_{Az}^l = -c^l \mathcal{D}_{AB}^l \frac{\partial x_A}{\partial z} + x_A (N_{Az}^l + N_{Bz}^l) \tag{6}$$

where c_A^l is the molar concentration and x_A the molar fraction of A in the liquid phase, ($c_A^l = c^l x_A$) and $\mathcal{D}_{AB}^l$ is the binary diffusion coefficient in the liquid phase. If, as in the gas phase, we were to also assume that the overall liquid molar concentration is constant, then

$$N_{Az}^l + N_{Bz}^l = N_z^l(t) \approx 0 \tag{7}$$

where the latter equation reflects the boundary condition of no-flux in the far-field. However, this assumption is not valid, in general, especially at higher pressures or when B is highly soluble. For the sake of simplicity, we will proceed first with the assumption of a spatially uniform liquid molar concentration, as this approximation allows for an exact solution to be obtained. The more general problem will be analyzed in more detail in a subsequent section. It will be shown that the error induced does not affect significantly the major conclusions of the section. Implicit in the analysis to follow is also the assumption of spatially uniform diffusion coefficients. While the similarity solution to be developed does not rely on this assumption, we decided to adopt it for simplicity in the calculations and because its effect was found not to be significant.

(i). Spatially constant overall molar concentration

With the assumption of constant overall concentration, the balances for components A and B, equations (1) and (5), respectively, become

$$\frac{\partial y_A}{\partial t} + \frac{N_z^v(t)}{c^v}\frac{\partial y_A}{\partial z} = \mathcal{D}_{AB}^v \frac{\partial^2 y_A}{\partial z^2} \tag{8}$$

and

$$\frac{\partial x_A}{\partial t} = \mathcal{D}_{AB}^l \frac{\partial^2 x_A}{\partial z^2} \tag{9}$$

Concentration fields are coupled at the interface (subscript e) by the following mass balances for the two species A and B

$$M_A N_{Az}^v - \rho_{Ae}^v v_z^I = M_A N_{Az}^l - \rho_{Ae}^l v_z^I \quad \text{at} \quad z = f(t) \tag{10}$$

$$M_B N_{Bz}^v - \rho_{Be}^v v_z^I = M_B N_{Bz}^l - \rho_{Be}^l v_z^I \quad \text{at} \quad z = f(t) \tag{11}$$

where ρ_{Ae}^l and ρ_{Be}^l denote mass densities of A and B in the liquid phase, respectively, hence $\rho_{Ae}^l = x_{Ae} c^l M_A$ and $\rho_{Be}^l = x_{Be} c^l M_B$; ρ_{Ae}^v and ρ_{Be}^v denote mass densities of A and B in the gas phase, respectively, hence $\rho_{Ae}^v = y_{Ae} c^v M_A$ and $\rho_{Be}^v = y_{Be} c^v M_B$; $f(t)$ denotes the position of

the interface, and v_z^I is the velocity of the gas-liquid interface. Thermodynamic equilibrium calculations at the interface (Prausnitz et al. [11]) or experimental data will be used to determine the interfacial compositions y_{Ae} and x_{Ae} as functions of P and T. The molar densities in the gas and liquid phase can be calculated from standard equations of state (for example the Peng-Robinson equation of state; Peng and Robinson [12]). The problem is completed by specifying far-field conditions. At the place where gas in injected ($z = 0$) we have $y_A = 0$, while initially and far from the interface in the liquid, the molar fraction is fixed ($x_A = x_{A\infty}$). This results in the counter-diffusion of A and B in the liquid phase, in addition to their counter-diffusion in the gas phase.

The solution of this problem admits a similarity solution using the similarity variable $\eta = \frac{z}{2\sqrt{\mathcal{D}_{AB}^v t}}$. We also take

$$f(t) = 2\lambda\sqrt{\mathcal{D}_{AB}^v t} \quad \text{and} \quad N_z^v(t) = \frac{\beta\sqrt{\mathcal{D}_{AB}^v}}{\sqrt{t}} \tag{12}$$

where λ is a dimensionless parameter to be determined, and β has dimensions of molar density (mol/volume). In terms of these similarity variables, the mass balances become

$$y_A'' + 2y_A'(\eta - \phi^v) = 0 \quad \text{in} \quad 0 < \eta < \lambda \tag{13}$$

and

$$x_A'' + 2\alpha^2 x_A'\eta = 0 \quad \text{in} \quad \lambda < \eta \tag{14}$$

where primes denote derivative with respect to η and we have denoted

$$\phi^v = \frac{\beta}{c^v} \quad , \quad \alpha = \sqrt{\frac{\mathcal{D}_{AB}^v}{\mathcal{D}_{AB}^l}} \tag{15}$$

The two equations (14) and (15) are subject to the interfacial conditions (10) and (11) (in the appropriate dimensionless form) and the following boundary conditions

$$y_A = 0 \ \text{ at } \ \eta = 0 \qquad \text{and} \qquad y_A = y_{Ae} \ \text{ at } \ \eta = \lambda \tag{16}$$

$$x_A = x_{A\infty} \ \text{ at } \ \eta = \infty \qquad \text{and} \qquad x_A = x_{Ae} \ \text{ at } \ \eta = \lambda \tag{17}$$

Note that because the integration interval in the gas phase is $0 < z < f(t)$ and $f(0) = 0$, there is no need to satisfy an initial condition for that phase (in contrast to the problems considered by Bird et al. [6], Cussler [13], and Slattery and Mhetar [9]). The interfacial conditions (10) and (11) can be recast in the form

$$\beta = -\lambda\left(\frac{\rho^l_{Ae} - \rho^v_{Ae}}{M_A} + \frac{\rho^l_{Be} - \rho^v_{Be}}{M_B}\right) \quad \text{hence} \quad \phi^v = -\lambda\left(\frac{1}{\epsilon} - 1\right) \tag{18}$$

where ϵ is the ratio of the molar densities, $\epsilon \equiv \frac{c^v}{c^l}$, and

$$y'_A - 2\phi^v y_{Ae} + 2\lambda\left(y_{Ae} - \frac{x_{Ae}}{\epsilon}\right) = \frac{x'_A}{\epsilon\alpha^2} \quad \text{at} \quad \eta = \lambda \tag{19}$$

Away from the critical point, $\epsilon \ll 1$.

The solution of the above system is readily found to be

$$\frac{y_A}{y_{Ae}} = \frac{\text{erf}(\eta - \phi^v) + \text{erf}(\phi^v)}{\text{erf}(\lambda - \phi^v) + \text{erf}(\phi^v)} \quad \text{and} \quad \frac{x_A - x_{A\infty}}{x_{Ae} - x_{A\infty}} = \frac{\text{erf}(\alpha\eta) - 1}{\text{erf}(\alpha\lambda) - 1} \tag{20}$$

where the unknown parameter λ satisfies the following transcendental equation

$$\mu(y_{Ae} - x_{Ae}) + \frac{y_{Ae}\exp[-\mu^2]}{\sqrt{\pi}\,[\text{erf}(\mu) - \text{erf}(\mu(1-\epsilon))]} = \frac{(x_{A\infty} - x_{Ae})}{\nu\sqrt{\pi}}\frac{\exp[-(\nu\mu)^2]}{\text{erfc}(\nu\mu)} \tag{21}$$

and where $\mu \equiv \frac{\lambda}{\epsilon}$ and $\nu \equiv \epsilon\alpha$, and erfc is the complementary error function. Equation (21) is the main result of this section. Its solution needs to be determined numerically. Before we proceed, however, it is useful to consider two special cases:

(i) In the limit $\nu \gg 1$, namely when $\alpha \gg \epsilon^{-1}$, $\mu\nu$ is at least of order 1. Using asymptotic properties, equation (21) simplifies to

$$\mu(x_{A\infty} - y_{Ae}) = \frac{y_{Ae}\exp[-\mu^2]}{\sqrt{\pi}\,[\text{erf}(\mu) - \text{erf}(\mu(1-\epsilon))]} \tag{22}$$

We note that the solution of this equation is independent of the mole fraction in the liquid at the interface, x_{Ae}, and in fact it coincides with the general equation (21) when $x_{Ae} = x_{A\infty}$. Therefore, this limit can be viewed as either infinitesimally slow diffusion in the liquid phase ($\alpha \gg 1$) or, equivalently, as a problem in which B does not dissolve in the liquid phase (in which case we need to take $x_{A\infty} = 1$ for self-consistency). Thus, (22) also expresses the solution of the problem in the special case of negligible dissolution in the liquid. This can be

further simplified by taking $\epsilon \ll 1$, as is typically the case, where a further expansion yields the result

$$\mu = \sqrt{\frac{y_{Ae}}{2(x_{A\infty} - y_{Ae})\epsilon}} \quad \text{hence} \quad \lambda = \sqrt{\frac{y_{Ae}\epsilon}{2(x_{A\infty} - y_{Ae})}} \tag{23}$$

From (23) we conclude that in the typical case, λ is of order $\sqrt{\epsilon}$. Some further simplification leads to the dilute solution limit

$$\lambda = \sqrt{\frac{y_{Ae}c^v M_A}{2\rho^l}} \tag{24}$$

In this limit, the convective term vanishes and the concentration field is quasi-static, namely it satisfies a Laplace equation, the base-state profile for the mole fraction being linear. This result was used as the basis for a stability analysis presented in Tsimpanogiannis et al. [3].

(ii) In the other limit, $\nu \ll 1$, on the other hand, parameter μ is small. Using asymptotic properties we find from (21) the result

$$\mu = \frac{y_{Ae}\sqrt{\pi}}{2(x_{A\infty} - x_{Ae})}\alpha \quad \text{hence} \quad \lambda = \frac{y_{Ae}\sqrt{\pi}}{2(x_{A\infty} - x_{Ae})}\alpha\epsilon \tag{25}$$

This equation shows a linear dependence on α, at small values of the latter. Given the definition of α^2 as the ratio of vapor to liquid diffusivities, this case is not physically realistic. However, it serves to illustrate the fact that μ and λ decrease (and vanish) as α decreases to zero (or as the mole fraction x_{Ae} decreases). Thus, accounting for diffusion in the liquid or for solubilization of the gas in the liquid will slow down the evaporation process, as originally conjectured. The specific extent of this decrease needs to be determined from the full equation (21), however.

(ii). Spatially variable overall molar concentration

In the general case, where we need to account for the dependence of the overall molar concentration c^l on the mole fraction x_A, the previous system still admits a similarity solution in terms of the same similarity variable. Corresponding to (14) we now have a system of two equations

$$-\eta\frac{d}{d\eta}\left(x_A c^l\right)+\frac{dN_{Az}^l}{d\eta}=0 \tag{26}$$

$$-\eta\frac{dc^l}{d\eta}+\frac{d}{d\eta}\left(\frac{N_{Az}^l+\frac{c^l}{2\alpha^2}\frac{dx_A}{d\eta}}{x_A}\right)=0 \tag{27}$$

where c^l is a function of x_A (as well as T, and P). These equations are to be solved subject to the boundary conditions (16) and (17) and the far-field condition

$$N_A^l=0 \quad at \quad \eta=\infty \tag{28}$$

Because the dependence $c^l(x_A)$ is generally non-trivial, an analytical solution of this two-point boundary-value problem is not possible, in general. For its solution we used an iterative approach. First, the unknown value of λ was guessed. Results from the previous section were used as initial guesses. Then, the boundary value problem (26)-(28) was solved by a shooting method, for which the solution at the far-field was also provided by the previous analytical solution. The numerical result was then inserted in the interface boundary conditions (10) and (11). If these were satisfied to the desired accuracy, the guessed value of λ was accepted, otherwise, a new value was taken and the algorithm was iterated until a satisfactory convergence was reached. Numerical examples are shown below.

Although the general problem does not admit an analytical solution, it is of interest to note that analytical results are possible in the limit $\alpha\to\infty$. In this limit, it can be shown that the variation of x_A occurs only in a boundary layer around $\eta=\lambda$ of thickness $\frac{1}{\alpha^2}$. In fact, the mole fraction varies in this boundary layer in a form that can be calculated exactly. After some manipulations, one can show that in this case, x_A is implicitly given from the following

$$(\eta-\lambda)\alpha^2=\frac{1}{2\lambda c^l(x_{A\infty})}\int_{x_{Ae}}^{x_A}\frac{c^l(x)dx}{x_{A\infty}-x} \tag{29}$$

Inserting the results from this equation in the interface conditions, one finds, after some algebra, that λ satisfies the same equation as (22), except that now $\epsilon=\frac{c^v}{c^l(x_{A\infty})}$. In other words, at large α, the analytical solution for λ previously developed under the assumption of a constant molar concentration holds, provided that the liquid molar concentration is

evaluated at the far-field molar fraction $x_{A\infty}$. This result will be used below to bound the variation of λ as a function of the thermodynamic variables.

RESULTS AND DISCUSSION

Based on the previous results we explored the effects of the various parameters on the velocity of the interface. For numerical results, the following input data are needed: **(i)** the equilibrium molar fractions at the gas-liquid interface, for both liquid and gas phases, (x_{Ae}, y_{Ae}); **(ii)** the molar concentrations of both liquid and gas mixtures, (c^l, c^v), and their dependence as a function of composition, T and P; and **(iii)** the ratio of the binary diffusion coefficient in the gas phase to the binary diffusion coefficient in the liquid phase, $(\frac{\mathcal{D}^v_{AB}}{\mathcal{D}^l_{AB}})$.

At high pressures, we used experimentally reported data for the equilibrium molar fractions x_{Ae} and y_{Ae}. These were obtained from Azarnoosh and McKetta [14] (n-decane/nitrogen); Poston and McKetta [15] (n-hexane/nitrogen); Sage et al. [16] (n-pentane/methane); and Besserer and Robinson [17] (n-pentane/carbon dioxide). At low pressures, y_{Ae} was approximated as a function of T using the expression $y_{Ae} = \frac{P^s_A(T)}{P}$, where $P^s_A(T)$ is the vapor pressure of the component A, obtained from published correlations (Prausnitz et al. [11]; Himmelblau [18]). For liquid and gas molar densities, high-pressure vapor-liquid equilibrium calculations were performed using the Peng-Robinson [12] cubic equation of state. However, since the equation of state was mainly used for volumetric calculations, a modified version, which includes a volume translation to improve volumetric predictions, was selected (Magoulas and Tassios [19]). For the case in which the liquid overall molar concentration was assumed spatially constant, its value corresponding to x_{Ae} was taken in the calculations. Reliable experimental data for the binary diffusion coefficients were obtained from Sigmund's correlation (Sigmund [20]; da Silva and Belery [21]). However we also considered the sensitivity of the results to various hypothetical cases in which α was kept constant.

First, we examined the validity of the assumption of spatially uniform liquid molar concentration. Figure 2 shows the variation of λ with pressure at a fixed temperature, for the two different systems n-pentane/methane (Fig. 2a) and n-pentane/carbon dioxide (Fig. 2b) and for the two cases analyzed, one in which $c^l = c^l(x_{Ae})$ and another in which c^l was allowed to vary with composition. Sigmund's correlation [20], [21] for the ratio of diffusivities

was considered in both cases. As expected, the two solutions are close to each other at low pressures, but deviate at higher pressures. Their difference increases with pressure, but falls within the range of uncertainty of the diffusion coefficient variation, as will be shown below. Plotted in Figure 2 is also the theoretical result corresponding to $\alpha \gg 1$. As anticipated, this curve bounds from above the velocity of the interface, with the curve corresponding to the uniform concentration assumption serving as a lower bound. Overall, the trend in all cases is an increase of λ as P increases.

Subsequently, we examined the validity of the two asymptotic limits (23) and (25). Figure 3 is a plot of the parameter λ vs. the square root of the diffusivity ratio, α, for the system hexane-nitrogen at 310.93 K and 68.9 bar. Shown are results for both of the previous cases (assumption of spatially constant molar concentration and the more general case). The dotted lines represent the asymptotes described in the two equations (23) and (25), respectively, in the two limits of large and small α, respectively. As expected, the asymptotic solutions represent quite well the behavior of the analytical solution as a function of the diffusivity ratio. The more general solution is also bounded at large α by the theoretical result (dash-dotted line), and is in general larger than the approximate analytical solution. At small values of α, the general solution follows a linear variation with α, similar to the analytical result (25). This dependence can, in fact, be proved analytically, by following a scaling analysis of the general problem in that limit. However, calculating the specific prefactor requires the numerical solution of the full problem. Similar behavior was found for other conditions or systems tested. Figure 3 reveals two important aspects: That, in general, λ is of order 10^{-1} or less, as expected from (23); and that in its expected range of variation $(1, 10^2)$, the diffusivity ratio has an effect on λ which is of the order of two or three, but not of an order of magnitude. This observation essentially provides the answer to the question we raised in the introduction concerning the effect of solubilization and diffusion of component B on the front velocity. In its absence, the rate of movement of the interface is faster. When it is taken into consideration, dissolution and diffusion will slow down the process. The amplification of this slowdown can be significant but it does not exceed an order of magnitude.

An increase in pressure will lead in general to an increase of the rate of movement of

the interface. Figure 4 shows plots of λ vs. pressure for the system n-pentane/methane at 310.93 K, where the initial liquid is pure n-pentane and where we used for simplicity the analytical solution. Plotted are predictions from (21) for various hypothetical cases: in some, parameter α was kept constant and in the range (1-∞), while in another it was taken from the correlation of Sigmund [20]. We note that the overall trend as the pressure increases is an increase in λ and also an increase in its sensitivity to the diffusivity ratio. For the particular correlation of Sigmund [20], the maximum variation of parameter λ is within a factor of two. Analogous results were found for the system n-pentane/carbon dioxide. For the latter, the sensitivity to the liquid diffusion is larger than for the n-pentane/methane shown in Figure 4 in the same range of pressure. For example, for the pressure of 63 bar, where experiments were reported by Le Romancer et al. [5], the effect of diffusion was found to slow down the evaporation front by a larger extent than in the case of n-pentane/methane. This result is consistent with the experimental findings.

The effect of the initial mole fraction of the liquid phase on the evaporation rate of the previous mixture at $P = 103.4$ bar is shown in Figure 5, where again the simpler analytical solution was used. As expected, the highest rate corresponds to an initial liquid mixture at equilibrium ($x_{A\infty} = x_{Ae}$), since in this case there is no dissolution of B in the liquid. Increasing $x_{A\infty}$ leads to an increased dissolution and to an accompanying decrease in the evaporation rate. Consistent with the previous plots, the decrease is generally within a factor of two of the value at equilibrium, regardless of the value of the diffusivity ratio.

More important is the effect of temperature, shown in Figures 6 and 7. Figure 6 shows high-pressure results for the two pairs, n-hexane/nitrogen and n-decane/nitrogen, over a range of temperatures, for various assumptions regarding α, and where the analytical solution is used. We note that the sensitivity to temperature is larger than that of either the pressure or of the initial mole fraction discussed above. This trend is expected. Results in Figure 7 correspond to low pressures ($P = 1$ bar), for the pairs n-pentane/nitrogen and n-decane/nitrogen. The effect of temperature on λ is quite significant. In fact, as the system approaches its boiling point, λ becomes infinitely large (although, strictly speaking, the present analysis will break down near that point). Under these conditions, the dependence of λ on temperature can be extracted by using (21) in the limit of large μ. Then, it is not

difficult to show the result

$$\lambda = \epsilon \sqrt{\frac{\ln\left(\frac{1-\epsilon}{1-y_{Ae}}\right)}{2\epsilon - \epsilon^2}} \tag{30}$$

where we have assumed $x_{A\infty} = 1$. This equation describes the asymptotic behavior of λ as the temperature approaches the boiling point (where $y_{Ae} = 1$). The latter equation appears to describe very well the behavior of λ in this region (see Figure 7).

CONCLUSIONS

In this section we presented a simple 1-D model of the evaporation of a liquid, immobilized or trapped in a porous medium, into a flowing gas outside the medium. The solution of this problem is useful as a building block for the treatment of the more general problem, where pore microstructure, and capillary and viscous effects are taken into account (see [3] for an application in the drying context). We have focused in particular on the effect of dissolution of gas B and its counter-diffusion in liquid A. It was found that the effect on evaporation is to slow down the evaporation rate, as also noted in related experiments in porous media. However, in the typical applications the degree of this reduction is generally within a factor of two or three, but not of an order of magnitude.

References

[1] Le Gallo, Y.; Le Romancer, J.F.; Bourbiaux, B.; Fernandes, G. Mass Transfer in Fractured Reservoirs During Gas Injection: Experimental and Numerical Modeling. SPE Annual Technical Conference and Exhibition, San Antonio, TX, October 1997; paper *SPE 38924*.

[2] Ho, C.K.; Lin, S.-W.; Udell, K.S. Propagation of Evaporation and Condensation Fronts During Multicomponent Soil Vapor Extraction. *J. Contam. Hydrol.* **1994,** *16,* 381.

[3] Tsimpanogiannis, I.N.; Yortsos, Y.C.; Poulou, S.; Kanellopoulos, N.; Stubos, A.K. Scaling Theory of Drying in Porous Media. *Phys. Rev. E.* **1999,** *59,* 4353.

[4] Shaw, T.M. Drying as an Immiscible Displacement Process with Fluid Counterflow. *Phys. Rev. Lett.* **1987,** *59,* 1671.

[5] Le Romancer, J.F.; Defives, D.; Kalaydjian, F.; Fernandes, G. Influence of the Diffusing Gas on the Mechanism of Oil Recovery by Gas Diffusion in Fractured Reservoir.IEA Collaborative Project of Enhanced Oil Recovery Workshop and Symposium, Bergen, Norway, 28-31 August 1994.

[6] Bird, R.B.; Stewart, W.E.; Lightfoot, E.L. *Transport Phenomena*; Wiley: New York, 1960.

[7] Slattery, J.C. *Momentum, Energy and Mass Transfer in Continua*; Krieger: New York, 1978.

[8] Taylor, R.; Krishna, R. *Multicomponent Mass Transfer*; Wiley: New York, 1993.

[9] Slattery, J.C.; Mhetar, V.R. Unsteady-State Evaporation and the Measurement of a Binary Diffusion Coefficient. *Chem. Eng. Sci.* **1997,** *52,* 1511.

[10] Mhetar, V.R.; Slattery, J.C. The Stefan Problem of a Binary Liquid Mixture. *Chem. Eng. Sci.* **1997,** *52,* 1237.

[11] Prausnitz, J.M.; Lichtenhaler, K.N.; de Azevedo, E.G. *Molecular Thermodynamics of Fluid-Phase Equilibria*; Prentice-Hall: Englewood Cliffs, 1986.

[12] Peng, D.Y; Robinson, D.R. A New Two-Constant Equation of State. *Ind. Eng. Chem. Fundamentals.* **1976,** *15,* 59.

[13] Cussler, E.L. *Diffusion: Mass Transfer in Fluid Systems*; 2nd ed.; Cambridge University Press: Cambridge, 1997.

[14] Azarnoosh, A.; McKetta, J.J. Nitrogen-n-Decane System in the Two-Phase Region. *Journal Chem. Eng. Data.* **1963,** *8,* 494.

[15] Poston, R.S; McKetta, J.J. Vapor-Liquid Equilibrium in the n-Hexane- Nitrogen System. *Journal Chem. Eng. Data.* **1966,** *11,* 364.

[16] Sage, B.H.; Reamer, H.H.; Olds, R.H.; Lacey, W.N. Volumetric and Phase Behavior of Methane-n-Pentane System. *Ind. Eng. Chem.* **1942,** *34,* 1108.

[17] Besserer, G.J.; Robinson, D.B. Equilibrium-Phase Properties of the n-Pentane/Carbon Dioxide System. *Journal Chem. Eng. Data.* **1973,** *18,* 416.

[18] Himmelblau, D.M. *Basic Principles and Calculations in Chemical Engineering*; Prentice Hall: New Jersey, 1996.

[19] Magoulas, K; Tassios, D. Thermophysical Properties of n-Alkanes from C_1 to C_{20} and their Predictions for Higher Ones. *Fluid Phase Equilibria.* **1990,** *56,* 119.

[20] Sigmund, P.M. Prediction of Molecular Diffusion at Reservoir Conditions. Part I. Measurement and Prediction of Binary Dense Gas Diffusion Coefficients. *J. Can. Pet. Tech.* April-June **1976,** 48.

[21] da Silva, F.V.; Belery, P. Molecular Diffusion in Naturally Fractured Reservoirs: A Decisive Recovery Mechanism. SPE Annual Technical Conference and Exhibition, San Antonio, TX, October 1989; paper *SPE 19672.*

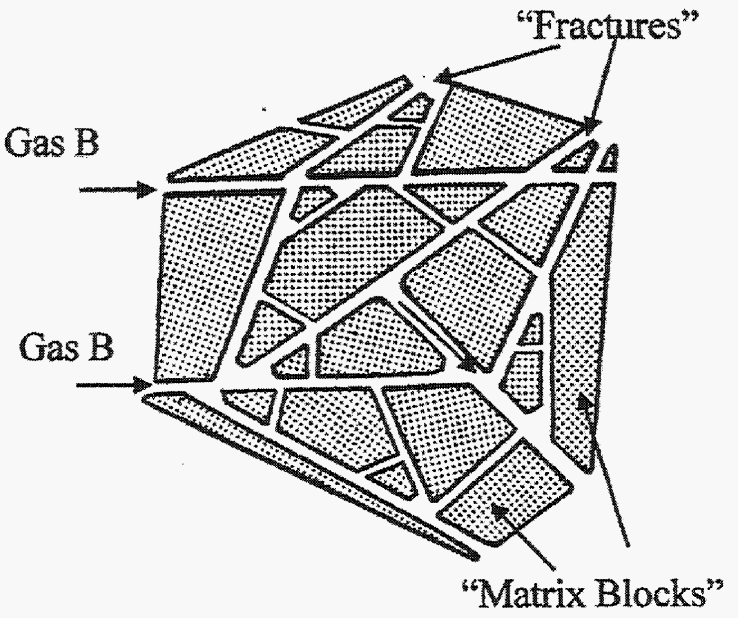

(a)

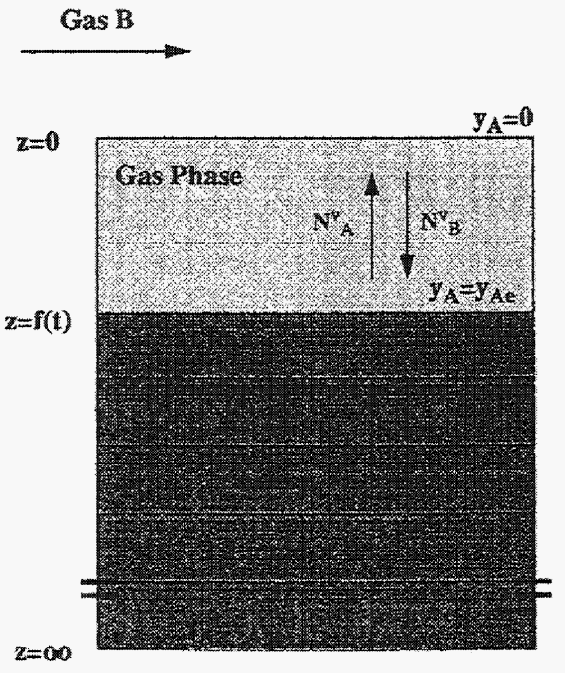

(b)

Figure 1: Schematic of the configuration considered. (a) Gas B flowing in a high permeability fracture network causes evaporation and diffusion of liquid A, trapped in matrix blocks (b) One-Dimension approximation, in which liquid A evaporates and diffuses in the gas phase, containing component B. The latter dissolves and diffuses in the liquid phase.

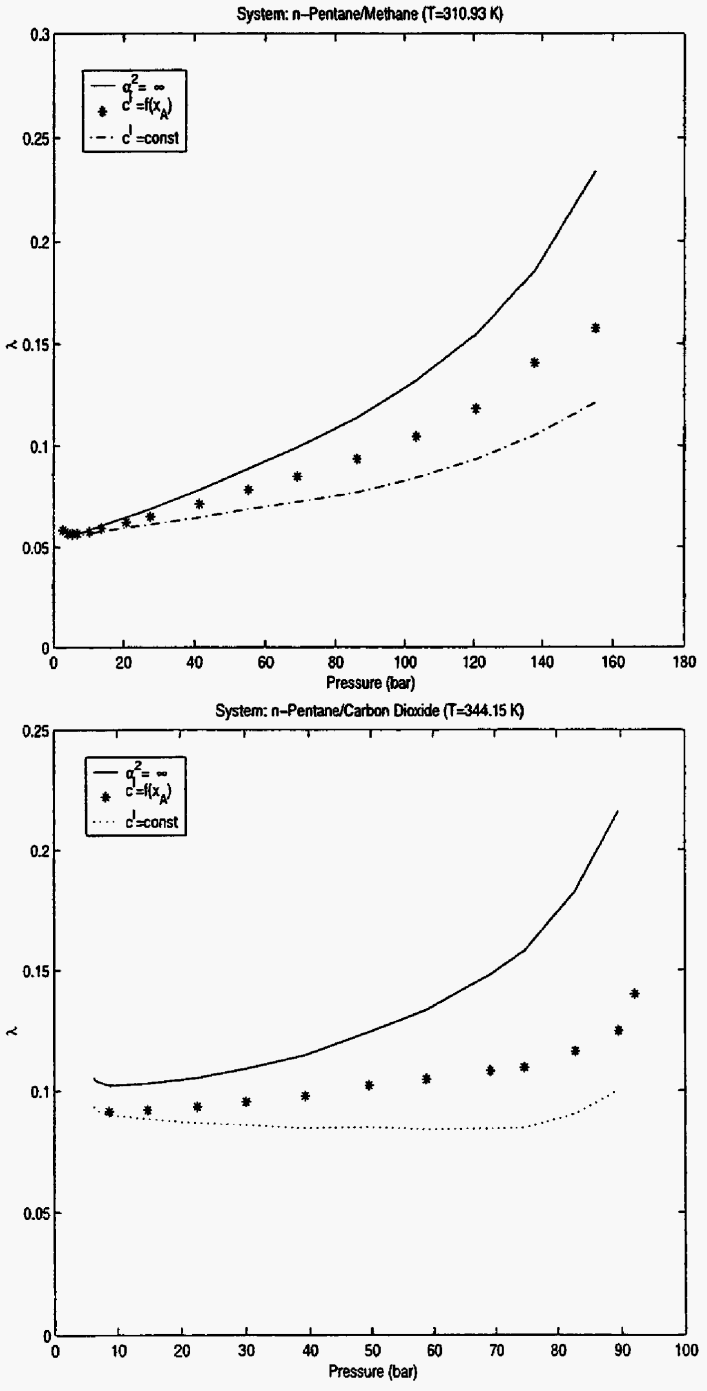

Figure 2: The effect of pressure on the velocity of the evaporation front for the systems: (**a**) n-pentane/methane at 310.93 K, and (**b**) n-pentane/carbon dioxide at 344.15 K. The dashed-dotted line corresponds to the analytical solution where $c^l = c^l(x_{Ae})$, the solid line is the theoretical result at large α, while * denotes the numerical results for the general case where $c^l = c^l(x_A)$.

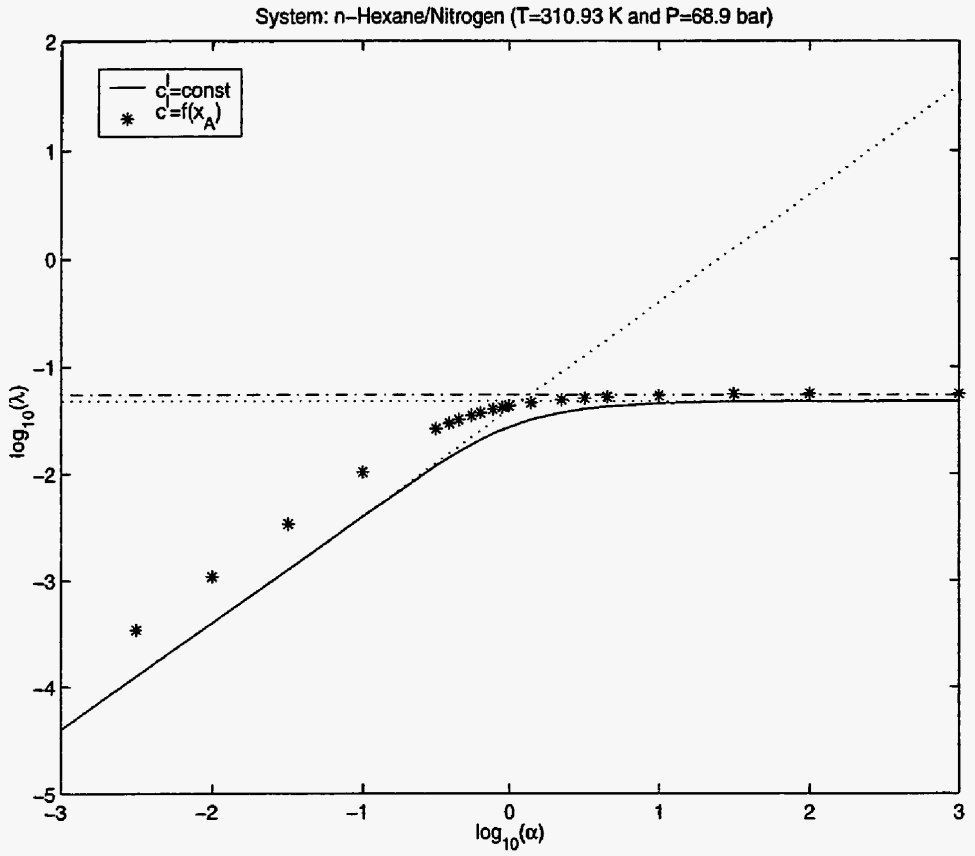

Figure 3: The effect of the ratio of diffusivities $\alpha^2 = \frac{\mathcal{D}_{AB}^v}{\mathcal{D}_{AB}^l}$ (gas-to-liquid), on the velocity of the evaporation front for the system n-hexane/nitrogen at 310.93 K and 68.9 bar. The dotted lines are the asymptotes expressed by (23) and (25), respectively, the dash-dotted line is the theoretical prediction for the general problem at large α.

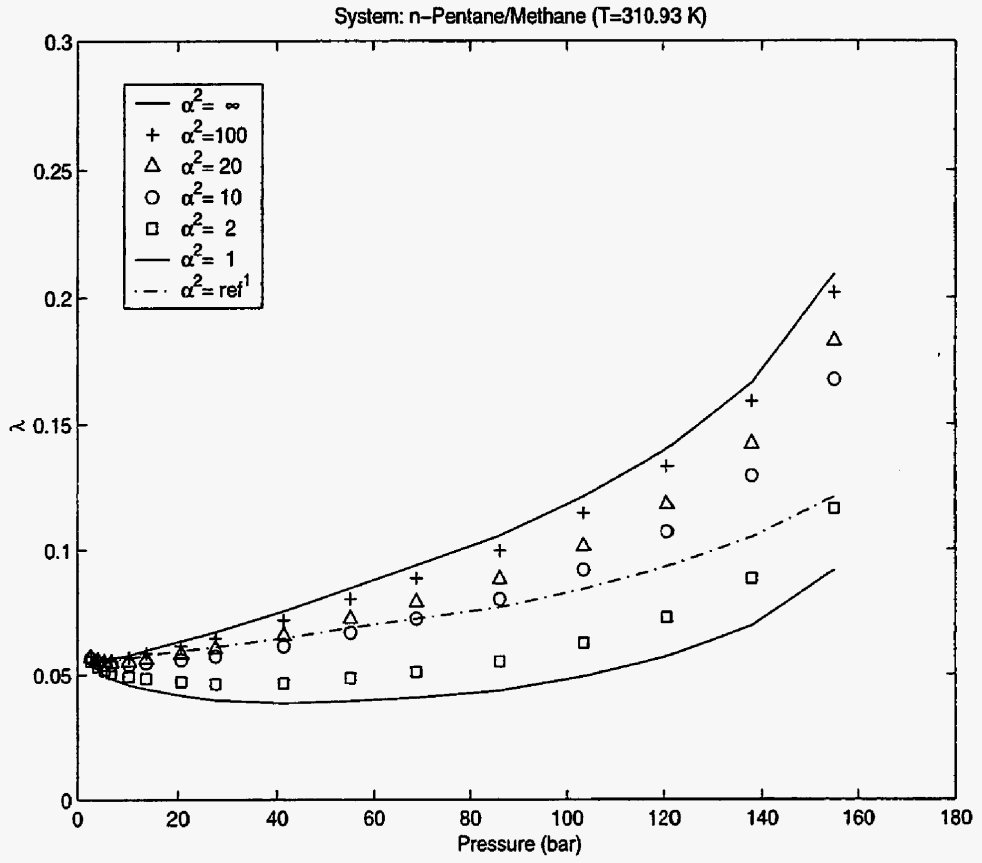

Figure 4: The effect of pressure on the velocity of the evaporation front for the system n-pentane/methane at 310.93 K. The two solid lines correspond to simulations where the ratio of diffusivities is equal to ∞ and 1, respectively. These curves envelope various curves corresponding to ratio of diffusivities equal to 100, 20, 10 and 2 (denoted with symbols +, $\triangle$, o, and $\square$ respectively), as well as a case (ref[1]) using the correlation of Sigmund [20] (denoted by dashed-dotted line).

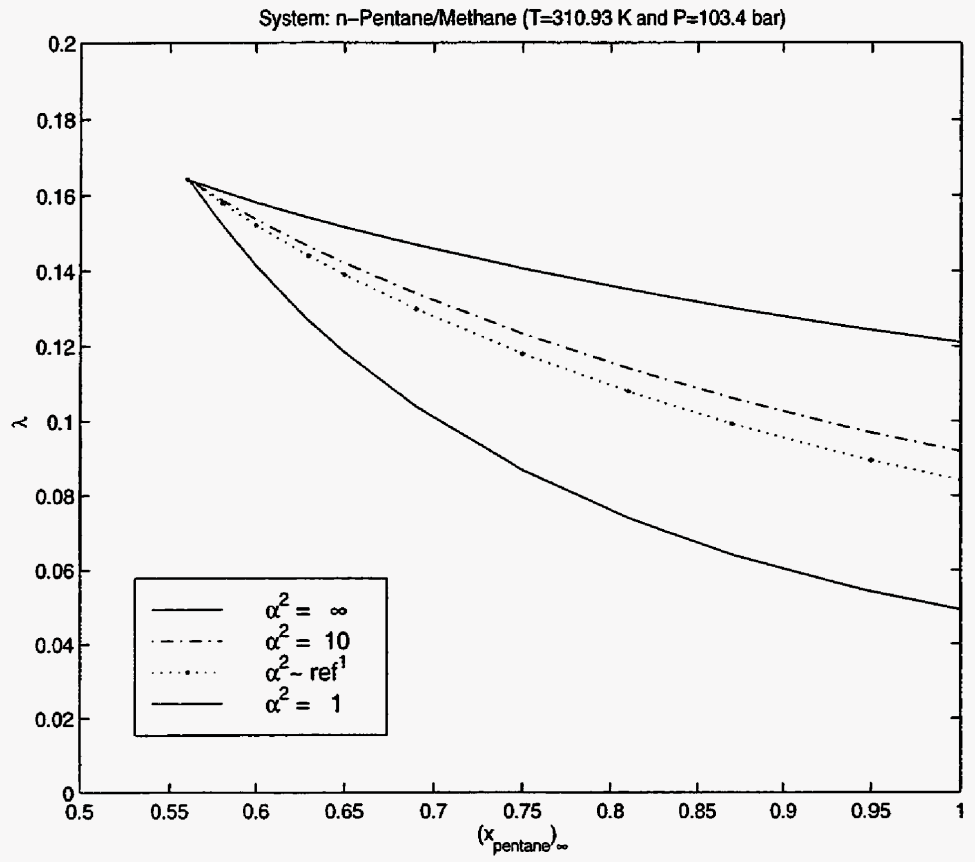

Figure 5: The effect of initial liquid composition on the velocity of the evaporation front for the system n-pentane/methane at 310.93 K and 103.4 bar. The various curves shown correspond to the values of the ratio of diffusivities equal to ∞, 10, and 1, as well as a case (ref[1]) using the correlation of Sigmund [20] (denoted by solid, dash-dotted, solid and dotted, respectively).

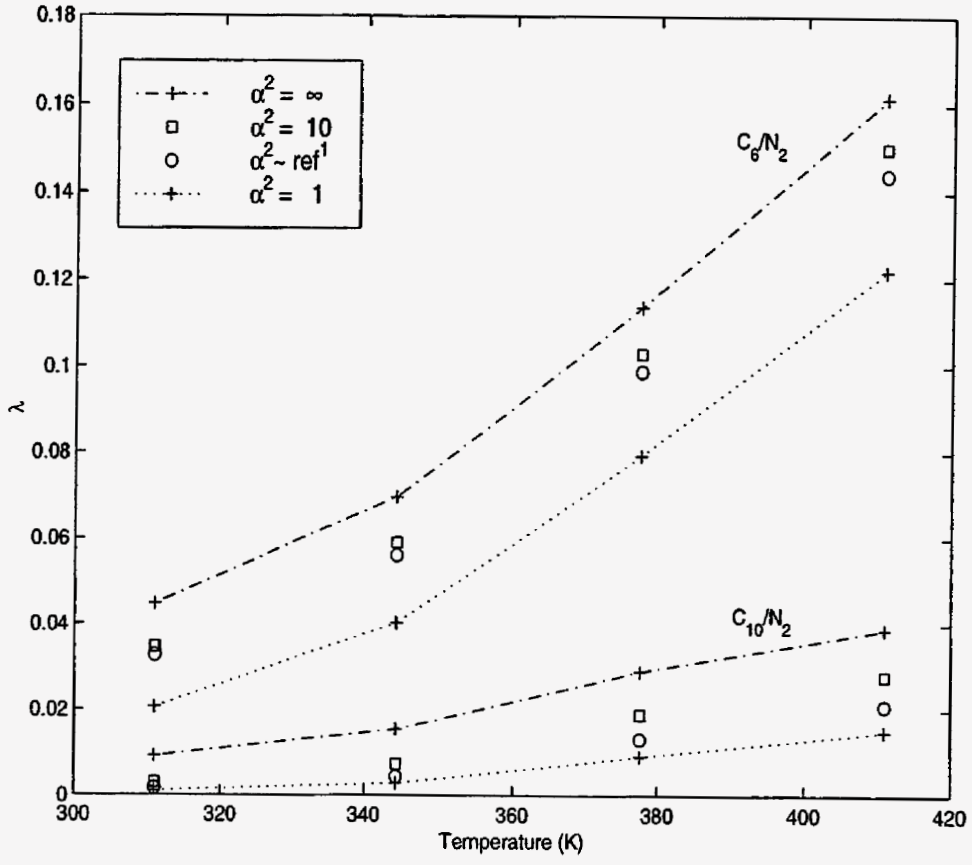

Figure 6: The effect of temperature on the velocity of the evaporation front for the two different systems n-hexane/nitrogen and n-decane/nitrogen at 103.4 bar. The various curves shown correspond to the values of the ratio of diffusivities equal to ∞, 10, and 1, as well as a case (ref[1]) using the correlation of Sigmund [20] (denoted by $- \cdot +$, $\square$, $\cdot \cdot +$, and o, respectively).

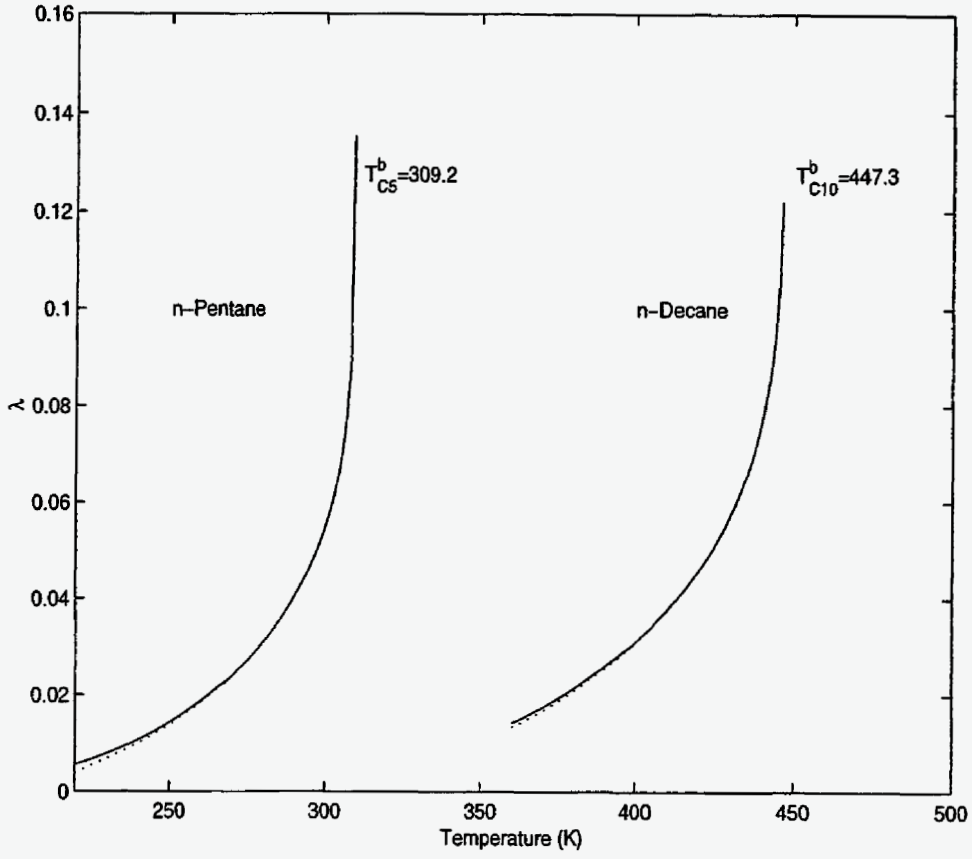

Figure 7: The effect of temperature on the velocity of the evaporation front for the systems n-pentane/nitrogen and n-decane/nitrogen at P=1 bar. The dotted line corresponds to the approximation (30).

A 2-D PORE-NETWORK MODEL OF THE DRYING OF SINGLE-COMPONENT LIQUIDS IN POROUS MEDIA

A.G. Yiotis, A.K. Stubos, A.G. Boudouvis and Y.C. Yortsos

INTRODUCTION

Drying of porous solids is a subject of significant scientific and technological interest in a number of industrial applications including coatings, food, paper, textile, wood, ceramics, building materials, granular materials, electronic devices and pharmaceuticals [1,4,7,19,20,27,28]. In a different context, drying in porous media is involved in distillation and vaporization processes associated with soil remediation [11], as well as in the recovery of volatile hydrocarbons from oil reservoirs by gas injection [15]. A variation of the latter is the main problem addressed here.

Generally, in drying, a single- or multi-component liquid phase gradually evaporates and is removed from the complex porous structure via combined heat and mass transfer processes. The traditional description relies on phenomenological approaches, in which the porous medium is a continuum, the dependent variables, like moisture content, are volume-averaged quantities and the relation of fluxes to gradients is through empirical coefficients [9,17,31,32,33]. Such approaches essentially ignore the effect of the pore microstructure which is of key importance for a quantitative understanding of the process. In fact, drying involves many pore-scale mechanisms, for example the motion of individual gas-liquid menisci residing in the pore space, diffusion in the gas phase (for a single-component liquid) and the liquid phase (for a multi-component liquid), viscous flow in both phases, capillarity and possibly liquid flow through connected films, all of which need to be accounted for. We should note that although it also involves the receding of liquid-vapor interfaces, drying is not a typical external displacement process, like external drainage, which has been well studied in the past. Rather similarities exist to processes like solution gas drive and/or boiling in porous media, where the displacement of the liquid phase is driven internally by mass or heat transfer and which have been only relatively recently investigated [16,25].

The physical context of the problem considered here is schematically depicted in Fig. 1a, which shows an exaggerated schematic of a fractured network. Liquid is trapped in the matrix and may vaporize as a result of an injected purge gas flowing primarily in the

fractures. The actual overall problem is quite complex, requiring the consideration of the network of fractures and the matrix continuum, gas flow and mass transfer in the fracture network and the multi-dimensional mass transfer from the matrix continuum to the fracture network. For simplicity, we will consider the much simpler geometry of the pore-network model shown in Fig. 1b, which involves a 2-D rectangular matrix block, all but one boundaries of which are impermeable to flow and mass transfer. We will also neglect gravity. Extension to 3-D geometries is, in principle, straightforward, although computationally costly, while equally feasible is the consideration of gravity effects. We consider isothermal conditions, under the assumption that heat transfer in the solid operates much faster than mass transfer in the gas phase. Finally, a single-component liquid phase is assumed. It is of note that this approach applies also to the vaporization of trapped NAPL's in low-permeability layers or regions [11].

At any time during the process, evaporation of the liquid leads to the receding of the liquid (drying) front, leaving behind disconnected clusters of liquid and liquid films (in corners of capillaries, or as thin films), the size and location of which change continuously with time. In general, four different spatial regions can be identified [30] (Fig. 1c):

(i) a far-field (from the fracture) region consisting of the initial liquid;

(ii) a region where both liquid and gas phases are macroscopically connected (this region may be absent in certain 2-D square pore-networks for topological reasons);

(iii) a region where the liquid phase is disconnected and consists of individual clusters of variable sizes (trapped islands of liquid); and

(iv) a near-field (to the fracture) region consisting primarily of the connected gas, with the liquid phase in the form of pendular rings, corner films or thin films on the solid surface, the thickness of which is progressively reduced towards a "totally dry" regime.

Evidently, the gas phase is macroscopically continuous in the last three regimes. On the basis of his experiments, Shaw [26] has postulated that liquid films may also provide hydraulic conductivity to the liquid phase in these regimes. We must point out that these four regimes only develop after the end of the Constant Rate Period (CRP). Prior to this, regions (iii) and (iv) cannot arise. Our model accounts for the full evolution of all these regimes, including the CRP, as will be shown below.

The conventional approach to modeling drying is based on a continuum description, the simplest model for which involves only the two limiting regions (the far-field and the near-field), separated by a planar drying front. The latter recedes due to diffusion-controlled mass transfer obeying a square-root time dependence. More sophisticated continuum models have also been developed, as discussed in Luikov [17], and Whitaker [33], among others. Recently, Tsimpanogiannis *et al.* [30] proposed a more complex 1-D model using transverse-averages. Their model involves various coefficients, which need to be evaluated from a pore-network study, however (see also Stubos and Poulou [29]). Tsimpanogiannis *et al.* [30] also developed a theory based on pore-scale considerations, for the description of the scaling properties of the drying front. Specifically, they showed that consideration of viscous effects makes drying equivalent to Invasion Percolation in a Stabilizing Gradient (IPSG) (e.g. see Xu *et al.* [34]). In particular, they emphasized that liquid flow in the porous matrix is driven by capillary pressure gradients (the so-called capillary pumping or capillary wicking effect, Ceaglske and Hougen [2]). The allowance of film flow could be an essential element of that theory. Based on the fact that drying is controlled by both capillarity and diffusion, in contrast to external drainage which is controlled by the injection rate, a power law relation of the evaporating front width with a modified, diffusion-based capillary number was obtained and shown to be compatible with the experimental data of Shaw [26]. However, other important features of the process, including the partition of the liquid phase in various regimes, the mass transfer rates, etc., were not explored.

Following recent trends in describing processes in porous media, several studies in recent years used a pore-network approach to model drying. Key to these approaches is the consideration of mass transfer, elements of which were described by Li and Yortsos [16] and Jia *et al.* [12], among others. Various pore-network models with specific applications to drying were proposed originally by Nowicki *et al.* [18], and more recently in a series of papers by Prat and co-workers [13,14,22,23]. In parallel, Pot *et al.* [21] used lattice-gas automata to simulate evaporation in a 2-D lattice. Nowicki *et al.* [18] presented a numerical simulation of the process at the pore-network level. However, the authors did not expand on the particular patterns and regimes obtained or on the associated effects on drying rates. Prat's studies represent the first attempt to characterize theoretically drying patterns and their rate of change in porous structures. Prat [22] studied the formation of drying patterns

assuming capillary control, neglecting viscous effects and considering mass transfer only by quasi-static diffusion. Laurindo and Prat [14] provided a macroscopic assessment of the importance of liquid films. Based on percolation patterns and isothermal conditions, they computed drying rates by solving a quasi-static diffusion equation in the gas phase. Prat and Bouleux [23] focused on diffusional mass transfer and the effect of gravity on the front structure, but also commented on viscous effects. In earlier experiments using horizontal glass-bead packs (Shaw [26]), viscous forces were found to be important for explaining the formation of an evaporating front (separating continuous liquid from gas) of a finite size. More generally, we expect that advection and viscous effects will have an impact on patterns and drying rates. Existing pore-network models address mostly slow drying, controlled by capillarity and/or gravity and by diffusion, ignoring advection and/or viscous effects. We note that consideration of advection in the gas phase requires knowledge of the pressure field, which is coupled to viscous flow in the two phases and capillary effects. Thus, these two processes must be treated simultaneously.

The present paper is motivated by the above lack of completeness and attempts to shed light to mass transfer and/or viscous effects on the development of drying patterns. It is also motivated by the need to provide reliable coefficients in the appropriate continuum models, and in a sense it represents a continuation of the work by Tsimpanogiannis *et al.* [30], except that film flows are ignored. We consider the isothermal drying (at room temperature) of a porous block, initially saturated with liquid (hexane), subject to flow of air in the fracture and in the absence of gravity. The paper is organized as follows: First, we present details of the pore-network approach. The various mechanisms described previously (diffusion in gas phase, viscous flow in both phases, capillarity and capillary wicking) are addressed. Then, simulation results are obtained for the drying patterns and rates, for various values of the dimensionless parameters governing the process. The latter involve a mass transfer-based capillary number and the Peclet number based on the gas velocity in the fracture. The results are subsequently analyzed using simpler statistical theories, such as Invasion Percolation (IP). Various limiting cases are identified and analyzed. In particular, we pay attention to the trapped islands surrounding the drying front, which due to their screening effect on mass transfer play an important role in the problem. Scale-up issues as

well as effects of various parameters not considered in the pore network are discussed in the last section.

FORMULATION

A discrete pore network model is used to simulate the drying of a porous block. The porous medium is represented by the standard approximation of a 2-D network of spherical pore bodies connected through cylindrical pore throats [3,5] (Figure 1b). The pore bodies serve as containers for either of the two phases and it is assumed that they have no capillary or flow resistance. Therefore, when a liquid-gas interface lies within a pore body, the pressures of both phases are taken to be equal and the interface recedes without any capillary forces restraining its movement (Figure 2b). This simplification can be relaxed at the expense of higher computational cost and could be subject to the uncertainty of the precise pore body geometry. The throats serve as conductors of the flow and mass transfer and they act as capillary barriers. When a stationary liquid meniscus (interface) lies at the entrance of a throat adjacent to a liquid pore (Figure 2a), an interfacial pressure difference, roughly equal to $2\gamma/r$, where γ is the surface tension and r the radius of the throat, develops between the two neighboring pores. The meniscus remains stationary until the pressure difference between the two pores exceeds that capillary pressure threshold. Then the meniscus will recede instantly (Figures 2c and 2d), since it is assumed that the throat has no volume and the gas phase penetrates the pore. In our simulations, pore body and throat radii were uniformly distributed in the range 0.37-0.74 mm and 0.16-0.32 mm, respectively. The lattice length ℓ (pore center to pore center) was taken to be 2 mm.

The 2-D network has three sides impermeable to flow and mass transfer. Alternatively, one could impose periodic boundary conditions at the sides. Along the fourth side runs a fracture, which is represented as 1-D chain of pore bodies and throats. The two ends of the fracture are open to flow and mass transfer. Pore body and throat radii are taken equal to 0.77 mm and 0.275 mm, respectively. We note that the dimensions of the fracture considered in the simulations are comparable to the mean dimensions of the network. This is rather unrealistic, since one would expect that a real fracture would have larger dimensions than the network. However, it is adopted here, in order to emphasize viscous effects in the porous medium. Higher fracture dimensions would require unrealistically high gas flows for

the pressure drop along the fracture to be sufficiently high to exceed the capillary pressure threshold at the throats of the network in direct contact with the fracture. The study of the viscous effects is one of the objectives of this work.

Initially the network is saturated by a single component liquid (hexane). The fracture, however, contains only air at the beginning of the drying process. At one end of the fracture a purge gas (air) is injected at a constant volumetric rate. The concentration of the liquid component vapors is assumed to be zero at the entrance and the exit of the fracture at all times. Perhaps, a more appropriate Dankwerts type boundary condition, in which the concentration gradient is zero at the exit, could be used. The present condition exaggerates slightly the drying rate. The pressure is assumed equal to atmospheric at the exit of the fracture and variable at the entrance of the flow, in order to maintain the constant rate condition. The gas injection results to a pressure gradient along the fracture, which eventually develops inside the porous block as well. As a result of the gas flow, the liquid evaporates initially at the interface pore throats along the fracture. Vapor flows by advection and diffusion.

Throughout the process, isothermal conditions are assumed, heat diffusion in the solid being faster than mass diffusion in the gas. This assumption will certainly not apply in the case of poorly conducting solids, however. The 2-D pore network is horizontal, thus gravity effects, which could be dominant, depending on the magnitude of the gravity Bond number [23], are not included. These can be readily implemented in the pore-network simulation. However, gravity can mask important mass transfer effects, while the understanding of the simpler drying process in its absence, is still incomplete, as noted above. Finally, the temperature is sufficiently far from the boiling point of the liquid, so that evaporation rates are diffusion-controlled and the binary mixture in the gas phase can be assumed to be dilute. Thus, the physical properties of the binary gas phase do not depend on the concentration of the liquid component vapors and are assumed to be constant and equal to those of the purge gas.

As a result of the ensuing drying process, the liquid will reside, in general, in two different and evolving regions (Fig. 1c): a "continuous" cluster (CC), which is part of the initial liquid cluster and can be defined as being "sample-spanning" across the two lateral edges of the matrix block; and various "disconnected" clusters (DC), which have become

disconnected from the CC and from one another, and they are not "sample spanning" (see below). Their geometry, size, configuration and location are important to drying patterns and rates. Of course, initially, the porous medium is only occupied by a CC. It is the subsequent rate of change of CC and the formation of DC clusters, which is a main objective of this work. Liquid may also reside in films (thicker corner films or thin films) in gas-occupied pores, that may provide hydraulic continuity between clusters and/or with the fracture. These are not considered here, although in all likelihood, they have non-trivial effects on drying patterns and rates, as will be discussed below. Receding of the liquid-gas interface in the various clusters occurs when the capillary pressure across a meniscus first exceeds the capillary threshold at the pore where the meniscus resides. Accounting for capillarity requires the consideration of pressure fields in the liquid and gas phases. Flow in the latter is assumed to be slow and viscous-controlled. We will discuss this in more detail below.

In drying applications we can distinguish three types of pore bodies (Figure 2): Those fully occupied by gas (belonging to the gas phase and denoted by G), those fully occupied by liquid (belonging to the liquid phase and denoted by L) and those at the gas-liquid interface (in which a meniscus resides, denoted by I). The latter may be further subdivided in completely empty (CE) and partly empty (PE) pores [30]. As noted above, this classification does not account for corner films.

Liquid evaporates at the gas-liquid interface at rates determined by mass transfer in the gas phase, which are governed by advection and diffusion. The evaporation rate at I-type pores is equal to

$$F_{ij} = D\frac{C_i - C_j}{\ell} \tag{1}$$

where F_{ij} is the evaporation flux through a throat connecting neighboring pores i and j, D is the diffusion coefficient of the liquid component vapors in the gas phase through the porous medium, C_i is the concentration at the liquid pore L, which is by default equal to the equilibrium concentration C_e of the liquid component vapors and C_j is the concentration at the I pore of type CE. Equation (1) also applies to I pores of type PE, where the interface

resides within the pore, the concentration in such pores also being equal to C_e, since they contain liquid. Then C_j is the concentration of the adjacent G pore (See Figure 2d).

Mass transfer of the vapor in the gas phase obeys the convection-diffusion equation

$$\frac{\partial C}{\partial t} + \boldsymbol{u} \cdot \nabla C = D\nabla^2 C \tag{2}$$

where C is the vapor concentration and $\boldsymbol{u}$ is the gas-phase velocity. In a G pore, this is further discretized as

$$V_i \frac{\Delta C_i}{\Delta t} = \sum_j \left[D\pi r_{ij}^2 \frac{C_i - C_j}{\ell} \right] + \sum_j \left[\frac{\pi r_{ij}^4 (P_i - P_j)}{8\mu_g \ell} \overline{C_{ij}} \right] \tag{3}$$

where V_i is the volume of pore i, ΔC_i is the change in C_i during the elapsed time Δt, r_{ij} is the radius of the throat connecting pores i and j, μ_g is the gas viscosity, P is the pressure and C is the concentration at the pore. Note that the advection term is upstream weighted, namely

$$\overline{C}_{ij} = C_i \qquad \text{if } P_i > P_j, \quad \text{and} \quad \overline{C}_{ij} = C_j \qquad \text{if } P_j > P_i$$

In I pores of type CE the advection term of equation (2) is not accounted for

$$V_i \frac{\Delta C_i}{\Delta t} = \sum_j \left[D\pi r_{ij}^2 \frac{C_i - C_j}{\ell} \right] \tag{4}$$

The pressure fields are obtained from a separate computation to be discussed below. We note the use of a simplified Poiseuille-type approximation for the flow across two adjacent pores, and the assumption that mass transfer between the pores is by diffusion and convection (namely, dispersion in a single pore is not considered). However, mass transfer between two adjacent pores, one of which resides in the fracture, is enhanced by considering a velocity-dependent mass transfer coefficient [24].

$$\left(\frac{K_f \ell}{D}\right) = 1 + Pe^a \tag{5}$$

where the Peclet number, Pe, is defined as

$$Pe = \left(V_f \frac{\ell}{D}\right) \tag{6}$$

a is an exponent that depends on the geometry of the fracture and V_f is the linear gas velocity through the fracture. Equation (5) introduces a quasi-empirical macroscopic diffusion coefficient at the boundary between the matrix block (porous medium) and the free area of the fracture. This diffusion enhancement is an attempt to model the influence of the gas flow rate to the mass transfer enhancement along the convective layer within the fracture. When a neighboring pore contains a meniscus (PE), its concentration is the vapor equilibrium concentration. The boundary conditions for mass transfer involve zero flux at the lateral boundaries, a constant volumetric flux at the entrance of the fracture and zero concentration at the entrance and exit of the fracture. The latter could be modified to a zero-concentration gradient condition, but this was not considered.

The single-component liquid in the liquid phase and the non-condensable gas in the gas phase satisfy continuity equations. For their calculation, we solve for the pressure fields in G and L pores. Fluxes between adjacent pores of the same type are computed by Poiseuille-law type flow resistances, where the viscosity is taken constant

$$Q_{ij} = \left(\frac{P_i - P_j}{\ell}\right)\frac{\pi r_{ij}^4}{8\mu} \tag{7}$$

$$\sum_j Q_{ij} = 0 \tag{8}$$

where μ is the viscosity of either of the two phases. The volumetric flux Q between an I of type CE pore and a L pore depends on the pressure difference between the two pores and the capillary pressure threshold of the connecting throat. We need to distinguish two cases: If

the pressure difference between the two pores (capillary pressure) is not large enough for the gas phase contained at the I (CE) pore to penetrate the connecting throat, the meniscus remains stationary. However, as long as evaporation continues, there is a net liquid flow (but no non-condensable gas flux) in that direction. Then, in this pore we assign only a gas pressure value and zero mass flux rates of gas towards the L pore. In the next time step, the meniscus may be subject to a sufficiently high capillary pressure that can lead to the subsequent penetration of an adjacent pore and liquid displacement. Then, the meniscus recedes instantly and the L pore becomes of type I, partly empty (PE). In I pores, a mass balance of the evaporating liquid gives the liquid velocity $u_{\ell n}$ at the interface as a function of the rate of emptying of the pore and the diffusive flux in the gas phase, namely [30]

$$-D\frac{\partial C}{\partial n} = \varrho_\ell (u_{\ell n} - u_n) \tag{9}$$

where ϱ_ℓ is the mass density of the liquid, u_n is the normal velocity of the meniscus and n denotes the normal to the interface. Likewise, conservation of mass of the non-condensable gas leads to [30]

$$u_n = u_{gn} \tag{10}$$

where u_{gn} is the gas velocity at the meniscus. These were used as interface conditions coupling the flow fields in the two phases. Therefore at liquid pores L adjacent to I pores of type CE, or at I pores of type PE adjacent to G pores, equation (7) has the following form which takes into account the above mentioned boundary conditions at the interface:

$$Q_{ij} = \left(\frac{P_i - P_j}{\ell}\right)\frac{\pi r_{ij}^4}{8\mu} + D\frac{C_i - C_j}{\ell \varrho_l} \tag{11}$$

The first term on the right accounts for hydraulic flows towards (or from) adjacent L pores and the second term accounts for the evaporating volumetric flux towards the adjacent G pores or I pores of type CE. Taking into account the volumetric evaporation rate at all

interface pores from equation (1) and the boundary conditions imposed to the interface by equations (9) and (10) results to the well-known phenomenon of capillary pumping or wicking. This corresponds to a liquid viscous flow from I pores of type PE, where there is no capillary resistance to the receding of the interface, towards L pores adjacent to I pores of type CE, where the menisci remain stationary due capillary effects. The volumetric rate of flow is equal to evaporation flux so that the menisci remain stationary and the mass balance is satisfied. We note that the above treatment of mass transfer applies in the dilute limit. In the case of non-dilute mixtures, counter-diffusion in the gas phase needs to be considered as well. Finally, the gas saturation at I pores of type PE is calculated by the following mass balance

$$S_i^{t+1} = S_i^t + \frac{\Delta t}{V_i} \cdot \sum_j Q_{ij} \tag{12}$$

where S_i^{t+1} is the gas saturation inside the pore at the next time step, S_i^t is the gas saturation at current time and Δt is the time step during which we assume constant flow rates Q.

For completeness, we provide a schematic of the way our algorithm accounts for the capillary pumping mechanism. As shown in figure 3, where two areas A and B along the interface are highlighted, if the throats R of the interface at area A have smaller radii than those of area B, they will result in higher capillary pressures Pc at the interfaces in area A. If the pressure in the gas phase is taken to be constant then we will have the logical sequence

$$R_A<R_B \rightarrow Pc_A>Pc_B \rightarrow Pgas_A\text{-}Pliq_A>Pgas_B\text{-}Pliq_B \rightarrow Pliq_B>Pliq_A$$

namely, due to the difference in radius, between the two sections of the interface, there results a capillary-induced liquid flow from area B to area A. In fact, during drying, the menisci in area A usually remain stationary and the evaporation flux from the interface of this section is balanced by the liquid flow towards section A from section B.

The simulation procedure in the network, the updating of interfaces and the marching in time is described in the Appendix A and can be qualitatively summarized as follows. At any given time, sites have the designation, G, L or I, and pressure and

concentration fields are known. The L sites can be part of the original liquid cluster (CC) or they belong to disconnected finite-size clusters (DC), which become trapped through the evaporation process. In the subsequent time step, the overall rate of evaporation from each of the liquid clusters is evaluated. Pressure fields are calculated and PE pores of type I are emptied according to the appropriate mass balances. The time step is selected such that it equals the minimum time required to empty completely any of the available PE pores. If at the current time, no PE pores are available to any (or all) of the clusters (namely all I pores are of the CE type) the throat with the smallest capillary threshold in the perimeter of any given cluster is the next throat to be invaded, at which time, the corresponding invaded pore becomes an I pore of the PE type. To determine this throat the liquid pressure is lowered uniformly in space inside the cluster, until the capillary pressure exceeds for the first time the smallest capillary threshold. Equivalently, this can be obtained by invading the throat with the smallest difference between the gas pressure in the pore and the corresponding capillary pressure threshold of the throat. Implicit to the above is the absence of hydraulic continuity between disconnected clusters, namely the absence of liquid films. Nonetheless, invasion must occur, since due to evaporation there is a continuous loss of mass from the liquid clusters. At the conclusion of the time step, concentration fields in the gas phase are computed and the process continues. This algorithm is essentially the same one used by Li and Yortsos [16] and Satik and Yortsos [25] in the related problems of phase change by solution gas-drive or boiling. All calculations are done explicitly in time. Pressure fields are computed using Successive Over-Relaxation, while concentration fields are obtained from (3) and (4) in a straightforward manner.

From a dimensional analysis of the problem, there are three main dimensionless groups: (i) a diffusion-based capillary number, Ca, defined as

$$Ca = D\mu_\ell C_e / \gamma \ell \varrho_\ell \tag{13}$$

where μ_ℓ is the viscosity of the liquid phase, expressing the ratio of viscous to capillary forces, based on a diffusion-driven velocity; (ii) a Peclet number, Pe, defined by (6), expressing the ratio of advection to diffusion in the gas phase, based on the linear velocity assuming only flow in the fracture; and (iii) the viscosity ratio, M, between liquid and gas

viscosities. The latter is typically large and will not be considered in the sensitivity analysis to follow. We point out that one may also define a capillary number based on the fracture velocity. Clearly, the latter would control high-rate processes at early stages, while the diffusion-based capillary number controls the process at later times. These two capillary numbers are linearly related through the Peclet number, thus only two of these parameters are linearly independent. In the presence of gravity, an additional dimensionless number, the Bond number

$$B = \frac{g(\rho_\ell - \rho_g)k}{\gamma} \tag{14}$$

expressing the ratio of gravity to viscous forces, must also be considered, where k is the permeability of the porous medium. Geometric parameters include the number of pores in the linear dimension $N=L/l$, where l is the typical pore length, the aspect ratio between mean pore size and pore length, as well as between mean pore size and mean throat size, a scaled variance of the size distribution, and the aspect ratio of the matrix block (here taken equal to 1). In this study, all geometric parameters are taken fixed, the aspect ratio of the matrix block is equal to 1, and emphasis is placed on the effect of the capillary and Peclet numbers. The effect of N will be addressed in the discussion on scale-up.

RESULTS

A number of runs were conducted to simulate drying of liquid hexane in a matrix block of size 50x50. The corresponding physical parameter values are shown in Table 1. To carry out a sensitivity study, we varied the injection rate in the fracture, the interfacial tension and the diffusion coefficient. Table 2 shows the set of runs conducted. The characteristic time t^* denotes the time at which the matrix block empties at the maximum drying rate (which occurs at the first time step at which all liquid-gas interfaces are at the fracture-matrix boundary) and it is used to non-dimensionalize time. All simulations correspond to a fixed realization of the pore network, which allows studying the sensitivity of drying patterns and rates to the other parameters. Results on drying patterns, concentration profiles, transversely-averaged saturation profiles and drying rates were

obtained. We note that in order to demonstrate strong advection effects, the values of the Peclet number used in certain runs in the above table are high (perhaps unrealistically high).

We will use run 2 and run 15 to illustrate typical features from the simulation. These runs are typical of two limiting regimes, one in which capillary forces are dominant and mass transfer occurs by diffusion, and another in which viscous forces dominate and mass transfer is by advection. In addition, we will discuss a case (run 12) involving capillary control in the phase partition, but advection control in mass transfer. As schematically depicted in Fig. 1c, the results show that the liquid phase consists of a main cluster (CC) and a number of discontinuous (DC) clusters at the perimeter of the CC (see Figs 4 and 5 for runs 2 and 15, respectively). These result from trapping of the liquid as the gas invades the liquid-occupied region. The patterns of the CC and/or the DCs depend on the value of the capillary pressure across the perimeter of each of these clusters as follows.

If viscous forces are not sufficiently strong across a given cluster (for example, as in run 15, Fig. 5), the capillary pressure variation is negligible, and the cluster takes the pattern of Invasion Percolation (IP), in which the next throat to be invaded by the gas is that with the smallest capillary threshold (here, the one with the largest size) among all perimeter throats of that cluster. This condition depends on the value of the capillary number, the rates of drying (which also set viscous pressure gradients [30]) and the size of the cluster. Under otherwise similar conditions, small DCs are more likely to follow an IP pattern. A detailed check of the sequence of invasion showed that run 15 followed IP rules at any time during the process, while run 2 did not. Patterns corresponding to IP and diffusion-only mass transfer were obtained in run 16, where $Pe=0$. The corresponding saturation patterns are shown in Fig. 6. Comparison with Figs. 4 and 5 shows substantial differences in the patterns between runs 2 and 15 (or 16) and some difference (at early times) between runs 15 and 16. The latter reflects mass transfer effects, due to the different Peclet numbers in the two runs.

Because of their relevance to real problems and the fact that capillary-dominated patterns eventually appear as late-time regimes, we provide here some additional discussion of their properties. We first recall that all simulations in this paper were conducted assuming the absence of film flows, thus DCs are hydraulically disconnected from each other and the CC. Under these conditions, in a capillary-controlled pattern (such as run 15 and 16), while each cluster obeys locally IP rules, the sequence of penetration is dictated by the mass

transfer rates across the perimeter of each cluster. In the related study of Li and Yortsos [16] this process was termed *local percolation*. Clusters closer to the open boundary are subject to a faster evaporation, compared to those further away, and are emptied faster. The end result is the development of gradients in the size of the isolated liquid clusters, with clusters closer to the fracture having smaller size (see also below). These gradients reflect mass transfer, rather than viscous effects. Nonetheless, the pattern of the CC is still dictated by IP rules. Clearly, however, the overall pattern would be a function of the drying rates, namely of the value of the *Pe*. We must note that under this regime of local percolation, different clusters may have different-size throats being invaded at the same time. In other words, it is possible that the drying of a given DC occurs by the emptying of a throat i, which is smaller than the largest perimeter throat, j, of another cluster, which due to negligible mass transfer is not being invaded (of course, as a result of capillary control, throat i is the largest among all perimeter throats of the first cluster).

The above analysis of capillary-controlled patterns is based on the assumption of negligible film flow. If, on the other hand, hydraulic continuity exists among all clusters (for example through liquid films) then, in the small *Ca* limit, the next throat to be penetrated will be the throat with the smallest threshold among *all* perimeter throats of *all* clusters. In the liquid-to-gas phase change study of Li and Yortsos [16], this was termed *global percolation*. In the absence of viscous or gravity gradients, such a process could lead to a deep penetrating front of a fractal nature, and liquid saturation gradients will not develop, in the sense that the proximity of a particular front site to the open boundary cannot influence the time at which it is invaded. Gradients in saturation will develop in the case of the viscous-capillary-gravity competition. This regime was implied in many previous studies, including the work of Tsimpanogiannis et al. [30]. We also note that deep penetrating fronts of fractal nature were not observed in the experiments of Ho and Udell [10]. Nonetheless, because of possible qualitative differences, it is evident that establishing hydraulic continuity is an important role played by liquid films and needs to be further explored.

In the limit when capillarity is negligible (as in run 2), the pattern deviates substantially from IP and almost follows a piston-like displacement (PD) (Fig. 4). Under these conditions, the capillary resistance of a throat is negligible, and the pattern is exclusively determined by mass transfer considerations, much like in the dissolution of a

solid. The rate of generation of DCs and their size are smaller and the liquid phase consists mostly of a CC. Such conditions are not likely to persist for a long time in the typical case, however, where late-time drying patterns are likely to be of the IP type. We need to add that when viscous forces in the gas phase are important in setting the pattern (as is the case in run 2, for example), the receding of the CC has some of the properties of IPSG in a fracture-matrix system (Haghighi *et al.* [8]). In such cases, the higher capillary pressure upstream leads to a preferential invasion in the matrix in the upstream direction, thus leading to patterns that appear to be slanted (from the upstream to the downstream direction) as shown in run 2 (Fig. 4).

Regardless of the magnitude of the capillary forces, the presence of discontinuous clusters is very significant in the development of the pattern. These clusters result in the screening of a part of the CC from the fracture, hence from the region of high concentration gradients, and lead to a balanced rate of drying between the two types of clusters, through the following stabilizing feedback mechanism. For example, if the mass transfer rates from the CC are too large, they will result in a faster rate of consumption of the CC, leading to the generation of a larger number of DCs, which in turn screen the CC from further mass transfer and slow down its rate of drying. Conversely, if the rate of drying of the CC is too small, most of the reduction in liquid saturation occurs from the DCs, the size and number of which decrease, leading to an increased mass transfer and a subsequent increased rate of consumption of the CC. It follows that for fixed values of the capillary and Peclet numbers, the statistics of the DCs, namely their number density and size distribution, remain approximately constant. In particular, the region where the DCs reside (which we may denote as the front region) is approximately of a constant width (Figs. 4-6). We should mention that similar findings were observed by Prat and Bouleux [23], although in the different situation where the gradients are provided by gravity rather than mass transfer. The size of the frontal region can be estimated using arguments from Invasion Percolation with Trapping (IPT) as described in the Appendix B.

The screening of the CC from the region of high mass transfer is evident in the concentration profiles (Figs. 7-8). Depending on the value of the Peclet number and the location of the front, the concentration field in the gas phase may or may not be sensitive to the detailed structure near the front. For small values of the Peclet number (as in run 15, Fig.

7), the process is almost diffusion-controlled and the concentration resembles the much smoother concentration field surrounding an effective continuum (as also found by Li and Yortsos [16]). This despite the rather complex geometry of the front (see Fig. 5), which is rather complex (and in fact, fractal, e.g. see Feder [6]). Almost identical patterns were obtained for run 16 and they are not shown. As advection increases and at early times, however, the region of concentration gradients is a narrow boundary layer surrounding the front. At later times (panel 3 in Fig. 8), this is not uniformly developed, as poorly accessible regions cannot be effectively probed by the flow field. This mass transfer effect is also evident in the simulations of run 12 (Fig. 9). This run has a Peclet number almost two orders of magnitude larger than in run 15, although the sequence of the liquid patterns is almost identical (and is not shown here for simplicity). However, because of the much stronger advection effects, concentration profiles are much steeper in most places in run 12, resulting in proportionally higher drying rates (Fig. 9). At the same time, the effect is non-uniform spatially, and there exist regions in which diffusion is controlling. Strong advection effects similar to these were also reported in a related problem of bubble growth driven by heat transfer [25].

Runs 2 and 15 are typical of the two limiting regimes and can be analyzed in a relatively straightforward fashion. Intermediate patterns are more difficult to analyze, as they have features from both regimes. When both capillarity and viscous forces compete, the receding of the drying front does not follow strictly IP or PD rules. Depending on the rates of evaporation as well as the size of the individual clusters, there may exist more than one pore of the PE type at the same time, and these pores may not necessarily correspond to the IP or the PD sequence. We must point out that Tsimpanogiannis *et al.* [30] estimated the spatial extent over which the front follows IP rules using scaling arguments, from which the following relation was developed for 3-D patterns

$$\sigma_{ft} \propto \left(\frac{2\Sigma X_{ft}}{Ca} \right)^{0.47} \tag{15}$$

where σ_{ft}, X_{ft}, Σ are non-dimensionalised front width, frontal position and variance of the pore size distribution, respectively. Implicit to this relation was the assumption of global

percolation (namely of hydraulic continuity via film flow). This result is not expected to hold here. Nonetheless, clusters of small size will erode following local IP rules. In larger-size clusters, however, the spatial extent over which IP rules apply would be limited. Thus, the problem acquires some of the characteristics of IPSG [30]. As time increases, drying rates decrease, as the front recedes further away, and the width of the front, where IP is exhibited, increases accordingly. One expects that after sufficiently long time, the process will approach a state where IP applies for all clusters. Some arguments from IPT are furnished in the Appendix B to estimate the size of the front in this problem.

A typical case in which viscous and capillary forces compete is run 4, shown in Figs. 10-11. The invasion pattern belongs to neither of the two limiting regimes. There is evidence of IPSG in the matrix, similar to run 2, but also a multiple number of DCs, similar to run 15. The concentration profiles for this run (Fig. 11) are similar to those of run 12, and suggest substantial concentration gradients in boundary layer regions near the front. At the same time, regions far from the fracture are effectively being screened, despite the large Peclet number in this run, leading to mass transfer similar to the diffusion-controlled case (run 15).

In macroscopic continuum models a quantity of interest is the transverse-averaged saturation profiles. Results for runs 15, 12, 4 and 2 are shown in Figs. 12-15, respectively, for four different values of the fraction of the liquid volume occupying the matrix (and which corresponds to the four panels of the previous figures). As expected, runs 15 and 12 have almost identical profiles (Figs. 12-13), their patterns being dictated by IP rules, even though their mass transfer characteristics are not the same. Differences due to the latter are reflected in their drying rates to be discussed below. Gradients in saturation develop, due to the continuous receding of the front. As discussed above and in the Appendix B, these gradients reflect the screening of inaccessible, deeper-lying parts of the liquid front from high concentration gradients, the resulting limited mass transfer, and the development of a frontal region of finite width (which is constant in the absence of viscous effects, but increases with time in their presence). The profiles in runs 4 and 2 (Figs. 14-15) reflect a more uniform penetration, at early times, due to the preferential receding of the liquid in the upstream direction as a result of strong viscous effects. These are not unlike the profiles in

the drainage of a matrix block [8]. As time increases, however, all profiles eventually approach a state which progressively becomes capillary- and diffusion-controlled.

Fig. 16 shows drying curves for the various runs simulated. As discussed, the time was made dimensionless with the time t^* it would take to empty the matrix block under conditions of the maximum rate. It then follows that the slope of the drying curves is the dimensionless rate of drying (relative to the maximum drying rate). Note that because the maximum rate depends on the Peclet number in the fracture (roughly as $Pe^{1/3}$) this plot emphasizes processes under convection control and should be interpreted with care, as far as the upscaling of the process is concerned. The figure shows clearly the existence of the conventional Constant-Rate-Period (CRP) (with the exception that film flow is not involved here) followed by a period of continuously declining rates. From an analysis of the patterns, we have found that the CRP lasts roughly until the time when the CC has lost continuity with the fracture. This is in qualitative agreement with indirect experimental findings from tests on chalk samples initially containing liquid pentane and dried by methane injection along the fracture [15]. In addition, macroscopic arguments set forth by Stubos and Poulou [29] on the basis of the same experimental data have led to the same conclusion. Indeed, as long as the liquid is continuously connected to the fracture, the combination of enhanced evaporation rate (through the coefficient given by equation (5)) and capillary gradients leads to a constant drying rate. This is evident when considering the low Peclet number run 15 or the IP run 16 in Fig. 16 where the CRP is very short due to the fast receding of the liquid phase from the fracture. A close examination of the drying curves shows that the highest rate and the longest CRP are found in run 4. In this "critical" case the gas pressure developing close to the entrance of the fracture is high enough to cause the breaking of menisci in the left side of the matrix block. On the contrary, this cannot happen on the right side sustaining for relatively large times sufficient liquid contact with the fracture (see patterns in Fig. 10). Thus the constant rate during the CRP reflects the detailed mass transfer characteristics during the process and is realization-dependent. By increasing the interfacial tension value in run 4 (runs 5 and 6 of Table 2), we find that the drying rate and the CRP drop to levels similar to the ones determined for the low Peclet number cases (Fig. 17). In fact, the gas pressure is not any more sufficient to overcome the capillary thresholds and the case resembles more and more to IP. When γ decreases on the other hand (run 3), all

menisci in contact with the fracture break at early times and the CRP is very short. The drying rate also drops accordingly (Fig. 17). For the case of IP-controlled processes, the end of the CRP in terms of the amount of liquid left can be readily estimated from the analysis in the Appendix B.

DISCUSSION

The above analysis was based on a number of simplifying assumptions, most of which were made to illustrate various effects. We single out the small size of the fracture pores and throats taken, in order to allow for a study of the viscous-capillary competition at the rates considered. At a larger contrast of fracture/matrix capillary and permeability characteristics, the onset of a PD regime will be delayed as far as the flow rate is concerned. We also note that the Peclet number in some of the runs can be considered unrealistically high. Such simulations were purposely made to exaggerate the effect of advection in mass transfer. In general, flow rate-driven effects will dominate the process at early times, and particularly during the CRP, which will be controlled, as a result, by the detailed geometry and process characteristics. It is in this regime and time period, where pore-network simulations, such as these, can have a significant impact. At later stages, the front recedes, viscous effects and advective mass transfer become less important and the process becomes capillary- and diffusion-controlled. In this regime, the analysis discussed in the Appendix B applies and various results from the theory of Invasion Percolation with Trapping can be used to describe the process.

A key simplification made in the paper concerns the absence of liquid films. As discussed, these can be important in providing hydraulic continuity between clusters, which can drastically alter the patterns and the location and size of the DCs and the CC, and can possibly affect macroscopic capillary pressure-saturation relationships. Work in this direction, in particular in the incorporation of film flows in the pore-network simulation, is currently under way. At present, their effect is difficult to assess. We also need to mention the restriction to single-component liquids, which eventually leads to the complete evaporation of the liquid clusters. In the presence of a non-volatile component, the disconnected liquid clusters will not disappear, but will affect adversely the mass transfer rates. Such effects need to be considered as well.

The results can be used for upscaling to macroscopic continuum models. Following the CRP, where the process becomes capillary- and diffusion-controlled, the theory of IPT discussed in the Appendix B can be used to elucidate the distribution of the liquid phase, and the size and extent of the DC region. This information can then be utilized to construct model diffusion problems, the solution of which can be implemented in the calculation of needed coefficients in macroscopic models (for example, as required in Tsimpanogiannis *et al.* [30]). Such work is also under way. On the other hand, the CRP is not necessarily amenable to such a statistical theory description, given that non-local effects of rate and viscous forces (or finite-size effects in the case of capillary control) are important. The solution of this problem must be sought by conducting extensive pore-network simulations, including the ensemble-averaging of results over many realizations, something that was not done here.

CONCLUSIONS

In this paper we presented a pore-network model for the drying of a single-component liquid in porous media. The model accounts for various processes at the pore-scale including mass transfer by advection and diffusion in the gas phase, viscous flow in liquid and gas phases and capillary effects at the gas-liquid menisci in the pore network. A 2-D version of the model under isothermal conditions in a rectilinear horizontal geometry was formulated. Drying is driven by the flow of a purge gas injected at a constant rate. The problem is characterized by two dimensionless parameters, a diffusion-based capillary number, Ca, and a Peclet number, Pe, in addition to the various geometrical parameters of the pore network. Results on the evolution of the liquid saturation, the trapped liquid islands and the drying rate were obtained as a function of time and the dimensionless parameters. In the absence of liquid film flow, the importance of trapped liquid islands in screening mass transfer to the continuous liquid cluster was emphasized. This results in saturation gradients, and the development of patterns which are different than in the case of flow continuity between the different clusters. For fixed parameter values, the drying front does not in general obey invasion percolation rules. However, as drying progresses, and depending on the relative magnitude of the capillary and Peclet numbers, a transition to a percolation-controlled problem occurs. In fact, it is likely that such is the case in many realistic

situations. Effects of capillarity and mass transfer on saturation profiles and drying rates were discussed. The results provide insight on the process. The pore network simulation can also be used to provide expressions for various coefficients in macroscopic continuum models, currently treated empirically. Work in this direction is in progress.

ACKNOWLEDGEMENTS

Partial funding by the JOULE Program of the European Commission is acknowledged (Contract JOF3-CT95-0008).

APPENDIX A

The essential elements of the algorithm are described below:

1. A random network of pores and throats is created using a uniform size distribution between the specified values.
2. The pressure drop along the fracture is calculated using equations (7) and (8).
3. All liquid-gas interfaces of isolated liquid clusters (DC's and the CC) are located and the type (I-CE or I-PE) of their interface pores is identified.
4. Flow conductivities at all network throats are calculated. When a liquid meniscus within a throat is found to be stationary then a zero hydraulic conductivity is assigned to the gas phase adjacent to it.
5. All throats where gas penetration occurs as the local capillary pressure exceeds the capillary pressure threshold are identified. If there is no such throat at a specific cluster, then the gas penetrates the throat that has the lowest capillary threshold along the interface, i.e. the one with the largest radius.
6. The evaporation rate through every throat across all interfaces is calculated using equation (1).
7. The pressure fields in both liquid and gas phases are solved, using equations (7) and (8) and (11).
8. The I pore of type PE that will be emptied first at the current flow rates is located and the corresponding time required is identified. These pores loose mass due to both evaporation and the viscous flows of the capillary-pumping phenomenon (as shown by equation (11)).

9. The time step is selected taking care not to allow the concentration value at a gas pore to drop bellow zero or exceed the equilibrium concentration.

10. The concentration field is calculated in the gas phase using equations (3) and (4) for the current time step. This calculation is straightforward based on the values of concentration at the end of the previous time step.

11. The gas saturation is calculated through equation (12) at all I pores of type PE for the current flow rates using the current time step.

12. If at the end of the current time step a pore becomes fully filled with gas (I pore of type CE) at any of the liquid clusters, the algorithm returns to step 3. If, despite the fact that gas saturation at all penetrated interface pores increases, there is no pore completely filled with gas at the current time step, then the return is to step 6.

The above procedure is repeated until all liquid in the porous media has evaporated.

APPENDIX B

Discontinuous clusters form as the perimeter of the CC recedes, due to gas invasion, and the receding phase becomes trapped. In the absence of mass transfer considerations and under capillary control, this is the well-known mechanism of Invasion Percolation with Trapping. In the latter, the statistics of the trapped clusters can be determined from knowledge of the percolation probability, q, at which the defending phase (here the liquid) is being invaded. In the particular process under consideration, the invasion of the CC is a drainage process in which the invading (gas) phase percolation probability is near its percolation threshold

$$p \sim p_c \ (=1/2 \text{ for a 2-D square lattice})$$

Then, the defending phase is at percolation probability $q=1-p \sim 1-p_c$. Knowledge of q allows one to estimate various statistics of the disconnected, trapped clusters, since the latter can be accurately approximated by the finite-size clusters of a mixed site-bond percolation process at percolation probability q. For example, the size of the largest DC follows the percolation scaling

$$\xi \sim |q-(1-p_c)|^{-\nu}$$

where ν is the correlation length exponent. Statistics are also available (or can be obtained) for other properties of these finite-size clusters. In the above, it is implicitly assumed that $p_c < 1/2$, and that $\xi << N$. When the latter condition fails, as is the case in the simulations here, where $p_c = 1/2$, the largest (cut-off) size is set by the width of the lattice N. The above analysis can be used to estimate the statistics of screened DCs around the front, which are not subject to substantial drying rates, although not of the DCs at the frontier with the gas phase, which are being exposed to strong concentration gradients and a time-varying size.

In the presence of viscous effects, the invasion process is similar to IPSG, in which, in the absence of mass transfer effects, the largest size of the DCs is set by the Bond number of the process, namely

$$\xi \sim B^{-\frac{\nu}{\nu+1}}$$

In drying, an equivalent Bond number can be defined as follows [30]

$$B = \frac{Ca}{2\Sigma X_{ft}}$$

However, the incorporation of an IPSG theory in the trapping problem is yet to be done. In general, we expect that such a theory would lead to the result that the average size of the DCs becomes smaller as viscous forces increase, as is the case with the problem without trapping [30], and also as shown in the simulations.

We also conjecture that the same length scale, namely the average size of the largest DC, is also the scale for the width of the frontal region, namely the region containing the trapped clusters (DC). Indeed, as we argued in the main text, the mass transfer screening from the DCs sets the balance between them and the CC. We expect that at least for diffusion-controlled problems, this screening will be effectively set by the distance between DCs, which are all sources of constant concentration. Given that the only characteristic length in the problem is the average size of the DCs completes the argument in support of this conjecture.

REFERENCES

[1] Bruin S, Luyben KCAM. Drying of food materials; A review of recent developments. Advances in Drying 1980;1: 155-215.

[2] Ceaglske NH, Hougen OA. Drying granular solids. Ind Eng Chem 1937;29: 805-813.

[3] Chandler R, Koplik J, Lerman K, Willensen JF. Capillary displacement and percolation in porous media. J Fluid Mech 1982;119: 249-267.

[4] Chen P, Pei DCT. A mathematical model of drying processes. Int J Heat Mass Transfer 1989;32: 297-310.

[5] Fatt I. The network model of porous media. Trans AIME 1956;207: 144-181.

[6] Feder J. Fractals. New York: Plenum, 1988.

[7] Fortes M, Okos MR. Drying theories:Their bases and limitations as applied to food and grains. Advances in Drying 1980;1: 119-154.

[8] Haghigi M, Xu B, Yortsos YC. Visualization and simulation of immiscible displacement in fractured systems using micromodels: I.Drainage. J Coll Interf Sci 1994;166: 168-179.

[9] Hartley JG. Coupled heat and moisture transfer in soil: A review. Advances in Drying 1987;4: 199-248.

[10] Ho CK, Udell KS. An experimental investigation of air venting of volatile liquid hydrocarbon mixtures from homogeneous and heterogeneous porous media. J Contam Hydrol 1992;11: 1-26.

[11] Ho CK, Udell KS. Mass transfer limited drying of porous media containing an immobile binary liquid mixture. Int J Heat Mass Transfer 1995;38: 339-350.

[12] Jia C, Shing K, Yortsos YC. Visualization and simulation of non-aqueous phase liquids solubilization in pore networks. J Contam Hydrol 1999;35: 363-387.

[13] Laurindo JB, Prat M. Numerical and experimental network study of evaporation in capillary porous media. Phase distributions. Chem Eng Sci 1996;51: 5171-5185.

[14] Laurindo JB, Prat M. Numerical and experimental network study of evaporation in capillary porous media. Drying rates. Chem Eng Sci 1998;53: 2257-2269.

[15] Le Gallo Y, Le Romancer JF, Bourbiaux B, Fernades G. SPE paper 1997;38924.

[16] Li X, Yortsos YC. Theory of multiple bubble growth in porous media by solute diffusion. Chem Eng Sci 1995;50: 1247-1271.

[17] Luikov AV. Heat and mass transfer in Capillary-Porous Bodies. Oxford: Pergamon Press, 1966.

[18] Nowicki SC, Davis HT, Scriven LE. Microscopic determination of transport parameters in drying porous media. Drying Tech 1992;10: 925-946.

[19] Pan SX, Davis HT, Scriven LE. Modeling moisture distribution and binder migration in drying paper coatings. Tappi Journal 1995;78: 127.

[20] Panagiotou NM, Stubos AK, Bamopoulos G, Maroulis ZB. Drying kinetics of a multi-component mixture of organic solvents. Drying Tech 1999;17: 2107-2122.

[21] Pot V, Appert C, Melayah A, Rothman DH, Zaleski S. Interacting lattice gas automaton study of liquid-gas properties in porous media. J Phys II 1996;6: 1517-1534.

[22] Prat M. Isothermal drying of non-hygroscopic capillary-porous materials as an invasion percolation process. Int J Multiphase Flow 1995;21: 875-892.

[23] Prat M, Bouleux F. Drying of capillary porous media with a stabilized front in two dimensions. Phys Rev E 1999;60: 5647-5656.

[24] Quintard M, Whitaker S. Convection,dispersion, and interfacial transport of contaminants: Homogeneous porous media. Adv Water Res. 1994;17: 221-239.

[25] Satik C, Yortsos YC. A pore network study of bubble growth in porous media driven by heat transfer. J Heat Trans 1995;118: 455-462.

[26] Shaw TM. Drying as an immiscible displacement process with fluid counterflow. Phys Rev Lett 1987;59: 1671-1674.

[27] Simpson WT. Drying wood: A review. Drying Tech 1983;2: 235-264.

[28] Simpson WT. Drying wood: A review. Drying Tech 1984;3: 353-368.

[29] Stubos AK, Poulou S. Oil recovery potential from fractured reservoirs by mass transfer processes. SPE paper 1999; 56415.

[30] Tsimpanogiannis IN, Yortsos YC, Poulou S, Kanellopoulos N, Stubos AK. Scaling theory of drying porous media. Phys Rev E 1999;59: 4353-4365.

[31] Van Brakel J. Mass transfer in convective drying. Advances in Drying 1980;1: 212-267.

[32] Waananen KM, Litchfield JB, Okos MR. Classification of drying models for porous solids. Drying Tech 1993;11: 1-40.

[33] Whitaker S. Heat and mass transfer in granular porous media. Advances in Drying 1980;1: 23-61.

[34] Xu B, Yortsos YC, Salin D. Invasion percolation with viscous forces. Phys Rev E 1998;57: 739-751.

Figure legends

Figure 1a Schematic representation of fractured porous media.
Figure 1b Pore-network model representation of a porous medium.
Figure 1c Classification of typical saturation patterns.
Figure 2 The evolution of drying at an isolated liquid cluster (DC) consisting of two liquid pores. (a) Initially the cluster is surrounded by I pores of type CE. (b) When the pressure difference at the upper throat exceeds its capillary resistance, the meniscus recedes and the pore is penetrated by the gas phase. The same transition takes place between (c) and (d).
Figure 3 Schematic representation of the capillary pumping phenomenon.
Figure 4 Phase distribution patterns for run 2 (Pe=596, $Q=0.45*10^{-6}$ m^3/s) at four different gas saturation fractions corresponding to 20%, 40%, 60% and 80% of the total pore volume. The liquid phase is black and the gas phase is white.
Figure 5 Phase distribution patterns for run 15 (Pe=0.66, $Q=0.5*10^{-9}$ m^3/s) at four different gas saturation fractions corresponding to 20%, 40%, 60% and 80% of the total pore volume. The liquid phase is black and the gas phase is white.
Figure 6 Phase distribution patterns for run 16 (Pe=0, $Q=0.0$ m^3/s) at four different gas saturation fractions corresponding to 20%, 40%, 60% and 80% of the total pore volume. The liquid phase is black and the gas phase is white.
Figure 7 Concentration patterns for run 15 (Pe=0.66, $Q=0.5*10^{-9}$ m^3/s) at the four different occupation fractions. Darker colors indicate smaller concentrations.
Figure 8 Concentration patterns for run 2 (Pe=596, $Q=0.45*10^{-6}$ m^3/s) at the four different occupation fractions. Darker colors indicate smaller concentrations.
Figure 9 Concentration patterns for run 12 (Pe=66, $Q=0.05*10^{-6}$ m^3/s) at the four different occupation fractions. Darker colors indicate smaller concentrations.
Figure 10 Phase distribution patterns for run 4 (Pe=331, $Q=0.25*10^{-6}$ m^3/s) at four different gas saturation fractions corresponding to 20%, 40%, 60% and 80% of the total pore volume. The liquid phase is black and the gas phase is white.
Figure 11 Concentration patterns for run 4 (Pe=331, $Q=0.25*10^{-6}$ m^3/s) at the four different occupation fractions. Darker colors indicate smaller concentrations.

Figure 12 Transversely-averaged saturation profiles for run 15 at the four different occupation fractions.
Figure 13 Transversely-averaged saturation profiles for run 12 at the four different occupation fractions.
Figure 14 Transversely-averaged saturation profiles for run 4 at the four different occupation fractions.
Figure 15 Transversely-averaged saturation profiles for run 2 at the four different occupation fractions.
Figure 16 Drying curves (gas volume fraction vs. dimensionless time) for various runs.
Figure 17 Drying curves (gas volume fraction vs. dimensionless time) for runs 3-6.

Tables

Table 1: Values of physical properties used.

Parameter	Value
Volumetric gas flow rates	$0.0\text{-}1.0*10^{-6}$ m/s
Surface Tension	$19*10^{-3}$ N/m
Diffusion Coefficient	$6.38*10^{-6}$ m^2/s
Equilibrium concentration	0.266 kg/m^3
Liquid phase viscosity	$2.85*10^{-4}$ Pa*s
Gas phase viscosity	$1.71*10^{-5}$ Pa*s
Liquid phase density	650 kg/m^3
Gas phase density	4.4 kg/m^3

Table 2: Set of simulation runs.

Run	Q $(m^3/s)*10^{-6}$	γ $(N/m)*10^{-3}$	D $(m^2/s)*10^{-6}$	a	Ca	Pe	t^* (s)
1	1.00	19	6.38	0.33	$1.68*10^{-6}$	1325	14238
2	0.45	19	6.38	0.33	$1.68*10^{-6}$	596	17983
3	0.25	1.9	6.38	0.33	$1.68*10^{-5}$	331	21340
4	0.25	19	6.38	0.33	$1.68*10^{-6}$	331	21340
5	0.25	60	6.38	0.33	$5.33*10^{-7}$	331	21340
6	0.25	100	6.38	0.33	$3.20*10^{-7}$	331	21340
7	0.25	19	6.38	1.00	$1.68*10^{-6}$	331	500
8	0.25	19	63.8	0.33	$1.68*10^{-5}$	33	4002
9	0.20	19	6.38	0.33	$1.68*10^{-6}$	265	22742
10	0.10	19	6.38	0.33	$1.68*10^{-6}$	132	27645
11	0.05	1.9	6.38	0.33	$1.68*10^{-5}$	66	33325

12	0.05	19	6.38	0.33	$1.68*10^{-6}$	66	33325
13	0.015	19	6.38	0.33	$1.68*10^{-6}$	19	45611
14	0.005	19	6.38	0.33	$1.68*10^{-6}$	6.7	57819
15	0.0005	19	6.38	0.33	$1.68*10^{-6}$	0.66	88752
16	0.0	19	6.38	0.33	$1.68*10^{-6}$	0.0	166132

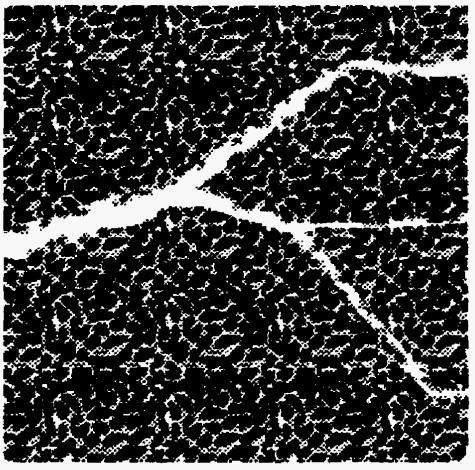

Figure 5a Schematic representation of fractured porous media.

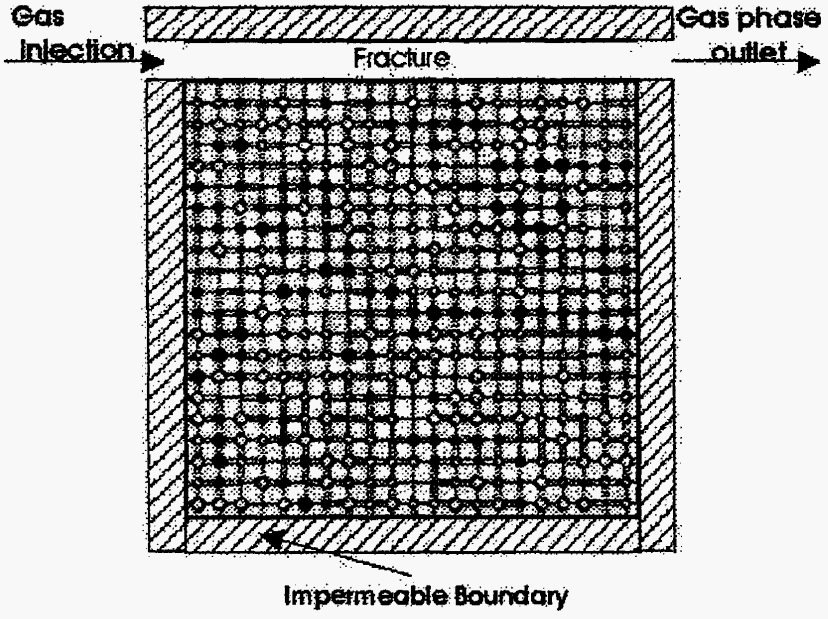

Figure 1b Pore-network model representation.

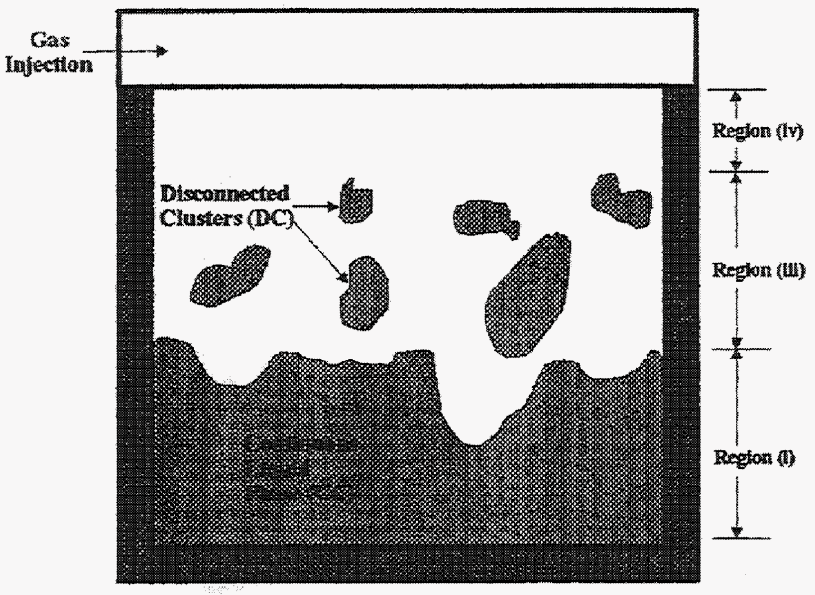

Figure 1c Classification of typical saturation pattern.

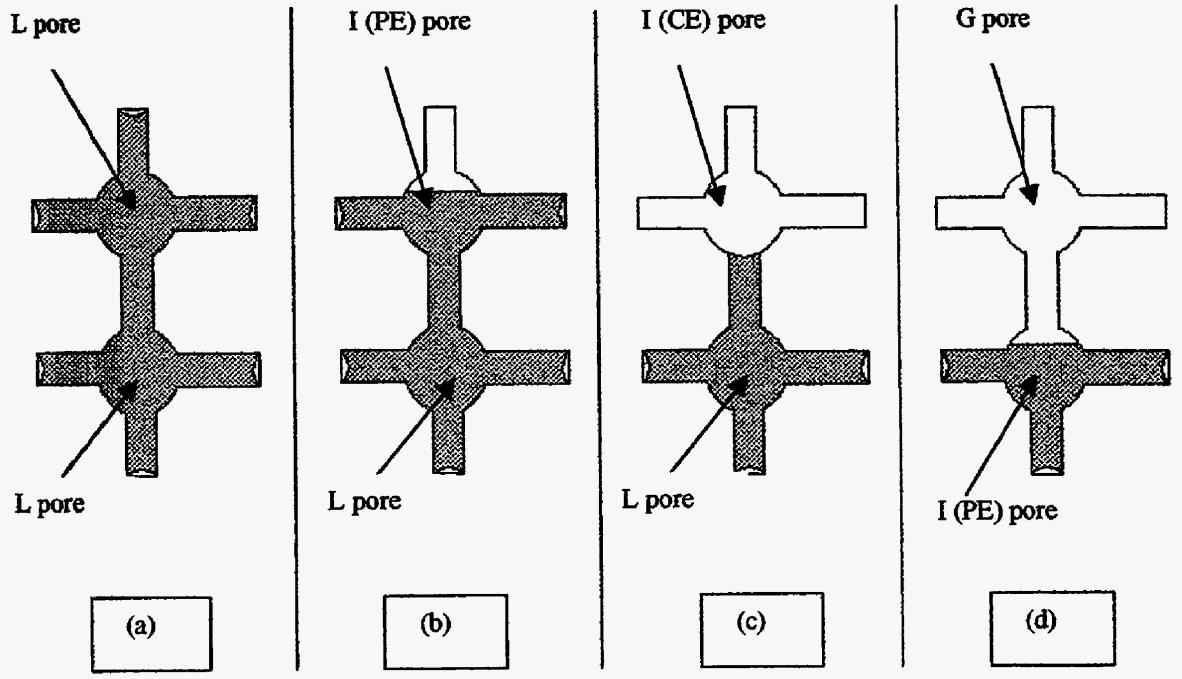

Figure 6 The evolution of drying at an isolated liquid cluster (DC) consisting of two liquid pores. (a) Initially the cluster is surrounded by I pores of type CE. (b) When the pressure difference at the upper throat exceeds its capillary resistance, the meniscus recedes and the pore is penetrated by the gas phase. The same transition takes place between (c) and (d).

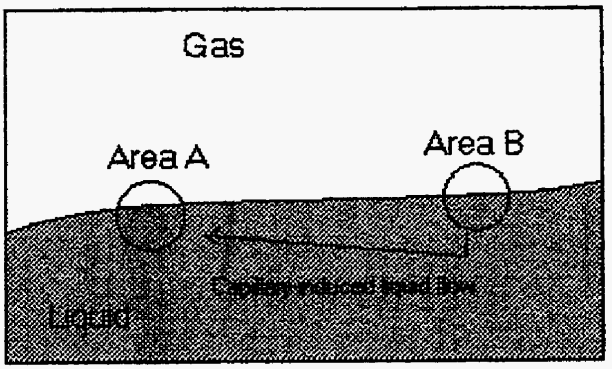

Figure 7 Schematic representation of the capillary pumping phenomenon.

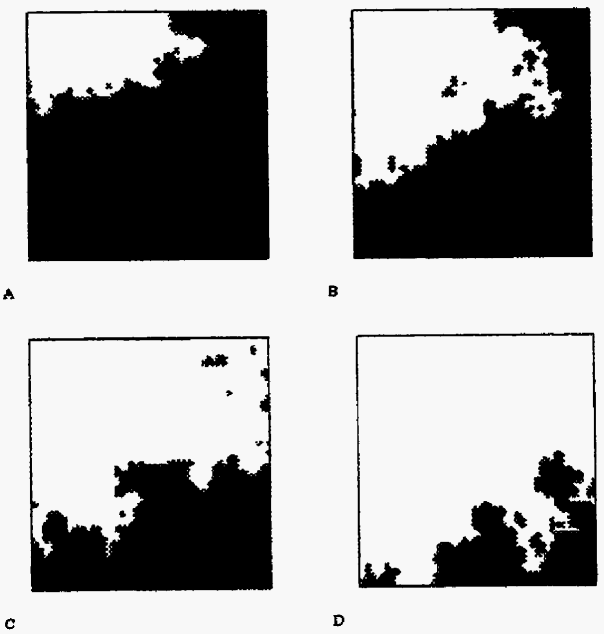

Figure 4 Phase distribution patterns for run 2 at four different liquid fractions corresponding to 20%, 40%, 60% and 80%. The liquid phase is black and the gas phase is white. Pe=596, $Q=0.45*10^{-6}$ m^3/s.

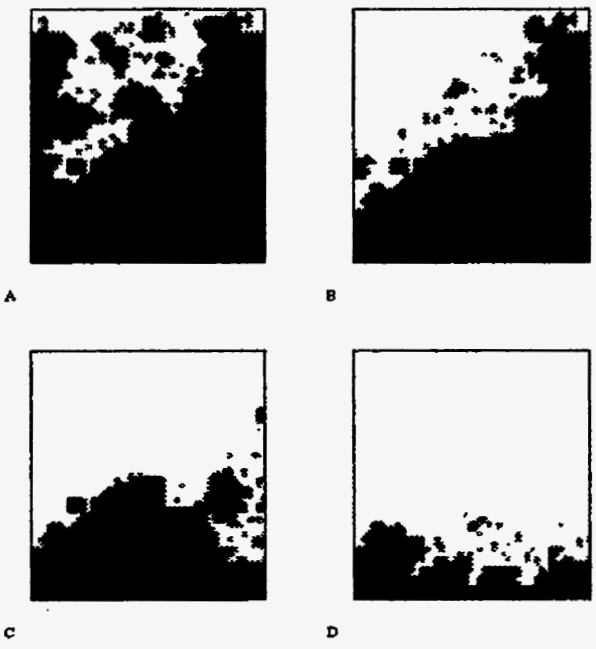

Figure 5 Phase distribution patterns for run 15 at four different liquid fractions corresponding to 20%, 40%, 60% and 80%. The liquid phase is black and the gas phase is white. Pe=0.66, $Q=0.5*10^{-9}$ m^3/s.

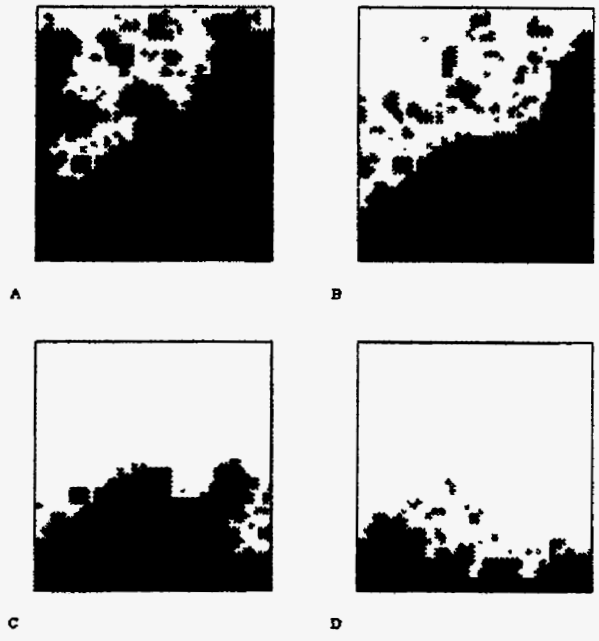

Figure 6 Phase distribution patterns for run 16 at four different liquid fractions corresponding to 20%, 40%, 60% and 80%. The liquid phase is black and the gas phase is white. Pe=0, Q=0.0 m^3/s.

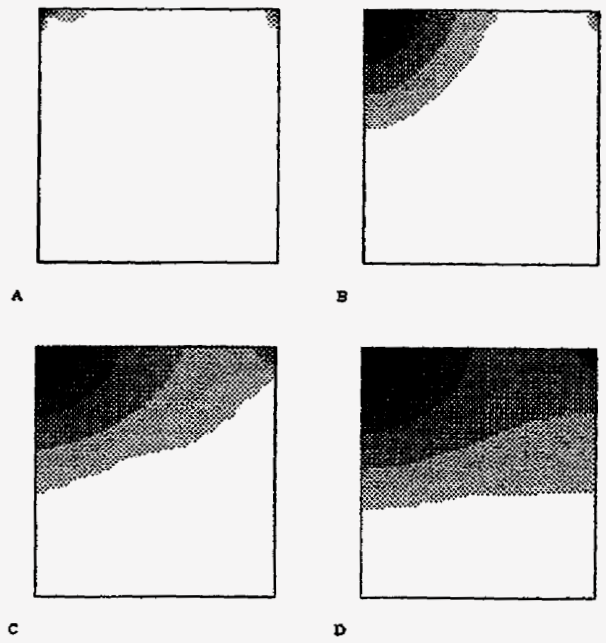

Figure 7 Concentration patterns for run 15 at the four different occupation fractions. Darker colors indicate smaller concentrations. Pe=0.66, $Q=0.5*10^{-9}$ m^3/s.

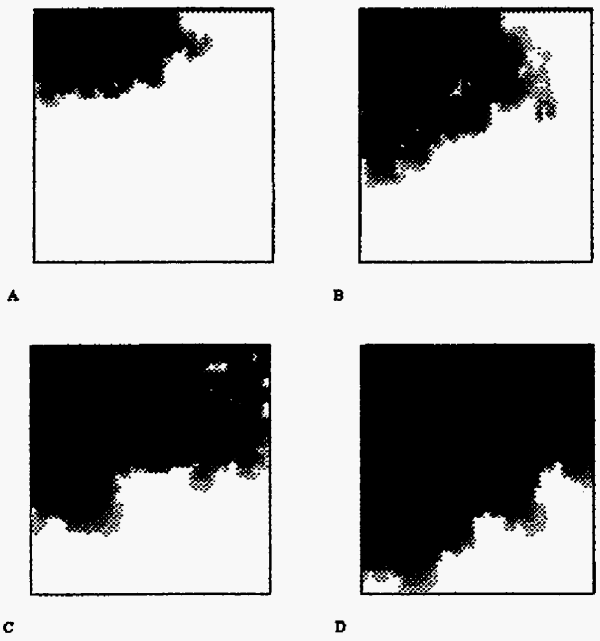

Figure 8 Concentration patterns for run 2 at the four different occupation fractions. Darker colors indicate smaller concentrations. Pe=596, $Q=0.45*10^{-6}$ m^3/s.

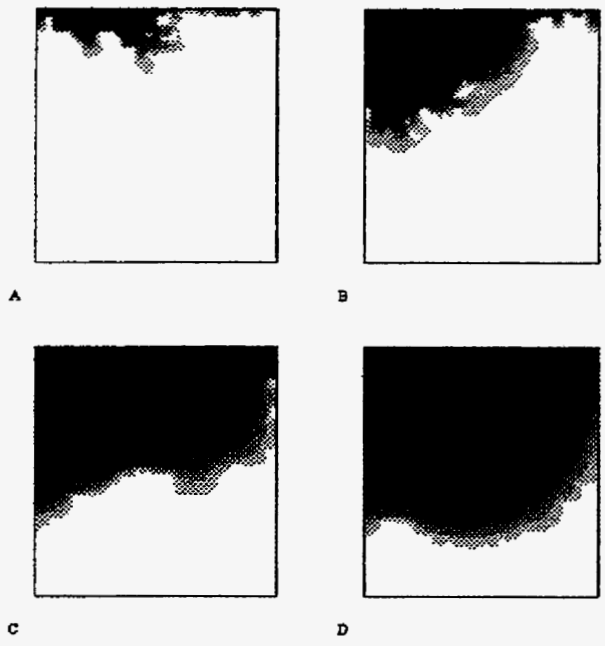

Figure 9 Concentration patterns for run 12 at the four different occupation fractions. Darker colors indicate smaller concentrations. Pe=66, $Q=0.05*10^{-6}$ m^3/s.

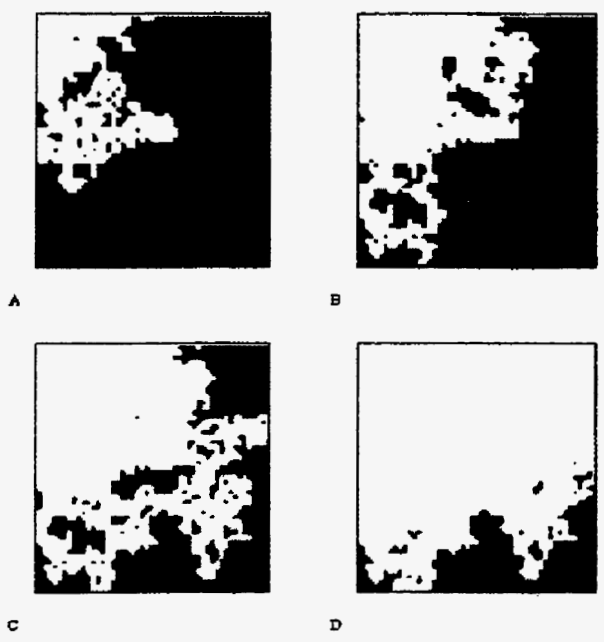

Figure 10 Phase distribution patterns for run 4 at four different liquid fractions corresponding to 20%, 40%, 60% and 80%. The liquid phase is black and the gas phase is white. Pe=331, $Q=0.25*10^{-6}$ m^3/s.

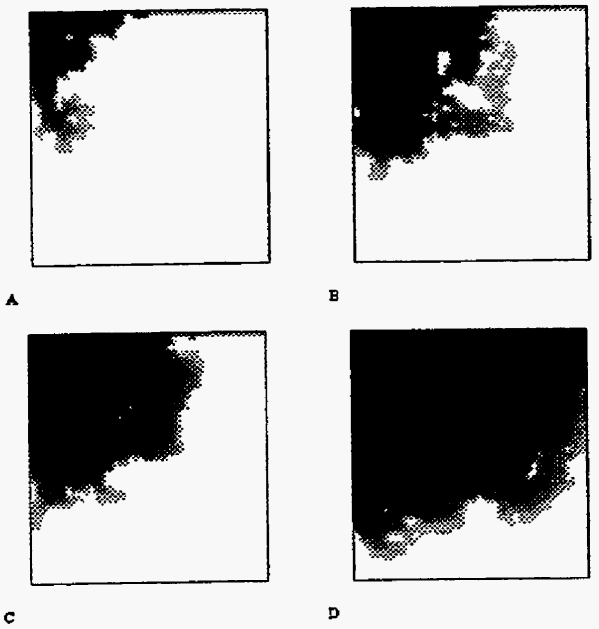

Figure 11 Concentration patterns for run 4 at the four different occupation fractions. Darker colors indicate smaller concentrations. Pe=331, Q=0.25*10^{-6} m^3/s.

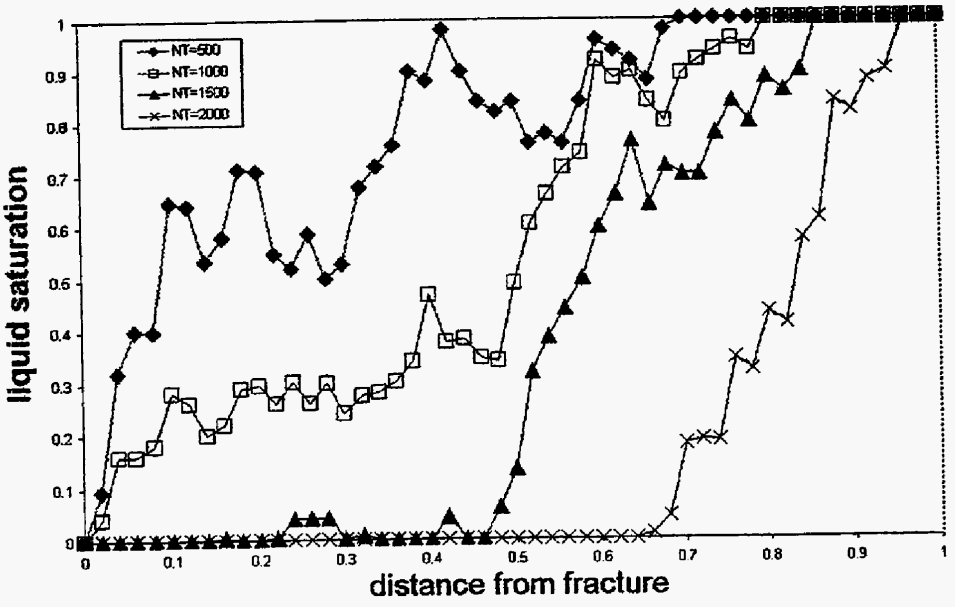

Figure 12 Transversely-averaged saturation profiles for run 15 at the four different occupation fractions.

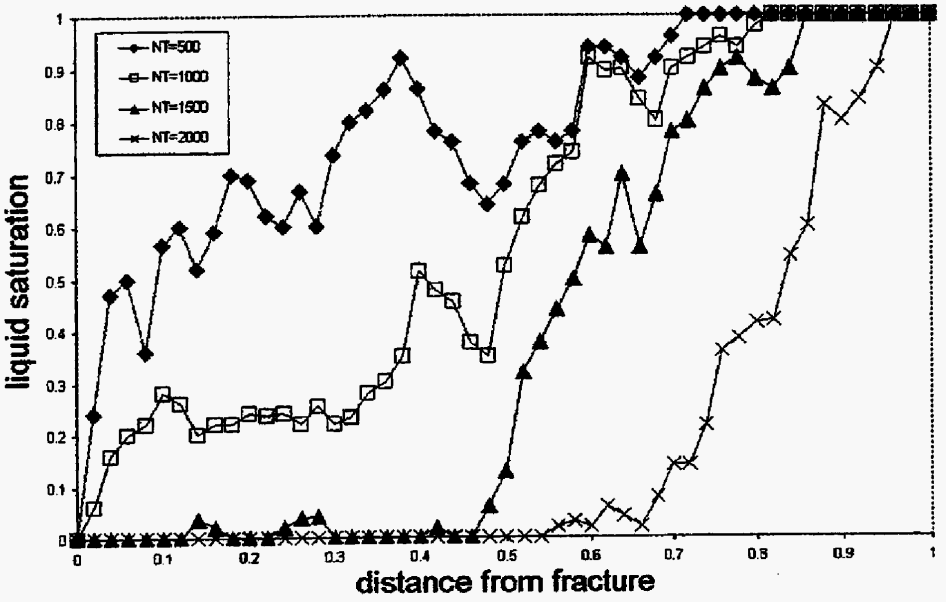

Figure 13 Transversely-averaged saturation profiles for run 12 at the four different occupation fractions.

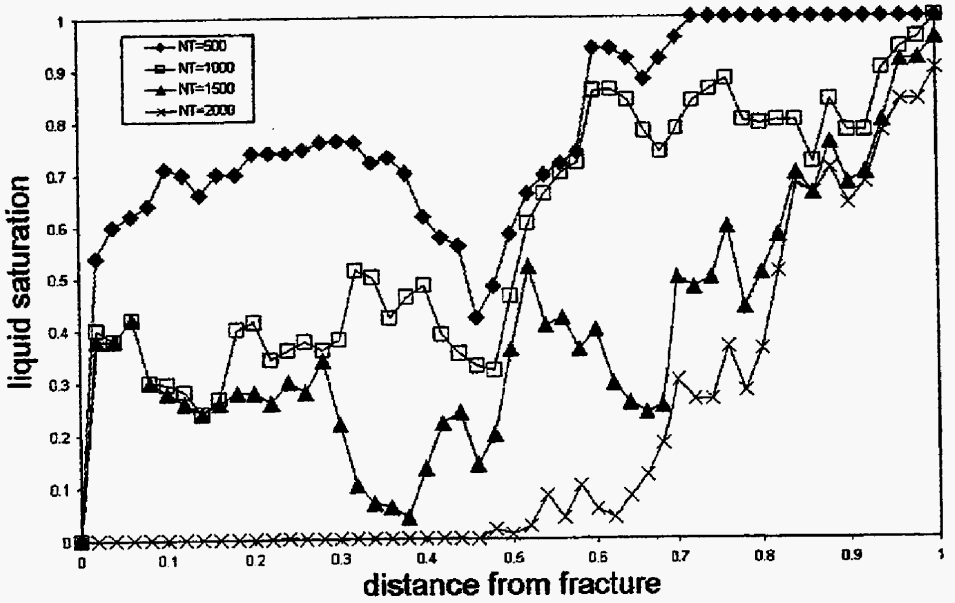

Figure 18 Transversely-averaged saturation profiles for run 4 at the four different occupation fractions.

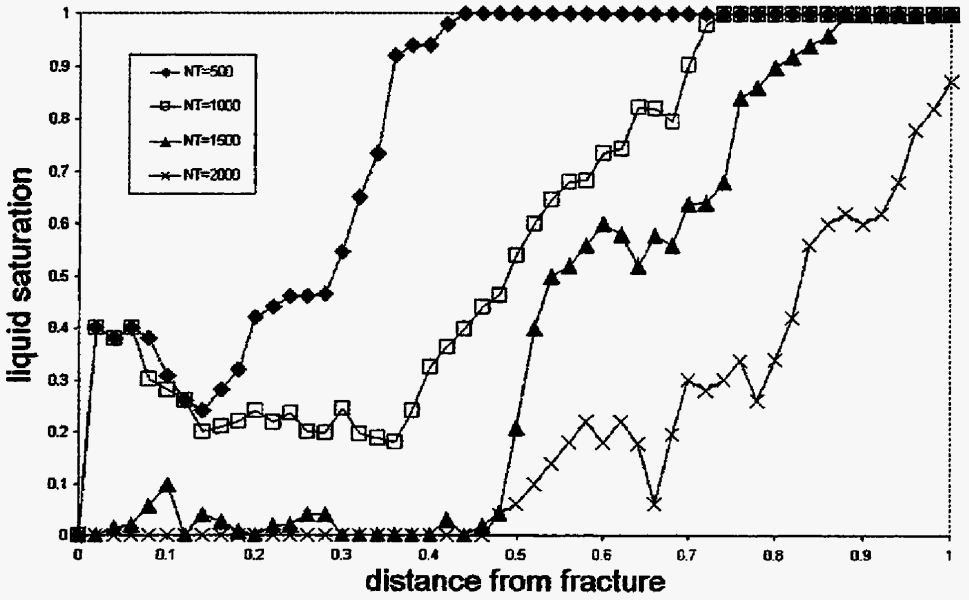

Figure 15 Transversely-averaged saturation profiles for run 2 at the four different occupation fractions.

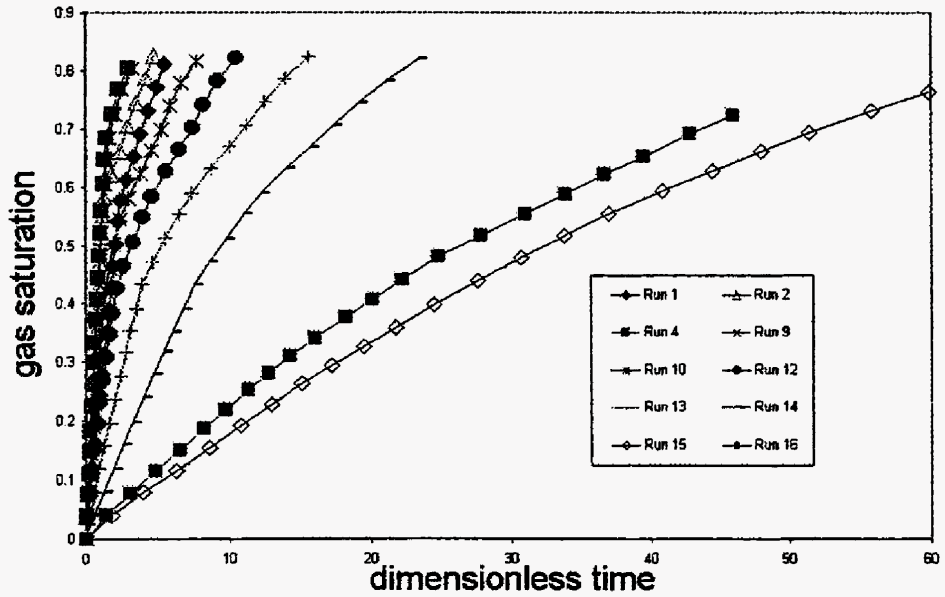

Figure 16 Drying curves (gas volume fraction vs. dimensionless time) for various runs.

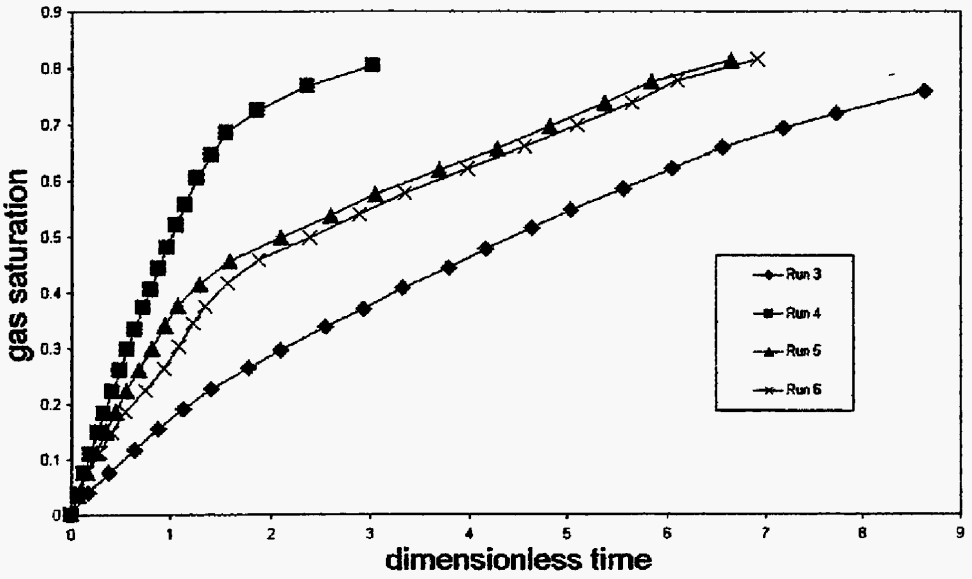

Figure 17 Drying curves (gas volume fraction vs. dimensionless time) for runs 3-6.

II. VAPOR-LIQUID FLOWS

The simultaneous flow of vapor and liquid phases is common to steam injection. Counter-current flows are encountered in Steam-Assisted-Gravity-Drainage (SAGD), and in steam injection in horizontal wells. They also appear in the context of heat pipes in a variety of processes (from geothermal to high-level numclear waste disposal). Concurrent flows are found in typical displacements, in solution gas-drives near wells, and various other contexts. The interaction between heat transfer, heat flux, buoyancy and fluid flow affects the occupancy of phases and the flow characteristics, such as relative permeabilities. In this section we report on two studies, one dealing with the steady-state and stability of vapor-liquid counterflow in a context typical of SAGD, but in the absence of a third phase, and another providing an analytical result, using conformal mapping theory, for the shape of a gravity finger, for example in the displacement of a liquid by a gas. Not included in the latter, however, are effects of heat transfer. On-going work, also not reported here, includes the extension of the counterflow problem to a third phase, namely of a draining oil phase, the description of three-phase flow at the pore-scale and the effect of heat transfer on the relative permeabilities of vapor-liquid systems. Progress in these areas will be reported in future publications and reports. In parallel, we must mention that we have initiated a new effort using a new approach, based on what we term Darcian Dynamics, to describe the dynamics of the flow of a disconnected phase, in the form of ganglia, in the flow field of a displacing continuous phase. This effort, which parallels the analogous effort in Stokes flows, called Stokesian Dynamics, is currently under way.

STABILITY OF HEAT PIPES IN VAPOR-DOMINATED SYSTEMS

Pouya Amili and Yanis C. Yortsos

INTRODUCTION

Heat pipes are steady-state, steam-water, countercurrent flow regimes in porous media driven by the application of a heat flux and gravity (White et al., 1971). Main characteristics of heat pipes are that their temperature is constant, and equal to the vapor saturation temperature at the prevailing pressure and that their liquid saturation is spatially constant (Udell, 1985). In theory, their spatial extent can be infinitely large, under the condition that the porous medium is homogeneous and that the temperature decrease due to the pressure drop is not significant (Satik et al., 1991, Stubos et al., 1993, Pestov, 1998). For a constant heat flux directed against the gravity vector, there are two possible steady-states, determined by the solution of the following equation, in the absence of heat conduction or capillary effects (Bau and Torrance, 1982, Udell, 1985, Stubos et al., 1993) (See schematic of Fig. 1).

$$\omega = \frac{q\,\nu_v}{k\,g\,L_v\left(\rho_l - \rho_v\right)} = \frac{1}{\frac{\nu_l}{\nu_v}\frac{1}{k_{rl}} + \frac{1}{k_{rv}}} \tag{1}$$

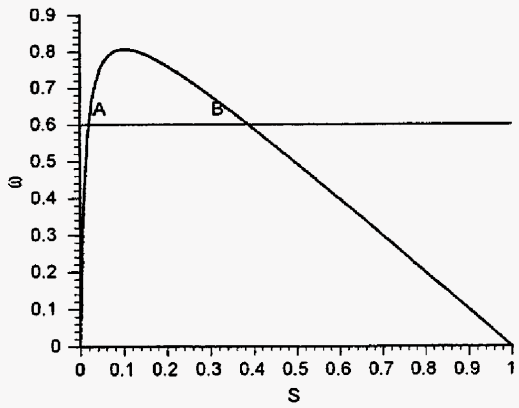

Fig. 1. The saturation of the base state

Here ω is a dimensionless parameter expressing the magnitude of the applied heat flux, and q, ν, k, g, L_v, ρ and k_r denote heat flux, kinematic viscosity, permeability, gravitional

acceleration, latent heat of vaporization, density and the relative permeability, respectively. Subscript l and v denote liquid and vapor, respectively.

In the illustration of Fig. 1, straight-line relative permeabilities with zero residual saturations were taken. The straight line corresponding to a constant heat flux, ω, intercepts the heat flux-saturation curve at two points, A and B, provided that the flux is smaller than a critical value, ω_{max} (equal to about 0.8 in the figure). The two steady states correspond to a vapor-dominated or to a liquid-dominated heat pipe, depending on whether the liquid saturation is small (point A) or large (point B), respectively. Above the critical value, a heat pipe per se, in the sense of a constant saturation region, does not form. Instead, a two-phase zone of considerably smaller extent forms, governed by the competition of capillary and gravity forces, where the saturation varies in the range (1,0) see Stubos et al. (1993).

The heat pipe regime can be connected to single-phase flow regimes above or below it. In applications when the liquid-dominated branch exists, a (subcooled) liquid layer overlies the heat pipe region. The point of transition between the heat pipe and the liquid depends on a variety of factors, including the heterogeneity of the medium (Stubos et al., 1993, Mc Guiness, 1996a, 1996b, Pestov, 1998). Typically, this application is encountered in boiling at low rates in porous media, where a liquid layer above the two-phase region is maintained, for example by keeping its temperature below boiling (Ramesh and Torrance, 1990, 1993). Conversely, a vapor-dominated heat pipe develops when a superheated vapor lies below the two-phase region. This situation, often referred to as "dryout", requires that superheated conditions exist below the two-phase regime. In either case, the transition between single-phase and two-phase flow regimes is also controlled by capillary forces (Stubos et al. 1993). While transitions between single-phase and two-phase flow regimes are possible, a transition between the two different heat pipe regimes, namely from liquid-dominated to vapor-dominated or vice-versa, is not possible (Mc Guiness et al., 1993, Stubos et al., 1993).

Regardless of the particular application, the existence of a heat pipe regime either below an overlying liquid or above an underlying vapor raises questions of stability. Consider, for example, the case of a liquid-dominated heat pipe. Given that the heat pipe is of a lower (although not by much) density than the overlying liquid, the possibility of a Rayleigh-Taylor type gravitational instability is apparent (Drazin and Reid, 1981). The onset of natural convection in the overlying liquid layer, due to its variable temperature, is also an important

factor. In porous media, the onset of natural convection under single-phase flow conditions requires that the single-phase Rayleigh number, defined as:

$$\mathrm{Ra} = \frac{k H g \beta \Delta T}{\alpha \nu} \tag{2}$$

exceeds the critical value of $4\pi^2$ (Lapwood, 1948, Gebhart et al., 1988). Here, H is the thickness of the single-phase region, across which a temperature difference, ΔT, is applied, β is the thermal expansion coefficient of the liquid and α is the effective thermal diffusivity. Stabilizing factors, on the other hand, include conduction, the phase change at the liquid-heat pipe interface, and capillary effects.

The stability of liquid-dominated heat pipes was explored by Ramesh and Torrance (1990, 1993) in the context of boiling in porous media. They also reported the existence of a critical Rayleigh number above which the 1-D configuration is unstable to 2-D disturbances, and is a function of wave length and dimensionless heat flux. However the minimum critical value found was about half of that for the onset of natural convection in single-phase flow, suggesting that the underlying two-phase region is destabilizing the flow. Stability at large wavelengths is associated with viscous flow, while that at smaller wavelengths is due to conduction. A window of unstable wave numbers exists for Rayleigh numbers larger than the critical. Pestov (1998), examined the stability of the two-phase region overlying a vapor-dominated heat pipe, which she found to be stable. However the stability of the combined vapor-dominated heat pipes has not been explored at this time.

Vapor-dominated heat pipes find applications in similar contexts as liquid-dominated heat pipes. A most interesting visualization was provided recently by Kneafsy and Pruess (1999), who studied the flow mechanisms in heat pipes in a fracture, such that superheated conditions were maintained below the two-phase region. Although that study focused mainly on the mechanics of liquid flow, many issues related to flow instability and possibility that downwards-percolating liquid may "penetrate" the superheated region, were raised. At present, the stability features of this configuration are not known. Some of these features should be similar to the liquid-dominated case. For example, we should expect the onset of a natural convection mechanism for the vapor underlying the two-phase region, and a gravitional instability due to the two-phase region above being heavier (although only by a

small amount) than the underlying vapor. The effect of the phase-transition at the interface is unclear, however, just as it has been unclear for the liquid-dominated heat pipes studied by Ramesh and Torrance (1990). In the context of other problems involving phase change in porous media, for example in steam injection processes for the recovery of heavy oil, we know that the condensation of steam at an advancing steam front is less destabilizing, than in non-condensing flows, due to the associated volume reduction. Conversely, the vaporization of liquid is more destabilizing, due to the associated volume expansion.

In this section, we study the linear stability of vapor-dominated heat pipes by following a linear stability approach similar to Ramesh and Torrance (1990, 1993). In addition to the base-state configuration, however, other differences exist between the present approach and that of Ramesh and Torrance. We consider an infinitely long two-phase zone (heat pipe), as there are no compelling reason to restrict the two-phase region to a given length. The same difference applies also between our work and Pestov's (1998). Also our stability analysis is done using analytical methods, which allow for an asymptotic treatment of the problem. On the other hand, in our analysis the compressibility of the vapor is not being considered, except for driving the natural convection (a Boussinesq type approximation). This section is organized as follows: First, we present a dimensionless formulation of the base state and discuss the properties of the vapor-dominated solution. Then, the linearized perturbation problem is presented based on normal modes. The stability analysis follows.

THE BASE-STATE

We consider the following base state. Due to the application of a heat flux, a dryout region of thickness H, consisting of a superheated vapor of almost constant pressure, P_v, underlies a two-phase region of infinite extent. The boundary between the two regions is a planar interface, with saturation temperature corresponding to P_v, denoted as t_{sat}. The two-phase region (heat pipe) corresponds to the vapor-dominated branch of the solution of equation (1). We assume that the heat flux is sufficiently small so that equation (1) has a solution (namely $\omega < \omega_{max}$). At base state conditions, the vapor is stagnant, and heat transfer is by conduction only. The two-phase zone, on the other hand, is a region of a constant temperature and constant saturation counter-current flow, where heat transfer is by

convection. Under base-state conditions (denoted by subscript 0), the dimensionless equations governing the problem are:

a. Vapor Region

$$\frac{dp_0}{dy} = Ra\,T_0 \tag{3}$$

$$T_0 = 1 - y \tag{4}$$

b. Two-phase Region:

$$\frac{dp_0}{dy} = -\frac{\omega M}{k_{rv}} \tag{5}$$

$$v_{10} = M\omega \tag{6}$$

$$T_0 = 0 \tag{7}$$

$$s = 0 \tag{8}$$

where P and T are dimensionless pressure and temperature, y is a dimensionless spatial coordinate directed upwards, V is velocity, the liquid saturation S is determined from equation (1) and we have made use of a Boussinesq type approximation. In the above we have also introduced the dimensionless two-phase Rayleigh number :

$$M = \frac{C_{pv} Hkg(\rho_l - \rho_v)}{v_v k_e} \tag{9}$$

where C_{pv} is the vapor heat capacity and k_e is the effective thermal conductivity of the porous medium. Note that our definition for the two-phase Rayleigh number is a factor of ρ_l/ρ_v larger than in Ramesh and Torrance (1990). In the above, we have neglected capillary effects.

STABILITY ANALYSIS

1. The Eigenvalue Problem

Subsequently, we carried out a linearized stability analysis of the problem by assuming that all dependent variables are perturbed in the transverse direction, x, and seeking the rates of growth of these disturbances in terms of normal modes. Thus, we take disturbances of the form

$$T = T_0 + \varepsilon\,\theta(y)\exp(i\kappa x + \sigma t) \tag{10}$$

where ε is a small parameter, θ is the eigenfunction, κ is the wavenumber and σ is the rate of growth of the disturbance, and x and t denote transverse coordinate and time, all dimensionless. Similar expansions are taken for the pressure, the saturation and the interface position. These expansions are then substituted in the governing equations and the boundary conditions, and the system is linearized. The details of this process are considerable and will not be presented in this section. The final results for the eigenvalue problem are shown below.

a. Vapor region

(denoted by superscript – where appropriate)

$$\kappa^2 \pi^- + Ra\frac{d\theta}{dy} - \frac{d^2\pi^-}{dy^2} = 0 \tag{11}$$

$$\left(\sigma^* - Ra + \kappa^2\right)\theta + \frac{d\pi^-}{dy} - \frac{d^2\theta}{dy^2} = 0 \tag{12}$$

where $\sigma^*=\beta_1\,\sigma$, and

$\beta_1= [(1-\phi)\,\rho_r\,C_{pr} + \phi\,\rho_v\,C_{pv}] / (\rho_v\,C_{pv})$ is the ratio of the heat capacities for rock and vapor (and it is of the order of 1000).

b. Two-phase region

(denoted by superscript + where appropriate)

$$c_1 \pi^+ + c_2 S - c_3 \frac{dS}{dy} - \frac{d^2\pi^+}{dy^2} = 0 \tag{13}$$

$$c_1 \pi^+ - c_4 S + c_5 \frac{dS}{dy} - \frac{d^2\pi^+}{dy^2} = 0 \tag{14}$$

where the constants are defined as,

$$c_1 = \kappa^2$$

$$c_2 = \frac{\varphi \sigma \mu_l}{k_{rl} \mu_v}$$

$$c_3 = \frac{1}{k_{rl}} \left(\frac{dp_0^+}{dy} + M \right)$$

$$c_4 = \frac{\phi \sigma}{k_{rv}}$$

$$c_5 = \frac{1}{k_{rv}} \frac{dp_0^+}{dy}$$

The differential equations in these regions are to be solved subject to boundary conditions of constant temperature and zero vapor flux at y=0, no-flux conditions for vapor and liquid at y=∞, and continuity of mass, energy, temperature and pressure at the interface (y=δ).

The eigenvalue problem was then solved analytically. By incorporating the boundary conditions we obtained a fourth-order homogeneous linear system, the determinant of which must vanish for a non-trivial solution to exist. We note that because we have neglected the compressibility of the vapor, the saturation disturbance in our problem turns out to be zero (in contrast to Pestov, 1998). The vanishing of the determinant provides the solution for the rate of growth σ (or σ*) as a function of the wavenumber κ and the various dimensionless parameters, among which key roles are played by the Rayleigh number and ω. Details of this calculation will not be presented here.

2. Results

Numerically accurate results were obtained by imposing the condition of vanishing of the fourth-order determinant. There are basically two parameters, that can vary independently, ω, which contains the dimensionless heat flux, and the two-phase Rayleigh number M. Note that the conventional Rayleigh number is related to these parameters via

$$Ra = \omega M^2 N \tag{15}$$

where we introduced the additional dimensionless parameter $N=(L_v \rho_v) / [C_{pv} (\rho_l - \rho_v) t_{sat}]$.

Typically, we find that the long waves are stable (see inset of Figs. 2 and 3 below). An asymptotic analysis shows that in the limit $\kappa \rightarrow 0$, we have

$$\sqrt{-\sigma^*} \tan\left(\sqrt{-\sigma^*}\right) = \kappa \tag{16}$$

where $\kappa >> 1$. This equation admits infinitely many solutions (which were confirmed numerically as well) the largest algebraically of which is $(-\pi^2/4)$. This is indeed confirmed in Fig.2b and Fig.3. The behavior is similar to the boiling problem of Ramesh and Torrance (1993). Intermediate wavenumbers can be unstable, depending on whether or not the Rayleigh number is larger than a critical number, as discussed below. Sufficiently small wavelengths are stable, as in Ramesh and Torrance (1990).

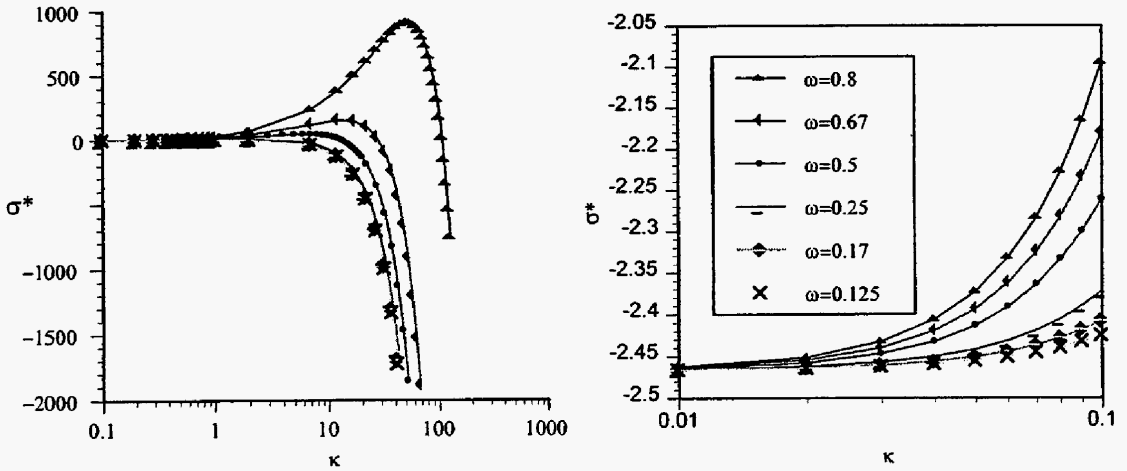

Fig. 2. (a) The σ^*-κ relation for different values of ω at constant M=50. (b)The plot at small κ.

Figure 2. shows the rate of growth vs. the wavenumber curve for fixed M and variable ω. It is to be noted that ω cannot exceed a maximum value, for a heat pipe region to exist. It is shown that as ω decreases, the configuration is less unstable, reflecting the facts that the density of the heat pipe region diminishes at smaller ω and that the overall Rayleigh number is also smaller

Figure 3.shows corresponding result for the case of fixed ω and variable M. The configuration is shown to be more destabilized as the two-phase Rayleigh number M increases. In all these calculations the other parameters affecting the Rayleigh number definition above, for example the latent heat of vaporization, were held constant. Under this condition, it was found that the data collapsed on the same curve, if the variables ω and M were combined so that the Rayleigh number was constant. However, this should not be interpreted to imply that the Rayleigh number is the only relevant parameter of the problem (see below).

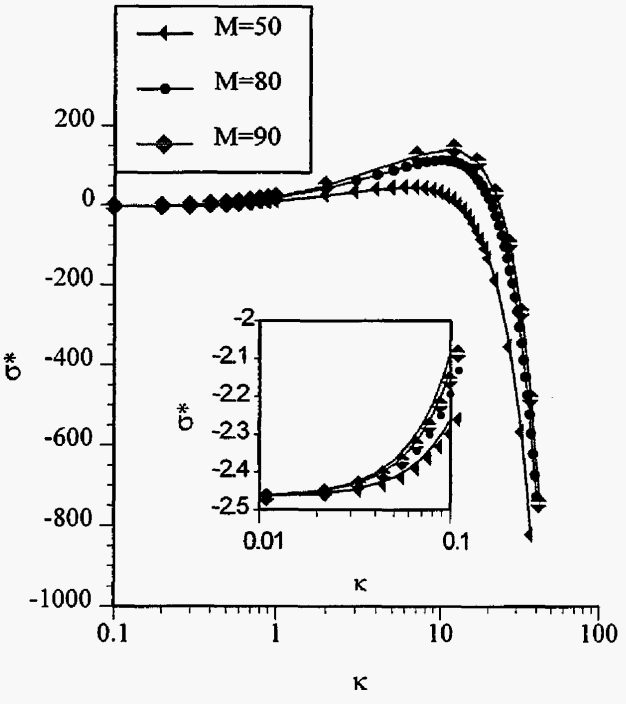

Fig. 3. The σ*-κ relation for different values of M at constant ω=0.5, and inset of the plot at small κ.

As in Ramesh and Torrance (1990), a critical Rayleigh number, Ra_{crit} exists which is a function of the other parameters of the problem, and particularly ω. Fig. 4 shows a plot of

Ra_{crit} vs. ω obtained assuming a constant N. It is shown that Ra_{crit} is considerably smaller than the critical number corresponding to either single-phase natural convection or the liquid-dominated problem treated by Ramesh and Torrance(1990). Furthermore, Ra_{crit} is found to increase as ω decreases.

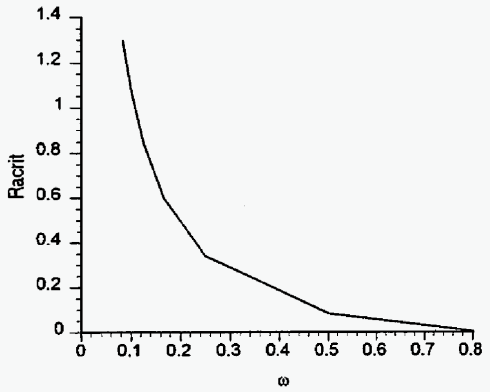

Fig. 4. The dependence of Ra_{crit} on ω.

To test the effect of the phase change process, we considered the sensitivity of the results to the latent heat, by keeping the Rayleigh number constant, namely we considered variable L_v but kept the product ω N (and M) constant. Results are shown in Fig. 5. It is shown that the problem becomes more unstable as the latent heat decreases, indicating the smaller energy requirements to sustain a destabilizing heat pipe above the vapor region as the latent heat is smaller.

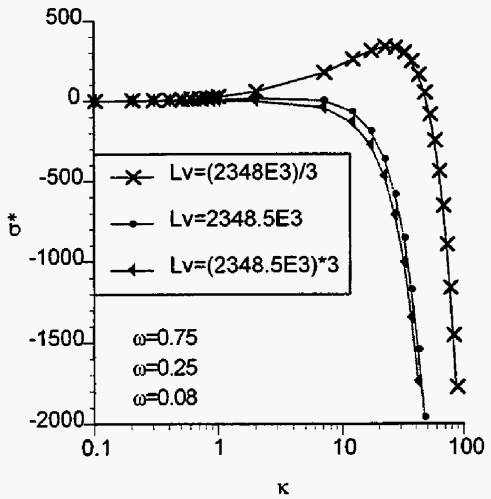

Fig. 5. The effect on stability of the variation in latent heat.

CONCLUSIONS

In this section, we studied the linear stability of a two-phase heat pipe zone (vapor-liquid counterflow) in a porous medium, overlying a superheated vapor zone. It was found that the problem has similarities with the liquid-dominated case, in that long and short waves are stable, but intermediate wavelengths can be unstable, depending on the parameter values. A critical Rayleigh number was identified and shown to be different than in natural convection under single-phase conditions in two respects: The critical value is significantly smaller (even smaller than liquid-dominated case), while the critical value is shown to also depend on the other parameters of the problem. In particular, we found that the latent heat affects the stability of the problem. The results find applications to geothermal systems, to enhanced oil recovery, as well as to the conditions of the proposed Yucca Mountain nuclear waste repository.

REFERENCES

Bau, H. H., and Torrance, K. E., 1982, "Boiling in Low-Permeability Porous Materials," International Journal of Heat Mass Transfer, **25**, 45-54.

Drazin, P. G. and Reid, W. H. 1981, *Hydrodynamic Stability*. Cambridge University Press.

Gebhart, B., Jaluria, Y, Mahajan, R., and Sammakia, B., (1988, *Bouyancy-Induced Flows and Transport*. Hemisphere Publishing Corporation.

Kneafsey, T. J. and Pruess, K., 1999, "Laboratory Experiments on Heat-Driven Two-Phase Flows in Natural and Artificial Rock Fractures", Water Res. Res., in press.

McGuinness, M. J., 1996a, "Steady Solution Selection and Existence in Geothermal Heat Pipes -I. The Convective Case", International Journal of Heat Mass Transfer, **39**, 259-274.

McGuinness, M. J., 1996b, "Steady Solution Selection and Existence in Geothermal Heat Pipes -II. The Conductive Case", International Journal of Heat Mass Transfer, **40**, 311-321.

McGuinness, M. J., Blakeley, M., Pruess, K. & O'Sullivan, M. J.,, 1993, "Geothermal Heat Pipe Stability: Solution Selection by Upstreaming and Boundary Conditions," Transport in Porous Media, **11**, 71-100.

Lapwood, E. R., 1948, Proc. Cambridge Philos. Soc. **44**, 508.

Pestov, I., 1998, "Stability of Vapor-Liquid Counterflow in Porous Media," Journal of Fluid Mechanics, **364**, 273-295.

Ramesh, P. S. and Torrance, K. E., 1990, " Stability of Boiling Porous Media," International Journal of Heat Mass Transfer **33**, 1895-1908.

Ramesh, P. S. and Torrance, K. E., 1993, ". Boiling in Porous Layer Heated from Below: Effects of Natural Convection and a Moving Liquid/Two Phase Interface" Journal of Fluid Mechanics, **257**, 289-309.

Satik, C., Parlar, M., and Yortsos, Y. C., 1991, "A Study of Steady-State Steam-Water Counterflow in Porous Media", International Journal of Heat Mass Transfer **34**, 1755-1771.

Stubos, A. K., Satik, C., and Yortsos, Y. C., 1993, "Effects of Capillary Heterogeneity on Vapory-Liquid Counterflow in Porous Media", International Journal of Heat Mass Transfer, **28**, 485-495

Udell, K. S., 1985, "Heat Transfer in Porous Media Considering Phase Change and Capillarity – the Heat Pipe Effect", International Journal of Heat Mass Transfer **28**, 485-495.

White, D. E., Muffler, L. J., and Truesdell, A. H., 1971, "Vapor-Dominated Hydrothermal Systems Compared with Hot-Water Systems", Economic Geol, **66**, 75-97.

THE SHAPE OF A GRAVITY FINGER

Lang Zhan and Yanis C. Yortsos

INTRODUCTION

Displacing a more viscous fluid from a reservoir by a less viscous fluid results in unstable viscous fingers. Saffman and Taylor made a historical discovery in a narrow Hele-Shaw cell experiment in which they found that the ratio of width of finger to width of channel λ is close to $\frac{1}{2}$ [8]. They also developed an analytical expression for the finger interface in which λ serves as a free parameter. If λ equals $\frac{1}{2}$, the analytical expression fits the developed finger shape of the experiment quite well. From then on, extensive studies have been performed to understand the selection of the parameter λ and its relationship to the instability of fluid displacements [7].

When the density of the resident fluid is different from that of the displacing, gravity will complicate the analysis because it may improve or deteriorate the stability of displacement. Craig et al. [3] used five-spot and line-drive experiments to demonstrate the significant effects of gravity fingers on oil recovery. Greenkorn and colleagues [5] studied the interface of the two phase immiscible flow by using Hele-Shaw cell experiments. They proposed a series solution to describe the interface shape of the finger as follows

$$x = \frac{Gy}{\lambda} - h\sum_{n=1}^{\infty} A_n \exp\{-\frac{n\pi Gy}{\lambda h}\}\cos\frac{n\pi y}{\lambda h} \tag{1}$$

where G is the gravity dimensionless number, h is the height of the cell and λ is the finger-cell width ratio. However, they did not specify how to determine these infinite coefficients A_n in (1). They also extended their research into a glass bead porous medium and observed that gravity can damp out some of the instability of the fingers and that the width of the developed finger depends strongly on the velocity, height of media and other fluid properties [9]. Fayers and Muggeridge provided a model for calculating gravity finger between miscible fluids in tilted reservoirs [4], based on the numerical solution of a partial differential equation

to obtain the finger width. More recently, Brener et al. [1, 2] proposed a three-parameter expression for describing the stable gravity finger shape, which reads as follows

$$x = \frac{W}{\pi}\left[(1-\lambda)\ln\sin(2\alpha) + 2y_0 \ln\tan(\alpha)\right] \tag{2}$$

$$y = W\left[y_0 - \frac{\lambda}{2} + \frac{2\lambda\cos(\epsilon\pi/2)}{\pi}\int_0^{\alpha}(\tan\alpha')^{\epsilon}d\alpha'\right]. \tag{3}$$

where λ is the relative width of finger, y_0 denotes the y coordinate of the center position of the finger departed from the center of a channel, $\epsilon = 1 - 2/\pi\beta$, $\beta = \arctan(1/\hat{N}_g\lambda)$, α takes values from 0 to $\pi/2$, W is the width of the channel and $\hat{N}_g$ is the gravity number that is defined as follows

$$\hat{N}_g = \frac{(g\rho\sin\omega)b^2}{12\mu V} \tag{4}$$

where ω represents tilt angle, ρ and μ are the density and viscosity of the resident fluid, V is the fluid velocity far ahead of interface, and b is the thickness of a Hele-Shaw cell. Like in [5, 8], they neglected the density and viscosity of displacing fluid.

In the following, we propose a new gravity finger model for two-phase fluid displacement in absent of interfacial tension. It has the advantages of the equations by Greenkorn et al. [5] and Brener et al. [1, 2] but without their drawbacks: (a) the model considers density and viscosity of both resident and displacing fluids; (b) it only involves one free parameter (as (1)); (c) it provides a closed form solution of the interface shape of a developed gravity finger (as (2) and(3)).

GOVERNING EQUATIONS AND BOUNDARY CONDITIONS

A typical schematic of a gravity finger is shown in Figure 1. The displacement occurs in a vertical cross-section of a channel of width H, where the flow direction is perpendicular to that of gravity. The displaced fluid, with subscript 1, has larger density, thus, the displacing

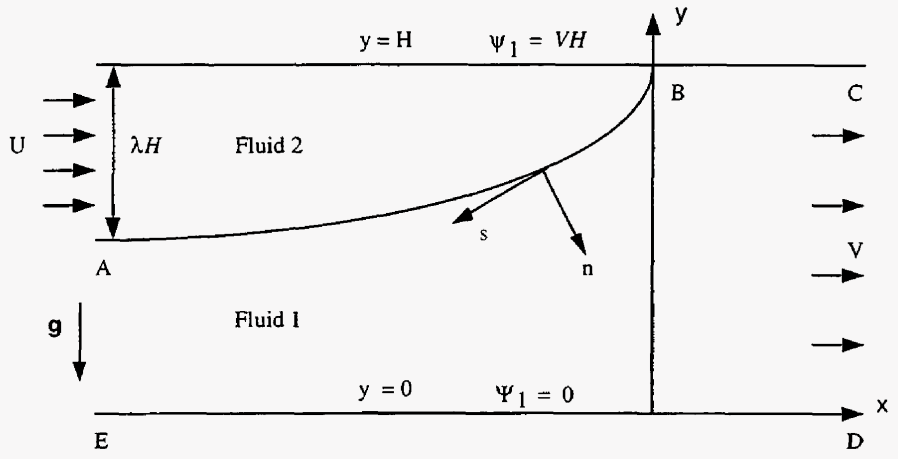

Figure 1: Schematic of a gravity finger

fluid (subscript 2) will evolve into a fully-developed single finger along the upper wall. Displacement at constant injection velocity V is considered. The interface of the two fluids will be denoted as AB, while the bottom wall is denoted as ED. The coordinate of the x axis is along ED. Because the injected fluid occupies less than the entire space, fluid 2 moves with velocity U for upstream, while the displaced fluid 1 moves with velocity V, far downstream. Without loss in generality, the streamfunction is zero along the bottom wall.

If we now define the relative finger width as $\lambda \equiv \frac{H_2}{H}$, where H_2 is the finger width at infinity upstream, the mass balances of two fluids read

$$V = \lambda U + (1-\lambda)\frac{U}{M} \tag{5}$$

$$U = \frac{V}{\lambda + \frac{1-\lambda}{M}}. \tag{6}$$

Here, we can see that if $M \geq 1$, $U \geq V$, and vice-versa.

Assuming incompressible fluids, we can write the following governing equations:

$$\vec{u}_1 = -\frac{k}{\mu_1}(\nabla p_1 - \rho_1 \vec{g}) \tag{7}$$

$$\vec{u}_2 = -\frac{k}{\mu_2}(\nabla p_2 - \rho_2 \vec{g}) \tag{8}$$

$$\nabla \cdot \vec{u}_1 = 0 \tag{9}$$

$$\nabla \cdot \vec{u}_2 = 0 \tag{10}$$

where $\vec{u}_j$, μ_j, p_j, ρ_j and k denote fluid velocities, fluid viscosities, fluid pressures, fluid densities and porous media permeability, $j = 1, 2$ represent the two fluids, and $\vec{g}$ is the acceleration of gravity vector. A solution of this problem is $u_{2x} = U$ and $u_{2y} = 0$ inside fluid 2, namely,

$$-\frac{k}{\mu_2}\frac{\partial p_2}{\partial x} = U \tag{11}$$

$$-\frac{k}{\mu_2}(\frac{\partial p_2}{\partial y} + \rho_2 g) = 0 \tag{12}$$

Integrating (12), we obtain the pressure in fluid 2 as

$$p_2 = -\rho_2 g y + c(x) \tag{13}$$

where $c(x)$ is a constant of integration obtained by substituting (13) into (11), and integrating

$$c(x) = -\frac{\mu_2 U}{k}x + \hat{a} \tag{14}$$

where $\hat{a}$ is a constant. Combining (13) and (14), the pressure in fluid 2 is

$$p_2 = -\rho_2 g y - \frac{\mu_2 U x}{k} + \hat{a} \tag{15}$$

Inside fluid 1, we do not have a simple solution for the pressure. Because of continuity of pressure on the interface, we have at any point

$$p_1 = p_2 = -\rho_2 g y - \frac{\mu_2 U x}{k} + \hat{a} \tag{16}$$

We can also deduce certain properties upstream and downstream. Far upstream, $u_{1y} = 0$, i.e.,

$$u_{1y} = -\frac{k}{\mu_1}(\frac{\partial p_1}{\partial y} + \rho_1 g) \Rightarrow 0 \tag{17}$$

Integrating the above equation, the far upstream pressure in fluid 1 is

$$p_1 \approx -\rho_1 g y + e(x), \tag{18}$$

where $e(x)$ is a constant of integration. We note that at that limit

$$\frac{\partial p_1}{\partial x} = e'(x). \tag{19}$$

Also far upstream, the interface is parallel to the x-axis, the y component velocities are null and in the absence of capillarity, the pressures in the two fluids satisfy

$$\frac{\partial p_1}{\partial x} = \frac{\partial p_2}{\partial x} \tag{20}$$

Combining equations (18), (19), and (20), the coefficient $e(x)$ can be found

$$e'(x) = -\frac{\mu_2 U}{k} \tag{21}$$

or

$$e(x) = -\frac{\mu_2 U x}{k} + \hat{e} \tag{22}$$

where $\hat{e}$ is another integration constant. Thus, the pressure of fluid 1 far upstream is

$$p_1 = -\rho_1 g y - \frac{\mu_2 U x}{k} + \hat{e} \tag{23}$$

Far downstream, the condition of a constant fluid velocity at steady-state gives

$$-\frac{k}{\mu_1}\frac{\partial p_1}{\partial x} = V \tag{24}$$

Up to now, we have solved the pressure in displacing fluid 2 and have found certain pressure boundary conditions in the displaced fluid 1. To proceed further, we will transform the above equations in the streamfunction and potential domain to solve for the fluid interface explicitly. Define the potential in displacing fluid 1 as

$$\Phi_1 = -\frac{k}{\mu_1}(p_1 + \rho_1 g y + \hat{d}) \tag{25}$$

where $\hat{d}$ is a constant, or using the pressure as a dependent variable

$$p_1 = -\frac{\mu_1 \Phi_1}{k} - \rho_1 g y - \hat{d} \tag{26}$$

At the interface between the two fluids, the potential can be obtained from equations (16) and (26),

$$\Phi_1 = \frac{U}{M}x - \frac{(\rho_1 - \rho_2)gyk}{\mu_1} - \frac{k}{\mu_1}\hat{d} - \hat{a} \tag{27}$$

Far upstream, equations (23) and (26) give

$$\Phi_1 = -\frac{k}{\mu_1}(\hat{d} + \hat{e}) + \frac{\mu_2 U x}{\mu_1} \tag{28}$$

Using the conventional definition $M \equiv \frac{\mu_1}{\mu_2}$, the condition on Φ_1 upstream can also be expressed as

$$\Phi_1 = \frac{U}{M}x - \frac{k}{\mu_1}(\hat{d} + \hat{e}) \tag{29}$$

and in differential form

$$\frac{\partial \Phi_1}{\partial x} = \frac{U}{M}, \qquad (x \to -\infty) \tag{30}$$

Far downstream, the differential condition from (24) and (26) gives

$$\frac{\partial \Phi_1}{\partial x} = V, \qquad (x \to +\infty) \tag{31}$$

To make further progress and under steady-state conditions, we define the traveling coordinate, $X = x - Ut$, and re-write $Y = y$. Then equations (27), (30) and (31) become

$$\Phi_1 = \frac{U}{M}X - \frac{\triangle\rho gk}{\mu_1}Y - \frac{\triangle\rho gk}{\mu_1}H \qquad (\text{on } AB) \tag{32}$$

$$\frac{\partial\Phi_1}{\partial X} = \frac{U}{M} \qquad (X \to -\infty) \tag{33}$$

$$\frac{\partial\Phi_1}{\partial X} = V \qquad (X \to +\infty) \tag{34}$$

and $\Phi_1(X = 0, Y = H) = 0$.

To obtain the interface function, we need the information on the streamfunction. Along the interface AB, the normal velocity can be written as follows

$$u_{1n} = \frac{\partial\Phi_1}{\partial n} = U\cos\theta \tag{35}$$

Because of the *Cauchy-Riemann* condition, $\frac{\partial\Phi_1}{\partial n} = -\frac{\partial\Psi_1}{\partial s}$, we also have

$$-\frac{\partial\Psi_1}{\partial s} = U\cos\theta \tag{36}$$

Now knowing the relationship $\cos\theta\, ds = -dY$, $\Psi_1|_{Y=H} = VH$, and $\Psi_1|_{Y=0} = 0$, we integrate Ψ_1 in equation (36) to give streamfunction on AB

$$\Psi_1 = UY + H(V - U) \tag{37}$$

Thus, our objective is to find two harmonic functions Φ_1 and Ψ_1 subject to the following

boundary conditions

$$\Psi_1 = VH; \qquad \text{on } Y = H \tag{38}$$

$$\Psi_1 = (V-U)H + UY; \qquad \text{on } AB \tag{39}$$

$$\Phi_1 = \frac{UX}{M} - \frac{\triangle\rho gk}{\mu_1}Y + \frac{\triangle\rho gkH}{\mu_1}; \qquad \text{on } AB \tag{40}$$

$$\Psi_1 = 0; \qquad \text{at } Y = 0 \tag{41}$$

$$\frac{\partial\Phi_1}{\partial X} = \frac{U}{M}; \qquad X \to -\infty \tag{42}$$

$$\frac{\partial\Phi_1}{\partial X} = V; \qquad X \to +\infty \tag{43}$$

Without loss the generality, we take $H = 1$, and transform equations (38) - (43) using the transformation

$$\tilde{W}_1 = \Phi_1 + i\,\Psi_1 - \frac{U}{M}\,Z \tag{44}$$

Then, we normalize the transformed equations by $V - \frac{U}{M}$, use Φ and Ψ as the normalized potential and streamfunction respectively, replace X and Y by x and y, and define the gravity segregation number

$$\begin{aligned} N_g &= \frac{\triangle\rho gk}{\mu_1(V - \frac{U}{M})} \\ &= \frac{\triangle\rho gk}{\mu_1(V - \frac{V}{\lambda M + (1-\lambda)})} \\ &= \frac{\triangle\rho gk\,[\lambda\,M + (1-\lambda)]}{\mu_1\,\lambda\,V\,(M-1)} \end{aligned} \tag{45}$$

Equations (38) to (43) are further simplified to

$$\Psi = 1; \qquad \text{on } y = 1 \tag{46}$$

$$\Psi = 1 - \frac{1-y}{\lambda}; \qquad \text{on } AB \tag{47}$$

$$\Phi = N_g\,(1-y); \qquad \text{on } AB \tag{48}$$

$$\Psi = 0; \qquad \text{on } y = 0 \tag{49}$$

$$\frac{\partial \Phi}{\partial X} = 0; \qquad X \to -\infty \tag{50}$$

$$\frac{\partial \Phi}{\partial X} = 1; \qquad X \to +\infty \tag{51}$$

THE INTERFACE SHAPE USING COMFORMAL MAPPING

To seek the solution of interface, we consider application of conformal mapping. Figure 2 shows the $\Phi - \Psi$ domain where Φ and Ψ need to be solved. With the definition of a new pseudo-streamfunction

$$\chi = \Psi - y \tag{52}$$

equations (47) and (48) can be rewritten as

$$\chi = (1-\Phi)\,(1-\lambda) \qquad (\text{on } AB) \tag{53}$$

Then our task changes to finding the solution of the Laplace equation for χ

$$\nabla^2 \chi = 0 \tag{54}$$

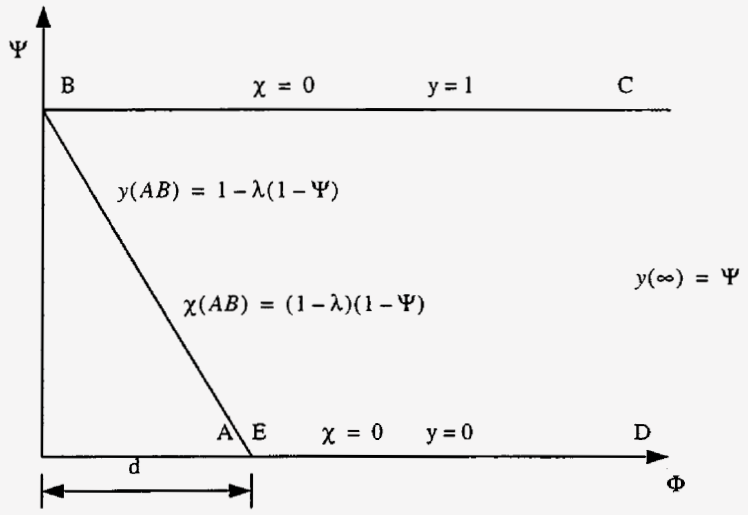

Figure 2: Potential - streamfunction plane

with boundary conditions

$$\chi = 0; \qquad \text{on } \Psi = 1 \tag{55}$$

$$\chi = 0; \qquad \text{on } \Psi = 0 \tag{56}$$

$$\chi = 0; \qquad \text{on } \Phi \to +\infty \tag{57}$$

$$\chi = (1 - \Psi)(1 - \lambda); \qquad \text{on } AB \tag{58}$$

To solve this problem, we use a *Schwarz-Christoffel* transformation [6] for mapping the strip domain in the $\Phi - \Psi$ plane into the $\xi - \eta$ upper half plane, as illustrated in Figure 3. Here, we let $d \equiv \frac{1}{\lambda N_g}$ and $\alpha \equiv \arctan(\frac{1}{d})$. Then, the transform angles are (see Figure 3)

$$\begin{aligned} \alpha_1 &= 0 \\ \alpha_2 &= \alpha \\ \alpha_3 &= \pi - \alpha \end{aligned} \tag{59}$$

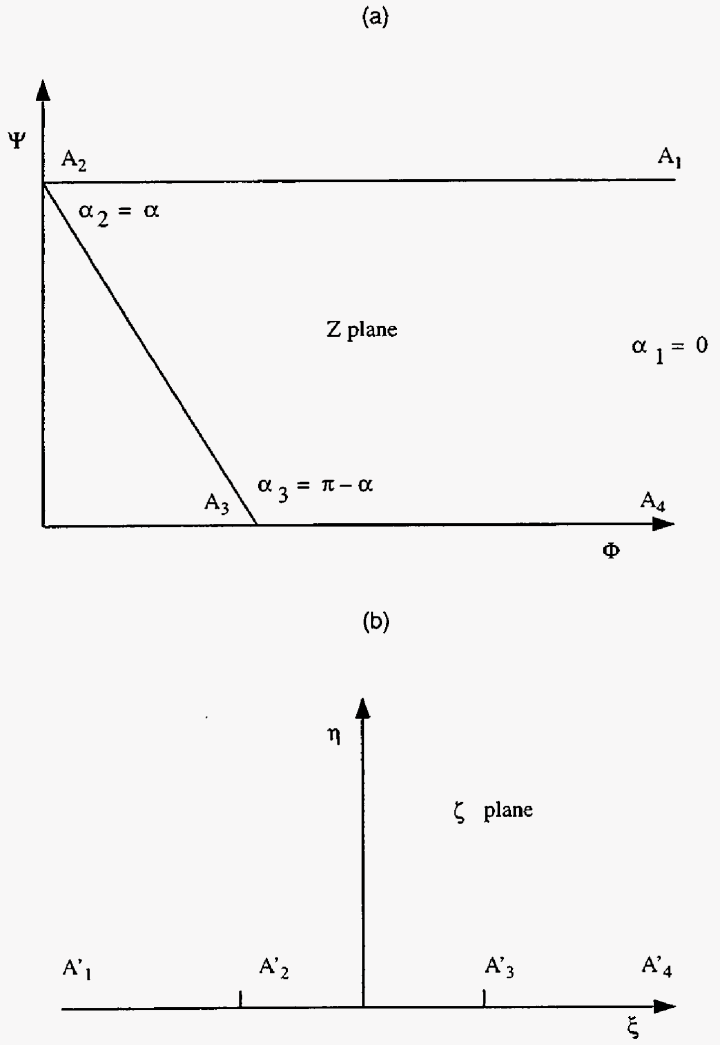

Figure 3: Schwarz-Christoffel transformation

The *Schwarz - Christoffel* transform can be obtained as follow

$$\frac{\partial Z}{\partial \zeta} = a(\zeta + 1)^{\frac{\alpha}{\pi}-1}(\zeta - 1)^{-\frac{\alpha}{\pi}}, \tag{60}$$

or in integral form

$$Z = \Phi + i\,\Psi = a\int_0^{\zeta} \frac{1}{(\zeta - 1)^{\frac{\alpha}{\pi}}(\zeta + 1)^{1-\frac{\alpha}{\pi}}} d\zeta + b \tag{61}$$

where a and b are constants of integration to be determined by the appropriate choice of the corresponding transformed points between the Z and ζ planes. Before we determine these constants, we first derive a relationship for the boundary values in the segment A_2A_3 between the two planes. From (47) and (48), we know that $\Phi = d(1 - \Psi)$, thus, the transformation (61) becomes

$$d(1 - \Psi) + i\,\Psi = a\int_0^{\zeta} \frac{1}{(\zeta - 1)^{\frac{\alpha}{\pi}}(\zeta + 1)^{1-\frac{\alpha}{\pi}}} d\zeta + b \tag{62}$$

and provides $\Psi(\xi)$ on $A_2'A_3'$. Hence, the relation $\chi = (1 - \lambda)(1 - \Psi)$ in Z maps onto $\chi = F(\xi)$ in ζ. Also, equation (52) gives the ordinate in Z by Ψ and χ, thus,

$$y = \Psi + \chi \tag{63}$$

If we find ω, the harmonic counterpart of χ, the relation between the boundary position A_2A_3 in Z and the harmonic functions on $A_2'A_3'$ in ζ can be obtained, namely

$$z = x + iy = \Phi + i\Psi + \omega + i\chi + c \tag{64}$$

The harmonic functions χ and ω are obtained by

$$\begin{aligned}\omega(\xi,\eta) &= \frac{1}{\pi}\int_{-\infty}^{\infty}\frac{(t-\xi)F(t)}{(t-\xi)^2+\eta^2}dt \\ &= \frac{1}{\pi}\int_{-1}^{1}\frac{(t-\xi)F(t)}{(t-\xi)^2+\eta^2}dt \end{aligned} \tag{65}$$

$$\chi(\xi,\eta) = -\frac{1}{\pi}\int_{-\infty}^{\infty}\frac{(t-\xi)\omega(t,0)}{(t-\xi)^2+\eta^2}dt$$

where all integrals are understood to be principal value integrals. Substituting equations (65), (47) and (48) into (64), we establish the interface shape as

$$\begin{aligned} x &= \frac{d(1-y)}{\lambda} + \omega(\xi,0) + c \\ &= \frac{d(1-y)}{\lambda} + \frac{1}{\pi}\int_{-1}^{1}\frac{(t-\xi)F(t)}{(t-\xi)^2}dt + c \\ &= \frac{d(1-y)}{\lambda} + \frac{1}{\pi}\int_{-1}^{1}\frac{F(t)}{(t-\xi)}dt + c \end{aligned} \tag{66}$$

where

$$F(\xi) = (1-\lambda)(1-\Psi) \tag{67}$$

ξ is related to y through the following transformation (formula (61))

$$\begin{aligned} Z &= \Phi + i\Psi \\ &= \frac{d(1-\lambda)}{\lambda} + i(1-\frac{1-y}{\lambda}) \\ &= a\int_{0}^{\zeta}\frac{1}{(\zeta-1)^{\frac{\alpha}{\pi}}(\zeta+1)^{1-\frac{\alpha}{\pi}}}d\zeta + b \end{aligned} \tag{68}$$

and Ψ is related to ξ through (62). Therefore, (66), (68) and (62) provide the equations for

solving the interface shape. To determine the coefficients a and b in (62) and (68), we fix the corresponding points between Z and ζ as $Z = i \Leftrightarrow \zeta = -1$ and $Z = d \Leftrightarrow \zeta = 1$. After some algebraic manipulations, the coefficients are given by

$$a = \frac{d-i}{I} \tag{69}$$

$$b = \frac{I_1 d + i I_2}{I} \tag{70}$$

where I_1, I_2 and I are the following integrals

$$I_1 = \int_{\frac{1}{2}}^{1} \frac{d\tau}{\tau^{\frac{\alpha}{\pi}}(1-\tau)^{1-\frac{\alpha}{\pi}}} \tag{71}$$

$$I_2 = \int_{0}^{\frac{1}{2}} \frac{d\tau}{\tau^{\frac{\alpha}{\pi}}(1-\tau)^{1-\frac{\alpha}{\pi}}} \tag{72}$$

$$I = I_1 + I_2 \tag{73}$$

Upon substitution of equations (67), (69) and (70) into (62), a solution for $F(\xi)$ is obtained

$$F(\xi) = \frac{(1-\lambda)}{I(1)} I(\xi); \qquad \xi \in (-1,1) \tag{74}$$

where the $I(\xi)$ is

$$I(\xi) = \int_{\frac{1-\xi}{2}}^{1} \frac{d\tau}{\tau^{\frac{\alpha}{\pi}}(1-\tau)^{1-\frac{\alpha}{\pi}}} \tag{75}$$

The principal value of (66) can be simplified as shown in the Appendix A. The final result is

$$x = \frac{d(1-y)}{\lambda} + \frac{1}{\pi}\left[\int_{-1}^{1} \frac{F(t)-F(\xi)}{(t-\xi)} dt + F(\xi)\log\frac{1-\xi}{1+\xi}\right] + c \qquad \xi \in (-1,1) \tag{76}$$

Note that there is an integration constant c in the above equation. To determine c, we let $\lim_{\xi \to -1} x = 0$ at the upper channel boundary $y = 1$ in (66). The following value is obtained

$$c = -\frac{1}{\pi} \int_{-1}^{1} \frac{F(t)}{t+1} dt \tag{77}$$

Thus, using expression (74), x can be written as

$$\begin{aligned} x = d\frac{I(\xi)}{I(1)} + \frac{1}{\pi}\frac{(1-\lambda)}{I(1)} \Bigg[& \int_{-1}^{1} \frac{I(t) - I(\xi)}{(t-\xi)} dt \\ & + I(\xi) \log \frac{1-\xi}{1+\xi} - \int_{-1}^{1} \frac{I(t)}{t+1} dt \Bigg] \qquad \xi \in (-1,1) \end{aligned} \tag{78}$$

The characters of two integrations in the above x expression are analyzed in the Appendix A. Upon substitution of (69) and (70) into (68), y is

$$y = 1 - \lambda \frac{I(\xi)}{I(1)} \qquad \xi \in (-1,1) \tag{79}$$

equations (78) and (79) represent the final results of the interface functions. When ξ takes values between -1 to 1, (78) and (79) provide the interface positions between two the fluids.

THE SAFFMAN-TAYLOR LIMIT ($N_g \to 0$)

To verify that equations (78) and (79) recover the *Saffman - Taylor's* solution [8] when gravity is absent, we consider $N_g = 0$, and $\alpha = \frac{\pi}{2}$. Then, $I(\xi)$ can be obtained as

$$\begin{aligned} I(\xi) &= \int_{\frac{1-\xi}{2}}^{1} \frac{dt}{\sqrt{t}\sqrt{1-t}} \\ &= \frac{\pi}{2} + \arcsin\xi \end{aligned}$$

From this, equations (78) and (79) are simplified to

$$x = \frac{1-\lambda}{\pi^2}\left[\int_{-1}^{1} \frac{\arcsin t - \arcsin\xi}{t-\xi}dt + (\frac{\pi}{2} + \arcsin\xi)\log\frac{1-\xi}{1+\xi} - \int_{-1}^{1} \frac{\frac{\pi}{2} + \arcsin t}{t+1}dt\right] \quad (80)$$

$$y = 1 - \frac{\lambda}{\pi}(\frac{\pi}{2} + \arcsin\xi) \quad (81)$$

The principal values in equation (80) are evaluated as follows

$$\begin{aligned} I_{x1} &= \int_{-1}^{1} \frac{\arcsin t - \arcsin\xi}{t-\xi}dt \\ &= \lim_{\epsilon\to 0}\left(\int_{-1}^{\xi-\epsilon} \frac{\arcsin t - \arcsin\xi}{t-\xi}dt + \int_{\xi+\epsilon}^{1} \frac{\arcsin t - \arcsin\xi}{t-\xi}dt\right) \end{aligned}$$

which is

$$I_{x1} = \frac{\pi}{2}\log(1-\xi^2) + \arcsin\xi\,\log\frac{1+\xi}{1-\xi} - \lim_{\epsilon\to 0}\left[\int_{-1}^{\xi-\epsilon} \frac{\log(\xi-t)}{\sqrt{1-t^2}}dt + \int_{\xi+\epsilon}^{1} \frac{\log(t-\xi)}{\sqrt{1-t^2}}dt\right] \quad (82)$$

$$\begin{aligned} I_{x2} &= -\int_{-1}^{1} \frac{\frac{\pi}{2} + \arcsin t}{t+1}dt \\ &= -\lim_{\epsilon\to 0}\int_{-1+\epsilon}^{1} \frac{\frac{\pi}{2} + \arcsin t}{t+1}dt \\ &= -\pi\log 2 + \lim_{\epsilon\to 0}\int_{-1+\epsilon}^{1} \log(t+1)\frac{1}{\sqrt{1-t^2}}dt \end{aligned} \quad (83)$$

Substituting I_{x1} and I_{x2} into equation (80), we are able to simplify the expression for x as follows

$$x = \frac{1-\lambda}{\pi}\log\frac{1}{2}(1-\xi) + \frac{1-\lambda}{\pi^2}\lim_{\epsilon\to 0}\left[-\int_{-1}^{\xi-\epsilon} \frac{\log(\xi-t)}{\sqrt{1-t^2}}dt - \int_{\xi+\epsilon}^{1} \frac{\log(t-\xi)}{\sqrt{1-t^2}}dt + \int_{-1+\epsilon}^{1} \frac{\log(t+1)}{\sqrt{1-t^2}}dt\right] \quad (84)$$

After a considerable amount of algebraic manipulation, the sum of the last three integrals turns out to be zero in the limit $\epsilon \to 0$. Thus, the final result for x is

$$x = \frac{1-\lambda}{\pi} \log \frac{1-\xi}{2} \tag{85}$$

Combining the x and y expressions, we obtain the interface shape when gravity is negligible as follows

$$x = \frac{1-\lambda}{\pi} \log \frac{1}{2}[1 + cos\frac{\pi}{\lambda}(1-y)] \tag{86}$$

which is the *Saffman - Taylor* solution.

NUMERICAL RESULTS

Numerical results for equations (79) (78) are shown in Figures 4 and 5. The unstable displacement interface corresponding to of $\lambda = 0.1$, $N_g = 0, 0.1, 5, 10$ ($\rho_1 > \rho_2$, $\mu_1 > \mu_2$, $N_g > 0$) is illustrated in Figure 4(a). The shapes of the fingers are almost identical to zero gravity curve when $N_g < 0.1$. As the effect of gravity increases, the interfaces near the center of the channel moves faster than those of small gravity number. This indicates that gravity tends to stabilize the finger tongue. When N_g is very large, the lower portion of the finger moves ahead of the upper part (not show). Although this result recovers the experimental observations in [5], we suspect that it may represent a mathematical rather than a physical reality, because there is an undetermined parameter λ in equations (79) and (78). Figure 4(b) shows interface shapes for $\lambda = 0.1, 0.3, 0.5, 0.7$ and value of gravity number equals $N_g = 0.3$. It indicates that the larger the λ, the flatter the head of a finger calculated from the solution at the condition of same gravity number. Due to the consideration of different density and viscosity between displacing and resident fluids in (79) and (78), one of the advantages of this work is that it reflects both unstable and stable displacement interfaces. Figure 4(c) shows the stable finger shapes ($\rho_1 > \rho_2$, $\mu_1 < \mu_2$, $N_g < 0$) along the upper wall for $\lambda = 0.1$

and value of gravity number $Ng = 0, 0.1, 5, 10$. For this group of fingers, the finger heads become sharper as the magnitude of the gravity number increases.

The solutions can also represents the fingers developed along the bottom wall of the channel. This group of fingers is plotted in Figure 5(a) with $\lambda = 0.1$ and $N_g = 0, 0.1, 5, 10$ ($\rho_1 < \rho_2$ and $\mu_1 < \mu_2$), and Figure 5(b) with $\lambda = 0.1, 0.3, 0.5, 0.7$ for the same $N_g = 0.3$. These represent stable gravity fingers. When the magnitude of N_g increases, the finger heads tend to be sharper. The results are similar to the solution of conditionally stable gravity tongues reported by Fayers and Muggeridge [4], although there are different underlying fundamentals between the two works. Figure 5(c) shows the unstable fingers ($\rho_1 < \rho_2$, $\mu_1 > \mu_2$) developed along the bottom wall with $Ng = 0, -0.1, -5, -10$ and $\lambda = 0.1$. The finger interfaces are exactly same with the corresponding upper wall fingers in Figure 4(a).

The equations (79) and (78) are also comparable with the Brener et al. solution (2) and (3). As we pointed out before, their solution involves three parameters, but without considering the density and viscosity of displacing fluid. Thus, (2) and (3) do not obtain the stable displacement. With taking $W = 1$, $\epsilon = 0$ and $y_o = 0.45$, we can compare (79) and (78) with equations (2) and (3). The results are shown in Figure 6. We could see that when for $\lambda = 0.1$ the two solutions results provide very similar interface shapes except there is difference in starting positions for the two solutions.

CONCLUSIONS

We have provided a new exact solution for the description of the interface shape of gravity segregated fingers. The solution considers the finite density and viscosity of the displacing fluid. Thus, it is able to represent both stable and unstable displacements, and finger development along either the upper wall or bottom wall of a channel. The solution has closed forms so that there is no need to determine the coefficients as the solution of Greenkorn et al. [5]. This solution is able to recover the *Saffman - Taylar* solution [8] if gravity is neglected. Computational results of equations (79) and (78) are very similar to the solutions (2) and (3) of Brener et al. [1] for the gravity number up to 10. However,

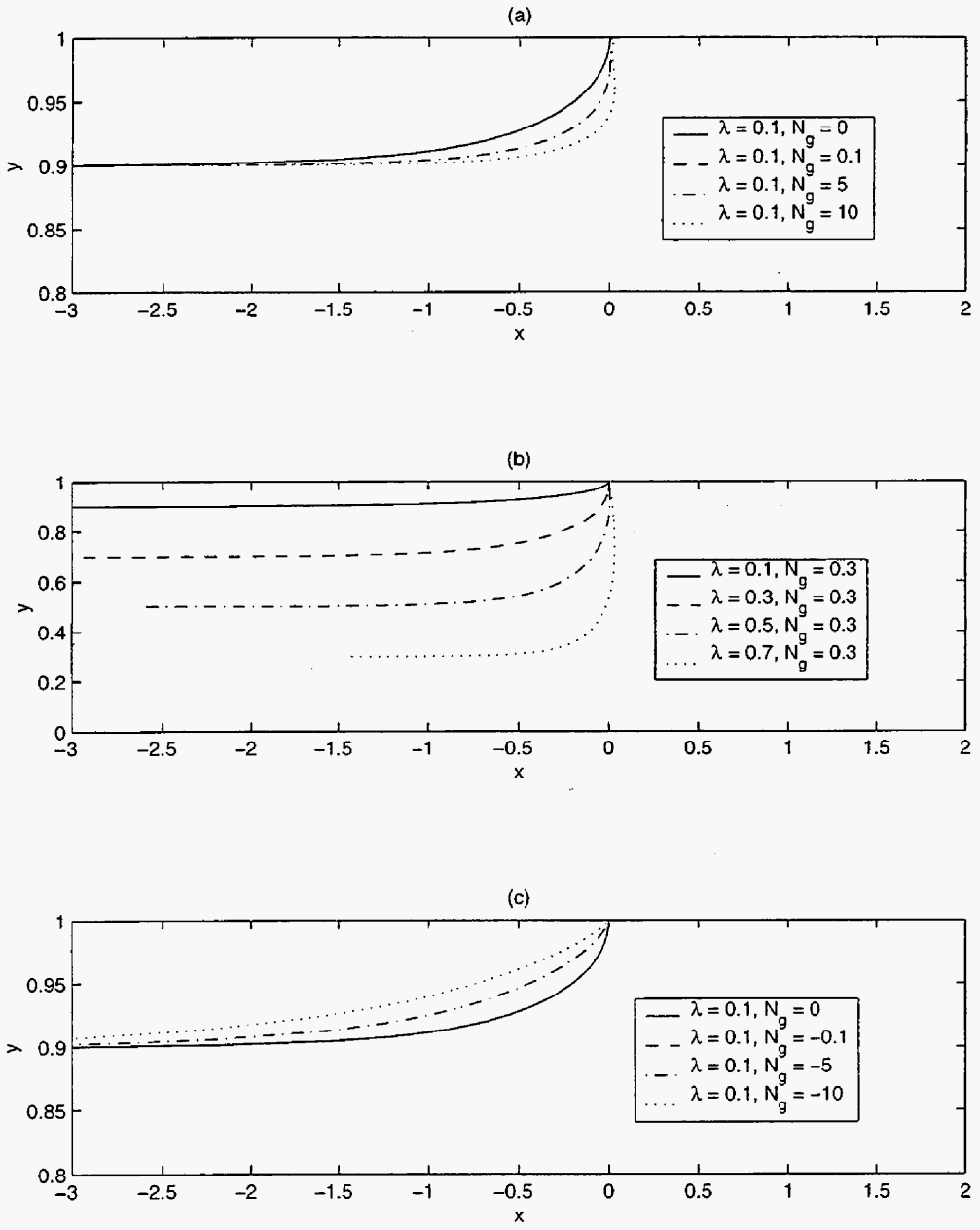

Figure 4: Upper wall finger interfaces: (a) unstable fingers, $\lambda = 0.1$, $N_g = 0, 0.1, 5, 10$; (b) unstable fingers, $\lambda = 0.1, 0.3, 0.5, 0.7$, $N_g = 0.3$; (c) stable fingers, $\lambda = 0.1$, $N_g = 0, -0.1, -5, -10$.

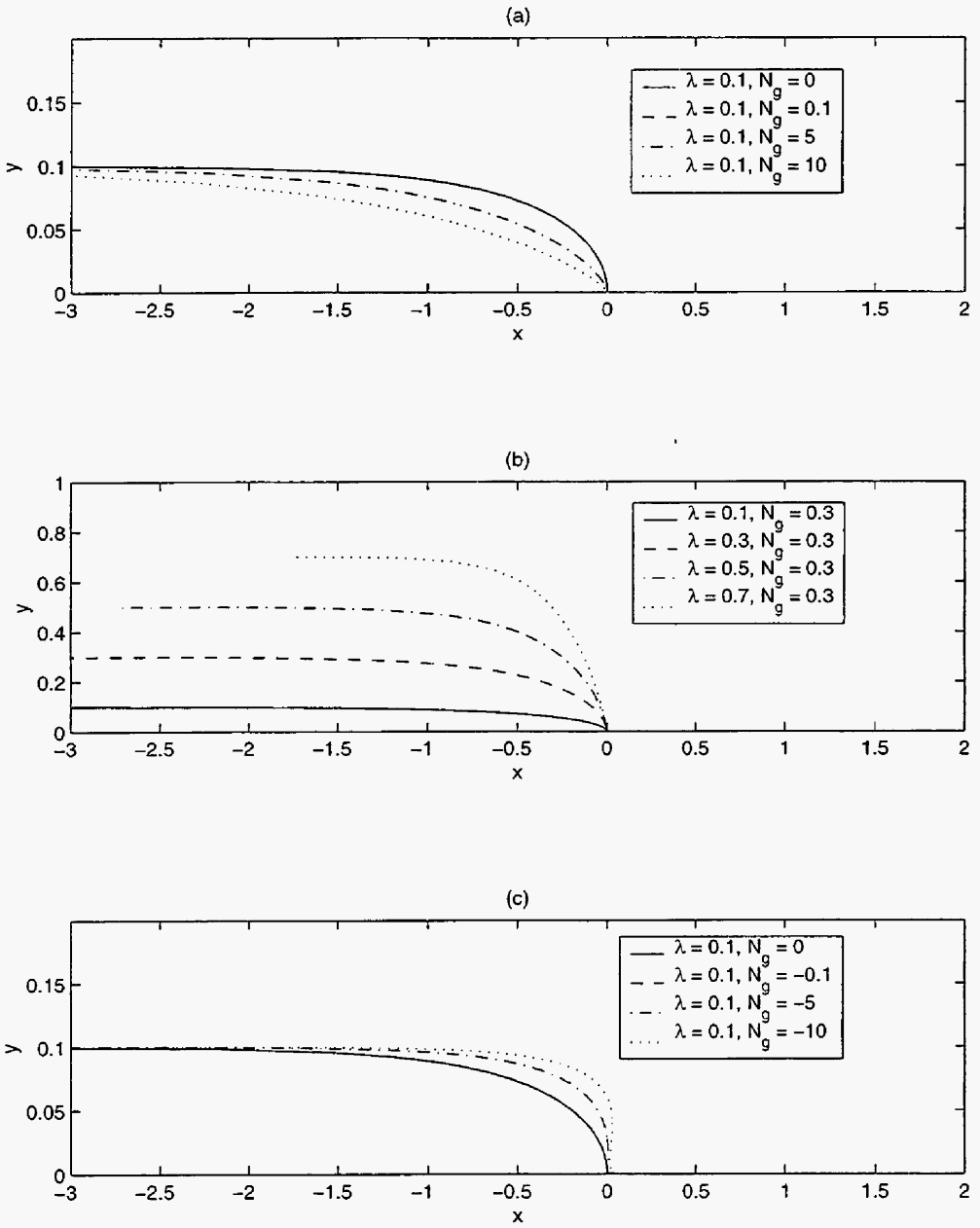

Figure 5: Bottom wall finger interfaces: (a) stable fingers, $\lambda = 0.1$, $N_g = 0, 0.1, 5, 10$; (b) stable fingers, $\lambda = 0.1, 0.3, 0.5, 0.7$, $N_g = 0.3$; (c) unstable fingers, $\lambda = 0.1$, $N_g = 0, -0.1, -5, -10$.

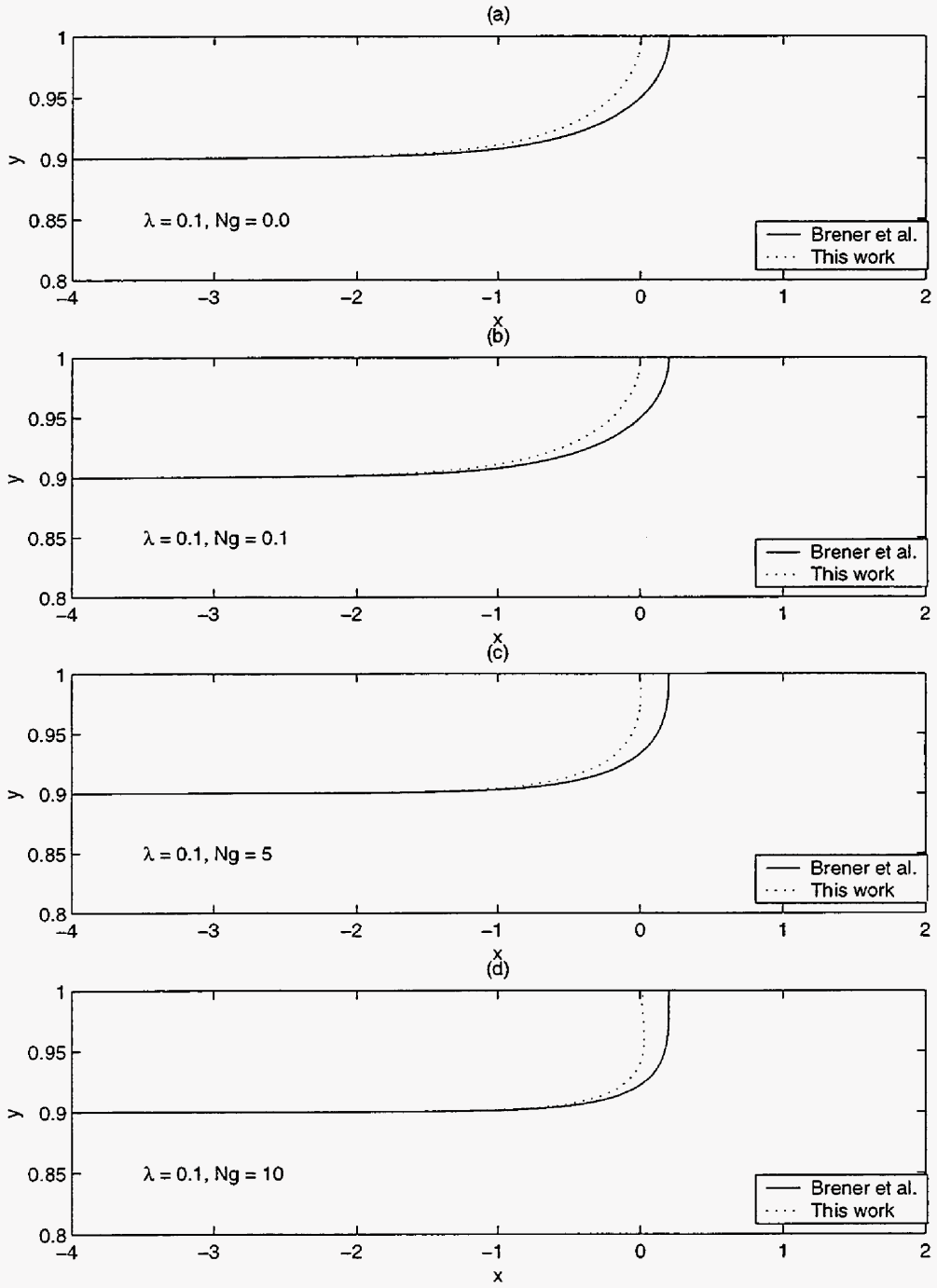

Figure 6: Comparison between solution of Brener et al. and equations (79) and (78), for $\lambda = 0.1$: (a) $N_g = 0.0001$; (b) $N_g = 0.1$; (c) $N_g = 5$; (d) $N_g = 10$.

the solution proposed in this work only has one free parameter while the solution of Brener et al. has three. The (79) and (78) also provide interface shapes similar to conditionally stable fingers calculated by the finger model of Fayer and Muggeridge [4], however, they are different by the underlying fundamentals.

References

[1] E. Brener, H. Levine, and Y. Tu. Nonsymmetric Saffman-Taylor fingers. *Phys. Fluids A*, 3(4):529–534, 1991.

[2] E. Brener, H. Levine, and Y. Tu. Effect of gravity on stable Saffman-Taylor fingers. *Phys. Review E*, 48(2):1066–1072, 1993.

[3] F. F. Craig, J. L. Sanderlin, Moore D. W., and T. M. Geffen. A laboratory study of gravity segregation in frontal drives. *Trans. AIME*, 210:275–281, 1975.

[4] F. J. Fayers and A. H. Muggeridge. Extensions to Dietz theory and behavior of gravity tongues in slightly tilted reservoirs. *SPERE*, 6(4):487–494, 1990.

[5] R. A. Greenkorn, J. E. Matar, and R. C. Smith. Two-phase flow in Hele-Shaw models. *AIChE Journal*, 13(2):273–279, 1967.

[6] P. M. Morse and H. Feshbach. *Methods of Theoretical Physics (I).* MaGraw-Hill Book Company, New York, 1953.

[7] P. Pelce. *Dynamics of Curved Fronts.* Academic Press, Boston, MA, USA, 1988.

[8] P. G. Saffman and G. I. Taylor. The penetration of a fluid into a porous medium or Hele-Shaw cell containing a more viscous liquid. *Proc. R. Soc. London, Series A.*, 245:312–329, 1958.

[9] J. E. Varnon and R. A. Greenkorn. Unstable two-fluid flow in a porous medium. *SPEJ*, 9:293–300, 1969.

APPENDIX: USEFUL TRANSFORMATIONS FOR PRINCIPAL VALUE INTEGRALS

In equation (66), $\xi \in (-1, 1)$, thus, when t integrates from -1 to 1, the integration has a singularity for each ξ. To find the principal value of the integral we us the following manipulation

$$\begin{aligned} I_p &= \int_{-1}^{1} \frac{F(t)dt}{t-\xi} \\ &= \lim_{\epsilon \to 0}\left[\int_{-1}^{\xi-\epsilon} \frac{F(t)dt}{t-\xi} + \int_{\xi+\epsilon}^{1} \frac{F(t)dt}{t-\xi}\right] \\ &= \lim_{\epsilon \to 0}\left[\int_{-1}^{\xi-\epsilon} \frac{F(t)-F(\xi)}{t-\xi}dt + F(\xi)\log(\xi - t)|_{-1}^{\xi-\epsilon}\right] \\ &+ \lim_{\epsilon \to 0}\left[\int_{\xi+\epsilon}^{1} \frac{F(t)-F(\xi)}{t-\xi}dt + F(\xi)\log(t - \xi)|_{\xi+\epsilon}^{1}\right] \\ &= \int_{-1}^{1} \frac{F(t)-F(\xi)}{t-\xi}dt + F(\xi)\log\frac{1-\xi}{1+\xi} \end{aligned}$$

This result was used to simplify (66) to (76). Using (74), the above integration can be expressed by $I(t)$.

To evaluate x when $\xi \to -1$, it is necessary to estimate the value of the logarithmic term in (78). We proceed as follows. Let

$$\frac{1-\xi}{2} = 1 - \epsilon \tag{87}$$

Then, $I(\xi)$ can be expressed as

$$I(\epsilon) = \int_{1-\epsilon}^{1} \frac{d\tau}{\tau^{\frac{\alpha}{\pi}}(1-\tau)^{1-\frac{\alpha}{\pi}}} \tag{88}$$

Using the change of variables $\tau = 1 - w$, and taking the limit $\epsilon \to 0$ the above becomes

$$
\begin{aligned}
I(\epsilon) &= -\int_{\epsilon}^{1} \frac{dw}{(1-w)^{\frac{\alpha}{\pi}} w^{1-\frac{\alpha}{\pi}}} \\
&\approx \int_{0}^{\epsilon} \frac{dw}{w^{1-\frac{\alpha}{\pi}}} \\
&\approx \frac{\pi}{\alpha} \epsilon^{\frac{\alpha}{\pi}}
\end{aligned}
$$

Thus, we have

$$
I(\xi) \approx \frac{\pi}{2} \left(\frac{1+\xi}{2}\right)^{\frac{\alpha}{\pi}} \qquad (\xi \to -1) \tag{89}
$$

This gives an approximation for the second integral term in equation (78), namely

$$
\begin{aligned}
I(\xi) \log \frac{1-\xi}{1+\xi} &\approx \frac{\pi}{2} \left(\frac{1+\xi}{2}\right)^{\frac{\alpha}{\pi}} [\log(1-\xi) - \log(1+\xi)] \\
&\approx -\frac{\pi}{2} \left(\frac{1+\xi}{2}\right)^{\frac{\alpha}{\pi}} \log(1+\xi) \qquad (\xi \to -1)
\end{aligned}
$$

Since $\lim_{x \to 0} x^{\frac{\alpha}{\pi}} \log x = \lim_{x \to 0} \frac{\alpha}{\pi} x^{\frac{\alpha}{\pi}} = 0$, we have the following final estimate of this term

$$
\lim_{\xi \to -1} I(\xi) \log \frac{1-\xi}{1+\xi} \to 0 \tag{90}
$$

This shows that the logarithmic term in (78) is bounded and approaches zero as $\xi \to 0$.

Same additional manipulations are needed for estimate of two integrals in (78) in order to calculate interface. If we expand $I(t)$ around ξ using a series expansion, then the first integral of (78) becomes

$$
\begin{aligned}
\int_{-1}^{1} \frac{I(t) - I(\xi)}{t-\xi} dt &= \int_{-1}^{1} \frac{I(\xi) + I'(\xi)(t-\xi) + \frac{1}{2!} I''(\xi)(t-\xi)^2 + \cdots - I(\xi)}{t-\xi} dt \\
&= \int_{-1}^{1} [I'(\xi) + \frac{1}{2!} I''(\xi)(t-\xi) + \cdots] dt
\end{aligned} \tag{91}
$$

where I is given in equation (75). The integral above is dependent on the character of the derivatives of $I(\xi)$ in the domain [-1, 1]. The first derivative of $I(\xi)$ is

$$I'(\xi) = \frac{1}{(1-\xi)^{\frac{\alpha}{\pi}}(1+\xi)^{1-\frac{\alpha}{\pi}}} \tag{92}$$

It is obvious that singular points, for $I'(\xi)$ and other higher derivatives of $I(\xi)$, occur only at $\xi = \pm 1$. Thus, equation (91) is not singular when $\xi \in$ (-1, 1) (In this work, we define $x = 0$ when $\xi = -1$. Also, we do not calculate the integral at $\xi = 1$ since it corresponds to the interface at negative infinity of x).

The second integration in equation (78) should be considered carefully, because the integration is singular when $t = -1$, i.e.

$$\begin{aligned} I_s &\equiv \int_{-1}^{1} \frac{I(t)}{t+1} dt \\ &= \lim_{\epsilon \to 0} \int_{-1+\epsilon}^{1} \frac{I(t)}{t+1} dt \\ &\overset{\theta=t+1}{=} \lim_{\epsilon \to 0} \int_{\epsilon}^{2} \frac{I(\theta)}{\theta} d\theta \end{aligned}$$

The integrand of the above expression is

$$\lim_{\epsilon \to 0} \frac{I(\theta)}{\theta} = \lim_{\theta \to 0} \frac{I(\varepsilon) + I'(\varepsilon)(\theta - \varepsilon) + \frac{1}{2!} I''(\varepsilon)(\theta - \varepsilon)^2 + \cdots}{\theta}; \qquad \varepsilon \in (0, \theta)$$

Since $\theta \to 0$, when $\varepsilon \to 0$, and $I(0) = 0$, then

$$\begin{aligned} \lim_{\epsilon \to 0} \frac{I(\theta)}{\theta} &\approx \lim_{\varepsilon \to 0} I'(\varepsilon) \\ &\approx \frac{1}{(2-\varepsilon)^{\frac{\alpha}{\pi}} \varepsilon^{1-\frac{\alpha}{\pi}}} \longrightarrow \infty \end{aligned} \tag{93}$$

If we define $f(t) \equiv \frac{I(t)}{t+1}$ and $g(t) \equiv \frac{1}{(t+1)^{1-\frac{\alpha}{\pi}}}$, we have

$$\begin{aligned}\lim_{t\to -1}\frac{f(t)}{g(t)} &= \lim_{t\to -1}\frac{\frac{1}{(1-t)^{\frac{\alpha}{\pi}}(1+t)^{1-\frac{\alpha}{\pi}}}}{(1+t)^{1-\frac{\alpha}{\pi}}} \\ &= 2^{\frac{\alpha}{\pi}}\end{aligned}$$

Because $\int_{-1}^{1} g(t)dt$ is convergent, I_s is also convergent. With the use of the estimate in (89), I_s can be calculated as

$$\begin{aligned}I_s &= \int_{-1}^{1}\frac{I(t)-\frac{\pi}{2}\left(\frac{1+t}{2}\right)^{\frac{\alpha}{\pi}}}{t+1}dt + \int_{-1}^{1}\frac{\frac{\pi}{2}\left(\frac{1+t}{2}\right)^{\frac{\alpha}{\pi}}}{t+1}dt \\ &= I_{s1} + I_{s2} \qquad (94)\end{aligned}$$

where

$$I_{s1} = \begin{cases} \frac{I(t)-\frac{\pi}{2}\left(\frac{1+t}{2}\right)^{\frac{\alpha}{\pi}}}{t+1}; & t \neq -1 \\ 0; & t = -1 \end{cases}$$

and

$$I_{s2} = \frac{\pi^2}{\alpha^2}$$

Finally, I_s can be obtained as follows

$$I_s = \begin{cases} \int_{-1}^{1}\frac{I(t)-\frac{\pi}{2}\left(\frac{1+t}{2}\right)^{\frac{\alpha}{\pi}}}{t+1}dt + \frac{\pi^2}{\alpha^2}; & t \neq -1 \\ \frac{\pi^2}{\alpha^2}; & t = -1 \end{cases}$$

III. DYNAMICS OF IN-SITU COMBUSTION AT VARIOUS SCALES

A well-established method for the recovery of heavy oils is in-situ combustion. Despite its long history, however, many aspects of the process are not well understood. Two particular aspects are analyzed in this project: The description of the process at the pore-network scale, and its upscaling at the large scale for field applications. A pore-network simulator is briefly described in the first study. It is the first of its kind, as far as we know, and although at a preliminary stage, it gives results consistent with previous findings. We present the basic aspects of the simulator, although further work is on-going for its fine-tuning. In the second study, we apply an asymptotic approach to describe the movement of combustion fronts in porous media as gas-dynamic discontinuities. This approach is essential for the upscaling of the process at the field scale and for the assessment of the effect of heterogeneity on issues such as stustained front propagation, extinction, efficiency, etc. This effort is on-going and we currently investigate the development of appropriate upscaling schemes, the effect of heat losses and the incorporation of low-temperature-oxidation reactions. In parallel, combustion experiments in micromodels, such as a Hele-Shaw cell are under way.

A PORE-NETWORKS MODEL FOR IN-SITU COMBUSTION

Chuan Lu, Y.C.Yortsos

INTRODUCTION

Combustion in porous media is an important problem in a variety of contexts. In-situ combustion is a useful technique for the recovery of heavy oils and has been investigated in the past several decades[1]. More recently, a number of articles have been published dealing with smoldering and filtration combustion[2,3], which is important to self-propagating high-temperature synthesis of materials, and to a host of other applications. Compared to conventional flame propagation, combustion in porous media involves a simplification in the fluid mechanics, where Darcy's law applies, but an added complication in the heat transfer, due to the presence of the solid phase, where conduction occurs. A variety of nonlinear phenomena, dealing with ignition, extinction, sustained propagation and patterns arise. So far, the majority of studies have addressed the problem at the continuum level, by treating the porous medium as an effective continuum. It is well known, however, that the reaction zone could be quite narrow, of the order of cm or less, and significant temperature, composition and depth of conversion changes may occur over equally short distances. This brings the issue of the effect of pore-scale phenomena on the overall process and on their upscaling. Recently, interesting fingering patterns were observed in Hele-Shaw cell experiments involving the reverse combustion of thin paper sheets[4]. In some way, this problem is related to viscous fingering in porous media (but not for the same reasons). The finger width and the distance between adjacent fingers of the obtained patterns were interpreted based on scaling arguments[5]. To assess pore-scale effects and ultimate to scale-up the process for a continuum description, we develop in this section a dual pore-network model for modeling combustion in porous media.

Pore-network models are useful tools for understanding pore-scale phenomena and their integration in continuum descriptions. The approach to be implemented is analogous to an earlier effort in modeling thermal processes at the pore-network scale, for example in

heat-transfer driven bubble growth[6], where heat transfer in the solid must be considered. The important difference is that here the exothermic combustion reaction at the pore

surface must also be included. We discuss the formulation of the pore-network problem, the method of solution and results obtained in specific cases.

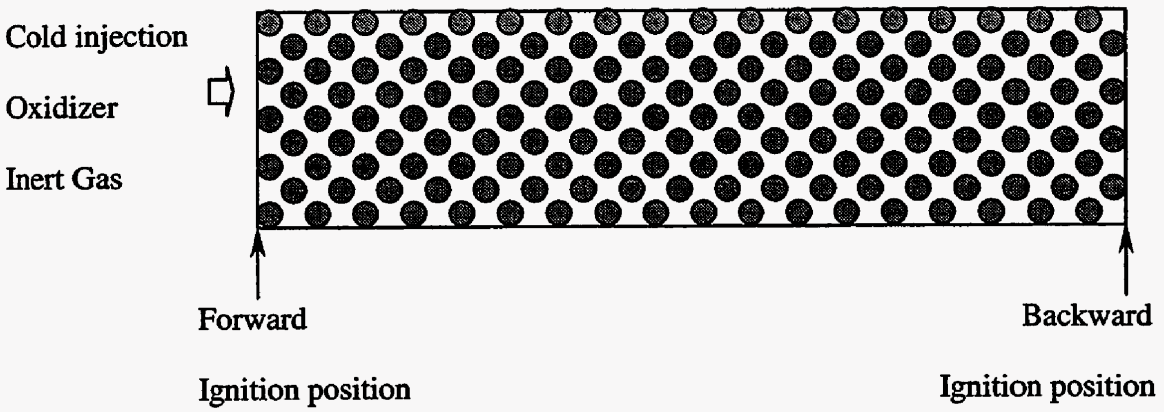

Figure 1. Sketch of the dual network and of the forward and reverse combustion Process.

THE PORE-NETWORK MODEL

The pore-network model consists of a dual network of pores and throats, which is embedded in a network of solid sites, representing the solid matrix. The pores (sites) are the place where reaction occurs and contain fuel of constant composition. They are interconnected via throats (bonds), which control transport of mass, momentum and heat, and which have distributed sizes. The network of solid sites is needed to account for heat transfer in the solid. The coupling of solid and pore-space occurs through heat transfer between pores and solid sites. A schematic is shown in Figure 1. In the 2-D simulations reported below, both networks are square lattices, each solid site communicating with 4 pore sites. Injection of a mixture of oxidant and inert gas occurs at one end, at constant pressure, temperature and composition. The outlet end is at constant pressure. Forward and reverse combustion are differentiated by controlling the ignition point, which is the

first row in the inlet for the case of forward combustion, and the row before the last in the outlet, for the reverse (see Figure 1). The following heterogeneous reaction

Solid Fuel + μ Gas Oxidizer→μ1 Solid Product + μ2 Gas Product (5.1)

is assumed, where μ, μ1, μ2 stand for the mass stoichiometric coefficients, the reaction rate expressed by the one-step kinetic model

$$R = k_0 P X_O H(V_f) \exp(-\frac{E_a}{RT}) \tag{5.2}$$

where H is the step function, V_f is the volume of fuel, P is the total pressure, k_0 is the kinetic constant, Xo the mass fraction of the oxidant and Ea the activation energy. The oxidizer in the gas phase is delivered by gas phase diffusion and convection, the flow in the pore throats controlled by Poiseuille's law. Within a pore site, thermodynamic equilibrium is assumed, such that concentrations, pressure and temperature are uniform. This also implies that fuel and gas are also at thermal equilibrium. However, heat transfer does take place between adjacent pore sites, between pore and solid sites and between solid adjacent solid sites. A heat transfer coefficient is used to model the pore-solid exchange. Thermodynamic and transport parameters are taken constant. The equations describing the process are listed below.

Pore Site I, Adjacent to Pore-Site j:

Gas Phase Component k Mass Balance

$$\frac{\Delta(\frac{P_i V_i}{RT_i} y_{i,k} M_k)}{\Delta t} = -\sum_j u_{ij} r_{ij}^2 \frac{P_i y_{i,k}}{RT_i} M_k - \frac{D_e}{lR} \sum_j r_{ij}^2 (\frac{P_i + P_j}{2})(\frac{2}{T_i + T_j})(y_{i,k} - y_{j,k}) + \mu_k (k_r A_i^r \frac{P_i y_{i,O_2}}{RT_i} \exp(-\frac{E_a}{RT_i})) H(V_{i,f}) \tag{5.3}$$

Solid Fuel Conservation

$$\rho_f \frac{\Delta V_{i,f}}{\Delta t} = k_r A_i^r \frac{P_i y_{i,O_2}}{RT_i} \exp(-\frac{E_a}{RT_i}) H(V_{i,f}) \tag{5.4}$$

Energy Balance

$$\frac{\Delta E_i}{\Delta t} = -\sum_j u_{ij} r_{ij}^2 \frac{E_{g,i}}{V_i} - \frac{K_{gs}}{l} \sum_j r_{ij}^2 (T_i - T_j) - h_s \sum_s A_{is}^h (T_i - T_s) - h_{L,P} A_{i,l}^h (T_i - T_0) \tag{5.5}$$

where, we defined the energy content of a site by

$$E_i = E_{f,i} + E_{g,i}, \tag{5.6}$$

$$E_{f,i} = m_{f,i}(C_{p,f} T_i + \Delta_c H_f) \quad \text{and} \quad E_{g,i} = \sum_k \frac{P_i V_i}{R T_i} M_k y_{i,k} (C_{pg,k} T_i + \Delta_c H_f)$$

Momentum Balance

$$u_{ij} = \frac{r_{ij}^4}{8\mu l}(P_i - P_j) \tag{5.7}$$

Solid Site Energy Balance

$$\rho V C_{ps} \frac{\Delta T}{\Delta t} = -\frac{k_s^h}{l} \sum_{s'} A_{ss'}^h (T_s - T_{s'}) + h_s \sum_j A_{js}^h (T_j - T_s) - h_{L,S} A_{s,l}^h (T_s - T_0) \tag{5.8}$$

* the notation being self-evident. The sum in the energy balances express heat exchange between pore and solid sites, while $h_{L,S}$ denotes heat loss to the surroundings. In addition, ideal gas behavior was assumed. Finally, the bond radius was correlated to the depth of conversion.

A dimensionless version of the above equations was solved using a standard implicit scheme. Because of the stiffness of the problem, a small time step is required. At the same time, the spatial scale needs to be large enough to investigate pattern development, which results in prohibitively long computations. In previous studies, but in homogeneous systems, various schemes were developed[7,8] to circumvent this difficulty. Unfortunately, these techniques do not apply in our system. Explicit schemes, even at very small time steps, do not lead to acceptable performance. To speed up the computation procedure, we implemented two simplifying assumptions, one regarding pressure and another regarding a quasi-steady state for the gas.

Since the gas viscosity is very small, the pressure variation could be ignored in all the governing equations except for the momentum balance. This technique has been widely used in the simulations of laminar flame propagation in open space. In our 1-D results, the total pressure difference is less than 10^3 Pa compared to pressures of the order of 10^5Pa (1 atm). As a result, the pressure variation effect on thermodynamic properties can be neglected. Likewise, because of the difference in the densities of gas and solid, the respective time scales are greatly different for the gas and the solid. Thus, one can proceed with the assumption of quasi-steady state for the gas. This assumption has been widely used for these kinds of processes and its validity was verified in our 1D simulations. Use of these two assumptions was found to improve significantly the computation speed (5-7 times faster from the first, and 2-3 times faster from the second assumption).

RESULTS

1-D SIMULATIONS

To test the validity of the model, we conducted 1-D simulations of forward combustion. Theoretically, we expect three possible situations[9], depending on the value of the parameter $\delta=(c_g\mu\rho_f)/c_s a_o$, which expresses a heat capacity ratio: a reaction-trailing pattern ($\delta<1$), where the reaction front trails the thermal front, a reaction-leading pattern ($\delta>1$), where the reaction front leads the thermal front, and a wave with maximum energy accumulation ($\delta=1$), in which the two fronts coincide and the temperature at the front increases with time, according to the equation $T_b - T_0 = Q_A a_0 \sqrt{G_0 l / \pi \lambda c_g}$. Our numerical results plotted in the left panel of Figure 2 are in good agreement with the theoretical predictions. In the first two cases, it is apparent that a traveling front solution is reached, which propagates asymptotically at a constant speed. It is worth to point out that in time-dependent problems, the speed and extent of the separation between the fronts also depend on other parameters, such as injection rate, the heat conductivity and capacity, etc. The capability of our simulation allows us to study the sensitivity of the results to heat losses. The right panel of Figure 2 shows the temperature profiles corresponding to

the three cases, but with heat losses included. Although parameter δ appears to still remain the determining factor in the classification of patterns, the heat loss is shown to decrease the front temperature, which at least in the reaction-trailing problem, appears to also decrease in time.

2-D SIMULATIONS

Results from 2-D simulations for reverse combustion are shown in Figure 3. In the cases studied, concentration, temperature and velocity patterns are rough, but generally compact. The patterns with the most interesting behavior are those of the extent of fuel conversion. Reverse combustion gives rise to fingering patterns. These patterns show behavior very similar to that observed in the typical viscous fingering problem, namely tip splitting, merging and shielding. The patterns appear to have some similarity to those reported by Zik and Moses[4] in Hele-Shaw cell experiments, which were explained based on Rayleigh convection. Our model is in fact different, yet the numerical results demonstrate similar results. The patterns were found to be affected by the Peclet number and to be very sensitive to the initial condition of the system.

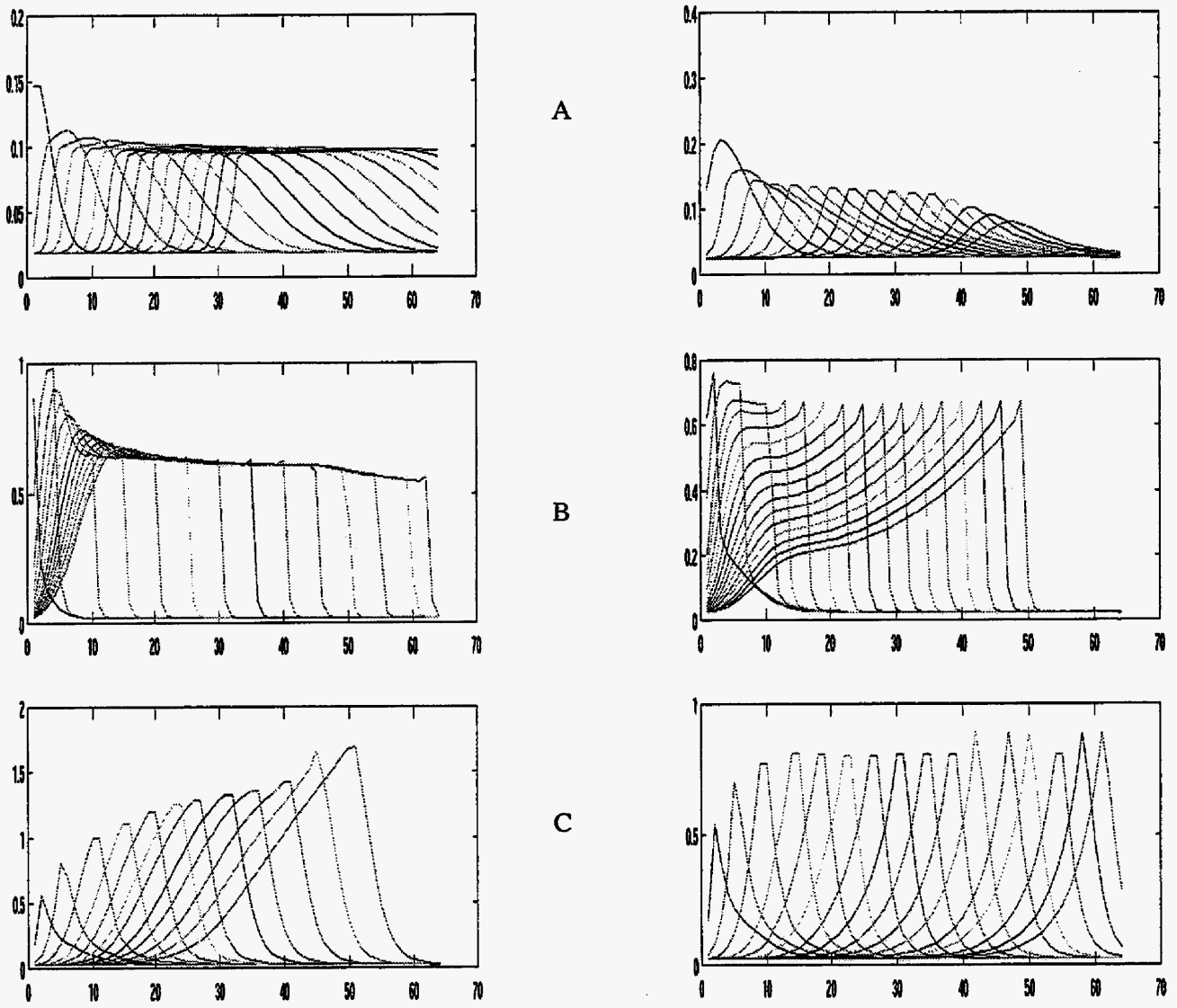

Figure 2 Temperature patterns from simulations of 1-D forward combustion for different values of time. Left panels correspond to zero heat losses, right panels account for heat losses to the surroundings. A: Reaction front trailing the temperature

front. B: Reaction front leading the temperature front. C: Maximum energy accumulation.

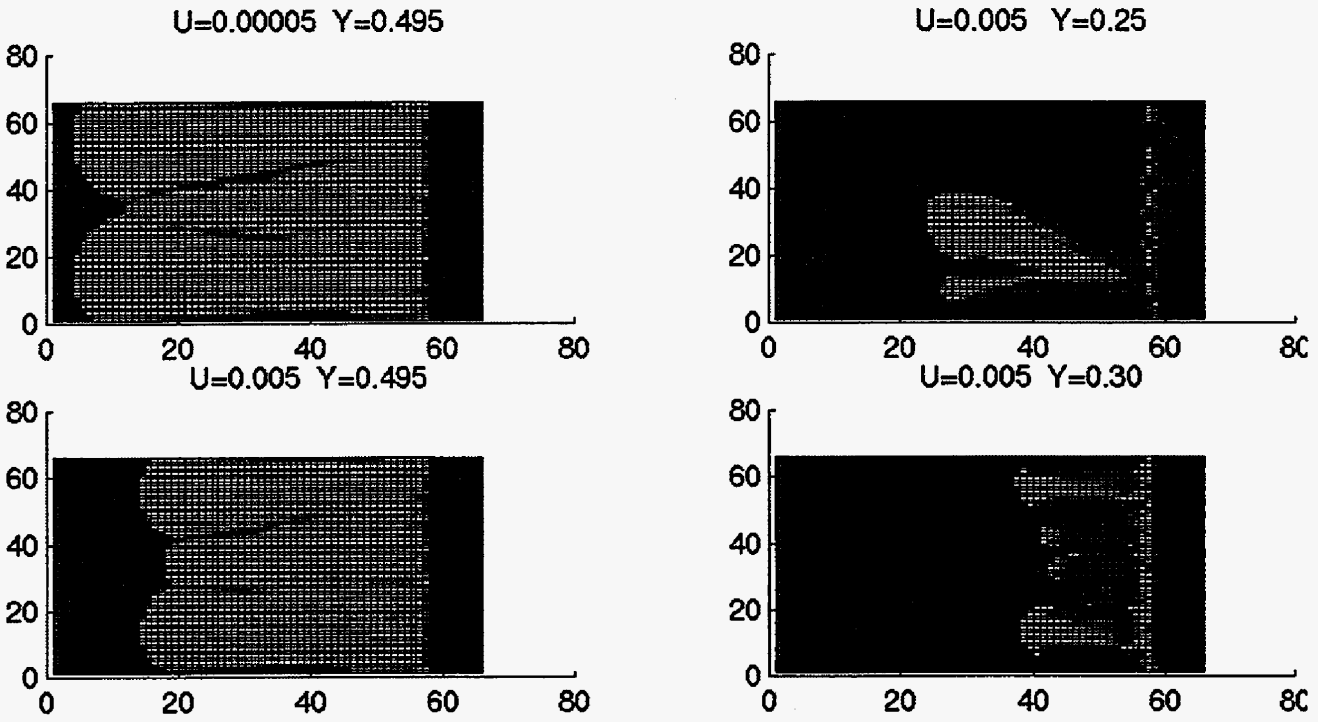

Figure 3. Fingering patterns of the depth of conversion in reverse combustion for different values of the injected composition Y and the injected velocity U.

REFERENCES

1. Miller,R.J., *DOE/NIPER SYMP ON IN SITU COMBUSTION PRACTICES-PAST, PRESENT AND FUTURE APPLICATIONS*, Tulsa, Oklahoma, 229-245, 1994.

2. Schult, D.S., Bayliss, A., and Matkowsky, B.J., *SIAM J. APPL. MATH.* **58(3)**, 806-852, 1998.

3. Schult, D.S., Matkowsky, B.J., Velpert, V.A., and Fernandez-Pello, A.C., *COMB. FLAME* **104**, 1-26, 1996.

4. Zik, O., Olami, Z., and Moses E., *PHYS. REV. LETT* **81(18)**, 3868-3871, 1998.

5. Zik, O., and Moses, E., *PHYS. REV. E* **60(1)**, 518-531, 1999.

6. Satik, C., and Yortsos, Y.C., *J. HEAT TRANSF.* **118**, 455-462, 1996.

7. Oran, E.S., and Boris, J.P., *NUMERICAL APPROACHES TO COMBUSTION MODELING*, American Institute of Aeronautics and Astronautics, 1991.

8. Issa, R.I., J. *COMP. PHYS* **93**, 388-410, 1991.

9. Aldushin, A.P., Rumanov, I.E., and Matkowsky, B.J., *COMB. FLAME* **118(1-2)** , 76-90, 1999.

DYNAMICS OF COMBUSTION FRONTS

İ. Yücel Akkutlu and Yanis C. Yortsos

INTRODUCTION

The propagation of combustion fronts in porous media is a subject of interest to a variety of applications, ranging from the in-situ combustion for the recovery of oil [1], to filtration combustion [5] and to smoldering combustion [7]. While these problems may differ in application and context, they share a common characteristic, namely that the main combustion reaction involves the burning of a stationary solid fuel, which in the first two applications is part of the initial state of the system, while in the second it is created by a preceding Low-Temperature-Oxidation (LTO) process. In-situ combustion for oil recovery has been studied quite extensively since the mid 1950s. The two texts by Prats [1] and Boberg [2] summarize the relevant literature on the subject until the late 1980s. A large number of experimental, analytical and numerical studies have been reported on a variety of in-situ combustion topics. Of interest to this section is a particular but important issue of in-situ combustion, specifically the dynamics of combustion fronts. They are influenced by a number of factors, including fluid flow of injection and produced gases, mass transfer of the injected oxidant, heat transfer in the porous medium and the surroundings, the rate of reaction(s), the heterogeneity of the medium and possibly the evolution of the pore morphology due to the combustion reaction. Understanding the dynamics is important to a number of issues, including front stability, the sustained propagation of combustion, the effects of heterogeneity, and the scale-up of the process. A specific feature that distinguishes combustion fronts from other front propagation problems is that due to the strong temperature dependence of the reaction rate, the combustion reaction occurs within a thin reaction zone, the extent of which is quite small, and certainly much smaller than the typical grid in field simulation. As a result, it is almost imperative to treat the reaction zone as a surface of discontinuity (a thin layer) within which the combustion reaction occurs, and across which appropriate conditions must apply. The propagation of frontal discontinuities makes the scale-up of the process a problem qualitatively different than ordinary displacement processes in porous media, for instance waterflooding.

The treatment of combustion fronts as frontal discontinuities has been studied extensively in the literature of combustion and flames. Among the great deal of articles published in this field we will refer to the earlier work of Matalon and Matkowsky [3], the monograph of Pelcé [4] and the more recent work of Schult and co-workers [7]. Ref. [3] discussed the propagation of flames in the combustion of premixed gases, in the absence of a porous medium, and treated the flame front as a surface of discontinuity, which separates two regions of different temperature and chemical composition. To capture phenomena occuring within the thin flame region, the methods of singular perturbation and matched asymptotic expansions were used. Pelcé [4] presents an interesting compilation of studies on combustion and flame propagation in a variety of geometries. In his work, common aspects are shown to exist between the seemingly different problems of viscous displacements in a Hele-Shaw cell (which gives rise to viscous fingering), dendritic solidification and flame propagation. This connection, and particularly with the viscous fingering problem, is of particular interest to our problem of combustion in porous media, as they are both subject to the effects of the medium heterogeneity and other factors. More recently, Aldushin and Matkowsky [5] have used this analogy to argue about the problem of the selection of the width of the Saffman-Taylor finger. We note in passing that the growth of a new phase in a porous medium, driven by diffusion, for example bubble growth in solution gas-drive processes, also shows common aspects with viscous displacements e.g. see Li and Yortsos [6].

In a recent series of papers, Schult et al. [7, 8], studied the combustion of a solid fuel embedded in a homogeneous porous medium. This problem, known as smoldering or filtration combustion, appears in a variety of applications. It differs in many respects from in-situ combustion, particularly on the lack of liquid flow ahead of the combustion front and the various physicochemical changes that accompany it, the fact that the solid fuel is a priori available, rather than being generated as a result of LTO, as is the case with in-situ combustion, and the existence of heterogeneities. At the same time, the two problems have the common feature of the propagation of a high-temperature reaction zone in which a gas-solid reaction process takes place. Schult et al. [7, 8], provided an asymptotic analysis of the problem following an approach essentially similar to the flame analysis of Ref. [3]. An analogous approach was attempted earlier by Britten and Krantz [14, 15] who examined the structure of the reaction

zone in reverse combustion in the context of gasification.

In this section, we will proceed to analyze the problem of in-situ combustion, by working along very similar lines. We must note that few related theoretical studies exist in the literature of in-situ combustion. Gottfried [9] modeled in-situ combustion by focusing on heat transfer and representing the combustion front as a discontinuity involving a point heat source, represented as a delta function. Beckers and Harmsen [10] detailed the propagation of various regimes in in-situ combustion and its variants (such as wet combustion). Burger and Sahuquet [11] analyzed the chemical aspects of the reaction processes. Ağca and Yortsos [12] proposed a simplified description, which takes into account the heat losses to the surroundings and discussed issues of sustained propagation and extinction. The stability of combustion fronts was analyzed by Armento and Miller [13] using a simplified front analysis.

The section is organized as follows: First, we provide a simplified approach using the method of characteristics, to define the large-scale features of the temperature profile and delineate the main heat transfer regimes in in-situ combustion. Then, we present the framework of the analysis and proceed with a detailed asymptotic treatment of the reaction front. The jump conditions derived are subsequently used to analyze the properties of planar combustion fronts. Finally, we comment on effects of heterogeneity and scale-up. Our model is a continuum model, in which effective values are used for the kinetic and transport parameters. A parallel effort is curently being conducted to model combustion at the pore-network scale (Lu and Yortsos, [16]), in order to understand the process at the small scale and to explain the formation of patterns in recent combustion experiments in Hele-Shaw cells [17].

Large-Scale Features of the Temperature Profile

Before we proceed, we consider a simplified analysis to derive some large-scale features of the typical temperature profile expected in in-situ combustion. For this, we formulate the energy balance in 1-D, when heat conduction is considered negligible compared to convection and consider the solution of a simple case in which the heat of reaction is a Dirac delta function. A justification of this assumption will appear later in this section. Assuming a constant flow

velocity $\tilde{v}$ and neglecting heat conduction we have

$$[(1-\phi)c_s\rho_s]\frac{\partial \tilde{T}}{\partial \tilde{t}} + c_g\rho_g\tilde{v}\frac{\partial \tilde{T}}{\partial \tilde{x}} = \tilde{Q}\delta\left(\tilde{x}-\tilde{x}_f(\tilde{t})\right) - h(\tilde{T}-\tilde{T}_o), \tag{1}$$

where the right-hand side involves the heat of reaction, due to combustion, and a convective-type expression for heat losses to the surroundings. In this notation, $\tilde{Q}$ expresses heat released per unit area and unit time. Initial conditions involve constant temperature $\tilde{T}_o$, initially and at injection ($\tilde{x}=0$).

Consider, first, the case where heat losses are negligible. Equation (1) is a hyperbolic equation with a singular source term at the combustion front $\tilde{x}=\tilde{x}_f(t)$. Outside of the front, the source term is negligible, and the solution of (1) is given using the method of characteristics, which in the present case are straight lines with a constant slope

$$\frac{d\tilde{x}}{d\tilde{t}} = \frac{c_g\rho_g\tilde{v}}{(1-\phi)c_s\rho_s} \equiv U. \tag{2}$$

Along the characteristics the temperature is constant. In general, there would be two characteristic velocities, one upstream (denoted by subscript III) and one downstream (denoted by subscript I) of the front, as the consumption and/or production of gases at the reaction front will affect the mass flux. Let the combustion front move with constant velocity V. If conditions are such that

$$V > U_I \quad \text{and} \quad V > U_{III} \tag{3}$$

the characteristics from the initial condition (the $\tilde{x}$-axis) will intersect the front trajectory (Figure 1), while those from the boundary (the $\tilde{t}$-axis) will not, creating an expanding simple

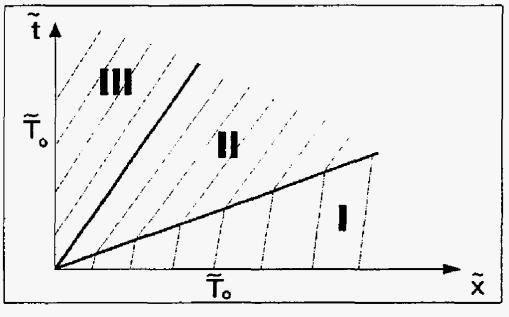

Figure 1: Characteristics Diagram for Combustion

wave region (region II in Fig. 1). In this case, the $(\tilde{t} - \tilde{x})$ plane consists of three regions, one corresponding to the initial (region I, of temperature $\tilde{T}_o$), another corresponding to the simple wave (region II, of a temperature to be determined), and a third corresponding to the injection (region III, of temperature $\tilde{T}_o$). The temperature across the front jumps to the value $\tilde{T}_f$, obtained by integrating the energy equation (1) across the combustion front,

$$\tilde{T}_f - \tilde{T}_o = \frac{\tilde{Q}}{[(1-\phi)c_s\rho_s](V - U_I)} \tag{4}$$

A more rigorous expression will be obtained later. Under condition (3), the simple wave region is also spanned by characteristics of slope U_{III}, except that these now emanate from the combustion front (as shown in Figure 1), hence they carry temperature $\tilde{T}_f$. Thus, the temperature profile at any time consists of two far-field regions with temperature $\tilde{T}_o$ and an intermediate expanding region of temperature $\tilde{T}_f$. This profile is sketched in Figure 2. Accounting for conduction will smoothen the discontinuities at the fronts.

In realistic cases, heat losses cannot be neglected. If we take the simple linear heat loss term shown in (1), the temperature in region II is not constant any longer, but decreases with time. We can readily show that the solution in this region is

$$\tilde{T} = \tilde{T}_o + (\tilde{T}_f - \tilde{T}_o)\exp\left[-\frac{h(V\tilde{t} - \tilde{x})}{[(1-\phi)c_s\rho_s](V - U_{III})}\right] \tag{5}$$

suggesting an exponential decay. The resulting profile is sketched schematically in Figure 3. Note that the temperature at the trailing edge of the region, $\tilde{T}_t$, declines exponentially in

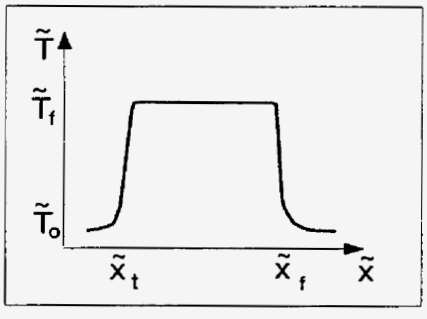

Figure 2: Temperature Profile for the Adiabatic Case

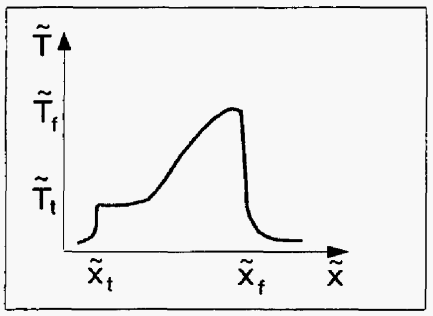

Figure 3: Temperature Profile for Adiabatic Sytem

time as

$$\tilde{T}_t = \tilde{T}_o + (\tilde{T}_f - \tilde{T}_o)\exp\left[-\frac{h\tilde{t}}{(1-\phi)c_s\rho_s}\right] \tag{6}$$

The situation is reversed, if the two inequalities (3) are reversed. Now the front moves slower, and it is the temperature downstream, which increases to $\tilde{T}_f$. Region II precedes, rather than trailing the combustion front, the simple wave expanding ahead of it. Analogous conclusions can be reached if one only of the inequalities in (3) is valid, etc.

Having obtained a qualitative understanding of the problem, we will now proceed with a more rigorous analysis.

FORMULATION OF THE PROBLEM

Typically, combustion reactions have large activation energies. A dimensionless measure is the Zeldovich number, $Z = \frac{E\tilde{T}_o}{R\tilde{T}_f^2}$, where E is the activation energy and $\tilde{T}_f$ denotes the front temperature (a simple expression for which was given in (4)). Typically, Z is large. Because of this condition and the fact that the reaction rate is strongly temperature dependent, all combustion reactions are confined to a thin reaction-dominated zone at the combustion front. It is within this zone, where reactions occur at a high rate, temperature, pressure and concentrations being approximately constant. The reaction zone is embedded within the heat transfer layer, as shown in Figure 4, where thermal and molecular diffusion are equally

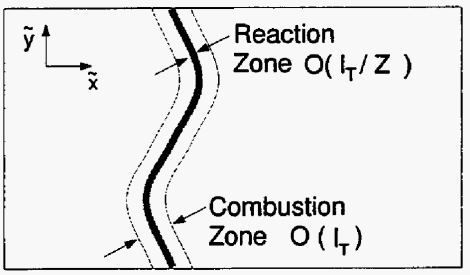

Figure 4: Definition of Reaction and Combustion Zones

important with convection. If l_T is the characteristic length of the heat transfer layer, the reaction zone has a thickness equal to l_T/Z. Expressions for l_T will be derived below.

The reaction zone and the heat transfer layer combine to form the combustion zone, Figure 4. Outside this zone, the problem is controlled by convective transport of energy and mass (and also by heat losses to the surroundings, if applicable). It is outside the combustion zone, where fluid dynamics and permeability heterogeneity are dominant. In the simplified example given previously, these would be regions I and III of Figure 1. Now, in all practical applications, the reaction zone has a sufficiently small width, so that it can be viewed as a front. Appropriate jump conditions can then be derived across it. In addition, it is likely that the heat transfer layer width is small compared to the fluid dynamical scale of the problem, l_S. If that is the case, we can define the small parameter $\delta = l_T/l_S$, and consider the combustion zone as a discontinuous front as shown in Figure 5. For such a description, additional jump conditions, now across the combustion front must be derived.

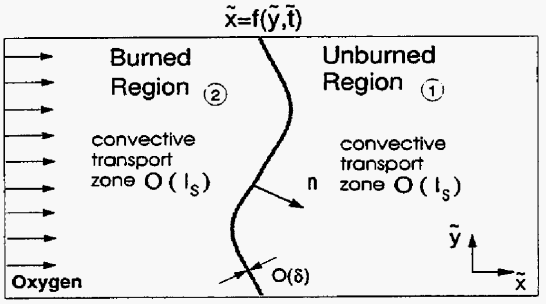

Figure 5: Combustion Front as a Discontinuity

Before we proceed further, let us recall some basic notions related to front propagation. For simplicity, we will restrict our discussion to two-dimensional problems, although an extension to 3-D is straightforward. Consider a front propagating in the positive $\tilde{x}$ direction and described by

$$F(\hat{x},\hat{y},t) \equiv \hat{x} - f(\hat{y},\hat{t}) = 0 \tag{7}$$

as shown in Figure 5. In our context, this equation separates a burned region ($F < 0$) from an unburned region ($F > 0$), where fresh solid fuel resides in the pore structure. Define the velocity of the surface by $\boldsymbol{\nu}$. Then, from definition, the normal velocity with respect to a fixed frame of reference, ν_n, is

$$\nu_n \equiv \boldsymbol{\nu} \cdot \boldsymbol{n} = \frac{-F_t}{|\hat{\nabla} F|} = \frac{f_t}{(1+f_{\hat{y}}^2)^{1/2}} \tag{8}$$

where $f_t = \partial f/\partial t$ and $f_{\hat{y}} = \partial f/\partial \hat{y}$, and $\boldsymbol{n}$ is the unit vector normal to the front pointing in the direction of the unburned region

$$\boldsymbol{n} = \frac{\hat{\nabla} F}{|\hat{\nabla} F|}. \tag{9}$$

In the flame propagation literature, a useful quantity is the net normal velocity with respect to the moving front,

$$S_f \equiv \hat{\boldsymbol{v}}_{0^-} \cdot \boldsymbol{n} - \nu_n = \frac{\hat{v}_{\hat{x}} - \hat{v}_{\hat{y}} f_{\hat{y}} - f_t}{(1+f_{\hat{y}}^2)^{1/2}} \tag{10}$$

where $\hat{\boldsymbol{v}}_{0^-}$ is the average gas mixture velocity evaluated at $F = 0^-$. In the case of porous media, however, the above must be modified, due to the presence of the porous medium, to read as

$$S_{fp} \equiv \hat{\boldsymbol{v}}_{0^-} \cdot \boldsymbol{n} - \phi \nu_n = \frac{\hat{v}_{\hat{x}} - \hat{v}_{\hat{y}} f_{\hat{y}} - \phi f_t}{(1+f_{\hat{y}}^2)^{1/2}} \tag{11}$$

where ϕ is porosity. This and related quantities will be encountered below.

In the following, we will consider in sequence, first a reaction front, and then a combustion front. Using asymptotic expansions, the structure in both fronts will be analyzed and appropriate jump conditions across the fronts will be derived. To proceed, we need first to formulate the governing equations of the problem.

Governing Equations

Consider the combustion in a porous medium of a solid fuel, of known initial composition and concentration. In in-situ combustion, this fuel is in reality produced as a result of the LTO step, preceding the combustion front. Given that the two processes are coupled, the concentration and composition of the fuel is, in principle, not known a priori and must be determined as part of the solution of the overall problem. In the following, we will assume that the initial density of the fuel per unit total volume is known and given by ρ_f^o.

At any time, the system consists of two phases, a solid phase including the solid matrix and the fuel, and a gas mixture of injected oxygen and reaction products. The matrix is non-reactive, stationary and its thermodynamic properties do not change during the process. The solid fuel reacts with injected oxygen, according to the following one-step heterogeneous reaction model

$$[\text{Fuel}] + \tilde{\gamma}\ [\text{Oxygen}] \longrightarrow \tilde{\gamma}_{gp}\ [\text{Gaseous Product}]$$

where we used pseudo-components for the fuel and the produced gases, and where $\tilde{\gamma}$ are stoichiometric coefficients. This simplification allows for a simple treatment of a complex problem. In formulating the conservation equations we will assume the following: locally, pore space and solid matrix are in thermal equilibrium, hence a one-temperature model is used for the energy balance; heat transfer by radiation, and energy source terms due to pressure increase, and work from surface and body forces are negligible; the ideal gas law is the equation of state for the gas phase; thermodynamic and transport properties, such as conductivity, diffusivity, heat capacity of the solid, heat of reaction, etc. remain constant. We also define a conversion depth $\eta(\tilde{x}, \tilde{y}, \tilde{t}\,) = 1 - \rho_f/\rho_f^o$, such that $\eta = 0$ corresponds to the initial state and $\eta = 1$ to the case of complete fuel conversion.

Conservation equations are written for the following quantities: the total energy, the oxygen mass, the total gas mass and the fuel mass, in terms of the temperature $\tilde{T}(\tilde{x}, \tilde{y}, \tilde{t}\,)$, the oxygen mass fraction $Y(\tilde{x}, \tilde{y}, \tilde{t}\,)$, the average gas density $\rho_g(\tilde{T}, \tilde{p})$ and the fuel conversion depth. We also use Darcy's law for the flow of the gas phase, in terms of the pressure $\tilde{p}(\tilde{x}, \tilde{y}, \tilde{t}\,)$. The dimensional form of these equations (superscript tilde) is shown below

energy

$$(1-\phi)c_s\rho_s\frac{\partial\tilde{T}}{\partial\tilde{t}} + c_g\rho_g\tilde{\boldsymbol{v}}\cdot\tilde{\nabla}\tilde{T} = \tilde{\nabla}\cdot(\lambda\tilde{\nabla}\tilde{T}) + \tilde{Q}\rho_f^o W - \dot{Q}_h \tag{12}$$

oxygen mass

$$\phi\frac{\partial(Y\rho_g)}{\partial\tilde{t}} + \tilde{\nabla}\cdot(Y\rho_g\tilde{\boldsymbol{v}}) = \tilde{\nabla}\cdot(D_M\rho_g\tilde{\nabla}Y) - \tilde{\mu}\rho_f^o W \tag{13}$$

total gas mass

$$\phi\frac{\partial\rho_g}{\partial\tilde{t}} + \tilde{\nabla}\cdot(\rho_g\tilde{\boldsymbol{v}}) = \tilde{\mu}_g\rho_f^o W \tag{14}$$

and depth of conversion

$$\frac{\partial\eta}{\partial\tilde{t}} = W \tag{15}$$

where, $\dot{Q}_h$ is a heat loss term and we introduced the rate of reaction W. Using the law of mass action we will take

$$W = k(\tilde{T})(Y\tilde{p})^n\psi(\eta) \tag{16}$$

where

$$k(\tilde{T}) = k_o e^{-E/R\tilde{T}} \tag{17}$$

E is the activation energy, k_o the pre-exponential factor, and n the exponent in the dependence on oxygen concentration and gas pressure. The dependence on η is through the dimensionless function ψ, the evaluation of which requires a more elaborate pore-level study [16]. Clearly, $\psi(1) = 0$.

In the above, c_i is the average specific heat capacity of species i (gas or solid) at constant pressure, ρ_i is the volumetric density of species i, and we assumed that the solid heat capacity is much larger than that of the gas. The average thermal conductivity, λ, is an effective value including the effects of gas and solid phases on conduction. Q represents the heat release of the fuel combustion reaction and is also assumed to be independent of temperature variations. Variable Y is the mass fraction of oxygen in the gas phase, D_M is an effective diffusion coefficient, while $\tilde{\mu}_g$ and $\tilde{\mu}$ are mass-weighted stoichiometric coefficients, $\tilde{\gamma}_i M_i/M_f$. The net

gas production due to reaction is determined by the sign of $\tilde{\mu}_g = \tilde{\mu}_{gp} - \tilde{\mu}$ so that $\tilde{\mu}_g > 0$ or $\tilde{\mu}_g < 0$ corresponds to gas production or consumption, respectively. Finally, we have Darcy's law

$$\tilde{\nabla}\tilde{p} = -\frac{\eta_g}{k(\eta)}\tilde{\boldsymbol{v}} \tag{18}$$

where $k(\eta)$ is the permeability and η_g is the gas viscosity, and the equation of state, assuming ideal gases

$$\tilde{p}M_g = \rho_g R\tilde{T} \tag{19}$$

The expression for heat losses can take the simple form shown in (1) or the more elaborate expression

$$\dot{Q}_h = \frac{2\sqrt{\lambda_h c_h \rho_h}}{\sqrt{\pi}H}\int_0^{\tilde{t}} \frac{\partial \tilde{T}}{\partial \tau}\frac{\partial \tau}{\sqrt{\tilde{t}-\tau}} \tag{20}$$

reflecting heat conduction to a semi-infinite overburden and underburden (Yortsos and Gavalas [18]). Here subscript h refers to the surroundings and H is the reservoir thickness.

In the next section, we will proceed with a scaling and non-dimensionalization of the above equations.

Scaling and Non-dimensionalization

As described earlier, also shown in Figures 4 and 5, the problem includes three spatial scales, each associated with different dominant processes: the scale of a reactive-diffusive reaction zone, l_R, the scale of a convective-diffusive combustion zone, l_T, and the convective scale l_S. In the combustion zone, convection and conduction are of the same magnitude, namely the Peclet number, $Pe = v_* l_T c_s \rho_s / \lambda$ is of order 1, where the reference velocity v_* is to be determined. This defines l_T. If the front temperature of a planar combustion layer is $\tilde{T}_f$, also to be determined from the solution of the problem, then we have

$$l_R \equiv \frac{l_T}{Z} \quad \text{where} \quad Z = \left[\frac{E\tilde{T}_o}{R\tilde{T}_f^2}\right],$$

$$l_T \equiv \frac{\lambda}{(1-\phi)c_s\rho_s v_*},$$

$$l_S \equiv \tilde{L}.$$

The characteristic parameters to be chosen depend on what is the focus of the analysis. If it is the reaction zone, the characteristic time is based on the reaction kinetics

$$t_R \equiv Z\left(k_o \tilde{p}_i^n e^{-E/R\tilde{T}_f}\right)^{-1}, \tag{21}$$

and the characteristic length is the combustion zone length l_T. If the focus is on the combustion zone, then we rescale both the characteristic time and length by δ^{-1}, where $\delta = l_T/l_S \ll 1$. Then, $t_* = \delta^{-1} t_R$ and $x_* = \delta^{-1} l_T$. In either case, we have the reference velocity $v_* \equiv \frac{x_*}{t_*} = \frac{l_T}{t_R}$. This further implies the relation

$$v_* = \sqrt{\frac{\lambda}{(1-\phi)c_s \rho_s t_R}}. \tag{22}$$

Scaling temperature with $\tilde{T}_o$ and density with the initial density ρ_{gi} and using the combustion zone formulation, we obtain the conservation equations in dimensionless form

$$\frac{\partial \theta}{\partial \hat{t}} + a\rho \boldsymbol{v} \cdot \hat{\nabla}\theta = \delta \hat{\Delta}\theta + \delta q \Phi - \dot{Q}_{hD} \tag{23}$$

$$\phi \frac{\partial (Y\rho)}{\partial \hat{t}} + \hat{\nabla} \cdot (Y\rho \boldsymbol{v}) = \frac{\delta}{Le}(\hat{\nabla} \cdot \rho \hat{\nabla} Y) - \delta \mu \Phi \tag{24}$$

$$\phi \frac{\partial \rho}{\partial \hat{t}} + \hat{\nabla} \cdot (\rho \boldsymbol{v}) = \delta \mu_g \Phi \tag{25}$$

and

$$\frac{\partial \eta}{\partial \hat{t}} = \delta \Phi \tag{26}$$

where

$$\Phi \equiv \delta^{-2} Z (Yp)^n \psi(\eta) \exp\left[Z\theta_f^2 \left(\frac{1}{\theta_f} - \frac{1}{\theta}\right)\right]. \tag{27}$$

In addition, we have

$$\hat{\nabla} p = -\kappa \boldsymbol{v} \tag{28}$$

and

$$\rho\theta = 1 + \Pi P. \tag{29}$$

In the above, we introduced the following variables and parameters

$$p = \frac{\tilde{p}-\tilde{p}_i}{\tilde{p}_{inj}-\tilde{p}_i}, \qquad \Pi = \frac{\tilde{p}_{inj}-\tilde{p}_i}{\tilde{p}_i}, \qquad \mu_i = \frac{\tilde{\mu}_i \rho_f^o}{\rho_{gi}}, \qquad q = \frac{Q\rho_f^o}{(1-\phi)c_s\rho_s\tilde{T}_o},$$

$$\kappa = \frac{\eta_g x_* v_*}{k(\tilde{p}_{inj}-\tilde{p}_i)}, \qquad Le = \frac{\lambda}{D_M(1-\phi)c_s\rho_s}, \qquad \dot{Q}_{hD} = \frac{\dot{Q}_h t_*}{(1-\phi)c_s\rho_s T_o},$$

$$a = \frac{c_g\rho_{gi}}{(1-\phi)c_s\rho_s}, \qquad \Phi = \delta^{-1}Wt_*,$$

where $\tilde{p}_i$ and $\tilde{p}_{inj}$ are the initial and the injection gas pressure in the system. Note that the spatial coordinates are nondimensionalized based on the system length, l_S, which in the limit $\delta \ll 1$ allows to approximate the combustion zone as a thin layer. To focus on the combustion zone, we simply change the scaling, which is equivalent to taking $\delta = 1$ in the above equations.

The boundary conditions depend on the extent of the combustion process. If we assume that the fuel is fully consumed, we will take for $\hat{t} \geq 0$:

$$Y = 1, \qquad \theta = \theta_f \qquad \eta = 1 \qquad ; \qquad \hat{x} \to -\infty \tag{30}$$

$$Y = Y_b, \qquad \theta = 1, \qquad \eta = 0 \qquad ; \qquad \hat{x} \to \infty \tag{31}$$

where θ_f and Y_b are to be determined. This is the fuel-deficient case. Otherwise, we have

$$Y = 1, \qquad \theta = \theta_f \qquad \eta = \eta_b \qquad ; \qquad \hat{x} \to -\infty \tag{32}$$

$$Y = 0, \qquad \theta = 1, \qquad \eta = 0 \qquad ; \qquad \hat{x} \to \infty \tag{33}$$

where θ_f and η_f are to be determined. This is the oxidant-deficient case. In the following, we will consider only the fuel-deficient case.

Moving Coordinates

The final step in the formulation of the problem is to convert to moving coordinates, moving with the combustion front, which in the fuel-deficient case can be defined as the position at

which $\eta = 1/2$. If we denote $x = \hat{x} - f(\hat{y}, \hat{t})$, $y = \hat{y}$ and $t = \hat{t}$, then the non-dimensional equations take the form:

$$\frac{\partial \theta}{\partial t} + (a\rho s - f_t)\frac{\partial \theta}{\partial x} + a\rho v_y \frac{\partial \theta}{\partial y} = \delta \Delta\theta + \delta q \Phi - \dot{Q}_{hD} \tag{34}$$

$$\phi \frac{\partial (Y\rho)}{\partial t} + \frac{\partial [Y\rho(s - \phi f_t)]}{\partial x} + \frac{\partial}{\partial y}(Y\rho v_y) = \left(\frac{\delta\rho}{Le}\right)\Delta Y - \delta\mu\Phi \tag{35}$$

$$\phi \frac{\partial \rho}{\partial t} + \frac{\partial [\rho(s - \phi f_t)]}{\partial x} + \frac{\partial}{\partial y}(\rho v_y) = \delta\mu_g \Phi \tag{36}$$

$$\frac{\partial \eta}{\partial t} - f_t \frac{\partial \eta}{\partial x} = \delta\Phi \tag{37}$$

$$\kappa v_x = -\frac{\partial p}{\partial x} \tag{38}$$

$$\kappa v_y = -\left[\frac{\partial p}{\partial y} + f_y \frac{\partial p}{\partial x}\right] \tag{39}$$

$$\rho\theta = 1 + \Pi p \tag{40}$$

Here,

$$s \equiv v_x - v_y \frac{\partial f}{\partial y}, \tag{41}$$

is the longitudinal velocity of the gas mixture in the moving frame and we defined the Laplace operator in moving coordinates

$$\Delta \equiv (1 + f_y^2)\frac{\partial^2}{\partial x^2} + \frac{\partial^2}{\partial y^2} - \frac{\partial^2 f}{\partial y^2}\frac{\partial}{\partial x} - 2\frac{\partial f}{\partial y}\frac{\partial^2}{\partial x \partial y}, \tag{42}$$

For simplicity in the presentation, the density term in the diffusion of oxygen was approximated as constant. However, this approximation is not made in the subsequent analysis. Having obtained the desired formulation, we proceed next with the analysis of the structure of the reaction zone and then with that of the combustion zone.

THE REACTION ZONE

Under the condition $Z \gg 1$, the reaction zone thickness, l_T/Z, is much smaller than l_T. To analyze the structure of the zone, we stretch the longitudinal moving coordinate, $X = Zx$, and expand the dependent variables in asymptotic series in Z^{-1}. Following [8] it can be shown that, to leading order, temperature, concentration, pressure and density are independent of X. Thus, we take

$$\begin{aligned}
\theta &\sim \theta^o(y,t) + Z^{-1}\theta^1(X,y,t) + \ldots, \\
Y &\sim Y^o(y,t) + Z^{-1}Y^1(X,y,t) + \ldots, \\
p &\sim p^o(y,t) + Z^{-1}p^1(X,y,t) + \ldots, \\
\rho &\sim \rho^o(y,t) + Z^{-1}\rho^1(X,y,t) + \ldots, \\
\eta &\sim \eta^o(X,y,t) + \ldots, \\
s &\sim s^o(X,y,t) + \ldots, \\
v_y &\sim v_y^o(y,t) + \ldots, \\
f &\sim f^o(y,t) + \ldots.
\end{aligned}$$

The respective leading-order terms are obtained after substitution in the governing equations. Combining the energy equation with the fuel balance, shows that the leading-order terms are $O(Z^{-1})$, in which case only conduction in the X direction and reaction participate, namely

$$\delta\left[1 + f_y^{o2}\right]\frac{\partial^2\theta^1}{\partial X^2} = q f_t^o \frac{\partial \eta^o}{\partial X} \tag{43}$$

(note that the heat loss term vanishes to leading order). For the oxygen mass balance, a similar analysis shows that the leading-order terms are convection, diffusion and reaction, hence

$$Le\rho^o Y^o(y,t)\frac{\partial s^o}{\partial X} - \delta\rho^o\left[1 + f_y^{o2}\right]\frac{\partial^2 Y^1}{\partial X^2} = \mu Le f_t^o \frac{\partial \eta^o}{\partial X}, \tag{44}$$

where we have taken into account that ρ^o is constant, while the total gas mass balance reads

$$\rho^o \frac{\partial s^o}{\partial X} = -\mu_g f_t^o \frac{\partial \eta^o}{\partial X}. \tag{45}$$

The equation for the fuel mass is expressed to leading-order as

$$\delta f_t^o \frac{\partial \eta^o}{\partial X} = -\left[Y^o(y,t)p^o(y,t)\right]^n \psi(\eta^o) e^{\theta^1} \tag{46}$$

where we used a power series expansion for the exponential term. Finally, to leading-order, pressure is constant within the reaction zone.

Integrating equations (43- 45) across the reaction zone determines the jumps in heat, oxygen mass and gas mass fluxes across the front in terms of the jump in depth of fuel conversion,

$$\delta \left[1 + f_y^{o2}\right] \left.\frac{\partial \theta^1}{\partial X}\right|_{-\infty}^{\infty} = q f_t^o \eta^o \Big|_{-\infty}^{\infty} \tag{47}$$

$$\delta \rho^o \left[1 + f_y^{o2}\right] \left.\frac{\partial Y^1}{\partial X}\right|_{-\infty}^{\infty} = -\left[\mu + Y^o(y,t)\mu_g\right] Le f_t^o \, \eta^o|_{-\infty}^{\infty} \tag{48}$$

$$\rho^o s^o \Big|_{-\infty}^{\infty} = -\mu_g f_t^o \, \eta^o|_{-\infty}^{\infty} \,. \tag{49}$$

The depth of conversion equation (46) can also be integrated across the reaction zone. For this, we first integrate equation (43) using the boundary conditions $\partial\theta^1/\partial X = 0$, $\eta^o = 1$ as $X \to -\infty$, to give

$$\delta \left[1 + f_y^{o2}\right] \frac{\partial \theta^1}{\partial X} = -q f_t^o (1 - \eta^o) \tag{50}$$

Then, multiplying equation (50) by (46) yields

$$q \left(f_t^o\right)^2 \left(\frac{1-\eta^o}{\psi(\eta^o)}\right) \frac{\partial \eta^o}{\partial X} = -\left[1 + f_y^{o2}\right] \left[Y^o(y,t)(1 + \Pi p^o(y,t))\right]^n e^{\theta^1} \frac{\partial \theta^1}{\partial X} \tag{51}$$

This equation can be now integrated across the reaction zone, to give the following result for the square of the normal front velocity

$$\frac{\left(f_t^o\right)^2}{1 + f_y^{o2}} = \frac{\left[Y^o(y,t)(1 + \Pi p^o(y,t))\right]^n}{q \int_0^1 \frac{(1-\eta^o)}{\psi(\eta^o)} d\eta^o} . \tag{52}$$

We note that the expression for the normal front velocity is primarily related to the unknown mass fraction of the oxidant at the completion of the reaction and the pressure at the front. Conditions (47-49) also express the jump of the corresponding quanities across the reaction zone. Namely, if we define the jump in a quantity of the combustion zone π across the

reaction front as $[\pi]^+_- = \pi(x=0^+) - \pi(x=0^-)$, we obtain for the deficient-fuel case (where $\eta^o|^{\infty}_{-\infty} = 0 - 1 = -1$)

$$[Y]^+_- = [\theta]^+_- = [p]^+_- = 0, \qquad [\eta]^+_- = -1, \tag{53}$$

and

$$\begin{aligned} \delta\left[1+f_y^{o2}\right]\left[\frac{\partial\theta}{\partial x}\right]^+_- &= -qf_t \\ \delta\rho\left[1+f_y^{o2}\right]\left[\frac{\partial Y}{\partial x}\right]^+_- &= [\mu + Y^o(y,t)\mu_g]\, Lef_t \\ [\rho(s-\phi f_t)]^+_- &= \mu_g f_t, \end{aligned} \tag{54}$$

In the above we have assumed full consumption of the fuel at *any* point of the front.

THE COMBUSTION ZONE

Consider, next, the combustion zone structure. Outside the reaction zone, the chemical reaction rates are insignificant. To analyze this problem, we must consider the conservation equations to either side of the reaction front, across which the jump conditions derived previously apply. For this, we need to consider an expansion valid inside the combustion zone, in which conduction and diffusion, but not chemical reaction, are taken into account.

In the context of the overall problem (Figure 5), the combustion zone has a dimensionless extent of order δ, hence we must introduce the stretched coordinate $\xi = x/\delta$ and seek inner expansions of the following form

$$\begin{aligned} \theta &\sim \theta_o + \delta\theta_1 + \ldots, \\ Y &\sim Y_o + \delta Y_1 + \ldots, \\ p &\sim p_o + \delta p_1 + \ldots, \\ \rho &\sim \rho_o + \delta\rho_1 + \ldots, \\ \eta &\sim \eta_o + \delta\eta_1 + \ldots, \\ s &\sim s_o + \delta s_1 + \ldots, \\ v_y &\sim v_{yo} + \delta v_{y1} + \ldots, \\ f &\sim f_o + \delta f_1 + \ldots, \end{aligned}$$

These expansions are then introduced in the equations in moving coordinates. Under the condition $\frac{\dot{Q}_h t_R}{(1-\phi)c_s\rho_s T_o} \ll 1$, the heat loss term does not contribute to leading order, thus the energy balance reads

$$A_o\frac{\partial\theta_o}{\partial\xi} - \left[1+f_{oy}^2\right]\frac{\partial^2\theta_o}{\partial\xi^2} = 0 \tag{55}$$

where

$$A_o(\xi,y,t) = a\rho_o s_o - f_{o_t} \tag{56}$$

and

$$s_o = v_{xo} - v_{yo}\frac{\partial f_o}{\partial y} \tag{57}$$

Oxygen, total gas and fuel mass balances become, respectively,

$$\rho_o B_o\frac{\partial Y_o}{\partial\xi} - \frac{1}{Le}\left[1+f_{oy}^2\right]\frac{\partial}{\partial\xi}\left[\rho_o\frac{\partial Y_o}{\partial\xi}\right] = 0 \tag{58}$$

$$\frac{\partial}{\partial\xi}\left[\rho_o B_o\right] = 0 \tag{59}$$

$$\frac{\partial\eta_o}{\partial\xi} = 0 \tag{60}$$

where

$$B_o(\xi,y,t) = s_o - \phi f_{o_t}. \tag{61}$$

Darcy's law gives

$$\frac{\partial p_o}{\partial\xi} = 0 \tag{62}$$

and the ideal gas law reads

$$\rho_o\theta_o = \text{const.} \tag{63}$$

Parameter a, representing the ratio of gas to solid heat capacities is small, thus, we expect $A_o < 0$. Also, for a propagating front along the positive x direction, we must have $s_o > \phi f_{o_t}$, hence $B_o > 0$. Experimental data obtained in combustion tube experiments (e.g. see Martin

et al. [19], or Mamora and Brigham [20]), confirm these assumptions. We can then proceed to integrate the above equations.

Because $A_o < 0$, the only possible solution for θ_o in the region $\xi < 0$ is a constant independent of ξ (otherwise, θ_o will become unbounded as $\xi \to -\infty$). To find the solution for $\xi > 0$, we integrate (55) and make use of the jump condition at the reaction front

$$\left[1 + f_{o_y}^2\right] \left[\frac{\partial \theta_o}{\partial \xi}\right]_-^+ = -q f_{o_t} \tag{64}$$

to obtain the result

$$\theta_o = \begin{cases} \theta_f(y,t) & : \quad \xi < 0 \\ 1 - \dfrac{q f_{o_t}}{A_o} e^{\left[\dfrac{A_o}{\left[1 + f_{o_y}^2\right]} \xi\right]} & : \quad 0 < \xi \end{cases}$$

showing that the temperature decays exponentially fast downstream of the combustion front. Working similarly, equation (58) shows that because $B_o > 0$, the solution for Y in $\xi > 0$ must be a constant independent of ξ. Equation (59) also shows that $\rho_o B_o$ is a constant. Then, by integrating (58) in the region $\xi < 0$, where ρ_o is constant, and making use of the jump condition across the reaction front,

$$\rho_o \left[1 + f_{o_y}^2\right] \left[\frac{\partial Y_o}{\partial \xi}\right]_-^+ = (\mu + Y_b(y,t)\mu_g)\, Le f_{o_t} \tag{65}$$

we obtain the final result

$$Y_o = \begin{cases} 1 - \left[\dfrac{(\mu + Y_b \mu_g) f_{o_t}}{\rho_o B_o}\right] e^{\left[\dfrac{Le \rho_o B_o}{\left[1 + f_{o_y}^2\right]} \xi\right]} & : \quad \xi < 0 \\ Y_b(y,t) & : \quad 0 < \xi \end{cases}$$

This equation gives the profile of the mass fraction upstream of the reaction front. Fianlly, equation (60) gives the expected result

$$\eta_o = \begin{cases} 1 & : \quad \xi < 0 \\ 0 & : \quad 0 < \xi \end{cases}$$

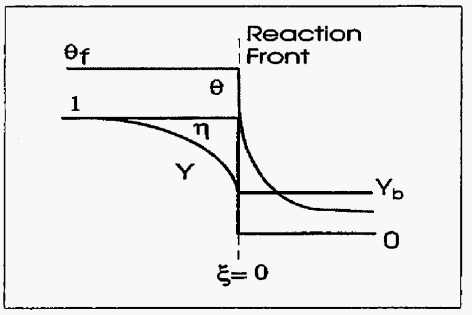

Figure 6: Schematic Profiles of Temperature, Oxygen Mass Fraction and Fuel Conversion in the Combustion Zone.

assuming, again, complete fuel combustion. Figure 6 show schematic profiles of temperature, mass fraction and conversion across the combustion zone.

Note that A_o in the temperature equation involves the mass flux $\rho_o s_o$ downstream of the reaction front (although its contribution to A_o may be very small due to $a \ll 1$), while B_o in the mass fraction expression involves the mass flux upstream of the reaction front. The two fluxes are related to each other through the jump condition

$$\left[\rho_o(s_o - \phi f_{o_t})\right] = \mu_g f_{o_t} \tag{66}$$

derived in equation set (54). The above equations represent the leading order "inner" expansion to the large scale problem, for which the combustion front appears as a discontinuity. In the section to follow we will consider the "outer" problem, on either side of the front (see Figure 5) by keeping only the convective transport term in the equations. To match the outer expansions we use the jump conditions derived from the inner problem, namely the problem in the combustion zone. These were derived previously to leading-order, and are summarized below.

$$\begin{aligned}
[\theta_o] &= 1 - \theta_f(y,t) \\
[Y_o] &= Y_b(y,t) - 1 \\
\left[\rho_o(s_o - \phi f_{o_t})\right] &= \mu_g f_{o_t} \\
[\eta_o] &= -1 \\
[p_o] &= 0
\end{aligned} \tag{67}$$

$$\left[\frac{\partial \theta_o}{\partial \xi}\right] = \left[\frac{\partial Y_o}{\partial \xi}\right] = \left[\frac{\partial p_o}{\partial \xi}\right] = 0$$

These equations must be considered along with equation (52) for the normal front velocity, where $Y^o(y,t) = Y_b$.

THE CONVECTIVE TRANSPORT REGION

The scale of the outer problem is the scale of the originally derived equations. Here, conduction, diffusion and reaction (but not heat losses) are negligible, and we seek expansions of the form

$$\begin{aligned}
\theta &\sim \Theta_o + \delta\Theta_1 + \ldots, \\
Y &\sim \Upsilon_o + \delta\Upsilon_1 + \ldots, \\
p &\sim P_o + \delta P_1 + \ldots, \\
\rho &\sim R_o + \delta R_1 + \ldots, \\
s &\sim S_o + \delta S_1 + \ldots, \\
v_y &\sim V_{yo} + \delta V_{y1} + \ldots.
\end{aligned}$$

Direct substitution in the original equations shows that the leading term of the expansions satisfy the following

$$\frac{\partial \Theta_o}{\partial t} + (aR_oS_o - f_{o_t})\frac{\partial \Theta_o}{\partial x} + aR_oV_{yo}\frac{\partial \Theta_o}{\partial y} = -\dot{Q}_{hD} \tag{68}$$

$$\phi\frac{\partial(\Upsilon_oR_o)}{\partial t} + \frac{\partial[\Upsilon_oR_o(S_o - \phi f_{o_t})]}{\partial x} + \frac{\partial(\Upsilon_oR_oV_{yo})}{\partial y} = 0, \tag{69}$$

$$\phi\frac{\partial R_o}{\partial t} + \frac{\partial(R_o(S_o - \phi f_{o_t})}{\partial x} + \frac{\partial(R_oV_{yo})}{\partial y} = 0, \tag{70}$$

$$\kappa V_{xo} = -\frac{\partial P_o}{\partial x}, \tag{71}$$

$$\kappa V_{yo} = -\left[\frac{\partial P_o}{\partial y} + f_{oy}\frac{\partial P_o}{\partial x}\right], \tag{72}$$

$$R_o\Theta_o = 1 + \Pi P_o, \tag{73}$$

$$S_o = V_{xo} - V_{yo}\left(\frac{\partial f_o}{\partial y}\right). \tag{74}$$

The fuel mass balance shows that the convective derivative of η_o in the moving coordinate system vanishes, implying that the depth of fuel conversion is constant in both regions, as expected,

$$\eta = \begin{cases} 1 & : \ x < 0 \\ 0 & : \ 0 < x. \end{cases}$$

The solution of the outer problem must be considered in the two regions on either side of the combustion front, across which the jump conditions previously derived apply. The solution can be attempted using the method of characteristics, or the method of streamlines depending on the complexity of the geometry and heterogeneity in permeability. In the general case, the problem must be solved numerically.

In the following section, we illustrate the application of the previous results by considering the particular example of a planar front.

CASE OF A PLANAR FRONT

For the case of a planar front, we have $A_o = am_{oD}^{+} - V_D$, where m_{oD}^{+} is the dimensionless mass flux downstream of the front and V_D is the dimensionless front velocity. Using the expression for the temperature profile inside the combustion zone, in conjunction with the continuity of temperature at $\xi = 0$, $[\theta_o]_{-}^{+} = 0$, gives an expression for the dimensionless temperature at the front, which reads as follows

$$\theta_f = 1 - \frac{qV_D}{am_{oD}^{+} - V_D}. \tag{75}$$

Note that $m_{oD}^{+} = m_{oD}^{-} + \mu_g V_D$ where m_{oD}^{-} is the incoming mass flux. Equation (75) is a more rigorous dimensionless expression for the temperature jump across the front, compared to equation (4). Note that if $am_{oD}^{+} \ll 1$, then θ_f is the adiabatic temperature rise

$$\theta_f = 1 + q \tag{76}$$

Table 1: Typical Values of Porous Medium and Fluid Parameters for Combustion

Parameter	Value
$\tilde{Q}$	17,000 Btu/lbm fuel
E	31,600 Btu/lbmole
R	1.987 Btu/lbmole-R
k_o	498 $s^{-1}atm^{-1}$
$\tilde{T}_o$	212 F
n	1
$\tilde{P}_i$	10 atm.
λ	12 Btu/ft-D-F
ϕ	0.3
ρ_{gi}	0.0765 lbm/ft^3
$c_g\rho_{gi}$	0.0184 Btu/ft^3-F
ρ_f^o	1.2 lbm/ft^3
$(1-\phi)c_s\rho_s$	30 Btu/ft^3-F
M_f	235 lbm/lbmole
$\psi(\eta)$	1-η
H/C Ratio	1.65
μ	51.2863
μ_g	16.9935

Source: References [1],[2] and [12]

However, as shown later, this is not generally the case.

In the planar case, the dimensionless velocity is given from

$$V_D^2 = \frac{[Y_b(1+\Pi p^o)]^n}{q\int_0^1 \frac{(1-\eta^o)}{\psi(\eta^o)}d\eta^o}. \tag{77}$$

the calculation of which requires an expression for Y_b. This is obtained from the expression for the oxygen mass fraction within the combustion zone, along with the requirement of continuity at $\xi = 0$, hence

$$Y_b = \frac{m_{oD}^- - (\phi\rho_o + \mu)V_D\rho_o}{m_{oD}^- + (\mu_g - \phi\rho_o)V_D\rho_o} \tag{78}$$

Note that for $Y_b > 0$, the condition $m_{oD}^- > (\phi\rho_o + \mu)V_D$ must apply, namely the total gas mass flux should be sufficiently large.

Expressed in dimensional form, equations (75), (77), (78) and equation (22) form a system of four algebraic equations in the four unknowns, T_f, V_D, Y_b and v_*. The problem was solved

numerically for the parameter values shown in Table 1. Before we proceed, let us note that for a burning temperature of 934°F (1394°R), we have l_T =0.26 inch (0.66 cm) for the combustion zone thickness, and l_R =0.047 inch (0.12 cm) for the thickness of the reaction zone. The very small thickness of these zones should be carefully considered in the implementation of direct numerical simulation of in-situ combustion, particularly at the field scale. Results for the dimensionless velocity of the front V_D, unreacted oxygen concentration Y_b, combustion front temperature T_f and the reference velocity are shown in Figures 7 through 10 as a function of the injection velocity. As expected, the variables increase with the injection velocity. The results show that the temperature and velocity of the reaction zone increase monotonically as the gas flux increases.

The analysis based on the model demonstrates the importance of gas flow on the combustion dynamics of forward combustion in porous media. For instance, equation (76), which is the adiabatic temperature in the absence of flow is equal to 1350.4°R for the reference data of in Table 1. Figure 9 shows that the actual front temperature is higher than this value, the difference increases with increasing gas velocity. Hence, the temperature in the reaction zone significantly exceeds the combustion temperature predicted by solely thermodynamic arguments.

CONCLUDING REMARKS

In this section, we proposed a method for modeling the propagation of combustion fronts in porous media, by treating the reaction region as a place of discontinuities in the appropriate variables, which include, for example, fluxes of heat and mass. It was shown that reaction and combustion fronts have a spatially narrow width, estimated to be of the order of cm, within which heat release rates, temperatures and species concentrations vary significantly. The narrow width calls for an approach in which these fronts are treated as surfaces of discontinuity.

Using a rigorous perturbation approach, similar to that used in the propagation of flames [3] and smoldering combustion [7], we derived appropriate jump conditions that relate the change in these variables across the front to leading order. The conditions account for the

kinetics of the reaction between the oxidant and the fuel, the changes in the morphology of the pore space and the heat and mass transfer in the reaction zone. Then, the modeling of the problem reduces to the modeling of the dynamics of a combustion front, on the regions of either side of which convective transport of momentum (fluids), heat and mass, but not chemical reactions, must be considered. Properties of the two regions are coupled using the derived jump conditions. This methodology allows to explicitly incorporate permeability heterogeneity effects in the process description, without the undue complexity of the coupled chemical reactions.

For the case of 1-D planar fronts, we derived explicit expressions, which allow to obtain the burning temperature, the front velocity and the amount of oxygen left unreacted, in terms of the process variables, such as injection rates and pressure. We showed that the front temperature and velocity increases monotonically with increasing injected gas flux, and the combustion fronts can propagate in porous media due to non-trivial effect of heat convection. For the case of fronts in two and three dimensions, particularly in heterogeneous porous media, a numerical method must in general be implemented. The analysis described must be extended to include higher-order terms in the small parameter δ. In progress is a stability analysis of the front, which also includes higher-order terms. Also neglected in the examples were heat losses. In any case, however, the proposed treatment of the front as a discontinuity calls for a different approach in the simulation and upscaling, when coarse grids, such as those at the field scale, must be used. Because of the hyperbolic nature of the equations in the outer regions, methods based on characteristics and, more generally, on front tracking would appear to be appropriate. However, a direct implementation of existing methods, for instance of streamline simulation, is not feasible, because fluid and temperature streamlines are generally not the same, due to the difference in the volumetric heat capacities of gas and solid. In addition, the reacted mass fraction are to be obtained from the solution of the overall problem. Further research is needed in this direction.

References

[1] Prats, M.: "Thermal Recovery," *SPE Monograph Series* SPE of AIME (1982).

[2] Boberg, T.C.: "Thermal Methods of Oil Recovery," *An Exxon Monograph Series* (1988).

[3] Matalon, M. and Matkowsky, B.J.: "Flames as Gasdynamic Discontinuities," *J. Fluid Mech.* (1982) **124** 239-259.

[4] Pelcé, P.: "Dynamics of Curved Fronts," *Academic Press* (1988).

[5] Aldushin, A.P. and Matkowsky, B.J.: "Instabilities, Fingering and the Saffman-Taylor Problem in Filtration Combustion," *Combust. Sci. and Tech.* (1998) **133**.

[6] Li, X. and Yortsos, Y.C.: "Bubble Growth and Stability in an Effective Porous Medium," *Phys. Fluids* (1994) **6** No.5 1663-77.

[7] Schult, D.A., Matkowsky, B.J., Volpert, V.A., and Fernandez-Pello, A.C.: "Forced Forward Smolder Combustion," *Combust. and Flame* (1996) **104** 1-26.

[8] Schult, D.A., Bayliss, A. and Matkowsky, B.J.: "Traveling Waves in Natural Counterflow Filtration Combustion and Their Stability," *SIAM J. Appl. Math.* (1998) **58** No.3 806-852.

[9] Gottfried, B.S.: "A Mathematical Model of Thermal Oil Recovery in Linear Systems," *SPEJ* (1965) 196-210.

[10] Beckers, H.L. and Harmsen, G.J.: "The Effect of Water Injection on Sustained Combustion in a Porous Medium," *SPEJ* (1970) 231-49.

[11] Burger, J.G. and Sahuquet, B.C.: "Chemical Aspects of *In Situ* Combustion — Heat of Combustion and Kinetics," *SPEJ* (1972) 54-66.

[12] Ağca, C. and Yortsos, Y.C.:"Steady-State Analysis of *In Situ* Combustion," Paper SPE 13624, presented at California Regional Meeting of SPE, Bakersfield, 447-362 (March 27-29 1985).

[13] Armento, M.E. and Miller, C.A.: "Stability of Moving Combustion Fronts in Porous Media," *SPEJ* (1977) 423-430.

[14] Britten, J.A. and Krantz, W.B.: "Linear Stability of Planar Reverse Combustion in Porous Media," *Combust. and Flame.* (1985) **60** 125-240.

[15] Britten, J.A. and Krantz, W.B.: "Asymptotic Structure of Planar Nonadiabatic Reverse Combustion Fronts in Porous Media," *Combust. and Flame.* (1986) **65** 151-161.

[16] Lu, C. and Yortsos, Y.C.: To be submitted.

[17] Zik, O. and Moses, E.: "Fingering Instability in Combustion: An Extended View," *Physical Rev. E* (1999) **60** 1518-1531.

[18] Yortsos, Y.C. and Gavalas, G.R.: "Heat Transfer Ahead of Moving Condensation Fronts in Thermal Oil Recovery Processes," *Int. J. Heat Mass Transfer* (1982) **305** No.3 305-316.

[19] Martin, W.L., Alexander, J.D. and Dew, J.N.: "Process Variabes of In Situ Combustion," *Petroleum Trans.* AIME (1958) **213** 28-35.

[20] Mamora, D.D. and Brigham, W.E.: "Implications of Low Temperature oxidation in Kinetic and Combustion Tube Experiments," UNITAR 6th. Symposium on Heavy Oil and Tar Sands (1995).

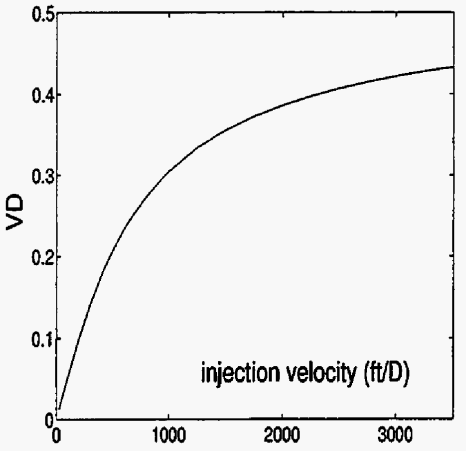

Figure 7: Front Velocity versus Injection Velocity

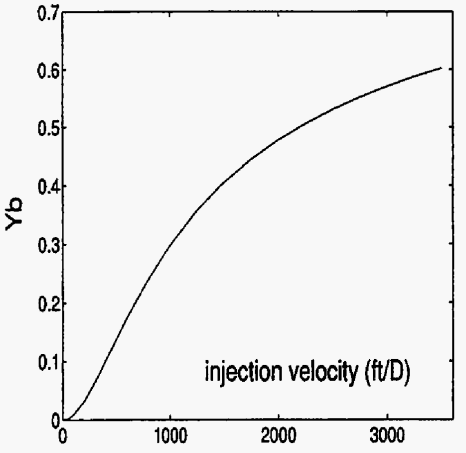

Figure 8: Unburned Oxygen Concentration versus Injection Velocity

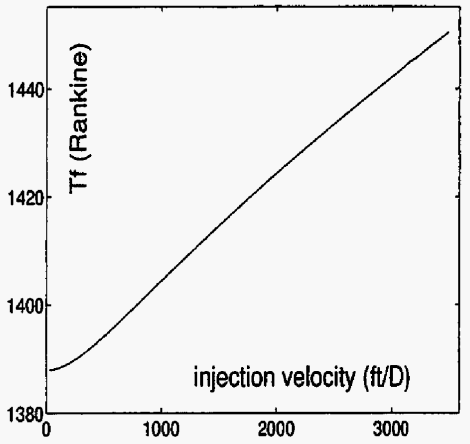

Figure 9: Front Temperature versus Injection Velocity

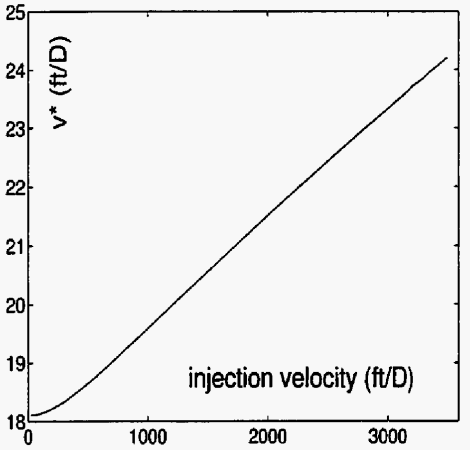

Figure 10: Reference Velocity versus Injection Velocity

IV. INSTABILITIES, HETEROGENEITY AND UPSCALING

Displacements of heavy oil are typically subject to viscous instabilities, given the adverse mobility ratio in most such applications. While viscous instabilities are well understood, their interaction with heterogeneity is not. In this section we report on a study which addresses the effect of a longitudinal heterogeneity in permeability on the stability of displacements with non-monotonically varying mobility. While the study nominally addresses miscible displacement in the absence of dispersion, it also applies by a simple extension to immiscible displacements, where non-monotonicity in mobility is the result of relative permeabilities. A non-trivial effect is found from the interaction of these two effects. Experimental work is under way with collaborators from the University of Paris, to test the theory. The section also reports on a project supported by this contract on the identification of the permeability heterogeneity of a porous medium by the injection of a passive tracer. It is worthwhile pointing out that this method is based on direct inversion, and also allows the estimation of the components of the permeability tensor in anisotropic porous media. Continuous on-going work is being done on the interaction between instabilities and heterogeneities and on the upscaling of unstable processes.

DISPLACEMENT IN HETEROGENEOUS POROUS MEDIA WITH NON-MONOTONIC PROFILES: STABILITY ANALYSIS

Maryam Shariati and Yanis C. Yortsos

INTRODUCTION

Almost without exception, porous media are heterogeneous both at the Micro-scale (pore-scale) and the macro-scale. Fluid displacements will consequently be affected by this heterogeneity. Currently, simulation of flow and displacements in porous media is invariably based on heterogeneous permeability fields, the influence of which on flow and transport has been found to be fundamental. In this paper we address a specific aspect, namely the effect of permeability heterogeneity in porous media on the stability of displacement fronts. We will show that interesting results are to be found when the profile is non-monotonic.

In the conventional stability analyses of displacement processes the porous medium is assumed to be homogeneous. The typical problem posed is to examine the frontal stability of a slightly perturbed base-state, the perturbation being imposed either externally or as a result of small fluctuations in permeability. In this sense, the analysis of the problem is similar to the classical Saffman-Taylor [1] problem of displacement in a homogeneous Hele-Shaw cell. As is well known, in the absence of gravity, and in the long-wave limit, displacements are stable, if the ratio of the end-point viscosities is smaller than one, $M = \frac{\mu_1}{\mu_2} < 1$, and unstable, otherwise. Here, subscripts 1 and 2 refer to the initial (downstream) and injected (upstream) fluids, respectively. Viscous Fingering (VF) emerges as the unstable pattern under conditions of instability.

Heterogeneity will interfere both with the onset and the development of the instability. Many numerical studies have focused on its effect on fully-developed instability. Based on numerical simulations, Waggoner and Lake [2] classified fully-developed displacement patterns in three regimes, Viscous Fingering, Dispersion and Channeling, depending on the values of M, the variance and the correlation length of the heterogeneity. In this classification VF is the unstable regime when both the variance and the correlation lengths are very small. Analogous ideas were expressed in an earlier work by Araktingi and Orr [3]. In these studies,

heterogeneity is modeled as a stationary, spatially correlated random field. Many studies since have expanded on the properties of these regimes.

The fully-developed interplay between heterogeneity and viscous instability has also been addressed analytically. Welty and Gelhar [4] derived effective equations for miscible displacements (including gravity) based on small-perturbation theory. They showed that a convection-dispersion equation is applicable when displacements are long-wave stable, but that in the unstable case the effective dispersion coefficient diverges with time. Lenormand [5] proposed a model that captures instability and heterogeneity through the additive contributions of a modified convective term, that follows the empirical Koval model, and of a dispersion term that follows the Gelhar and Axness [4] passive tracer dispersion. Recently, Zhang and co-workers [6] have applied small perturbation theory to a variety of displacement processes to derive equations for ensemble-averaged quantities.

The effect of heterogeneity on the stability of displacement fronts has also been considered. Using numerical simulation, Tan and Homsy [7] inferred that resonance between the most dominant wavelength of the instability, as determined by a stability analysis in a homogeneous medium, and the heterogeneity can enhance the instability. This idea was revisited several years later by de Wit and Homsy [8], [9], who provided a stability analysis of miscible displacement with dispersion in a sinusoidal, periodic permeability field. Using a small amplitude expansion they showed that unstable wavelengths are amplified when they are in resonance with the underlying heterogeneity, the effect being largest at higher values of M and when the heterogeneity is transverse to the direction of displacement, for example in a displacement in a layered system, where the layers are parallel to the main flow direction. Numerical evidence confirming these results was reported in Chen and Meiburg [10]. Essentially the opposite case, where the displacement is in a direction perpendicular to a layered system, was studied numerical by Chen and Neuman [11]. These authors investigated the stochastic evolution of instabilities of a wetting front in a random permeability field.

In this paper we consider the latter problem but in the context of miscible displacement. Miscible displacements find applications in various areas such as enhanced oil recovery, channeling in packed columns and in-situ solvent injection techniques for groundwater remediation. The specific question we address is what is the effect of a longitudinal variation in

permeability on the stability of displacement fronts. Heterogeneity is assumed only in the direction of displacement, as would be the case in displacements perpendicular to a layered system (Figure 1). This restriction is made in order to isolate a specific heterogeneity effect, although applications involving displacements under such conditions are not uncommon in natural porous media and soils, many of which are layered. The analysis follows the asymptotic approach of Hickernell and Yortsos [12] for uncovering the stability of perturbations of long- and short- wavelengths. Although this approach assumes the absence of dispersion, the latter can be readily incorporated in the results, as described in Loggia et al [17].

We find the surprising result that longitudinal heterogeneity can affect qualitatively (in addition to quantitatively) the long-wave instability. Namely, we find that displacements which are predicted to be either stable or unstable, based on end-point stability criteria (such as the Saffman-Taylor), can in fact become unstable or stable, respectively, by appropriate changes in permeability. A particularly simple such variation is a sudden discontinuity in the permeability. Interestingly, in the absence of gravity, this change of stability occurs only if the base-state mobility profile is non-monotonic (otherwise, the effect is only quantitative, there being no change of sign on the rate of growth of the disturbance). However, in the presence of gravity, the effect exists for monotonic profiles as well. This effect is not due to the change in the total mobility, but rather arises from the fact that mobility is concentration-dependent, hence it can be convected, in contrast to the permeability heterogeneity, which remains frozen. We note that non-monotonic mobility profiles arise in various applications, for example in oil recovery as a result of the dependence of the total mobility in immiscible displacement on relative permeabilities (Chikhliwala et al. [14]), and in in-situ solvent injection for soil remediation due to the non-monotonic dependence of viscosity on the local concentration [15]. The stability of non-monotonic profiles in porous media has been analyzed by Manickam and Homsy [16] (see also Loggia et al. [17]). In a sense this chapter extends the discussion of non-monotonic profiles, but now at the macro-scale, where flow in the porous medium is assumed to obey Darcy's law.

FORMULATION

Consider the miscible displacement of fluid 1 by fluid 2 at constant rate q_T, in a layered

system of constant porosity ϕ, in a direction x perpendicular to the heterogeneity, as shown in Fig. 1. Without loss in generality, the displacement can be characterized by the concentration (volume fraction) of the injected fluid, C, which we take to be equal to 1 at injection and 0 initially. Viscosities and densities are functions of C. We follow Hickernell and Yortsos [12] and write in the absence of diffusion, dispersion and gravity

$$\nabla \cdot \mathbf{q} = 0 \tag{1}$$

$$\mathbf{q} = -\frac{k(x)}{\mu}\nabla P \tag{2}$$

$$\phi\frac{\partial C}{\partial t} + \mathbf{q}\cdot\nabla C = 0 \tag{3}$$

where $\mathbf{q}$ is the flow velocity, P is the pressure, $k(x)$ the permeability of the porous medium, varying in the direction of displacement x and $\mu(C)$ is the fluid viscosity, a function of concentration, to be specified in more detail below. Effects of density are also described in a later section. Under the above assumptions, there exists an one-dimensional base-state satisfying

$$(q_T - \phi v)\frac{dC}{d\xi} = 0 \tag{4}$$

in terms of the moving coordinate $\xi = x - vt$, where

$$v = \frac{q_T}{\phi} \tag{5}$$

In view of (5), equation (4) admits an arbitrary solution for the base-state concentration profile. In fact, however, the analysis can be extended to account for the effect of dispersion, by separately including longitudinal dispersion in the base state, and transverse dispersion in the perturbation, as suggested by Loggia et al. [17], as will be further elaborated below (Figure 1b). Hence, without loss in generality, we can assume that the base state concentration has an erfc-type profile, and this will indeed be used in the numerical simulations below. The base state viscosity profile varies according to the specified viscosity-concentration relation. A schematic, that accounts for a non-monotonic dependence, is shown in Fig. 1c.

We next introduce appropriate dimensionless variables, denoted by subscript D, and transform the equations in dimensionless moving coordinates

$$\nabla\cdot(\frac{k_D}{\mu_D}\nabla P_D) = 0 \tag{6}$$

$$\mathbf{q}_D = -\frac{k_D}{\mu_D}\nabla P_D \tag{7}$$

$$\frac{\partial C_D}{\partial t_D} + (\mathbf{q}_D - \mathbf{i})\cdot\nabla C_D = 0 \tag{8}$$

where $\mathbf{i}$ is the unit vector in the x direction. Then, we perform a linearized stability analysis by taking small perturbations and normal modes. Denoting the base state by overbar and dropping the subscript D for convenience, we have

$$C = \bar{C}(\xi) + c\exp(i\alpha y + \omega t) \tag{9}$$

$$P = \bar{P}(\xi) + p\exp(i\alpha y + \omega t) \tag{10}$$

$$\mu = \bar{\mu}(\xi) + \frac{d\bar{\mu}}{dC}c\exp(i\alpha y + \omega t) \tag{11}$$

where α and ω denote the wavenumber and rate of growth of the disturbance, respectively. Substitution in the governing equations and linearization leads after some manipulations to the following equation

$$\frac{d}{d\xi}\left[\frac{k}{\bar{\mu}\left(\omega - \frac{d\ln\bar{\mu}}{d\xi}\right)}\frac{dp}{d\xi}\right] - \frac{\alpha^2 kp}{\bar{\mu}\omega} = 0 \tag{12}$$

To further proceed, we introduce the streamfunction perturbation ψ, defined by

$$\frac{d\psi}{d\xi} = \frac{kp}{\bar{\mu}} \tag{13}$$

Substitution in (12) and integration leads to the final equation

$$\frac{d}{d\xi}\left[\frac{\mu}{k}\frac{d\psi}{d\xi}\right] = \frac{\alpha^2}{\omega}\left[\frac{\mu}{k}\omega - \frac{1}{k}\frac{d\mu}{d\xi}\right]\Psi \tag{14}$$

where for simplicity we also removed the overbar from the base-state viscosity profile. This is the final eigenvalue problem to be solved. Before we proceed, we make the following remarks:

1. In the above k is a function of the moving coordinate ξ, where the tacit assumption was made that the permeability is frozen during the subsequent evolution of the perturbation. Freezing of the base-state is a common assumption in related stability problems (for example, see Tan and Homsy [18]).

2. The effect of permeability does not enter in the eigenvalue problem solely as a total mobility (k/μ) effect, but there is a decoupling of the two mobility contributions (of k and of μ). This reflects the fact that viscosity is only a function of concentration, the perturbation of which is convencted with the flow and also diffuses, while the permeability heterogeneity is position-dependent only.

3. The above can be modified to account for transverse (but not longitudinal) dispersion, which exerts a stabilizing effect. Indeed, by following a similar analysis as in Loggia et al. [17], we can show that accounting for lateral diffusion is equivalent to making in (14) the substitution

$$\omega \to \omega + D_T \alpha^2 \tag{15}$$

where D_T is a normalized transverse dispersion coefficient. In this approximation, transverse dispersion can be linearly added to the solution of the eigenvalue problem (14). On the other hand, incorporating longitudinal dispersion will raise the order of the eigenvalue problem to fourth (e.g Tan and Homsy [18], Manickam and Homsy [16]), and will not be considered here.

In the subsequent we will provide asymptotic solutions of (14) in the two limits of small and large α, respectively, which will be verified by the full numerical solution of the problem.

Asymptotic Analysis at Large Wavelengths

We follow an a analysis similar to Hickernell and Yortsos [12]. We consider the limit

$$\sigma = \alpha^2/\omega \to 0 \tag{16}$$

and take the expansion

$$\alpha = \alpha_1\sigma + \alpha_2\sigma^2 + \cdots \tag{17}$$

from which it follows that

$$\omega = \alpha_1\alpha + \frac{\alpha_2}{\alpha_1}\alpha^2 + \cdots \tag{18}$$

In this limit we consider an inner region, $|\xi| \ll \alpha^{-1}$, and two outer regions, $|\xi| \gg \ln\omega$. The solution in the inner region is denoted $\tilde{\psi}$ and in the outer $\hat{\psi}^{(s)}$, where s is the sign variable ($\pm$). We then expand all in terms of powers of σ

$$\tilde{\psi} = \tilde{\psi}_0 + \sigma\tilde{\psi}_1 + \sigma^2\tilde{\psi}_2 + \cdots \tag{19}$$

$$\hat{\psi}^{(s)} = \hat{\psi}_0^{(s)} + \sigma\hat{\psi}_1^{(s)} + \sigma^2\hat{\psi}_2^{(s)} + \cdots \tag{20}$$

Under the assumption that the permeability approaches constant far-field values k_s, in the far fields, which will be assumed here, the outer solutions are exponential functions

$$\hat{\psi}_j^{(s)} = \hat{\psi}_{j\infty}^{(s)}\exp(-s\alpha\xi) \tag{21}$$

The inner expansion has a leading-order solution which is constant,

$$\tilde{\psi}_0 = 1 \tag{22}$$

and a first-order solution which reads after one integration

$$\frac{\mu}{k}\frac{d\tilde{\psi}_1}{d\xi} = -\frac{\mu}{k} + \int_0^{\xi}\mu\frac{dk^{-1}}{d\xi}d\xi + K_1 \tag{23}$$

Expanding (21) and matching with (22) and (23) allows the determination of α_1 (and K_1). The result reads

$$\alpha_1 = \frac{\frac{\mu_+}{k_+} - \frac{\mu_-}{k_-} + \int_{-\infty}^{\infty}\frac{\mu}{k^2}\frac{dk}{d\xi}d\xi}{\frac{\mu_+}{k_+} + \frac{\mu_-}{k_-}} \tag{24}$$

and

$$K_1 = \frac{(\alpha_1 + 1)\mu_-}{k_-} + \int_{-\infty}^{0} \mu \frac{dk^{-1}}{d\xi} d\xi \tag{25}$$

Equation (24) can also be re-written as

$$\alpha_1 = \frac{\int_{-\infty}^{\infty} \frac{1}{k} \frac{d\mu}{d\xi} d\xi}{\frac{\mu_+}{k_+} + \frac{\mu_-}{k_-}} \tag{26}$$

Working likewise for the higher-order terms, we can determine the next order in the expansion. The final result is

$$\alpha_2 = -\frac{(I + 2M_+)(I - 2M_-)}{(M_+ + M_-)^3} \int_{-\infty}^{\infty} \frac{kH}{\mu} d\xi \tag{27}$$

where

$$H = \left[\frac{\mu}{k} + \frac{M_-(I + 2M_+)}{I - 2M_-} - \frac{M_+ + M_-}{I - 2M_-} \int_{-\infty}^{\xi} \frac{\mu}{k^2} \frac{dk}{d\xi} d\xi \right] \left[\frac{\mu}{k} - M_- + \frac{M_+ + M_-}{I + 2M_+} \int_{-\infty}^{\xi} \frac{\mu}{k^2} \frac{dk}{d\xi} d\xi \right] \tag{28}$$

and where we defined the far-field inverse mobilities $M_s = \frac{\mu_s}{k_s}$ and the integral $I = \int_{-\infty}^{\infty} \frac{\mu}{k^2} \frac{dk}{d\xi} d\xi$. From an analysis of (24) we remark the following:

1. In the case of a homogeneous medium, Equation (24) reduces to the well-known result

$$\alpha_1 = \frac{\mu_+ - \mu_-}{\mu_+ + \mu_-} = \frac{M - 1}{M + 1} \tag{29}$$

as expected.

2. The effect of heterogeneity on the long-wave limit is due to the additional term $\int_{-\infty}^{\infty} \frac{\mu}{k^2} \frac{dk}{d\xi} d\xi$. As shown in (24) and (26), this is not merely a total mobility effect. Compared to the end-point mobility values, instability is enhanced if permeability increases in the direction of displacement, and weakened in the opposite case. However, equation (26) indicates that this effect remains quantitative, namely it does not affect the sign of α_1, if the base-state viscosity profile is monotonic, in which case the derivative of viscosity has a constant sign.

3. The effect can be non-trivial when the base-case viscosity is non-monotonic, in which case, an appropriate form of heterogeneity may lead to a change in the sign of α_1 from what is predicted based on the end-point ratio (29).

4. It must be also noted that as in [12] in the absence of dispersion, the eigenvalue problem admits an infinite family of eigenvalues, one of which scales with α in the long-wave limit, all others scaling with α^2. In the presence of dispersion, however, the latter become sub-dominant, and it is only the mode scaling with α that dominates the system response.

A simple example that demonstrates the heterogeneity effect corresponds to the case of a variable mobility profile and a sharp discontinuity in permeability at $\xi = 0$, where the expression for α_1 becomes

$$\alpha_1 = \frac{\left(\frac{\mu_0-\mu_-}{k_-} - \frac{\mu_0-\mu_+}{k_+}\right)}{\frac{\mu_+}{k_+} + \frac{\mu_-}{k_-}} \tag{30}$$

where $\mu_0 = \mu(\xi = 0)$. Now, for an end-point unstable displacement, $M = \frac{\mu_+}{\mu_-} > 1$, and a non-monotonic profile with $\mu_0 > \mu_-, \mu_+$, the displacement will actually be stabilized if the permeability decreases in the direction of displacement, such that

$$\frac{k_-}{k_+} > \frac{\mu_0 - \mu_-}{\mu_0 - \mu_+} > 1 \tag{31}$$

Conversely, for an end-point stable displacement, $M = \frac{\mu_+}{\mu_-} < 1$, and a similar non-monotonic profile, the displacement will actually be destabilized if the permeability increases in the direction of displacement, such that

$$\frac{k_+}{k_-} > \frac{\mu_+ - \mu_0}{\mu_- - \mu_0} > 1 \tag{32}$$

Additional numerical results will be shown below. A similar analysis of α_2 is not as easy, due to its complex dependence, and requires a numerical evaluation. Before we proceed, however, we will briefly comment on the short-wave limit.

Asymptotic Analysis at Small Wavelengths

By following the analysis of Hickernell and Yortsos [12], it can be readily shown that in the limit of small wavelengths and in the absence of dispersion, the largest eigenvalue of the rate of growth ω_{max} is dictated by the maximum in the logarithmic derivative of the viscosity profile, namely

$$\omega_{max} = \max\left[\frac{d\ln\mu}{d\xi}\right] \tag{33}$$

This result is *independent* of the heterogeneity and suggests instability any time the base state has a segment of increasing viscosity, as is the case with a non-monotonic profile. Of course, transverse dispersion, which scales at large α (small wavelengths) as $-D_T\alpha^2$ (compare with (15), will dominate over (33) in this limit. Thus, in its presence, the most dominant wavelength is approximately the one corresponding to the maximum of $\omega(\alpha) - D_T\alpha^2$, where $\omega(\alpha)$ is the solution of the dispersionless eigenvalue problem (14). Thus, the effect of a longitudinal heterogeneity in permeability on the stability is a long-wave effect.

NUMERICAL RESULTS

To verify the analytical predictions, the eigenvalue problem (14) was solved numerically using a shooting method as described in Chikhliwala et al. [14]. For convenience we considered a dispersion-like base-state concentration profile

$$C = \frac{1}{2}\mathrm{erfc}(\xi) \tag{34}$$

and the non-monotonic model of Manickam and Homsy, the parameters of which are the ratio in end-point viscosities, M, and the maximum (or minimum) viscosity. To model a monotonic change in permeability we took the two-parameter model

$$k = 1 + a\tanh\left(\frac{\xi}{b}\right) \quad ; \quad -1 < a < 1 \tag{35}$$

where $a > 0$, or $a < 0$, indicates a permeability increase, or decrease, respectively, and b scales the region over which a permeability change occurs.

We first show the predictions from the asymptotic analysis. Fig. 2-3 shows the variation of α_1 as a function of a for the case $b = 1$ and for two different base-state viscosity profiles, one corresponding to an end-point stable displacement ($M = 0.2 < 1$) (Fig. 2), and another to an end-point unstable displacement ($M = 5 > 1$) (Fig. 3), respectively. The base-state profiles are also shown in the respective figures. We note that the large intermediate viscosity values in these examples were only taken for convenience and are not indicative

of any strong restriction on viscosity. As predicted, heterogeneity can alter the end-point predictions: For the stable end-point case ($M = 0.2$), the displacement becomes unstable above a critical value of $a = 0.5$. Conversely, for the unstable end-point case ($M = 5$), there is a corresponding critical value $a = -0.5$, below which the displacement is stabilized.

These predictions were tested against the numerical solution of the eigenvalue problem. These predictions were tested against the numerical solution of the eigenvalue problem. Fig. 4 shows the full dispersion relation $\omega(\alpha)$ for the case $M = 0.2$ and $a = 0.5$, for which the asymptotic theory predicts instability ($\alpha_1 = 0.3366$). Clearly, the theory is in good agreement with the numerical solution. At small α, the behavior is linear, with a slope close to the predicted, while the large α behavior asymptotes the limiting value (33), which for this particular example is 0.9671. Fig. 4 shows the full dispersion relation $\omega(\alpha)$ for the case $M = 5$ and $a = -0.7$, for which the present long-wave theory predicts stability ($\alpha_1 = -0.1613$). The corresponding curve in Fig. 5 is the one corresponding to the smallest eigenvalue ω, as noted above. It is shown to satisfy well the theoretical predictions.

We have also numerically studied the stability of various other forms of longitudinal heterogeneity, including sinusoidal and random perturbations. The results obtained were consistent with the previous analysis. Heterogeneity affects the stability only as long as it is coupled with mobility changes (compare with (24) or (26)). For example, in the case where the viscosity varies in the range ξ_-, ξ_+, then equation (24) becomes

$$\alpha_1 = \frac{\left(\frac{\mu_+}{k(\xi_+)} - \frac{\mu_-}{k(\xi_-)} + \int_{-\xi_-}^{\xi_+} \frac{\mu}{k^2}\frac{dk}{d\xi}d\xi\right)}{\frac{\mu_+}{k_+} + \frac{\mu_-}{k_-}} \tag{36}$$

Multiple changes in permeability (for example a two-step variation) tend to enhance the effect considered, if both steps are in the same direction and to diminish it otherwise.

A MECHANISTIC INTERPERTATION

For a mechanistic interpretation of this interesting heterogeneity effect we consider the vortices formed at large wavelengths. It is in this limit, where the effect of longitudinal heterogeneity is strongest, as found above, and where we can benefit from the asymptotic analysis. At large wavelengths, there is a single row of (either stabilizing or destabilizing)

vortices formed. The center of each vortex is the place where the streamfunction is maximum, which from (23) is the place ξ^* where

$$-\frac{\mu^*}{k^*} + \int_0^{\xi^*} \mu \frac{dk^{-1}}{d\xi} d\xi + K_1 = 0 \tag{37}$$

To understand the effect of heterogeneity in a non-monotonic viscosity profile, consider, first, a homogeneous displacement. Then, use of (25) in (37) leads to

$$\mu^* = \frac{2\mu_-\mu_+}{\mu_- + \mu_+} \tag{38}$$

namely the vortex center is at the place where the viscosity is the harmonic average of the end point viscosities, or, equivalently, where the mobility is the arithmetic average of the end-point mobilities. This interesting result is independent of whether or not the profile is non-monotonic. Consider, next, a heterogeneous field with a sharp discontinuity at $\xi = 0$, for the sake of simplicity. The vortex center will shift as a function of the imposed heterogeneity. By a simple manipulation of (37) and (25), it is shown that the new position is determined from the following two equations: If $\xi^* < 0$, then

$$M^* = \frac{2(M - a(M - M_0))}{M + 1 - a(M - 1)} \tag{39}$$

and if $\xi^* > 0$, then

$$M^* = \frac{2M(1 + a - M_0 a)}{M + 1 - a(M - 1)} \tag{40}$$

where we defined $M^* = \frac{\mu^*}{\mu_-}$ and $M_0 = \frac{\mu_0}{\mu_-}$. As a varies, the vortex center, hence the corresponding M^*, moves along the base-state profile, in a direction determined from the two parameters M and M_0. Interestingly, the different branches of the non-monotonic profile (where there exists multiplicity of viscosity, for example the regions $\xi < 0$ and $\xi > 0$ in the profiles of Fig 2) are reached by different forms of heterogeneity. Indeed, M_0 is the limit of both (39) and (40), however it is reached from the left ($\xi \to 0_-$, equation (39)) when $a \to 1$ and from the right ($\xi \to 0_+$, equation (40)) when $a \to -1$.

To be more concrete, consider non-monotonic profiles of the type shown in Fig. 2, and take first, the case of an end-point stable displacement, where $M < 1$ but $M_0 > 1 > M$

(Fig. 6a). In the homogeneous case ($a = 0$), M^* is the harmonic average of 1 and M, and consequently the vortex center is located somewhere in $\xi > 0$ (point I in Fig. 6a). As a decreases to negative values, the vortex center shifts in the direction of increasing μ, which here is the direction of decreasing ξ (points I to O in Fig. 6a). However, we can show that it always stays in the branch corresponding to $\xi > 0$, namely that which has a decreasing viscosity in the direction of displacement. Indeed, equation (40) shows that $M^* \leq M_0$ as a decreases, the equality reached in the limit $a \to -1$ (where $k_+ \to 0$). Because the vortex remains in a region of decreasing mobility in the direction of displacement, the displacement remains stable (see below for further elaboration of this point). On the other hand, when a increases to positive values, the vortex center shifts in the opposite direction of decreasing μ, which is now the direction of increasing ξ (points I to P_∞ in Fig. 6a). Larger values of a result in the vortex moving further to the right. If large-wvalength instability conditions do not hold, namely if the profile is monotonic, $M_0 < 1$, the vortex center will reach a limiting point (P in Fig. 6a) where $M^* = M(2 - M_0)$, and the displacement remains stable. However, if the profile is non-monotonic, the vortex moves further and further away, as a increases, and at the limiting value

$$a_\infty = \frac{1 - M}{2M_0 - M - 1} \tag{41}$$

it approaches P_∞. This moving away from the region where mobility changes occur, weakens the stabilizing influence of the profile and at the limiting point the displacement is neutrally stable. As can be shown by a direct comparison with (30)-(32), this is the point where heterogeneity qualitatively affects the stability ($\alpha_1 = 0$) and renders the displacement unstable. From this point on, further increases in a can only be accomodated if the vortex center jumps to the other branch of the profile, where now an increase in a makes the vortex center to move in the direction from M_∞ to O (Fig. 6a). Since the vortex resides in the region where the viscosity increases in the direction of displacement, the displacement is now unstable.

A similar interpretation holds for the other case, where the displacement is end-point unstable ($M > 1$ with $M_0 > M > 1$, Fig. 6b). In the homogeneous case ($a = 0$), the vortex is located somewhere in $\xi < 0$ (point I in Fig. 6b). As a increases, the vortex center shifts in the direction of increasing μ, which here is the direction of increasing ξ (points I

to 0 in Fig. 6b). As with the analogous case, the vortex always stays in the branch with $\xi < 0$, namely that with increasing viscosity in the direction of displacement, the value M_0 being approached in the limit $a \to 1$ (where $k_- \to 0$). Because the vortex remains in a region of increasing mobility, the displacement remains unstable. On the other hand, when a decreases to negative values, the vortex shifts in the opposite direction of decreasing μ, which is now the direction of decreasing ξ (points I to M_∞ in Fig. 6b). If the profile is monotonic, $M_0 < M$, the vortex center will reach a limiting point M*, where $M^* = 2 - \frac{M_0}{M}$, and the system remains unstable. However, if the profile is non-monotonic, the vortex moves further and further away, as a decreases, and at the limiting value a_∞, it approaches M_∞. Again, this moving away from the region where mobility changes occur, weakens the destabilizing influence of the profile and at the limiting point the displacement is neutrally stable. From this point on, further increases in a can be accomodated if the vortex center jumps to the other branch of the profile, where now a decrease in a makes the vortex center to move in the direction from P_∞ to O (Fig. 6b). Since the vortex resides in the region where the viscosity decreases in the direction of displacement, the displacement is now stable.

A few additional remarks are needed to strengthen the above arguments. First, we need to show that vortices in a region of decreasing viscosity profiles are stabilizing, and vice versa. For this we borrow arguments similar to Manickam and Homsy [19] (although in this long wavelength limit, there is only one row of vortices in contrast to the pair of rows considered in the short wave analysis of Manickam and Homsy). In the region of decreasing viscosity in the direction of displacement, any two adjacent counter rotating vortices bring low viscosity fluid from the downstream to the upstream direction and high viscosity fluid from the upstream to the downstream direction (Fig. 7a). This will increase the flow resistance in the direction of the basic flow and will lower it where flow is not preferred, thus stabilizing the flow. Conversely, in the region of increasing viscosity in the direction of displacement, two adjacent vortices will bring high viscosity fluid from the downstream to the upstream direction and low viscosity fluid from the upstream to the downstream direction (Fig. 7b). This will decrease the flow resistance in the direction of the basic flow and will increase it where flow is not preferred, thus further destabilizing the flow.

It is of interest to note that the previous arguments also hold when the base-state profile

has more complex non-monotonic segments in the two regions considered. For example, for the profile shown in Fig. 8a, which is the counterpart of Fig. 6a, application of the previous arguments and equations (39) and (40) shows that the vortex center will move in a monotonic fashion following the arrows indicated, thereby bypassing the regions of multiplicity. Likewise for the profile of Fig. 8b. We note an interesting hysteretic feature in the way the base-state profile is visited, which is dictated by the overall features of the displacement. This is probably worth of future analysis.

To demonstrate the previous analysis we plot a single vortex as obtained from the numerical solution of the eigenvalue problem for a fixed value of the wavenumber ($\alpha = 0.001$) and for two different cases. Fig. 9 shows three snapshots corresponding to the end-point stable profile of Fig. 6a (where $M = 0.2$ and $M_0 = 3$) for three different values of a (0,-0.5 and 0.5). Here, $a_\infty = 0.1667$, thus the second case corresponds to stable displacement, while the last case to unstable displacement. It is clear from Fig. 9 that the vortex shifts to the left as a decreases and that for $a > a_\infty$, it jumps to the destabilizing branch $\xi < 0$. Conversely, the case corresponding to an end-point unstable profile is shown in Fig. 10 (where $M = 5$ and $M_0 = 10$) for $a = 0$, -0.5 and 0.5. The first two values of a correspond to unstable displacement, while the last to a stabilized displacement. It is clear that the vortex stays in the unstable branch for the first two cases, moving in the direction predicted from above, while it jumps to the stabilizing branch in the latter case, as a decreases below the limiting value $a_\infty = -0.2857$.

EFFECT OF GRAVITY

The above analysis can be readily extended to account for effects of gravity, when the density is allowed to vary with concentration. We consider the case in which gravity acts only in the direction of displacement, as for example, in 2-D inclined systems, where the transverse direction,-y, is the horizontal. The analysis also covers the important case of a vertically stratified system, where the displacement occurs in the vertical direction.

When density is a function of concentration the governing mass and momentum equations are given by

$$\frac{\partial \rho}{\partial t} + \nabla \cdot (\rho \mathbf{q}) = 0 \tag{42}$$

$$\mathbf{q} = -\frac{k}{\eta}(\nabla P - \rho \mathbf{g}), \tag{43}$$

where g is the acceleration of gravity and ρ the density of fluid. We proceed as before and in parallel with [12]. After considerable manipulations, the final eigenvalue problem reads

$$\frac{d}{d\xi}\left[\frac{\mu}{k}\frac{d\psi}{d\xi}\right] = \frac{\alpha^2}{\omega}\left[\frac{\mu}{k}\omega - \frac{1}{k}\frac{d\mu}{d\xi} + G\frac{d\rho}{d\xi}\right]\Psi \tag{44}$$

where all variables are dimensionless, the density is normalized with a reference density ρ_0, and we have defined the gravity number $G = \frac{k_0 \rho_0 g_x}{q_T \mu_-}$. Proceeding as before, we can obtain the solution of (44) in the two asymptotic limits of small and large α.

In the limit of small α, the leading coefficient α_1 is given by

$$\alpha_1 = \frac{\left(\frac{\mu_+}{k_+} - \frac{\mu_-}{k_-} - G(\rho_+ - \rho_-) + \int_{-\infty}^{\infty} \frac{\mu}{k^2}\frac{dk}{d\xi}d\xi\right)}{\left(\frac{\mu_+}{k_+} + \frac{\mu_-}{k_-}\right)} \tag{45}$$

where $(\rho_+ - \rho_-)$ is the normalized density difference of the initial to the injected fluid. We note that heterogeneity can have an important effect on the onset of instability, which in its absence will occur when $M - 1 - G(\rho_+ - \rho_-) = 0$. However, unlike the previous case, a qualitative effect and the change of the sign of α_1 do not necessarily require that the viscosity profile is non-monotonic. This can be readily seen by rewriting (45) as

$$\alpha_1 = \frac{\int_{-\infty}^{\infty}\left[\frac{1}{k}\frac{d\mu}{d\xi} - G\frac{d\rho}{d\xi}\right]d\xi}{\left(\frac{\mu_+}{k_+} + \frac{\mu_-}{k_-}\right)} \tag{46}$$

Then, it is the variable $\mu - G\int k d\rho$ that plays the role of an effective viscosity profile (compare with (26)), and which, therefore, can become non-monotonic by a suitable choice of G, k or ρ. We will illustrate this effect with a simple example shortly below. For completeness, we also give the asymptotic result for the short wave limit. Here,

$$\omega_{max} = \max\left[\frac{d\ln\mu}{d\xi} - G\frac{k}{\mu}\frac{d\rho}{d\xi}\right] \tag{47}$$

It is clear that in the presence of gravity, heterogeneity will also affect the short-wave rates of growth. However, in view of the dominant effect of dispersion in that limit, we elect to not consider this limit any further.

We demonstrate the longitudinal heterogeneity effect by considering a step change in permeability at $\xi = 0$ and a monotonic viscosity profile, in which case (45) reads

$$\alpha_1 = \frac{\left(\frac{\mu_0-\mu_-}{k_-} - \frac{\mu_0-\mu_+}{k_+} - N\right)}{\left(\frac{\mu_+}{k_+} + \frac{\mu_-}{k_-}\right)} \tag{48}$$

where we introduced $N = G(\rho_+ - \rho_-)$. For simplicity, we will consider an exponential viscosity dependence on concentration (see Chen and Meiburg [10], de Wit and Homsy [8], [9]), which allows us to identify $\mu_- = 1$, $\mu_+ = M$ and $\mu_0 = M^{1/2}$ (recall that $C(\xi = 0) = 1/2$). Then, (48) becomes

$$\alpha_1 \sim a^2 N - a(M + 1 - 2\sqrt{M}) + M - 1 - N \tag{49}$$

We will use (49) to study the effect of heterogeneity a on the shift of the onset of instability. For a homogeneous displacement, the onset of the long-wave instability occurs when $M - 1 = N$. Using the latter to eliminate N from (49) we find

$$\alpha_1 \sim a(\sqrt{M} - 1)[a(\sqrt{M} + 1) - (\sqrt{M} - 1)] \tag{50}$$

Equation (50) has a different behavior depending on the value of M. For $M > 1$ (in which case $N > 0$ at the neutral stability condition), α_1 is positive in the intervals $-1 < a < 0$ and $a^* < a < 1$, and negative in the interval $0 < a < a^*$, where $a^* = \frac{\sqrt{M}-1}{\sqrt{M}+1}$ (Fig. 11a). For $M < 1$ (in which case $N < 0$), α_1 is positive in the interval $a^* < a < 0$, and negative in the intervals $0 < a < 1$ and $-1 < a < a^*$ (Fig. 11b). Thus, a jump in permeability can promote or suppress the onset of instability, depending on the specific conditions. This can be physically translated as follows:

In the case when a less viscous and lighter fluid is displacing downwards a more viscous and heavier fluid (or a heavier fluid is displacing upwards a lighter fluid, $N > 0$) gravity is stabilizing. An increase in permeability in the direction of displacement will further stabilize the displacement, provided that the permeability ratio does not exceed the value $\sqrt{M}$ (for

the present case of an exponential viscosity-concentration dependence). If it does, or in the case of a permeability decrease in the direction of displacement, the displacement will be destabilized.

Conversely, in the case when a more viscous but heavier fluid is displacing downwards a less viscous but lighter fluid (or a lighter fluid is displacing upwards a heavier fluid, $N < 0$) gravity is destabilizing. A decrease in permeability in the direction of displacement will destabilize the displacement, as long as the permeability ratio is larger than $\sqrt{M}$ (for the exponential viscosity-concentration dependence). If it does, or in the case of a permeability increase in the direction of displacement, the displacement will be stabilized.

CONCLUSIONS

This linear stability analysis allowed for the derivation of short and long wavelength asymptotic expansions of the growth rate of disturbances with non-monotonic viscosity profiles with longitudinally varying permeability. It is found that heterogeneity introduces a qualitatively different effect only in the case when the viscosity depends in a non-monotonic way on the concentration of the miscible displacement process. In this case, the Saffman-Taylor criterion fails to address the onset of instability which is now additionally dependent on the heterogeneity of the permeability field.

Numerical solutions indicate that at long wave asymptotic expansions, for a fluid with a non-monotonic viscosity profile, a permeability increase in the direction of displacement enhances the propensity for viscous fingering instability to occur even though the end point viscosity ratio is smaller than one. By contrast, nominally unstable displacements can be stabilized if the permeability decreases in the direction of displacement. This behavior is possible only if the viscosity profile is non-monotonic. Short wave stability analysis remain unchanged regardless of the nature of the viscosity dependence.

Future investigation should extend the stability analysis on the effects of heterogeneity in both longitudinal and transverse to further generalize the contributions and compared with previous findings [8], [9].

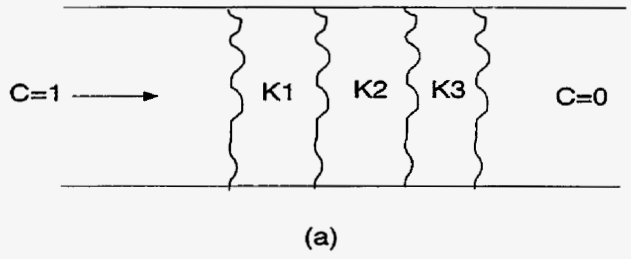

(a)

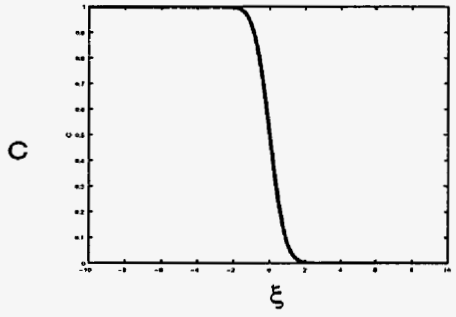

(b)

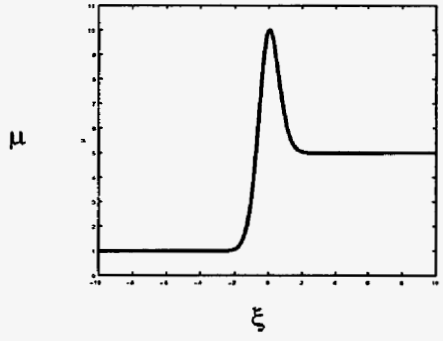

(c)

Figure 1: Physical Characteristics of the System: (a) Displacement in a Stratified Medium, (b) Base State Concentration, (c) Non-monotonic viscosity concentration profile.

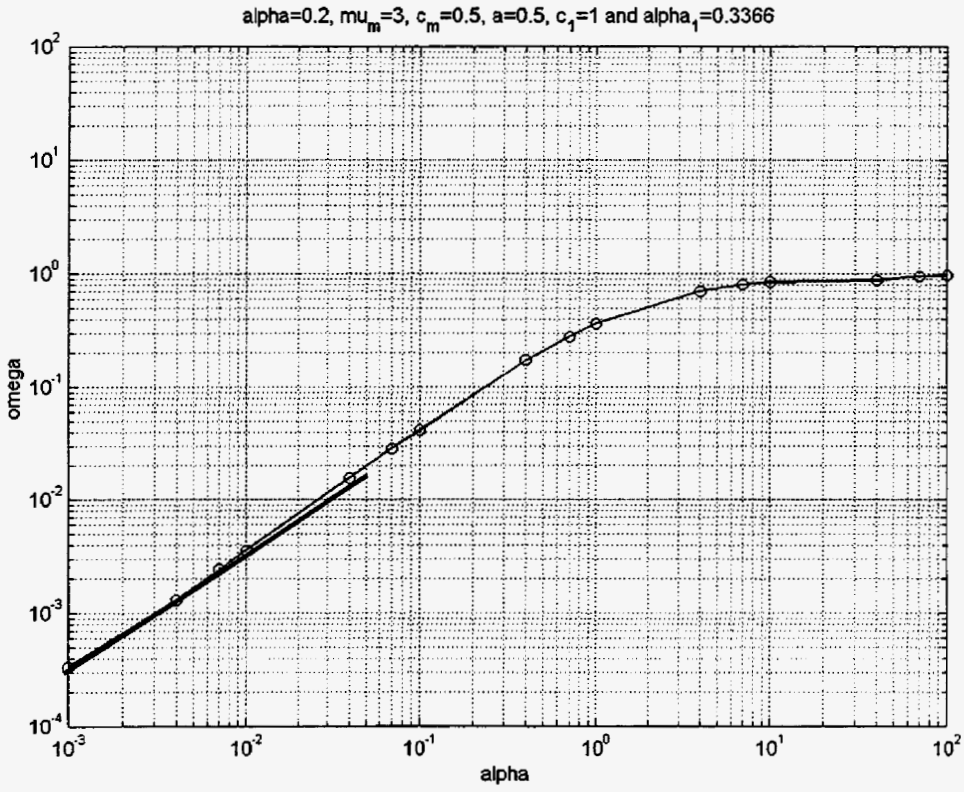

Figure 4: Stability Dispersion Relation for M= 0.2 and $\mu_m = 3$. The heavy solid line is the analytical prediction.

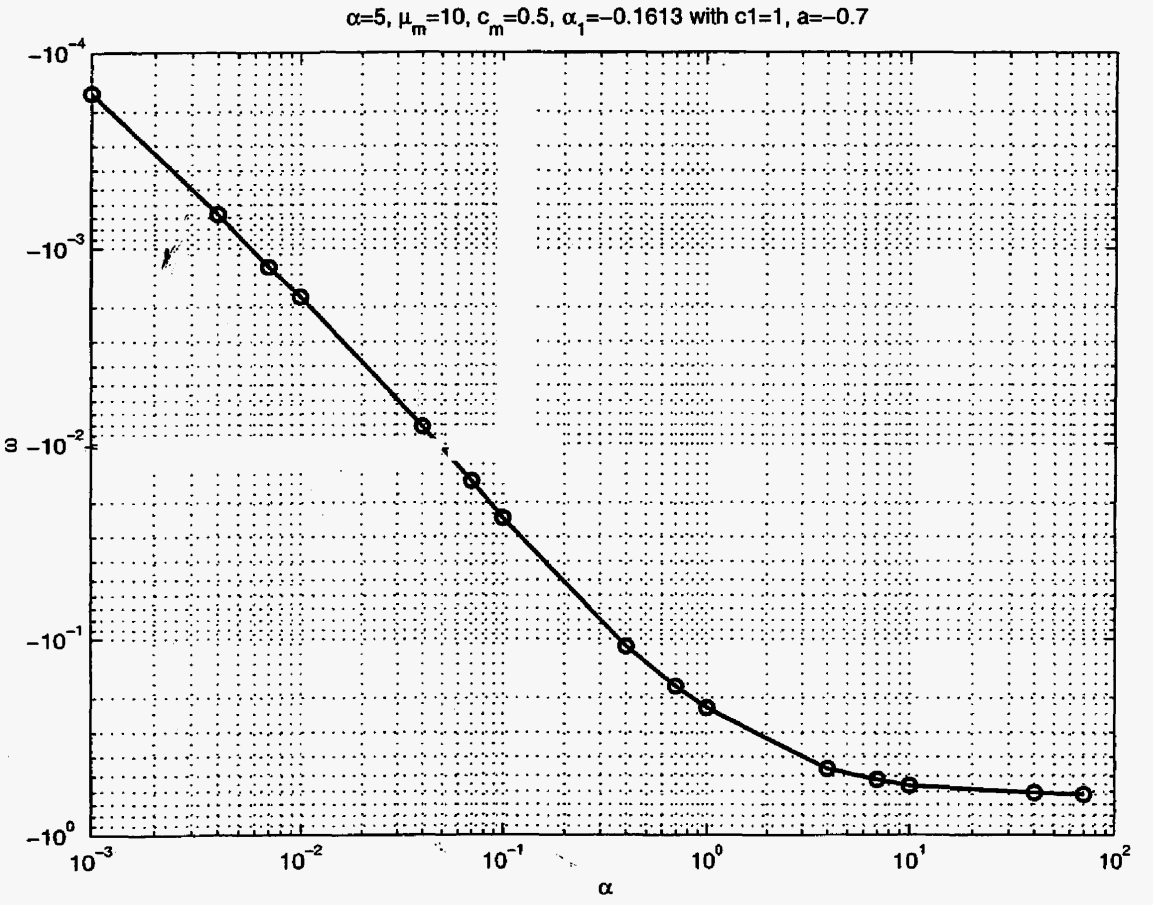

Figure 5: Stability Dispersion Relation for M= 5 and $\mu_m = 10$. The heavy solid line is the analytical prediction.

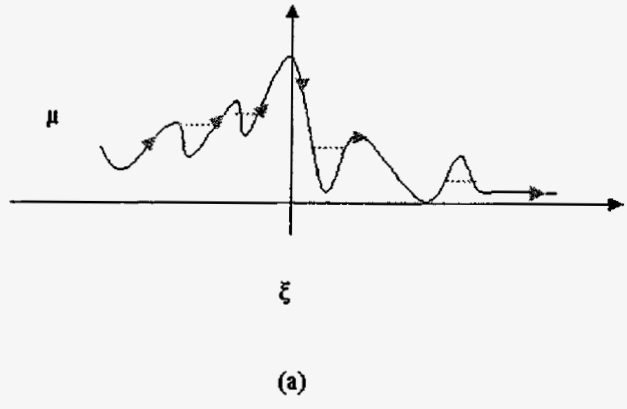

Figure 8: Evolution of Vortex Motion in the Direction of Displacement for : (a) an Endpoint Stable Displacement,(b) an Endpoint Unstable Displacement.

References

[1] Saffman, P.G., Taylor, G.I., "The Penetration of a Fluid into a Porous Medium or Hele-Shaw Cell Containing a More Viscous Liquid," *Proc. R. London Ser.*, **A.245**, 312-329 (1958).

[2] Waggoner, J.R., Castillo, J.L., and Lake, L.W., "Simulation of EOR Processes in Stochastically Generated Permeable Media," paper SPE 21237 (Feb. 1984).

[3] Araktingi, U.G., Orr, F.M. ,Jr., "Viscous Fingering in Heterogeneous Porous Media," SPE-18095 (Oct, 1988).

[4] Gelhar, L.W., Anxness, C.L., "Three-Dimensional Stochastic Analysis of Macrodispersion in Aquifers," *Water Resources Res.*, **19**, 161-180 (1983).

[5] Lenormand, R., "Proc. 3rd European Conference on the Mathematics of Oil Recovery," Delft, Holland (1992).

[6] Zhang, Y, Shariati, M., Yortsos, Y.C., "The Spreading of Immiscible Fluids in Porous Media Under the Influence of Gravity," *Transport in Porous Media*, **38**, 117-140 (2000).

[7] Tan, C.T., Homsy, G.M., "Stability of Miscible Displacements in Porous Media: Rectilinear Flow," *Phys. Fluids*, **29**, 3549 (1986).

[8] DeWit, A., Homsy, G.A., "Viscous Fingering in Periodically Heterogeneous Porous Media. I. Formation and Linear Instability," *J. Chem. Phys.*, **107**, 22, (1997).

[9] DeWit, A., Homsy, G.A., "Viscous Fingering in Periodically Heterogeneous Porous Media. II. Numerical Simulations," *J. Chem. Phys.*, **107**, 22, (1997).

[10] Chen, C.Y., Meiburg, E., "Miscible Displacements in Capillary Tubes. Part 2 Numerical Simulations," *J. Fluid Mech.*, **326**, 57-65 (1996).

[11] Chen, G., Neuman, S.P., "Wetting Front Instability in Randomly Stratified Soils," *Phys. of Fluids*, **8**, 353-356 (1996).

[12] Hickernell, F.J., Yortsos, Y.C., "Linear Stability of Miscible Displacement Processes in Porous Media in the Absence of Dispersion," *Stud. Appl. Math.*, **74**, 93-115 (1986).

[13] Loggia, D., Salin, D., Yortsos, Y.C., "The Effect of Dispersion on the Stability of Non-monotonic Mobility Profiles in Porous Media," *Physics Fluids*, **10**, No. 3 (1998).

[14] Chikhliwala, E.D., Yortsos, Y.C., "Theoretical Investigations on Finger Growth by Linear and Weakly Nonlinear Stability Analysis," *SPE 14367*, Soc. Pet. Eng. Dallas, TX (1985).

[15] Manickam, O., Homsy, G.M., " Fingering Instabilities in Vertical Miscible Displacement Flows in Porous Media," *J. Fluid Mech.*, **288**, 75-102 (1995).

[16] Manickam, O., Homsy, G.M., "Stability of Miscible Displacements in Porous Media with Nonmonotonic Viscosity Profiles," *Phys. Fluids*, **A.5**, 1356-1367 (1993).

[17] Loggia, D., Salin, D., Yortsos, Y.C., "The Effect of Dispersion on the Stability of Non-monotonic Mobility Profiles in Porous Media," *Physics Fluids*, **10**, No. 3 (1998).

[18] Tan, C.T., Homsy, G.M., "Simulation of Nonlinear Viscous Fingering in Miscible Displacement," *Phys. Fluids*, **31**, 1330-1338 (1988).

[19] Homsy, G.M., "Viscous Fingering in a Porous Media," *Ann. Rev. Fluid Mech.*, **19**, 271-311 (1987).

IDENTIFICATION OF THE PERMEABILITY FIELD OF A POROUS MEDIUM FROM THE INJECTION OF A PASSIVE TRACER

Lang Zhan and Yanis C. Yortsos

INTRODUCTION

Permeability heterogeneity is a most important feature of natural porous media, as it affects significantly flow and fluid displacement properties. These dictate flow paths, and the migration and dispersion of in-situ or injected fluids in porous media, with applications ranging from the recovery of in-situ fluids to the fate of environmental contaminants in the subsurface [1]. Heterogeneity is manifested at various scales, from the laboratory (core) to the megascopic (field) scale. Its ubiquitous and multi-scale nature has attracted the interest of many investigators, and a variety of studies have been devoted to its characterization and identification [2].

The classical approach for identifying permeability heterogeneity is based on the inversion of pressure data, under single-phase flow conditions [3]. Given that the transient flow of slightly compressible fluids in porous media obeys the diffusion equation, a variety of field tests (well tests) have been devised to infer permeability features by matching pressure data at well locations to the solution of the diffusion equation. Pressure transient methods have also been applied to characterize the heterogeneity of laboratory cores, using mini-permeameters [4]. These devices essentially conduct mini-well tests on the surface of a laboratory core (by injecting a small pulse of air and monitoring the resulting pressure transient), which are used to infer a map of the permeability heterogeneity at the external surface of the sample.

An alternative approach to permeability identification is based on the analysis of the arrival times during the injection of passive tracers (namely of tracers which do not affect the fluid viscosity and density). Various efforts have been made at the field scale to relate the arrival times to the permeability, and to match assumed permeability fields to such data [5]. These techniques are usually indirect, based on optimizing arbitrary (or constrained)

initial guesses to match data at various, usually sparse, locations. As a result, they suffer from non-uniqueness. Nonetheless, useful information can be extracted, which can be used to constrain images of the subsurface permeability field.

When knowledge of the displacement front at successive time intervals is available, for example through visual or tomographic techniques, arrival time methods should in principle be able to provide direct maps of the heterogeneity. Brock and Orr [6] reported one such attempt, based on the visualization of displacements in a 2-D heterogeneous bead pack. Withjack et al. [7] proposed a model to infer the permeability heterogeneity of laboratory samples from the analysis of concentration contours obtained from X-ray Computerized Tomography (CT). Their model is based on a number of simplifying assumptions, the main of which is that each flow streamtube has constant (but unknown) permeability and porosity, which is thus tantamount to an assumption of a layered structure. Although restrictive, the work of Withjack et al. [7] was the first to point out the potential of CT in identifying the permeability heterogeneity. CT techniques are now routinely applied to monitor displacement fronts in porous media at the laboratory scale. Advances in field scale tomography, for example by seismic methods or cross-hole tomography, are also likely to lead to analogous results at the field scale [8]. Yet, well-defined methods to invert such information to determine the permeability heterogeneity are currently lacking.

In this section, we propose a new method which focuses on this question, namely on how to invert data on arrival times at various (and numerous) points in the porous medium to map the permeability field. The method, elements of which were briefly described in [9], is based on a direct inversion of the data, rather than on the optimization of initial random (or partly constrained) guesses of the permeability field. It is based on two basic premises, that Darcy's law for single-phase flow in porous media is valid, and that the dispersion of the concentration of the injected tracer is negligible. Based on these conditions, we formulate a non-linear boundary value problem, the coefficients of which depend on the experimental arrival time data. Combined with information on the permeability or the pressure at the bounding (no-flow) surface of the porous medium we obtain a solution of the boundary-value problem, from which the permeability field can be directly calculated. The requirement that pressure or permeability values at a boundary must be known makes the method more

suitable to laboratory applications. An important feature of the method is that it can be applied to determine the heterogeneity of anisotropic media, where the permeability field is a tensor, as is often the case in many natural porous media. For this, displacements in two (for 2-D) or three (for 3-D) different directions must be conducted, as described below.

As described below, the experimental information on arrival times enters in the technique in the form of spatial derivatives. As a result, the solution method is sensitive to errors in their estimation, which are expected to increase when variations in the permeability are sharper and larger. The errors are magnified around certain limiting streamlines, the width of which increases in the downstream direction, and may lead to poor estimates of the permeability in some regions. To circumvent the problem in such cases, we have modified the inversion method by considering a *forth-and-back* hybrid approach, in which arrival times are recorded a second time by repeating the tracer displacement in the reverse direction. This approach is then combined with an optimization technique to improve the resulting estimates. The need to repeat the displacement in two directions in such cases, is an additional limitation on the applicability of the method to field cases.

The section is organized as follows: In subsection II we describe the inversion method for the case of isotropic media. Subsection III shows numerical examples which test the applicability of the method to various forms of permeability heterogeneity and its sensitivity to permeability variation and spatial correlation. Subsection IV describes the hybrid approach for inverting permeability fields with sharp and large contrasts. A sensitivity study of the effect of measurement errors is also provided. The extension of the method to anisotropic media of known and fixed principal axes is presented in subsection V. We close with concluding remarks.

DIRECT INVERSION ALGORITHM: ISOTROPIC MEDIA

Consider the injection of a passive tracer in a heterogeneous and isotropic porous medium. In the absence of dispersion, the concentration $C(\mathbf{x}, t)$ satisfies the equation

$$\phi(\mathbf{x})\frac{\partial C}{\partial t} + \mathbf{v} \cdot \nabla C = 0 \tag{1}$$

where $\phi(\mathbf{x})$ is the porosity of the medium and $\mathbf{v}$ is the superficial fluid velocity. Under slow, viscous flow conditions, the latter satisfies Darcy's law

$$\mathbf{v} = -\mathbf{K} \cdot \nabla\Phi \tag{2}$$

and the continuity equation

$$\nabla \cdot \mathbf{v} = 0 \tag{3}$$

assuming incompressible fluids. Here, $\mathbf{K}(\mathbf{x})$ is the (symmetric) permeability tensor, and Φ is a flow potential, $\nabla\Phi = \frac{1}{\mu}(\nabla p - \rho\mathbf{g})$, where μ is viscosity, taken as a constant, p is pressure, ρ is density, also assumed constant, and $\mathbf{g}$ is the acceleration of gravity. For isotropic media we take $\mathbf{K}(\mathbf{x}) = k(\mathbf{x})\mathbf{I}$, where $\mathbf{I}$ is the identity tensor. The anisotropic case is discussed in subsection V. In the absence of dispersion, we define a front location by the equation

$$\mathcal{F}(\mathbf{x}, t) \equiv t - f(\mathbf{x}) = 0 \tag{4}$$

where, assuming constant or monotonic injection rates, the function $f(\mathbf{x})$ is single-valued, thus associated with a given point $\mathbf{x}$ is a single arrival time. Then, the concentration is given by

$$C(\mathbf{x}, t) = C_i(t)H(t - f(\mathbf{x})) \tag{5}$$

where $C_i(t)$ is the injection concentration, and H is the Heaviside step function.

The direct algorithm is based on the following. First, we equate the two expressions for the normal velocity at the front, given by the kinematics and by Darcy's law, respectively. Noting that the normal at the front is given by

$$\mathbf{n} = \frac{\nabla\mathcal{F}}{|\nabla\mathcal{F}|} = -\frac{\nabla f}{|\nabla f|} \tag{6}$$

we combine (5) and (6) with (1) to obtain a kinematic expression for the normal velocity there, namely

$$v_n = -\frac{\phi(\mathbf{x})}{|\nabla f|} \tag{7}$$

Darcy's law (equations (2) and (6)) gives another expression for the same quantity

$$v_n = \frac{k(\mathbf{x})\nabla\Phi\cdot\nabla f}{|\nabla f|} \tag{8}$$

From (7) and (8) we obtain the following result for the permeability

$$k(\mathbf{x}) = -\frac{\phi(\mathbf{x})}{\nabla\Phi\cdot\nabla f} \tag{9}$$

which, in principle, can be evaluated in terms of Φ and f. Substituting the above expression in Darcy's law and making use of the continuity equation (3) we obtain a non-linear equation for Φ, which reads

$$\nabla\cdot\left[\frac{\phi(\mathbf{x})\nabla\Phi}{\nabla\Phi\cdot\nabla f}\right] = 0 \tag{10}$$

The two equations (9) and (10) constitute the keys of the direct inversion method. Equation (10) is a partial differential equation which determines Φ, given appropriate boundary conditions, and information on the porosity, $\phi(\mathbf{x})$, and the arrival time function, $f(\mathbf{x})$. From its solution, the permeability field can be directly calculated using (9).

The following remarks are in order:

1. For the solution of (10), the porosity must be a known function of the spatial coordinates. For applications using CT, this is readily available.

2. Although, at first glance, equation (10) appears to be an elliptic (Laplace type) equation, it is in fact a system of first-order hyperbolic equations. This can be readily shown, e.g. in 2-D, by introducing

$$u \equiv \frac{\frac{\partial\Phi}{\partial y}}{\frac{\partial\Phi}{\partial x}} \tag{11}$$

in which case (10) becomes

$$\frac{\partial}{\partial x}\left[\frac{\phi(\mathbf{x})}{f_x + uf_y}\right] + \frac{\partial}{\partial y}\left[\frac{\phi(\mathbf{x})u}{f_x + uf_y}\right] = 0 \tag{12}$$

where subscripts indicate partial derivatives. (A similar analysis holds for 3-D). The two equations (11) and (12) form a pair of first-order hyperbolic equations. For their solution, and thus for the solution of (10), information on the potential Φ at the (no-flow) boundaries

is necessary. Equivalently, this information can be furnished from a knowledge of the permeability at the boundaries (which, for instance, can be obtained for a laboratory sample by a mini-permeameter, as previously noted). At no-flow boundaries (where in the normal direction $\frac{\partial \Phi}{\partial n} = 0$), equation (9) becomes a partial differential equation for the variation of Φ along the boundary, which can be integrated, given k and f at the boundary, to yield the required profile. In this way, the numerical method utilizes information from all boundaries, essentially solving an elliptic-like, rather than a hyperbolic system. In the applications to be shown below we solved (10) assuming known pressure profiles at all boundaries.

3. A notable feature of (9) and (10) is that they depend on the gradient of the front arrival time rather than on the arrival time itself. On the positive side, this reflects a desirable sensitivity of the method to heterogeneity. However, this dependence also introduces numerical instability which can lead to problems when the permeability contrast is sharp and large. A technique to circumvent these problems and its sensitivity to error measurements is described later in subsection IV.

In summary, supplied with boundary conditions on the potential, equations (9) and (10) can be solved directly to yield the permeability field in a heterogeneous porous medium based on information on arrival times and the porosity heterogeneity. The resolution of the inverted permeability field depends, among others, on the resolution of the arrival time contours.

A Streamfunction Approach for 2-D Geometries

Before proceeding, it is worthwhile to note that in 2-D geometries, an alternative inversion method is possible, based on the use of the streamfunction Ψ, where $\frac{\partial \Psi}{\partial y} = v_x$ and $\frac{\partial \Psi}{\partial x} = -v_y$. Streamfunction-based methods were proposed by Brock and Orr [6] and Withjack et al. [7], using heuristic arguments, as noted previously. To proceed with such an approach, we first rearrange (7) to read

$$\frac{\partial f}{\partial y}\frac{\partial \Psi}{\partial x} - \frac{\partial f}{\partial x}\frac{\partial \Psi}{\partial y} = -\phi(\mathbf{x}) \tag{13}$$

This is a first-order, hyperbolic differential equation for Ψ, the characteristics of which are

curves of constant f, namely of constant arrival time, which are available experimentally. Hence, the streamfunction can be computed by integrating along these contours, for example

$$\Psi = \Psi_0 + \int_{y_0}^{y} \frac{\phi}{f_x} dy \tag{14}$$

where, in the case of a rectilinear sample with a no-flow boundary at $y_0 = 0$, we can take $\Psi_0 = 0$ without loss. To estimate the permeability we also need to compute the potential. In the isotropic case, we make use of the fact that equipotentials are orthogonal to the streamlines, thus

$$\frac{\partial \Psi}{\partial x}\frac{\partial \Phi}{\partial x} + \frac{\partial \Psi}{\partial y}\frac{\partial \Phi}{\partial y} = 0 \tag{15}$$

Equation (15) is also a hyperbolic equation, which can be integrated subject to appropriate boundary conditions. Then, the permeability can be estimated from (9), or from the alternative expression $k = \frac{\partial \Psi}{\partial y} / \frac{\partial \Phi}{\partial x}$. This approach does not rely on the restricitve approximations made by the previous authors. Illustrative examples will be discussed below.

APPLICATIONS USING SIMULATED DATA

The direct inversion method was subsequently tested based on simulated data. We used a high-resolution finite-difference simulator (the main features of which are described in [10]), or a streamline-based method, to simulate tracer displacement at constant-rate and in the absence of gravity and provide data on arrival times and the pressure profile at the boundaries. Parenthetically, we note that the forward problem belongs to the general class of problems recently discussed by Sethian [11], and can also benefit from the application of a Fast Marching Technique. Such was not implemented here, however. The numerical results thus obtained, were considered "error-free" data to be used as input for the solution of (10). The boundary value problem (10) was solved using a standard SOR finite-difference formalism, which was suitably iterated until convergence. For example, for the 2-D geometry we used the five-point scheme

$$\Theta^m_{i+1/2,j}\Phi^{m+1}_{i+1,j} + \Theta^m_{i-1/2,j}\Phi^{m+1}_{i-1,j} + \Theta^m_{i,j+1/2}\Phi^{m+1}_{i,j+1} + \Theta^m_{i,j-1/2}\Phi^{m+1}_{i,j-1}$$

$$-(\Theta^m_{i+1/2,j} + \Theta^m_{i-1/2,j} + \Theta^m_{i,j+1/2} + \Theta^m_{i,j-1/2})\Phi^{m+1}_{i,j} = 0 \qquad (16)$$

where $\Theta^m_{i,j}$ is the conductivity coefficient at block (i,j) at iteration level m. All other coefficients were evaluated using the harmonic average between $\Theta^m_{i,j}$ and its nearest neighbor. An interpolation routine was used to interpolate the arrival times, when necessary. The spatial derivatives of f were calculated using three-point differences. Equation (16) was solved using prescribed pressure profiles on the two no-flow boundaries.

Figs. 1-3 show results of the application of the inversion method in three 2-D heterogeneity fields of a moderate permeability contrast, corresponding to a layered medium, a medium with a smoothly varying heterogeneity and a permeability distribution following fBm (fractional Brownian motion) statistics. Each figure shows true and directly inverted permeability fields, along with true and directly inverted and potential profiles. In all these examples, the direct inversion was found to give very good results.

Fig. 1 shows that the method handles well permeability contrasts transversely to the direction of displacement, with some expected dispersion around the discontinuity. Potential profiles are also reproduced well, again with some differences noted around the discontinuity. We must emphasize that, particularly in this example, the success of the method rests on the availability of the potential profile at the boundary, which removes the non-uniqueness of the problem. (Indeed for a 1-D displacement at constant injection rate in a piecewise constant permeability, equation (10) becomes indeterminate.) Likewise, good results were found when the permeability contrast was in the direction parallel to the displacement. The ability of the method to invert the permeability field in the presence of an arbitrary closed region of sharp permeability contrast is discussed later.

The permeability field of Fig. 2 is smoothly varying and contains two peaks and one valley, with a permeability contrast of about 2. It was generated in a 64$\times$ 64 grid using Franke's test function from MATLAB [12]. This function often serves as a test for the interpolation of scattered data. We first note that the arrival times are more sensitive to the heterogeneity, than the pressure profiles, which are essentially parallel to the transverse direction. This feature was also noted in all other cases, where the permeability variation is relatively smooth. Fig. 2 shows that the comparison between actual and inverted fields (in permeability and potential profiles) is very good. This example is characteristic of the

success of the method in smoothly varying permeability fields.

A more stringent test is shown in Fig. 3 involving a similar permeability contrast. The permeability field is of the fBm type with a Hurst exponent $H = 0.8$, and it is a typical example of a self-affine field, containing large-scale correlations [13]. fBm statistics with a Hurst exponent larger than 0.5 are often taken to describe the heterogeneity in the horizontal permeability of natural rocks [14]. Fig. 3 shows that the match between actual and inverted data is also quite good. Potential profiles are closely matched. The inverted permeability reproduces well the main features of this field, specifically the regions where the permeability is high, medium or low. However, discrepancies do exist in the detailed point-by-point variation of the permeability, the inverted field being somewhat smoother than the actual. The ability to capture long-wavelength, as opposed to high-frequency, variations is typical of this technique and was noted in other examples, as well. Fig. 4 shows a statistical analysis of actual and inverted permeabilities. Histograms and the correlation structure (the semi-variograms) match quite well, and the scatter plot is satisfactory. The dispersion around the 45° line indicates a small degree of point-by-point mismatch, as also evidenced in Fig. 3.

The direct inversion technique can be equally well applied to 3-D geometries. Before we proceed, however, it is instructive to compare inversion results using the 2-D streamfunction method described in the previous subsection. Figs. 5 and 6 show the resulting permeability estimates, along with the associated streamfunctions, corresponding to Figs. 2 and 3, respectively. The streamlines are well reproduced, and the inverted permeability fields maintain the large correlation features. However, it is evident that the inverted fields miss many details. There are also apparent defects extending along slice-shaped regions, which arise from the integration along the arrival time contours. A statistical analysis, not shown here for lack of space, shows that the inverted permeability reproduces reasonably well the semi-variograms. However, the histograms, and to a greater degree, the scatter plot, have large errors in several places. The streamfunction method is prone to relatively large numerical errors, as it involves a threefold interpolation for spatial derivative estimation and the integration of hyperbolic equations (for determining the streamfunction). These weaknesses make the method unfavorable compared to the direct solution of (9) and (10) (as seen in the comparison of Figs. 2 to 5 and 3 to 6). Advantages of the method, on the other hand,

are that the permeability is inverted fast, compared to the previous, while one also readily obtains streamfunction and streamline profiles. These may be useful in certain applications, particularly in the field.

To demonstrate the applicability of the direct inversion method to three dimensions, we considered the 3-D permeability field shown in Figs. 7a and 7b, consisting of a log-normal distribution generated by Sequential Gaussian Simulation, with a natural logarithmic mean of 2.0, a standard deviation of 0.2 and a dimensionless correlation length (with respect to the sample size) of 0.5. The permeability variation is somewhat larger than before. Characteristic arrival time contours from the simulation of the forward problem in a $16\times16\times16$ lattice are shown in Figs. 7c and 7d. The direct inversion algorithm was applied by using a 3-D version of (16) along with boundary conditions supplied from the forward problem. The results of the permeability inversion are shown in Fig. 8. They appear to be in relatively good agreement with the actual (Fig. 7a and 7b). A more quantitative comparison is shown in the statistics of Fig. 9, calculated by GSLIB [15]. In general, the comparison is good. The inverted field shows a smaller range of variation than the actual, as reflected in both the semi-variogram and the histogram. We note that the spatial correlation structure of the former is well captured in the inverted data. The scatter plot indicates a somewhat larger dispersion, compared to the fBm field of Figs. 3-4, which is expected, given the larger permeability contrast here.

In the above examples, where the permeability contrast is not too large, or where the permeability has relatively large spatial correlations, the direct inversion method gives good results. When the contrast increases and variations in permeability are sharper, however, the method is subject to increased errors. These arise primarily from the approximation of the spatial gradients of the arrival time in regions where the latter varies sharply. Fig. 10 shows arrival time contours, calculated analytically (see Appendix), for flow around an embedded sphere of lower permeability. Even though the permeability contrast is relatively modest (0.6:1), there exist two thin layers, extending downstream of the sphere and centered around the two limiting streamlines tangent to the sphere, where the arrival times exhibit sharp spatial variations. In these regions, the evaluation of the coefficients of (10) is likely to introduce errors and accordingly poor estimates for the permeability in certain places.

These limiting streamlines also exist in any other fields containing regions of sharp permeability contrast. Because the respective layers extend downstream of the region of the sharp contrast, however, the associated errors in permeability estimates are different depending on the direction of displacement. We have conjectured, therefore, that the estimates of the direct method could be improved substantially, if we were to combine information from two different displacements, one in the forward and the other in the reverse direction.

A HYBRID ALGORITHM

To circumvent the problems posed by high permeability contrasts we implemented the following hybrid procedure:

1. Carry out a tracer displacement in the forward direction and directly invert to obtain one permeability estimate, $k_f(\mathbf{x})$.

2. Carry out a tracer displacement in the reverse direction and directly invert to obtain a second permeability estimate, $k_b(\mathbf{x})$.

3. Retain the estimates in those places, where they differ in absolute value by no more than a prescribed value, and discard in all others. Assign estimates in these regions by an interpolation algorithm (known in the geostatistics literature as kriging).

4. Use an optimization algorithm (to be briefly described below) to fine-tune the so obtained composite permeability estimates.

The optimization algorithm is based on standard gradient methods [16] and will not be discussed here in detail. We briefly note that we used the following objective function

$$\mathcal{J} = \frac{1}{2}\{[\mathbf{f}(\mathbf{k})-\mathbf{f}^m]^T\cdot\mathbf{W_1}\cdot[\mathbf{f}(\mathbf{k})-\mathbf{f}^m]+[\mathbf{k}-\mathbf{k}^p]^T\cdot\mathbf{W_2}\cdot[\mathbf{k}-\mathbf{k}^p]+[\mathbf{\Phi_b}-\mathbf{\Phi_b^m}]^T\cdot\mathbf{W_3}\cdot[\mathbf{\Phi_b}-\mathbf{\Phi_b^m}]\} \quad (17)$$

consisting of three inner product terms. The first is the weighted sum of the squares of the differences between the current estimates of the front arrival times, $\mathbf{f}$, obtained from the simulator response, and the "error-free" data, $\mathbf{f^m}$. The weight $\mathbf{W_1}$ is a diagonal matrix whose elements are the inverse of the variances of the errors of the measured arrival times. The third term is the analogous inner product for the differences between the current estimates for the potential at the no-flow boundaries, $\mathbf{\Phi_b}$, and the data, $\mathbf{\Phi_b^m}$, with $\mathbf{W_3}$ being the corresponding

diagonal matrix. The second term represents the mismatch between the current permeability estimate, $\mathbf{k}$, and its prior, $\mathbf{k}^p$. It is a regularization term, as required by Tikhonov's theory [17], and restricts the parameters being optimized to not deviate greatly from the prior information. Here, $\mathbf{W_2}$ denotes the inverse of the covariance matrix of the prior. Numerical experience has demonstrated its necessity for stable and convergent solutions. However, the accuracy of the initial guess plays a pivotal role in the convergence to the true solution. It is in this context, that the hybrid algorithm offers an important advantage. In our method, the prior information is supplied using the direct inversion method, outlined in steps 1-3 above, which is generally close to the true permeability field. As a result, in many of the cases tried, the optimization method converges close to the true values. By contrast, in other related inverse problems, the prior permeability is typically generated by a geostatistical algorithm constrained to (usually) sparse measurements, and its convergence to the true solution is generally uncertain (e.g. see [18]). At the same time, we must stress that we have also encountered many problems involving sharp permeability contrasts, which cannot be successfully handled even with the hybrid algorithm, as shown below. For completeness, we mention that in order to match arrival times and boundary pressures as well as possible, we often had to increase their weights in the objective function by multiplying with a large number.

Applications of the hybrid algorithm using simulated data are illustrated in Figs. 11-14 for three different examples. The medium in Fig. 11 contains two blocks of low permeability with a 1:5 contrast. This particular configuration corresponds to the experimental Hele-Shaw cell used in [19], and was discretized by a 22×10 lattice. The top of Fig. 11 (panels a,b) shows the prior estimate fed to the optimization algorithm, following steps 1-3. Due to the sharp permeability contrast between low and high permeable regions, the spatial derivatives of the arrival times have significant numerical errors in certain regions, and lead after steps 1 and 2 to a mismatch between true and inverted values in various places. Through step 3 (where estimates were discarded when they differed by more than 30%), these errors have been minimized. The directly inverted field, after step 3, (Fig. 11, a,b) has the main trends of the true field, although it is obvious that the contrast is not as sharp as the actual, and is in need of fine-tuning. Results following the application of the optimization algorithm of

step 4, using 40 iterations, and based on the initial guess after kriging (Figs. 11a, 11b), is shown in the middle of Fig. 11 (panels c,d). The results are much improved and, with a few exceptions, they are very close to the actual. Although not shown, potential and arrival time profiles are also matched very well. By contrast, if in the optimization algorithm we used a uniform initial guess, instead of that corresponding to the direct method (panels a, b in Fig. 11), the resulting estimate (after the same number of iterations) is poor in many places, as shown in the bottom of Fig. 11 (panels e,f). This is despite the fact that arrival times and potential profiles are also matched very well. We conclude that, at least for this example, the application of the hybrid method gives a substantial improvement.

Fig. 12 shows the application of the algorithm to a correlated log-normal distribution with a logarithmic mean of 2.0, a standard deviation of 0.5 and a dimensionless correlation length of 0.25. In this example, the block-to-block permeability variation is much larger than in the fBm field of Fig. 3 or the 3-D field of Fig. 7, the largest contrast being of an order of magnitude. The application of the direct inversion method followed by kriging leads to the results shown in the middle of Fig. 12 (panels c,d). Although capturing the general features of the true field, the estimates are generally coarser and smoother than the actual values. Comparison of arrival times and potential profiles based on the inverted field (not shown for lack of space) indicates a mismatch with the actual in certain places. To fine-tune the results and recover some of the high-frequency variations, we applied the optimization algorithm of step 4. Results after 40 iterations are shown on the right of Fig. 12 (panels e,f). The algorithm does not fully reproduce the actual field, and some errors around large variations of permeability are detectable. However, it is obvious that a significant improvement has been achieved. Fig. 13 shows the corresponding statistical comparison. The mean and the variance from the hybrid algorithm agree very well with the actual. (By contrast, in results that are not shown here, the variance from kriging is underestimated by about 20%, although the mean is the same.) The two histograms are roughly equal, while the semi-variograms have the same correlation structure. The scatter plot shows that good agreement exists over a good range of lower permeabilities, although an increasing scatter can be seen at larger permeabilities. In this example, these are typically associated with large contrasts. We need to reiterate that the success of the hybrid algorithm depends to a large extent on the

accuracy of the initial guess, which is here provided by the direct method and positions the optimization scheme close to the true solution. By contrast, the estimates resulting from the application of the same optimization algorithm after bypassing steps 1-3 and utilizing a uniform initial guess were quite poor, even though arrival times and potential matched nearly perfectly with the true values.

At the same time, we must point out that we have also encountered several cases where the hybrid algorithm was not as successful as desired. Fig. 14 (panels a,b) is an example of a "checkerboard"-pattern heterogeneous field, with a permeability contrast of 1:4. A pattern similar to this was used in some previously reported tracer displacement experiments [20]. The results of the algorithm at the end of the kriging step are shown in the middle of Fig. 14 (panels c,d). The mismatch with the true data is quite apparent. The 2-D projection in the middle of Fig. 14 reproduces roughly the places of maximum permeability variation, but the picture is clearly "out of focus". The results of the application of the optimization method are shown in the right of Fig. 14 (panels e,f). We note a clear improvement, compared to the previous step, and a better focused image. Yet, there is also clear evidence of mismatches in various places, including a smoothing of the sharp contrast around the edges of discontinuity, and of other defects, which altogether preclude an exact matching. Thus, although overall the hybrid algorithm appears to be a promising alternative in cases involving large contrasts, we caution that this is not uniformly true and that many counter-examples can readily be constructed where this algorithm will not be as successful.

SENSITIVITY STUDY

The sensitivity of the algorithm to sharp permeability contrasts is a reflection of its relatively weak robustness to errors in arrival time and/or boundary pressure. To asses the latter, we studied the sensitivity of the directly-inverted permeability values to random errors in the arrival time and the boundary pressure, using again synthetic data. For this purpose, the forward numerical solutions for the arrival time and boundary pressure, $\mathbf{f}^m$ and $\mathbf{\Phi_b}^m$, respectively, assumed to represent true (error-free) results, were randomly perturbed as follows

$$\mathbf{f}_\epsilon = \mathbf{f}^m + \theta_\epsilon \min[\mathbf{f}^m] \tag{18}$$

and

$$\mathbf{\Phi_b}_\epsilon = \mathbf{\Phi_b}^m + \theta_\epsilon \min[\mathbf{\Phi_b}^m] \tag{19}$$

where θ_ϵ is a random Gaussian noise with mean equal to zero and standard deviation equal to ϵ. The minimum taken in (18) and (19) reflects the assumption that in a realistic experiment, the resolution of the measuring device is independent of the value of the quantity being measured. The results from (18) and (19) were then used in (9) and (10) to invert the permeability field following the hybrid algorithm.

Shown in Fig. 15 are the sensitivity results for the permeability field of Fig. 12 (inversion error vs. ϵ). Two curves are shown, one corresponding to the full hybrid algorithm (steps 1-4) and another corresponding to the results after only steps 1-3 were completed, namely after kriging the direct estimates from the forward and backward displacements. As a measure of the inversion error, we used the standard deviation of the inverted from the true permeability, normalized with respect to the mean, the error in the input data being proportional to ϵ. For each ϵ, a total of 10 realizations were performed. The curves in Fig. 15 represent the mean values of the results obtained, with the standard deviation also denoted. First, we observe that even in the case of "error-free" input, the inverted data have a residual error. This was already noted in the discussion of Fig. 12, and was attributed to the relatively sharp changes in permeability for that field. We also note that inversion errors, following the full hybrid algorithm, are considerably smaller than those based on kriging, as also discussed before. As the error in the input data increases, however, the inversion errors for the hybrid algorithm, both in mean and variance, increase faster than those based on kriging. In fact, the latter is actually not very sensitive to errors in the input data, and in a sense is quite robust compared to the full hybrid algorithm. The latter outperforms kriging at small values of input error. However, it is subject to increasing inversion errors beyond a certain level of input error. The origin of this discrepancy is due to the two different objectives satisfied by the two algorithms. In the hybrid algorithm, the optimization aims to match arrival time and pressure data (even if they are inaccurate). In kriging, this matching is ignored,

after the completion of steps 1-2. Similar behavior was found with other types of synthetic permeability fields used. We conclude that the successful implementation of the technique proposed relies on input data of good accuracy.

DIRECT INVERSION ALGORITHM: ANISOTROPIC MEDIA

On the other hand, a strong attribute of this technique is that it can be applied to anisotropic porous media. In this subsection, we consider for simplicity 2-D geometries, where the principal directions of the permeability tensor are constant and coincide with the rectangular coordinates x and y, namely we take

$$\mathbf{K} = \begin{vmatrix} k_x(\mathbf{x}) & 0 \\ 0 & k_y(\mathbf{x}) \end{vmatrix} \tag{20}$$

An extension to the more general case is under consideration and will be presented elsewhere. Under these conditions, the equations analogous to (9) and (10) read as follows

$$(\mathbf{K}\cdot\nabla\Phi)\cdot\nabla f = -\phi(\mathbf{x}) \tag{21}$$

and

$$\nabla(\cdot\mathbf{K}\cdot\nabla\Phi) = 0 \tag{22}$$

Using scalar notation, and substituting from (20), we further have

$$k_x\frac{\partial\Phi}{\partial x}\frac{\partial f}{\partial x} + k_y\frac{\partial\Phi}{\partial y}\frac{\partial f}{\partial y} = -\phi \tag{23}$$

and

$$\frac{\partial}{\partial x}\left[k_x\frac{\partial\Phi}{\partial x}\right] + \frac{\partial}{\partial y}\left[k_y\frac{\partial\Phi}{\partial y}\right] = 0 \tag{24}$$

Equations (23) and (24) constitute a pair of two equations in three unknowns (k_x, k_y and Φ) and require additional information for their solution. One possible approach, by which this information can be obtained, is by conducting two tracer displacements, one in the x-direction with no-flow boundaries perpendicular to the y-axis, and another in the y-direction

with no-flow boundaries perpendicular to the x-axis. If we denote the arrival time functions and the potentials of the two displacements by f_I and f_{II}, and Φ_I and Φ_{II}, respectively, Eq. (23) becomes

$$k_x \frac{\partial \Phi_I}{\partial x}\frac{\partial f_I}{\partial x} + k_y \frac{\partial \Phi_I}{\partial y}\frac{\partial f_I}{\partial y} = -\phi, \tag{25}$$

$$k_x \frac{\partial \Phi_{II}}{\partial x}\frac{\partial f_{II}}{\partial x} + k_y \frac{\partial \Phi_{II}}{\partial y}\frac{\partial f_{II}}{\partial y} = -\phi \tag{26}$$

for the respective displacements. Then, the permeability components can be determined from the two equations

$$k_x = -\frac{\phi}{A}\left[\frac{\partial \Phi_{II}}{\partial y}\frac{\partial f_{II}}{\partial y} - \frac{\partial \Phi_I}{\partial y}\frac{\partial f_I}{\partial y}\right] \tag{27}$$

and

$$k_y = -\frac{\phi}{A}\left[\frac{\partial \Phi_I}{\partial x}\frac{\partial f_I}{\partial x} - \frac{\partial \Phi_{II}}{\partial x}\frac{\partial f_{II}}{\partial x}\right] \tag{28}$$

where

$$A = \frac{\partial \Phi_I}{\partial x}\frac{\partial f_I}{\partial x}\frac{\partial \Phi_{II}}{\partial y}\frac{\partial f_{II}}{\partial y} - \frac{\partial \Phi_{II}}{\partial x}\frac{\partial f_{II}}{\partial x}\frac{\partial \Phi_I}{\partial y}\frac{\partial f_I}{\partial y} \tag{29}$$

given the data f_I and f_{II}, and the calculated potentials Φ_I and Φ_{II}. The latter can be obtained by solving equation (24), with k_x and k_y given by (27)-(29), and with the appropriate boundary conditions corresponding to the two different displacements. The following iterative algorithm was implemented to solve the resulting coupled system:

1. Based on the ν-level estimates for the potentials Φ_I^ν and Φ_{II}^ν, use Eqs. (27) and (28) to estimate the ν-level iterates k_x^ν and k_y^ν. At the initial level ($\nu = 0$), an initial guess, typically in the form of a linear variation, was supplied for the potentials.

2. Based on explicit (ν-level) estimates for k_x^ν and k_y^ν, integrate (24) twice, using SOR finite differences to calculate the potentials at the next iteration level, $\Phi_I^{\nu+1}$ and $\Phi_{II}^{\nu+1}$.

This algorithm was found to work well for the various cases tested.

The method was subsequently applied to the anisotropic permeability field shown in the left of Figs. 16-17 (panels a,b). Its statistics are similar to Fig. 7, and involve a log-normal

spatially correlated distribution with the same mean and standard deviation. By simulating a forward tracer displacement in the two directions, x and y, respectively, we obtained arrival time functions and potentials at the no-flow boundaries, which were then used for the inversion according to the above scheme. The directly inverted fields (in the absence of optimization or kriging) are shown in the right of the two Figs. 16-17 (panels c,d). Given the coupled nature of the problem, the reconstruction of the two permeability components can be considered generally good. The method reproduces relatively well the regions of high and low permeability. Compared to the isotropic case under the same permeability contrast, however, the reconstruction is not as sharp, and the projections of the inverted images appear slightly "out of focus" in certain places. This mismatch reflects an underlying mismatch in the arrival times and the potential profiles, which is not shown here. Further work is under way to improve the algorithm and fine-tune the direct inversion method, including the implementation of a hybrid algorithm, as in the isotropic case.

CONCLUDING REMARKS

In this section we presented a method for the direct inversion of the permeability of porous media, based on arrival time contours and information on the pressure profiles at the boundaries. In real systems, the former can be obtained using techniques of visualization, computerized tomography (or seismic and cross-hole tomography for field applications). The method utilizes Darcy's law for flow in porous media in combination with the kinematics of flow, as expressed in the arrival times, to derive a boundary-value problem, the solution of which leads to a direct reconstruction of the permeability field. An important feature of the technique is that it requires information from the pressure at the boundaries, to solve an elliptic-like formulation, rather than the two hyperbolic equations, which formally describe the problem. The algorithm developed is a rigorous, although not necessarily robust, tool for the analysis of arrival time contours.

Using simulated data, the method was found to work well for cases, where the permeability contrast is not very large, and the field is spatially correlated. In general, the technique captures well variations corresponding to larger wavelengths, but not as well fine-scale details. For sharper contrasts, a hybrid version of the algorithm was developed, in which the

direct method is used to generate the initial guess in an optimization algorithm. The hybrid version minimizes the sensitivity of the method to errors in spatial derivatives, which are augmented in the presence of sharp contrasts. Numerical examples in two and three dimensions using simulated (assumed "error-free") data demonstrated that the hybrid algorithm works well and that it is superior to the more conventional case, where the initial input is a uniform distribution. However, other examples can also be constructed, involving sharp contrasts and/or errors in the input data, where the inversion technique is not as satisfactory and requires further improvement. A sensitivity analysis showed that the method is prone to increasing inversion errors, as the quality of the input data deteriorates. On the other hand, a non-trivial advantage of the direct inversion technique is its potential to invert the permeability tensor in anisotropic porous media. Preliminary results for the case where the principal axes of anisotropy are fixed and known were presented and found to be promising. Further work is currently under way to fine-tune the method and to also extend it to the more general case, where the permeability tensor is full.

The various requirements for its implementation suggest that the technique proposed is best suited for laboratory applications. Even then, its applicability relies on several conditions: the availability of pressure profiles at the system boundaries, the absence, or the minimization, of dispersion during the tracer displacement and the adequate resolution in arrival time contours. The first requirement appears to be the most difficult to meet, in view of the demand for adequate spatial resolution, which presently available tools may not possess, and the need to enforce Darcy's law near no-flow boundaries. Alternatively, this profile can be obtained by locally probing the surfaces with a mini-permeameter to construct a surface permeability map, from which the pressure profile can be computed. A certain amount of pore-scale dispersion in real porous media is also unavoidable, given that the dispersion coefficient is proportional to the velocity, thus leading to a constant Peclet number and a finite amount of dispersion. However, for relatively small dispersivities, such dispersion effects could be minimal. Sufficient spatial resolution on arrival times would allow to capture fine-scale variations, at the expense of increased computational time in the optimization routine of the hybrid algorithm, and possible instabilities as the degree of resolution increases and the input error increases. However, it must also be remarked that in

our experience, so far, a coarse-grid reconstruction can adequately capture the large-scale features of the permeability field, both in the isotropic and the anisotropic cases.

Regarding field applications, the absence of boundary pressure data and the difficulty in conducting displacements in different directions, impose constraints that make difficult the application of the present technique. One could still use arrival time contours, if available through seismic or cross-hole tomography, to reconstruct streamfunctions and streamtubes, as outlined in the text for a 2-D problem. However, such information is not sufficient for the inversion of the permeability field, although it may be useful for other purposes.

APPENDIX: ARRVIAL TIMES FOR CIRCULAR PERMEABILITY HETEROGENEITY

In this appendix, we provide analytical solutions for a simple 2-D problem involving tracer displacement in an infinite domain of constant permeability 1, in which a circular inclusion of radius $r = 1$ and permeability κ is embedded. Hence, the permeability is the step function

$$k = (1 - \kappa)H(r - 1) + \kappa \tag{A-1}$$

To solve this problem, we subtract the homogeneous solution $(-x)$ from the potential, and thus consider the problem

$$\nabla \cdot [k\nabla(x + \psi)] = 0 \tag{A-2}$$

where $\psi = -\Phi + x$. In view of (30) this further reads

$$\nabla \cdot (k\nabla\psi) = -(\kappa + 1)\delta(r - 1)\frac{x}{r} \tag{A-3}$$

where δ denotes the Dirac delta function. To solve (A-3) we use polar coordinates (r, θ) and the following interface conditions at the place of permeability discontinuity

$$\psi|_{r=1_+} = \psi|_{r=1_-} \tag{A-4}$$

and

$$\kappa \frac{\partial \psi}{\partial r}|_{1-} - \frac{\partial \psi}{\partial r}|_{1+} = (1-\kappa)\cos\theta \tag{A-5}$$

The solution follows readily

$$\psi = \left(\frac{1-\kappa}{1+\kappa}\right) r\cos\theta \quad ; \quad r \leq 1 \tag{A-6}$$

$$\psi = \left(\frac{1-\kappa}{1+\kappa}\right) \frac{1}{r}\cos\theta \quad ; \quad r > 1 \tag{A-7}$$

from which the velocity components can be calculated. We find,

$$\begin{aligned} v_x &= \frac{2\kappa}{1+\kappa} \quad ; \quad r \leq 1 \\ v_x &= 1 + \left(\frac{1-\kappa}{1+\kappa}\right) \frac{y^2 - x^2}{(x^2+y^2)^2} \quad ; \quad r > 1 \end{aligned}$$

and

$$\begin{aligned} v_y &= 0 \quad ; \quad r \leq 1 \\ v_y &= -\left(\frac{\kappa(1-\kappa)}{1+\kappa}\right) \frac{2xy}{(x^2+y^2)^2} \quad ; \quad r > 1 \end{aligned}$$

Thus, the streamlines are the solution of

$$\begin{aligned} \frac{dy}{dx} &= 0 \quad ; \quad r \leq 1 \\ \frac{dy}{dx} &= -\frac{2(1-\kappa)xy}{(1+\kappa)(x^2+y^2)^2 + (1-\kappa)(y^2-x^2)} \quad ; \quad r > 1 \end{aligned}$$

from which the arrival times are obtained by integrating along the streamlines

$$t - t_0 = \int_{x_0}^{x} \frac{\phi}{u_x(x', y)} dx' \tag{A-8}$$

where ϕ is the porosity. These results were used to compute the streamlines and the arrival time contours of Fig. 10 in the text.

REFERENCES

[1] L. W. Lake, *Enhanced Oil Recovery*, (Prentice Hall, Englewood Cliffs, NJ, 1989); L. W. Gelhar, *Stochastic Subsurface Hydrology*, (Prentice-Hall, Englewood Cliffs, NJ, 1993).

[2] W. G. Yeh, Water Resources Res., **22**(2), 95 (1986); N. Z. Sun, *Inverse Problems in Groundwater Modeling*, (Kluwer Academic Publishers, Netherlands, 1994); D. McLaughlin and L. R. Townley, Water Resource Res., **32**(5), 1131 (1996).

[3] C. S. Matthews and D. G. Russell, *Pressure Buildup and Flow Tests in Wells*, (SPE Monograph Vol. 1, Dallas, 1967); R. C. Earlougher, *Advances in Well Test Analysis*, (SPE Monograph Vol. 5, Dallas, 1977); R. N. Horne, *Modern Well Test Analysis*, (Petroway, Palo Alto, CA, 1995).

[4] S. C. Jones, in Soc. Petrol. Eng. 67th Annual Meeting Proceedings, SPE paper 24757 (1992); S. Ganapathy, D. Wreath, G. Pope and K. Sepehrnoori, Soc. Petrol. Eng. Formation Evaluation, **9**, 273 (1993).

[5] C. F. Harvey and S. M. Gorelick, Water Resources Res., **31**(7), 1615 (1995); B. J. Wagner, J. Hydrology, **135**, 275 (1992); A. Datta-Gupta, S. Yoon, I. Barman and D. W. Vasco, J. Petrol. Tech., **50** (12), 72, (1998).

[6] D. C. Brock and F. M. Orr, in Soc. Petrol. Eng. 66th Annual Meeting Proceedings, SPE paper 22614 (1991).

[7] E. M. Withjack, S. M. Graham, and C. T. Yang, Soc. Petrol. Eng. Formation Evaluation, **7**, 447 (1991).

[8] D. E. Lumley and R. A. Behrens, Soc. Petrol. Eng. Reservoir Evaluation and Engineering, **1**, 528 (1998).

[9] L. Zhan and Y. C. Yortsos, 10th European Symposium on Oil Recovery Proceedings, Brighton, UK (1999).

[10] Z-M. Yang and Y. C. Yortsos, Phys. Fluids, **9**(2), 286 (1997).

[11] J. A. Sethian, *Level Set Methods and Fast Marching Methods*, Cambridge University Press, New York (1999).

[12] *Spline Toolbox User's Guide*, The Mathworks, Inc. (1999).

[13] R. F. Voss, in *The Science of Fractal Images*, (Springer-Verlag, New York, 1988); J.

Feder *Fractals*, (Plenum Press, New York, 1988).

[14] T. A. Hewett, in *Reservoir Characterization 2*, (Society of Petroleum Engineers, Houston, TX, 1989).

[15] C. V. Deutch and A. C. Journel, *GSLIB: Geostatistical Software Library and User's Guide*, (Oxford University Press, Oxford, UK, 1992).

[16] A. Tarantola, *Inverse Problem Theory, Methods for Data Fitting and Model Parameter Estimation*, (Elsevier Science Publishers, Amsterdam, 1987).

[17] A. N. Tikhonov and V. Y. Arsenin, *Solutions of Ill-posed Problems*, (Halsted Press, New York, 1977).

[18] P. R. Ballin, A. G. Journel and K. Aziz, J. Can. Petrol. Tech., **31**(4), 52 (1992).

[19] P. Berest, N. Rakotomalala, J.P. Hulin and D. Salin, Eur. Phys. J. A.P **6**, 309 (1999).

[20] R. Lenormand, Transport in Porous Media, **18**, 245 (1995).

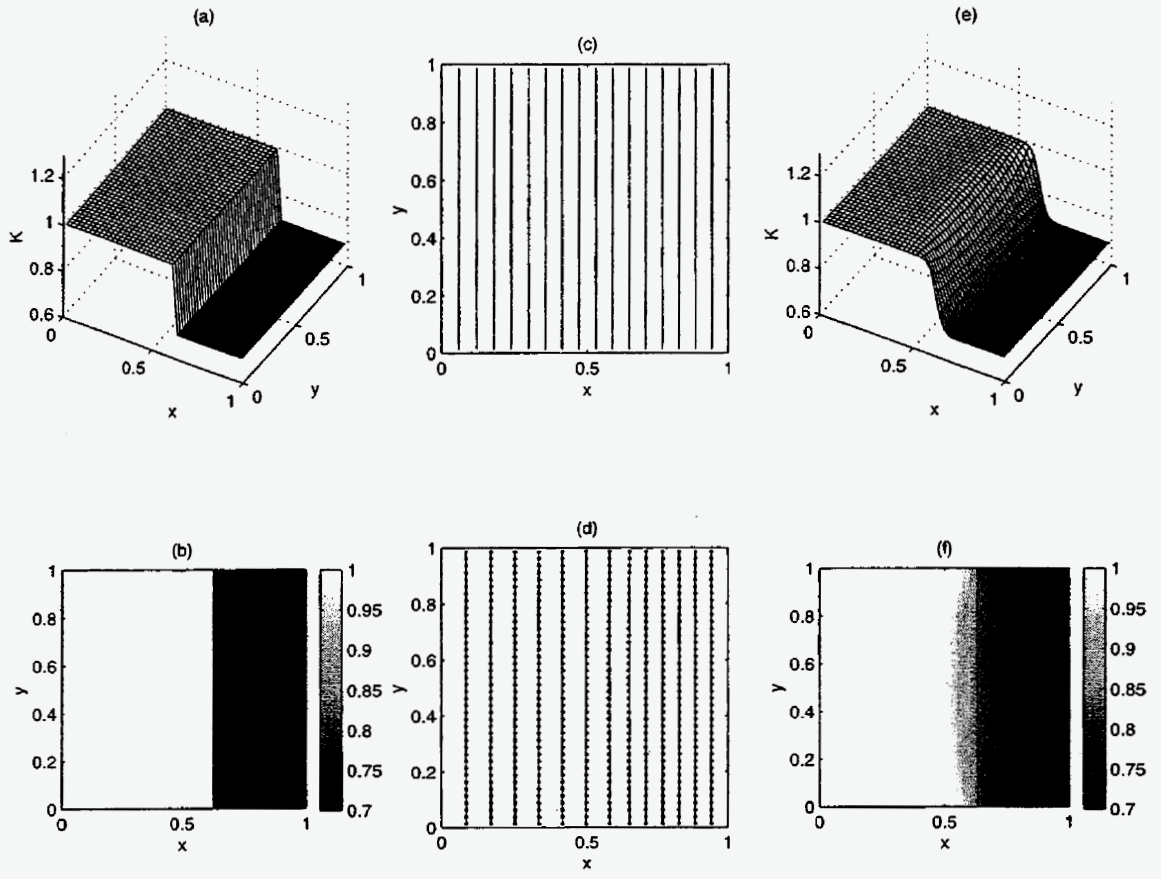

Figure 1: Application of the direct inversion method to the layered system: (a)-(b) actual permeability plots; (c) actual arrival times; (d) actual (solid lines) and inverted (dotted lines) potential profiles; (e)-(f) inverted permeability plots.

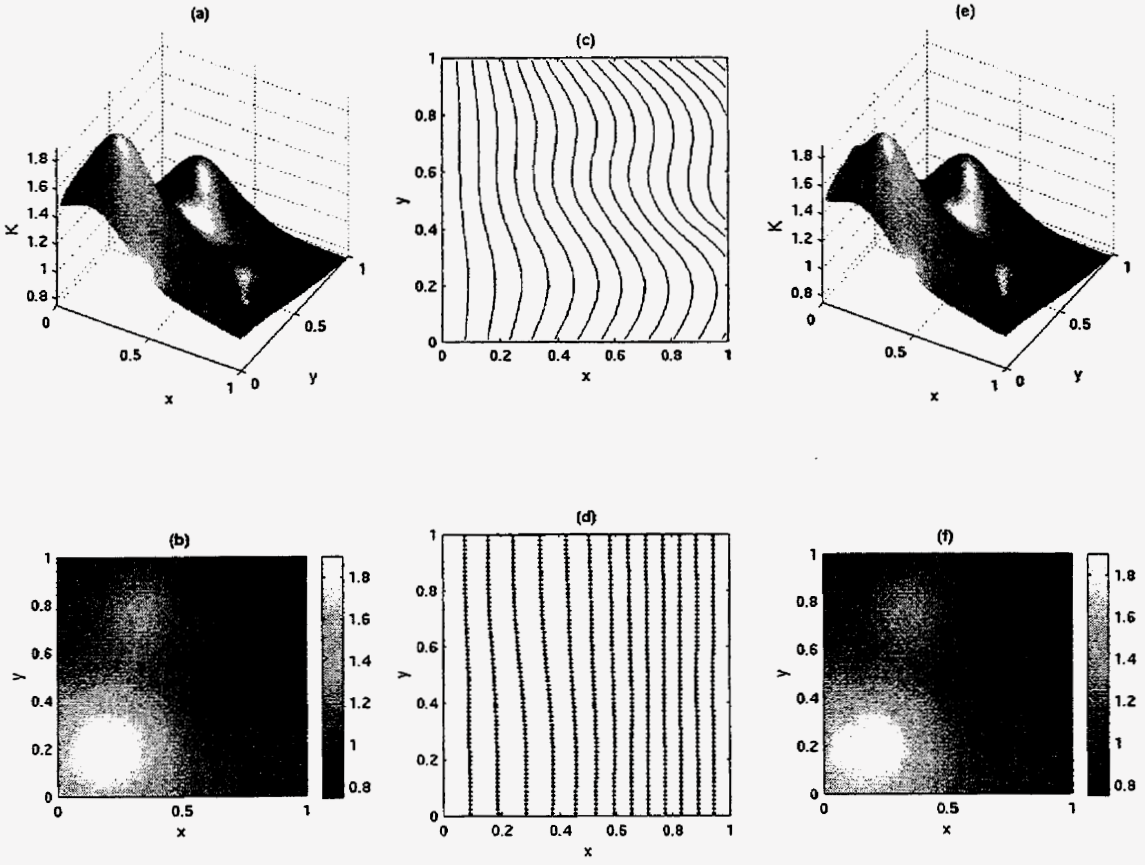

Figure 2: Application of the direct inversion method to a smoothly varying field: (a)-(b) actual permeability plots; (c) actual arrival times; (d) actual (solid lines) and inverted (dotted lines) potential profiles; (e)-(f) inverted permeability plots.

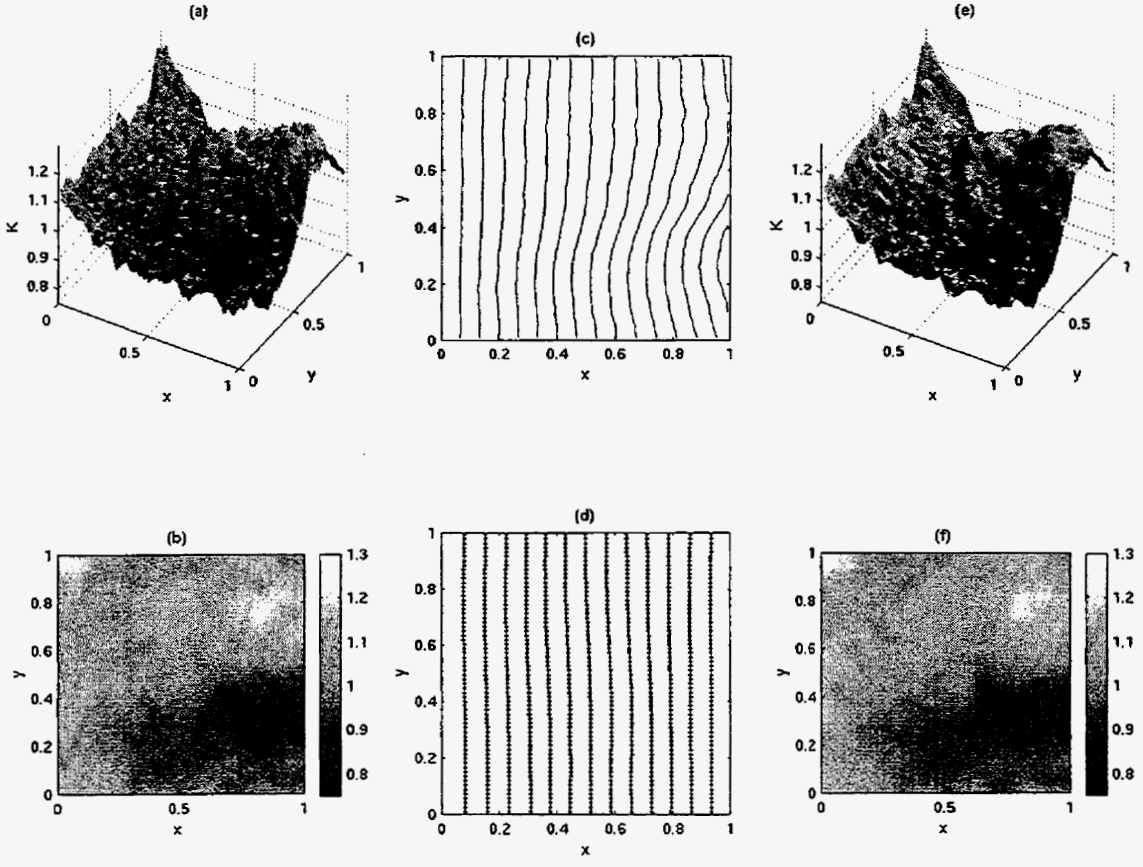

Figure 3: Application of the direct inverse method to an fBm field with $H = 0.8$: (a)-(b) actual permeability plots; (c) actual arrival times; (d) actual (solid lines) and inverted (dotted lines) potential profiles; (e)-(f) inverted permeability plots.

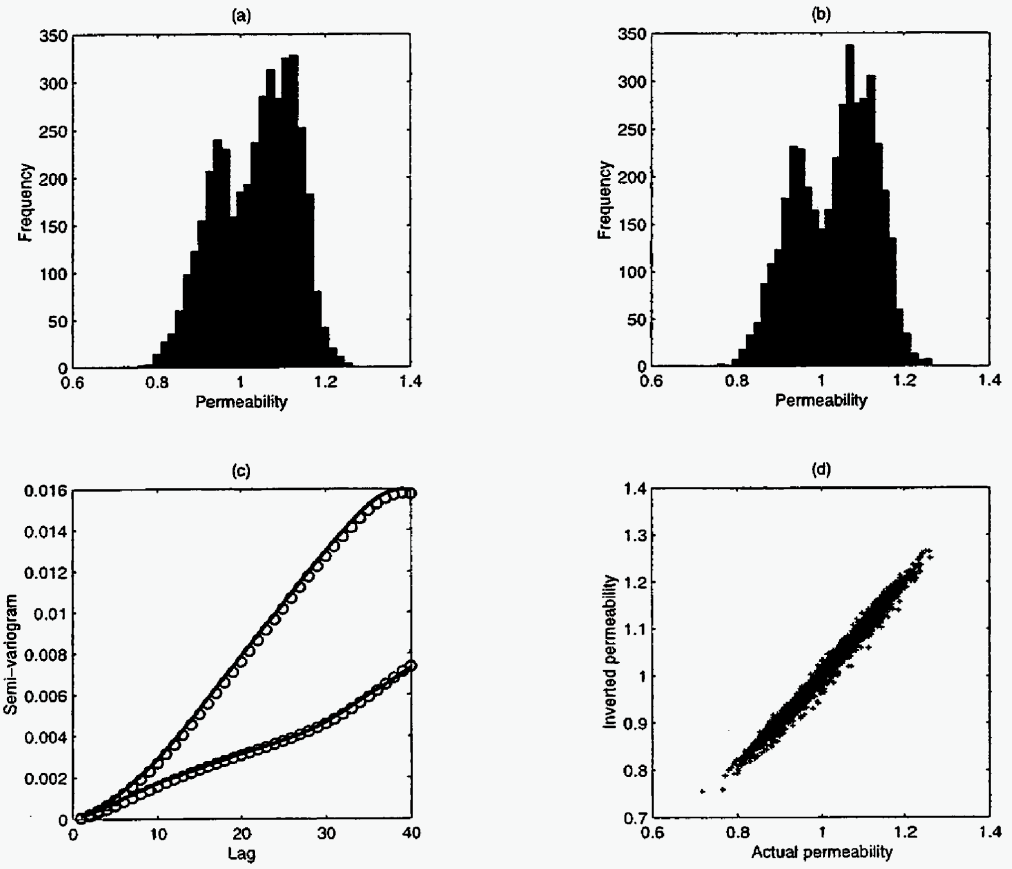

Figure 4: Statistical comparison between actual and inverted permeabilities of Fig. 3: (a) histogram of actual permeability; (b) histogram of inverted permeability; (c) semivariogram in two different directions of the actual (solid lines) and inverted (circles) data; (d) scatter plot of actual and inverted data.

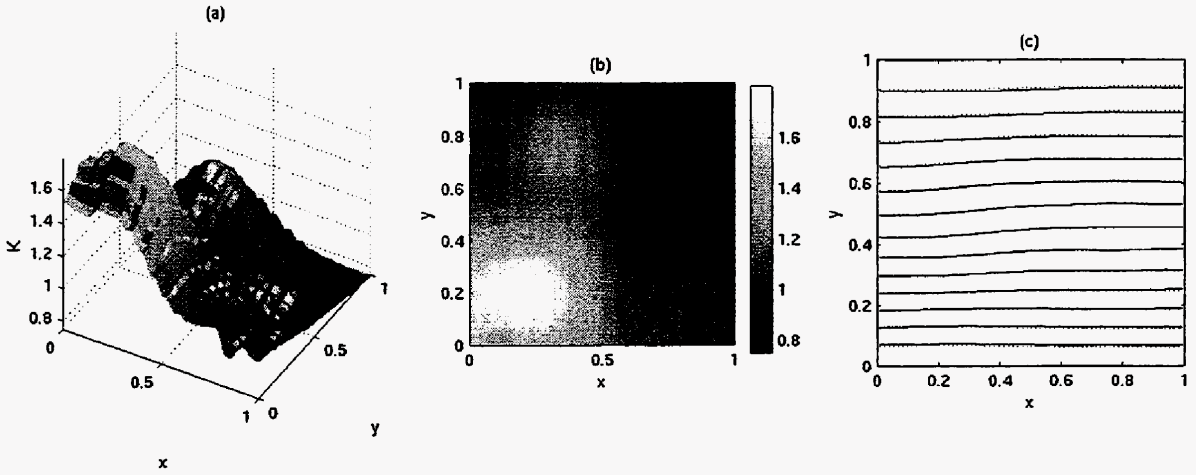

Figure 5: Application of the streamfunction approach to the medium of Fig. 2: (a)-(b) inverted permeability plots; (c) actual (solid lines) and inverted (dotted lines) streamlines.

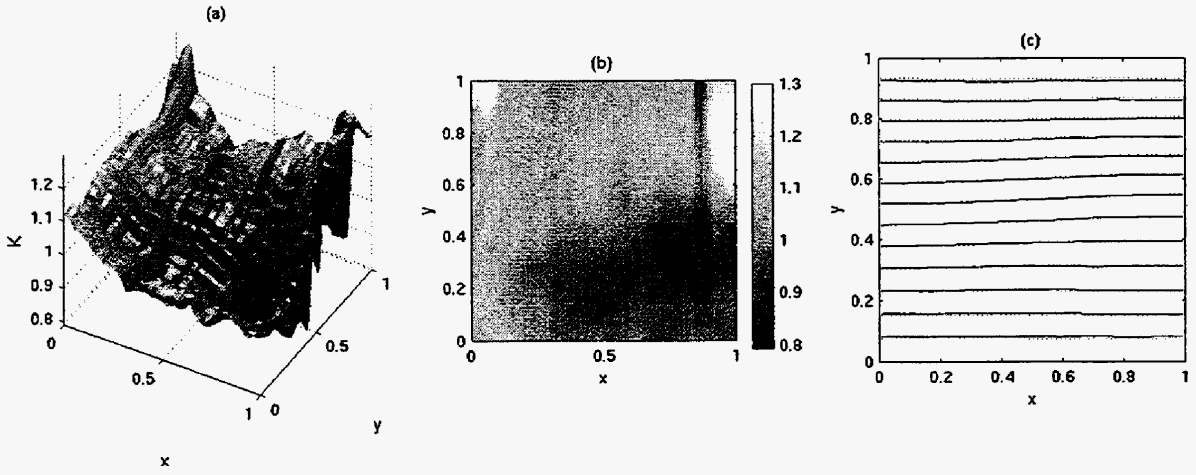

Figure 6: Application of the streamfunction approach to the medium of Fig. 3: (a)-(b) inverted permeability plots; (c) actual (solid lines) and inverted (dotted lines) streamlines.

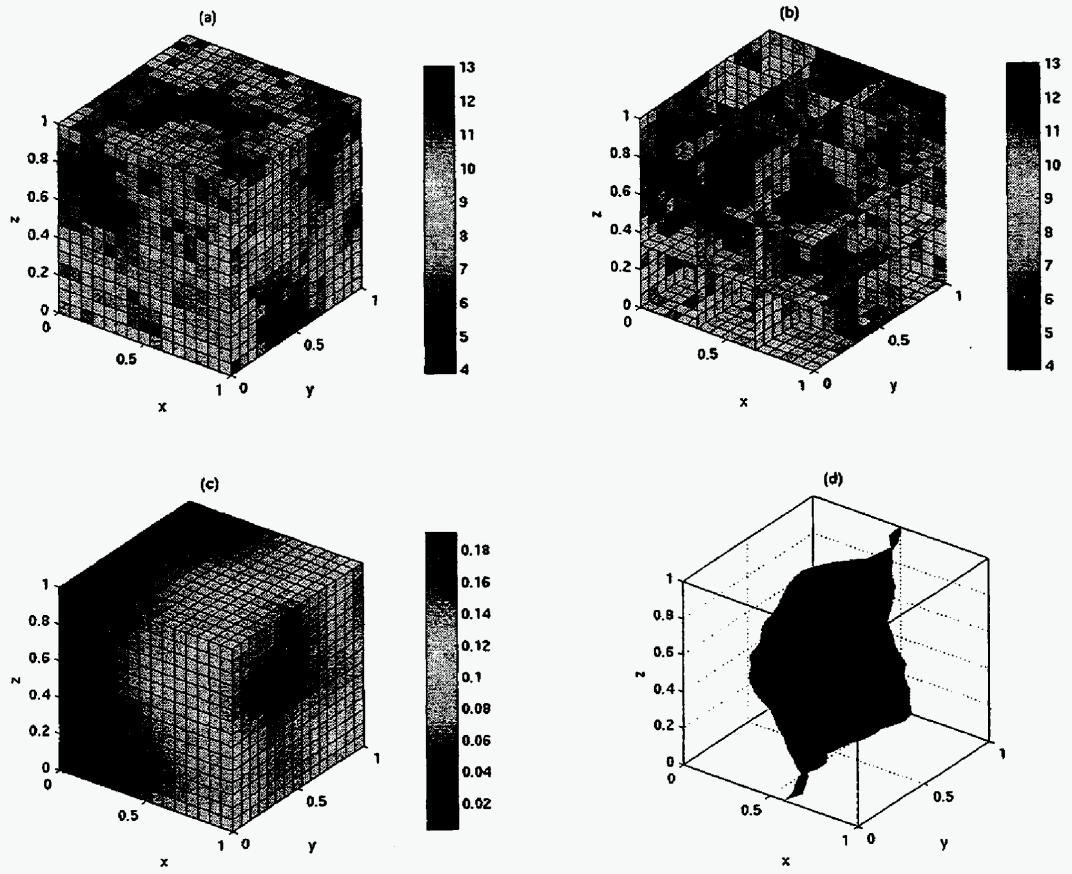

Figure 7: A 3-D permeability field and corresponding arrival times: (a)-(b) the actual permeability field in different cross-sections; (c) the arrival time distribution; (d) arrival time isosurface at $t = 0.07$.

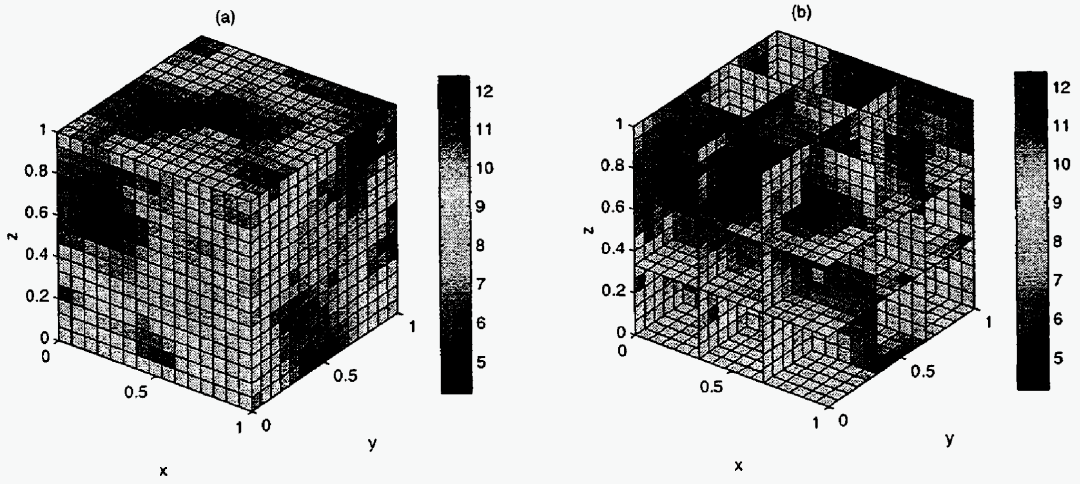

Figure 8: Application of the direct inversion method to the 3-D field of Fig. 7: (a)-(b) representation of the inverted data in different cross-sections.

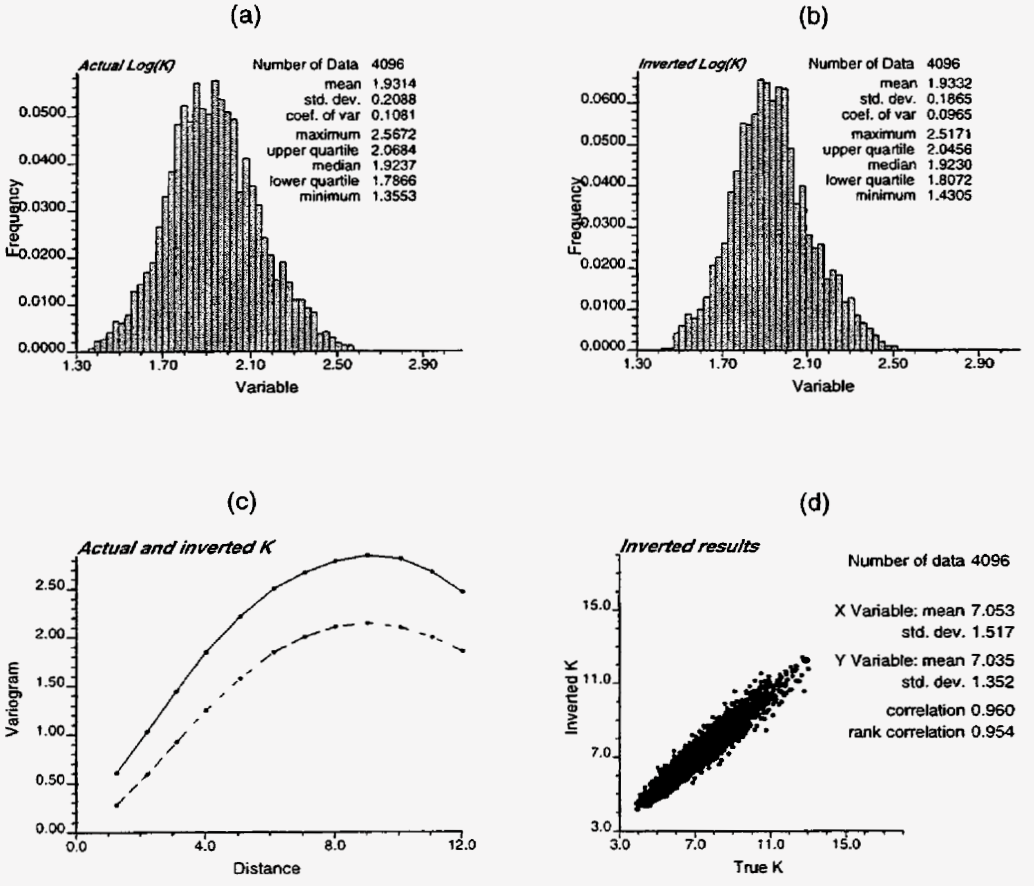

Figure 9: Statistical comparison between actual and inverted permeabilities of Fig. 8: (a) histogram of actual permeability; (b) histogram of inverted permeability; (c) omni-direction semivariogram of the actual (solid lines) and inverted (dash lines) data; (d) scatter plot of actual and inverted data.

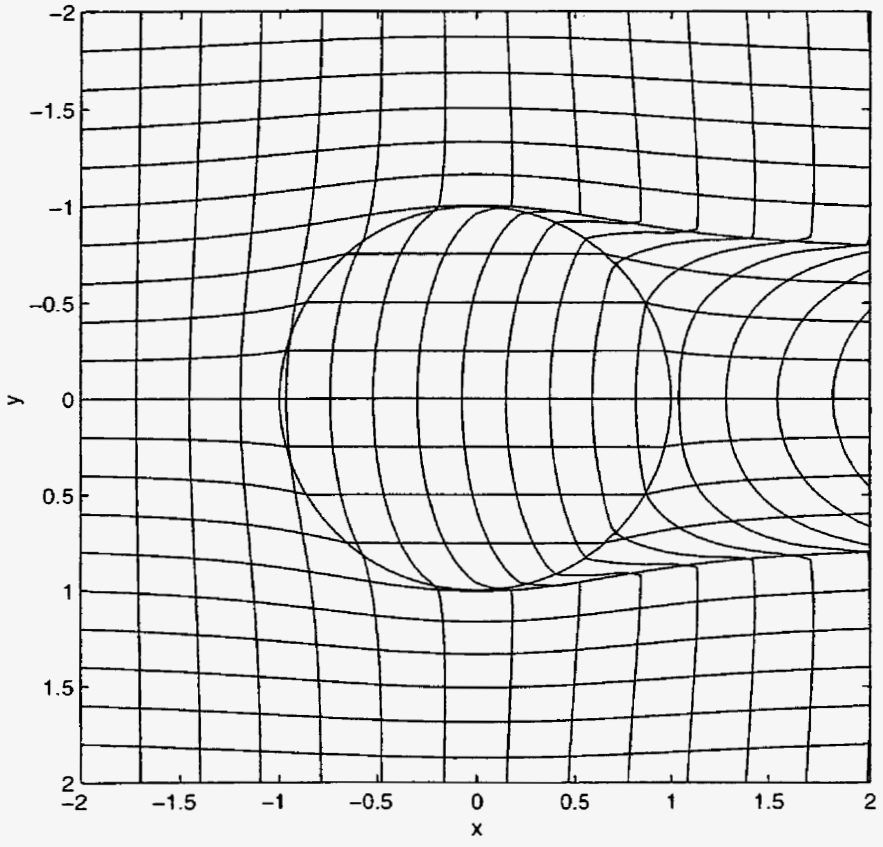

Figure 10: Streamlines and arrival time contours corresponding to a medium of uniform permeability in which a circular inclusion of lower permeability is embedded (permeability contrast is 0.6:1). The contours are calculated analytically (see Appendix). Displacement is from left to right.

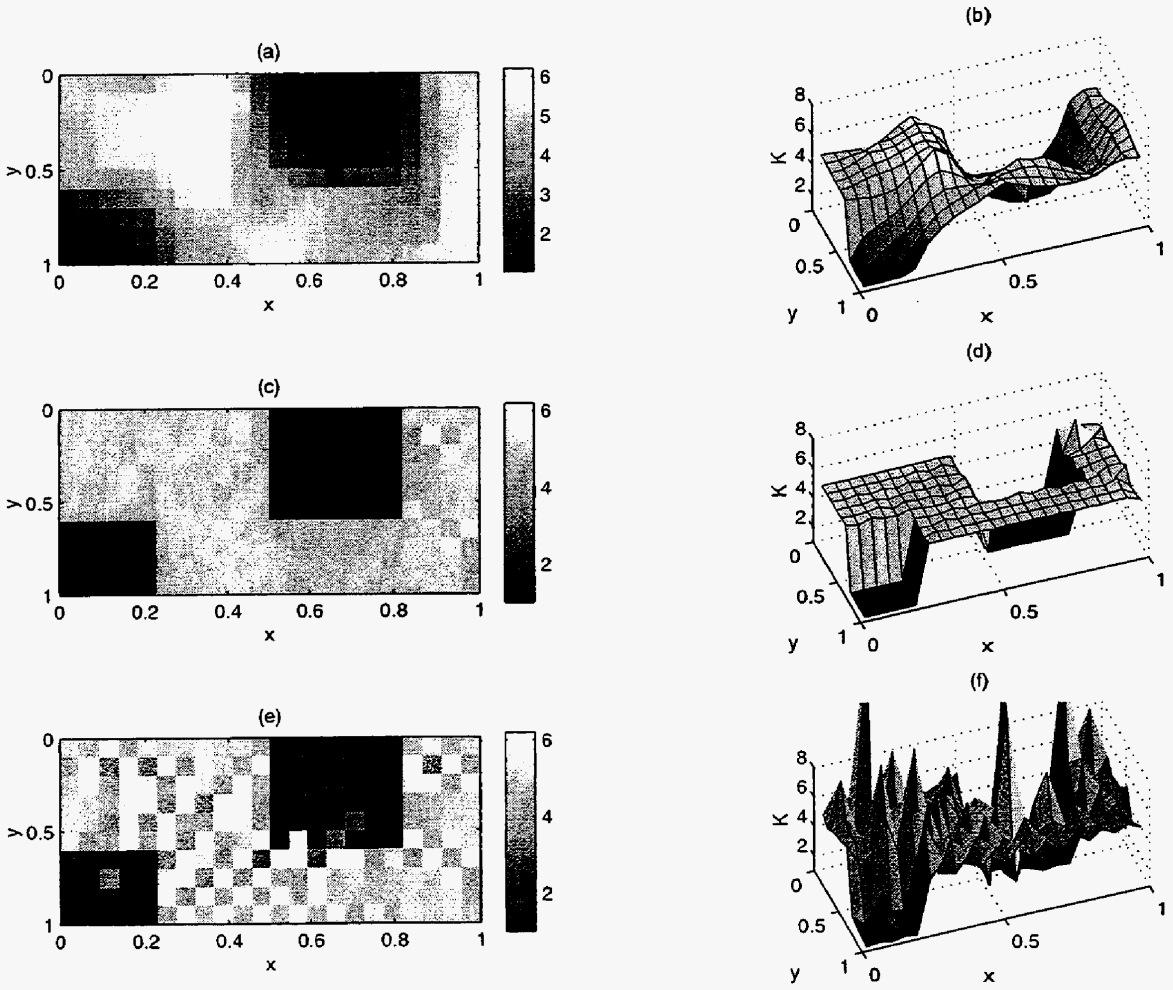

Figure 11: Application of the hybrid algorithm to a system with block discontinuities in permeability (permeability contrast is 1:5): Top two plots (a)-(b) show permeability estimates after steps 1-3 (kriging). Middle two plots (c)-(d) show permeability estimates after step 4 (optimization). Note the closeness to the actual data. Bottom two plots (e)-(f) show permeability estimates using the optimization method but with a uniform permeability initial guess.

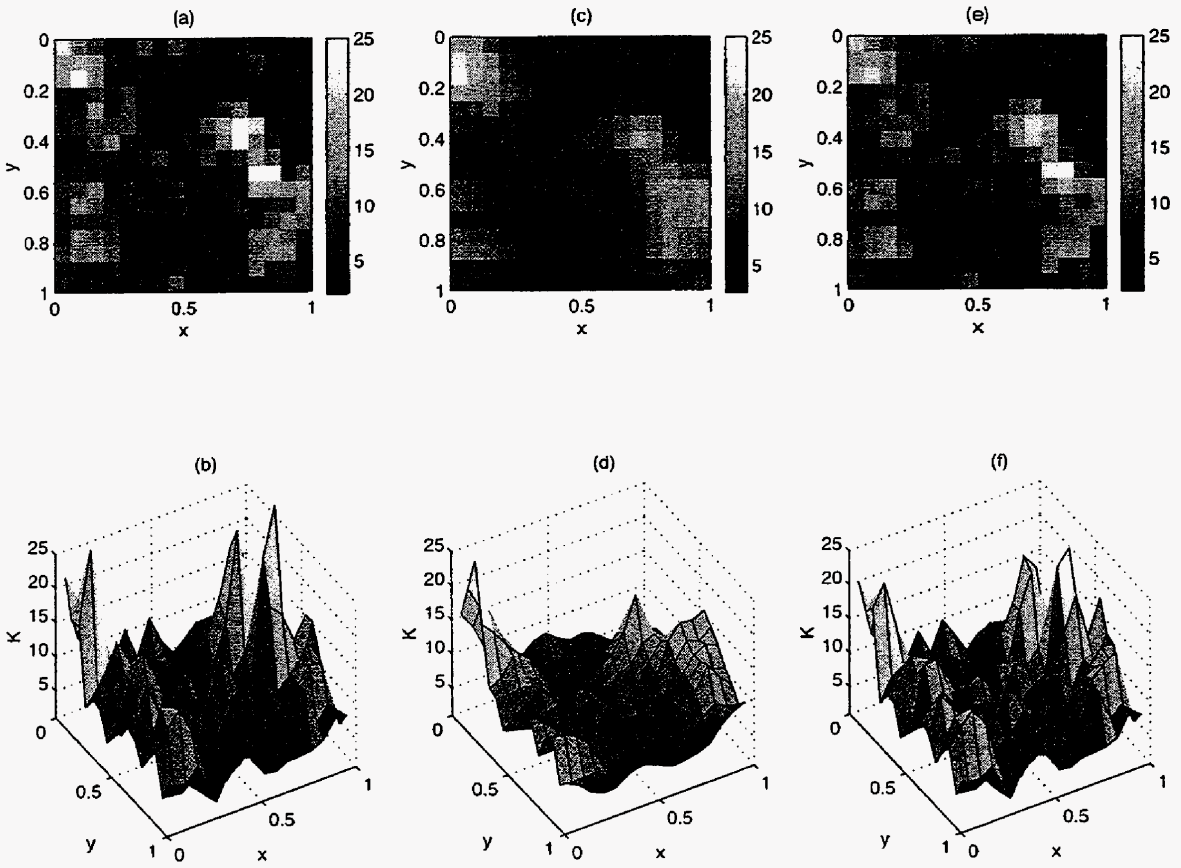

Figure 12: Application of the hybrid algorithm to a field with a log-normal distribution with maximum contrast of about 10: (a)-(b) actual permeability plots; (c)-(d) plots of permeability estimates after steps 1-3 (kriging); (e)-(f) plots of permeability estimates after step 4 (optimization). Note that the cut-off value of the colorbars in the image plots is set at 25.

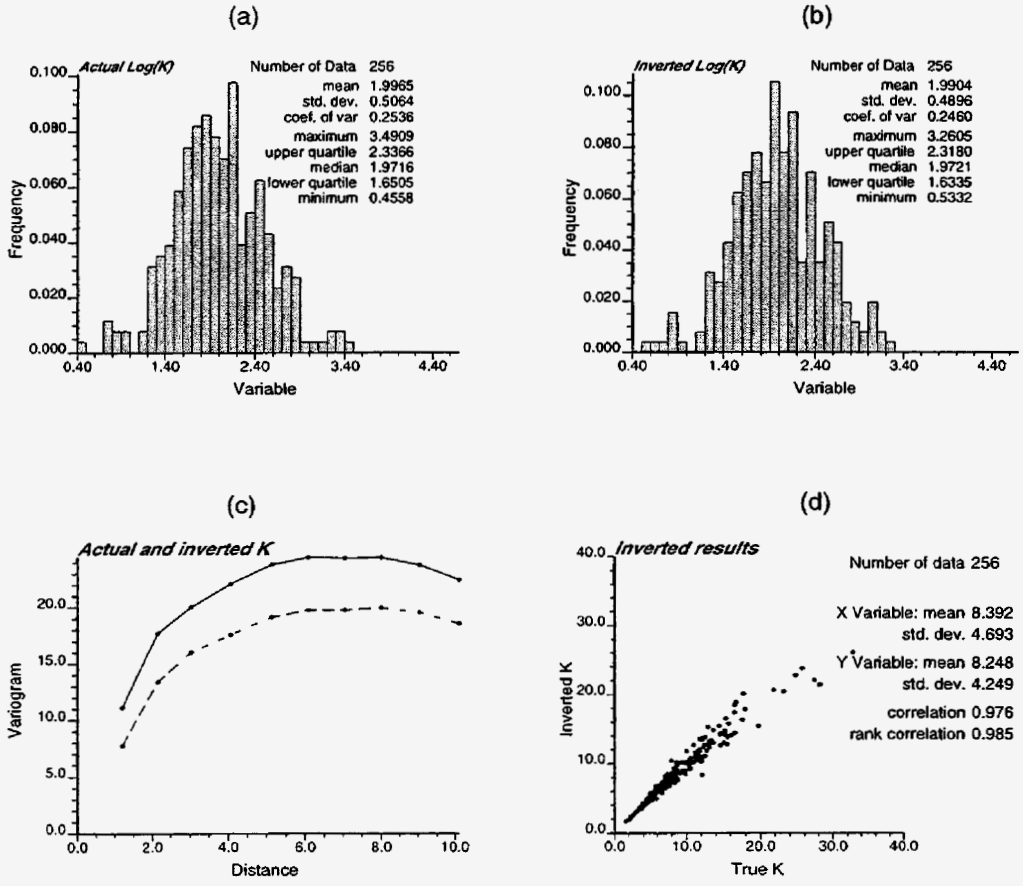

Figure 13: Statistical comparison between actual and inverted (after steps 1-4) permeabilities of Fig. 12: (a) histogram of actual permeability; (b) histogram of inverted permeability; (c) omni-direction semivariogram of the actual (solid lines) and inverted (dash lines) data; (d) scatter plot of actual and inverted data.

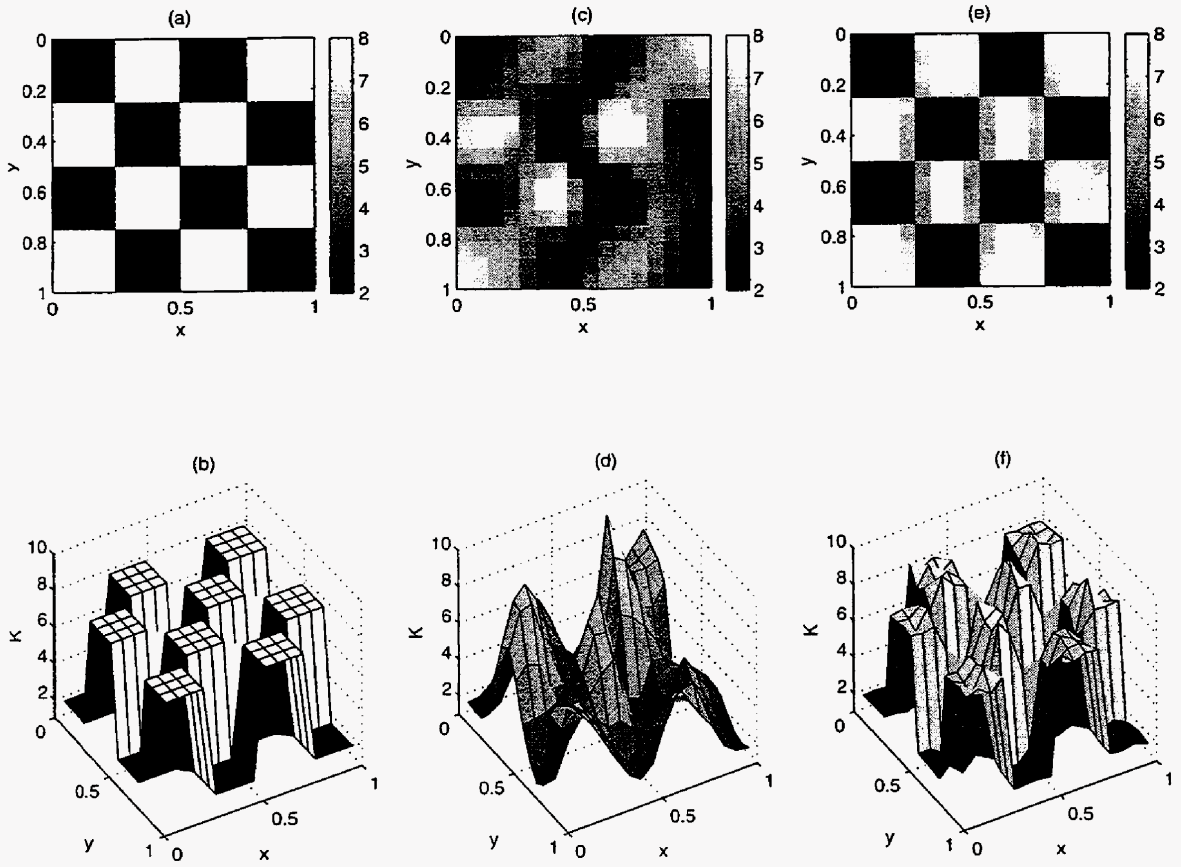

Figure 14: Application of the hybrid algorithm to a checkerboard permeability pattern (contrast is 2:8): (a)-(b) actual permeability plots; (c)-(d) plots of permeability estimates after steps 1-3 (kriging); (e)-(f) plots of permeability estimates after step 4 (optimization). Note that the cut-off value of the colorbars in the image plots is set at 8.

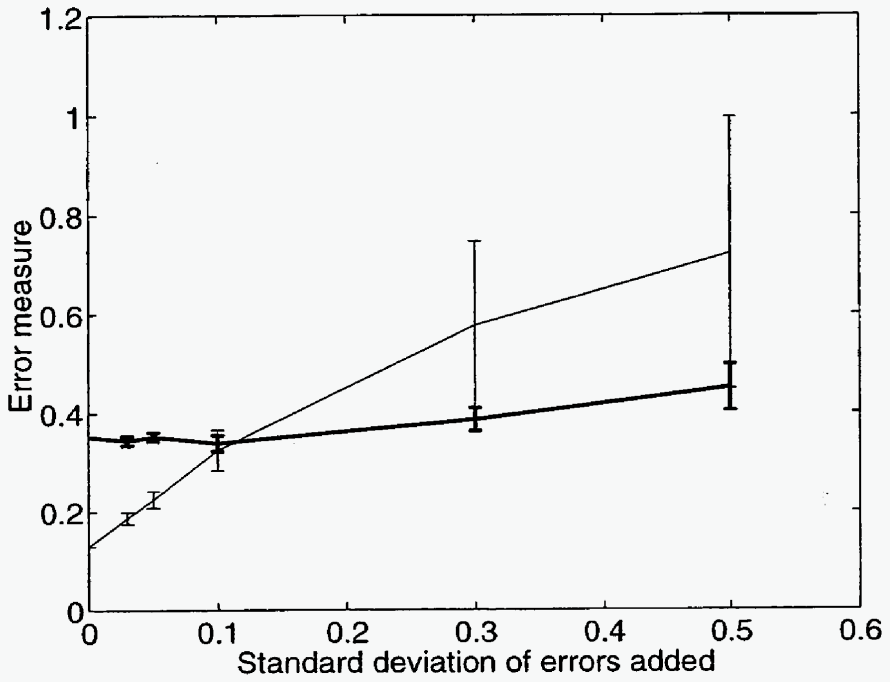

Figure 15: Sensitivity of the inverted permeability field of Fig. 12 to errors in arrival times and boundary pressure data. Inversion based on the hybrid algorithm (steps 1-4) (thin line) and on the kriging algorithm (steps 1-3) (thick line). The error measure is the normalized standard deviation of the inverted from the actual permeabilities. The input error is as described in (18) and (19).